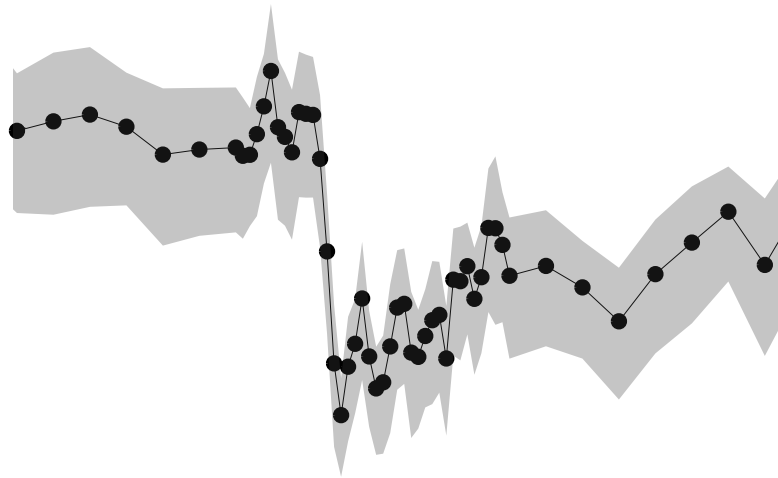


# Ultrafast demagnetization in metallic ferromagnetic / antiferromagnetic heterostructures



## Dissertation

zur Erlangung des Grades eines  
Doktors der Naturwissenschaft  
(*Dr. rer. nat.*)

am Fachbereich Physik  
der Freien Universität Berlin  
vorgelegt von

**Ivar Kumberg**

Berlin 22. November 2022

**Tag der Disputation:** 11.11.2022

- 1. Gutachter:** Prof. Dr. Wolfgang Kuch
- 2. Gutachter:** Prof. Dr. Tobias Kampfrath

## **Declaration of authorship**

Name: Kumberg

First name: Ivar

I declare to the Freie Universität Berlin that I have completed the submitted dissertation independently and without the use of sources and aids other than those indicated. The present thesis is free of plagiarism. I have marked as such all statements that are taken literally or in content from other writings. This dissertation has not been submitted in the same or similar form in any previous doctoral procedure.

I agree to have my thesis examined by a plagiarism examination software.

Date:

Signature:



# Abstract

This thesis summarizes experimental work performed on thin-film metallic and magnetic systems by time-resolved soft X-ray reflectivity and magneto-optical Kerr effect measurements. The delay-time-dependent magnetization dynamics in Co, Mn, and Ni after laser excitation are investigated in layered systems. The work aims to study the effects of antiferromagnetic coupling on de- and remagnetization dynamics in an adjacent ferromagnetic film on the ultrafast timescale. The presented work bridges the timescale from the first femtoseconds to macroscopic dynamics after several microseconds. The thesis is divided into a literature review covering the treatment and scientific context of the investigated phenomena and experimental reports where the findings of this work are presented and discussed. The presentation of the experiments is divided into four chapters.

First, differences between the ultrafast demagnetization in a Cu/Co/NiMn/Cu(001) system recorded at high and low sample base temperatures are investigated. The report shows that the antiferromagnetic alignment in the NiMn system, present at low temperature, facilitates a faster demagnetization of the adjacent Co layer compared to a magnetically disordered NiMn layer at high temperatures.

The second investigation covers the timescale of laser excitation and presents experimental evidence of the optically induced intersite spin transfer in a  $(\text{Co/Mn})_{x6}/\text{Cu}(001)$  multilayer system. An increase in the magnetic contrast in the antiferromagnetically ordered Mn layer is observed. The magnetic contrast lives for the time of excitation and indicates a realignment of the magnetic moments of the interface layers of Mn in the direction of Co.

The third chapter treats simulations of the X-ray reflectivity after laser excitation. The multilayer system investigated in the aforementioned experiment is analyzed with respect to its magneto-optical properties, and the observations recorded with the X-rays are directly correlated with the transient optical response function of the elements. Furthermore, we compare the results of the simulations of the X-ray reflectivity considering structural, electronic, and magnetic effects.

The last presented study is concerned with time-dependent magnetization dynamics recorded in Pt/Co multilayers. We investigate the delay-time-dependent Kerr effect and present experimental evidence for different dynamics in a Pt/Co bilayer system compared to a Pt/MnPt/Pt/Co system. Lastly, we investigate the effects of the spatial pump-probe overlap on the magnetization dynamics and link the observation to thermal and lateral transport phenomena.



# Kurzfassung

Diese Arbeit fasst experimentelle Untersuchungen an metallischen und magnetischen Dünnschichtsystemen zusammen, die mit zeitaufgelösten Messungen der Reflektivität weicher Röntgenstrahlung und dem magneto-optischen Kerr-Effekt untersucht wurden. Die verzögerungszeitabhängige Magnetisierungsdynamik in Co, Mn und Ni nach Laseranregung wird in geschichteten Systemen untersucht. Ziel der Arbeit ist es, die Auswirkungen der antiferromagnetischen Kopplung auf die De- und Remagnetisierungsdynamik in einem benachbarten ferromagnetischen Film auf der ultraschnellen Zeitskala zu untersuchen. Die vorliegende Arbeit überbrückt die Zeitskala von den ersten Femtosekunden bis zur makroskopischen Dynamik nach mehreren  $\mu\text{s}$ . Die Arbeit ist unterteilt in eine Literaturübersicht über die Beschreibung und den wissenschaftlichen Kontext der untersuchten Phänomene und in experimentelle Berichte, in denen die Ergebnisse dieser Arbeit vorgestellt und diskutiert werden. Die Darstellung der Experimente ist in vier Kapitel unterteilt.

Zunächst werden die Unterschiede zwischen der ultraschnellen Entmagnetisierung in einem Cu/Co/NiMn/Cu(001)-System untersucht, welche bei hoher und niedriger Proben temperatur aufgezeichnet wurde. Die Untersuchung zeigt, dass die antiferromagnetische Ordnung im NiMn-System, die bei niedriger Temperatur vorhanden ist, eine schnellere Entmagnetisierung der angrenzenden Co-Schicht im Vergleich zu einer magnetisch ungeordneten NiMn-Schicht bei hohen Temperaturen ermöglicht. Die zweite Untersuchung deckt die Zeitskala der Laseranregung ab und präsentiert experimentelle Daten für den optisch induzierten Intersite-Spintransfer in einem  $(\text{Co/Mn})_{x6}/\text{Cu}(001)$ -Mehrschichtsystem. Es wird eine Zunahme des magnetischen Kontrasts in der antiferromagnetisch geordneten Mn-Schicht beobachtet. Der magnetische Kontrast bleibt für die Dauer der Anregung bestehen und deutet auf eine Neuausrichtung der Magnetisierungsrichtung der magnetischen Grenzflächenschichten von Mn in Richtung von Co hin. Das dritte Kapitel befasst sich mit Simulationen der Röntgenreflexion nach der Laseranregung. Das im vorgenannten Experiment untersuchte Mehrschichtsystem wird hinsichtlich seiner magneto-optischen Eigenschaften analysiert, und die mit der Röntgenstrahlung aufgenommenen Beobachtungen werden direkt mit der transienten optischen Antwortfunktion der Elemente in Verbindung gebracht. Darüber hinaus werden die Ergebnisse der Simulationen der Röntgenreflexion, unter Berücksichtigung struktureller, elektronischer und magnetischer Effekte, verglichen. Die letzte vorgestellte Studie befasst sich mit der zeitabhängigen Magnetisierungsdynamik, die in Pt/Co-Multilayern aufgezeichnet wird. Wir messen den verzögerungszeitabhängigen Kerr-Effekt und präsentieren experimentelle Beweise für eine unterschiedliche Dynamik in einem Pt/Co-Zweilagensystem im Vergleich zu einem Pt/MnPt/Pt/Co-System. Schließlich untersuchen wir die Auswirkungen des räumlichen Pump-Probe-Überlapps auf die Magnetisierungsdynamik und verknüpfen die Beobachtungen mit thermischen und lateralen Transportphänomenen.

*Kurzfassung teilweise übersetzt mit [www.DeepL.com/Translator](http://www.DeepL.com/Translator) (kostenlose Version)*

# Contents

<b>Abstract</b>	<b>i</b>
<b>Kurzfassung</b>	<b>iii</b>
<b>1 Introduction</b>	<b>1</b>
1.1 What is ultrafast magnetization dynamics? . . . . .	1
1.2 Contribution by this study . . . . .	3
<b>2 Experimental means to follow sub-ps dynamics</b>	<b>5</b>
2.1 Optical probes . . . . .	5
2.1.1 Light sources . . . . .	6
2.1.2 Polarization, magnetization and interfaces . . . . .	8
2.1.3 Time-resolved MOKE . . . . .	14
2.2 X-rays to investigate magnetism . . . . .	21
2.2.1 Pulsed X-rays . . . . .	22
2.2.2 Magnetic interaction . . . . .	24
2.2.3 Resonant X-ray scattering and reflectivity . . . . .	28
2.3 Very low and high frequencies and other notable techniques . . . . .	30
2.4 Summary . . . . .	32
<b>3 Emergence and treatment of ultrafast magnetization</b>	<b>35</b>
3.1 Ultrafast quench and temperature models . . . . .	35
3.1.1 The three-temperature model (3TM) . . . . .	36
3.1.2 The microscopic 3TM . . . . .	38
3.2 Spin transport . . . . .	39
3.3 Optically induced spin transfer . . . . .	41
3.4 Summary . . . . .	42
<b>4 Accelerated demagnetization in a FM/AFM bilayer</b>	<b>45</b>
4.1 The Co/NiMn/Cu(001) system . . . . .	45
4.1.1 Thin film deposition . . . . .	46
4.1.2 Sample characterization . . . . .	50
4.2 X-ray magnetic circular dichroism in reflectivity . . . . .	54
4.2.1 Angle- and energy-resolved magnetic reflectivity . . . . .	54
4.2.2 Time-resolved dynamics . . . . .	57
4.3 Accelerated demagnetization due to ultrafast transport . . . . .	64
4.4 Summary and conclusion . . . . .	70

<b>5</b>	<b>Magnetization in the presence of the laser field</b>	<b>73</b>
5.1	The Co/Mn system . . . . .	73
5.2	Light-induced magnetism in an AFM . . . . .	77
5.3	Summary and Conclusion . . . . .	81
<b>6</b>	<b>Light-induced magneto-optics in the soft X-ray range</b>	<b>83</b>
6.1	Simulations of the X-ray reflectivity . . . . .	84
6.2	Time-dependent optical refraction . . . . .	94
6.3	Effects of electronic redistribution . . . . .	104
6.4	Photon energy dependence of the XRR . . . . .	108
6.5	Summary and Conclusion . . . . .	110
6.6	Appendix . . . . .	112
6.6.1	Examples . . . . .	112
<b>7</b>	<b>Demagnetization in Co/Pt bilayers</b>	<b>117</b>
7.1	Ultrafast magnetization dynamics in Co/Pt . . . . .	117
7.1.1	Comparison of Co/Pt and Co/Pt/MnPt . . . . .	118
7.1.2	Slow and fast magnetic recovery in Co/Pt . . . . .	121
7.2	Summary and conclusion . . . . .	133
<b>8</b>	<b>Conclusion</b>	<b>135</b>
	<b>List of Publications</b>	<b>137</b>
	<b>Bibliography</b>	<b>143</b>
	<b>Acknowledgments</b>	<b>163</b>

# Chapter 1

## Introduction

### 1.1 What is ultrafast magnetization dynamics?

The term "ultrafast" contains the Latin *ultra* which translates to *extremely*, thereby setting the relevant timescale. However, what is the timescale of interest?

It is consensus to label events happening faster than 1 ns, or in other words, with durations shorter than  $10^{-9}$  s, as ultrafast. Typically the unit of measurement for these time intervals is femtoseconds, i.e.,  $10^{-15}$  s, on which observations are made. In other numbers, an ultrafast process that takes less than 1 ns could be theoretically observed more than one billion times per second. Since this is the timescale for atomic and molecular processes, it seems natural that a macroscopic feature like magnetization, inherently linked to the construction of matter by atoms and charges, exhibits interesting behavior at ultrafast timescales. That this is not the case and that coherent magnetization effects on this timescale are to some extent a surprise, which makes them a pretty exciting research topic, is outlined in the following.

Magnetic phenomena are governed by the spin property of matter, most importantly the electron's intrinsic spin and the magnetic moment arising from the electrons orbital "motion". The nuclear contribution appearing for isotopes with an odd number of nuclei is not considered in the following since the contribution to the magnetization is more than five orders of magnitude smaller than the electronic one and furthermore, the techniques employed here are only sensitive to the electronic magnetic moment. It is not in the scope of this thesis to derive basic models of magnetism and explain their intrinsic quantum nature. However, it is enough to consider intuitive arguments coming from established models to understand why manipulation of magnetization at sub-ps timescales is not trivial.

Magnetization dynamics is typically governed by the precessional motion of spins and the recovery thereof into a steady state. Generally, the Larmor precession, which describes the spin precession around an applied field axis, results in a time of about 2 ps for one spin revolution at a field of 1 T, setting the boundary for coherent magnetization reversal to 1 ps in reasonable fields. This is roughly matched by experiments performed at the Stanford linear accelerator with very high and short magnetic field pulses that found a limit of 2 ps for deterministic spin reversal by precession [2]. The image of the rotating three-dimensional Heisenberg-like spin can still be employed to a certain degree, but with shorter time intervals the reservoirs contributing to the magnetization are not in an equilibrium anymore, and the exchange of energy and angular momentum between electrons and lattice have to be treated separately to describe observations. The field of ultrafast magnetism, which became accessible with the advent of

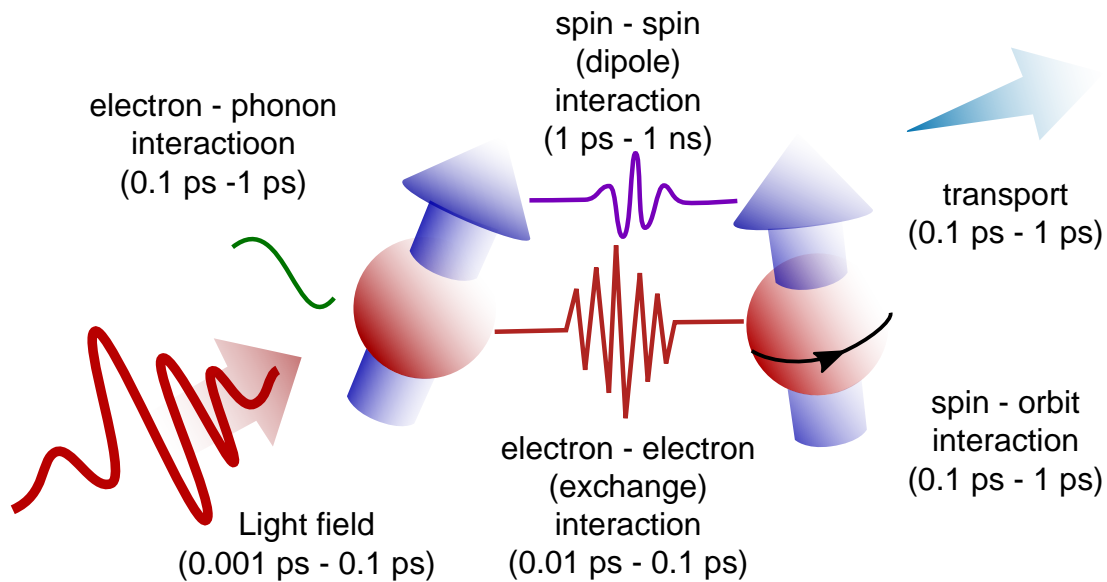


**Figure 1.1:** Depiction of the involved processes in ultrafast magnetization experiments together with typical equilibration timescales. The discussion of magnetization dynamics revolves around the interplay of the spin and electron system with the surrounding. At ultrafast timescales the relevant coupling parameters, like the spin-orbit and exchange interaction, are becoming time-dependent parameters themselves and the fundamental interactions cannot be described with equilibrium models anymore. After the electronic excitation by light, the interaction with the lattice, transport, and lastly spin precession become relevant. Time scales are reproduced from [1].

ultrashort laser pulses, thus aims to explore a timescale where controlled precession is not accessible anymore. Therefore, control of the magnetic properties involves understanding and tailoring more fundamental interactions such as the spin-orbit coupling and the exchange interaction itself. The relevant timescales, along with the mentioned processes in condensed matter, are depicted schematically in Fig. 1.1.

Academically, this is a challenge pushing the boundaries of our understanding of the building blocks of nature. As a scientist, the opportunity to unveil new effects and achieve a deeper understanding of the interplay of magnetic moments, electronic population, and lattice dynamics is already rewarding. Nevertheless, the questions addressed go beyond a purely scientific purpose since the possibility to flip magnetic states on timescales faster than 1 ps could enable a whole new class of devices for information storage, transfer, and manipulation. A modern magnetic memory requires about 1 ns to write/read one bit. Clocking speeds of contemporary processing units reached gigahertz frequencies leading to a billion operations per second. One could say that modern information technology stands right at the frontier of ultrafast technology. Having access to low-energy picosecond read/write speeds integrated into a non-volatile magnetic recording device does directly supply the demand for faster and more energy-conserving data handling [3, 4].

## 1.2 Contribution by this study

This thesis connects to the ultrafast magnetism research by investigating light-induced magnetization effects that exist only for some picoseconds in coupled metallic thin-film systems. This includes the quench of magnetization happening faster than 1 ps, the recovery taking hundreds of ps, and almost instantaneous effects happening only in the presence of the light field. Since others have already established models of ultrafast magnetization in ferromagnets - a short review of the models is presented in chapter 3 - this work is concerned with the coupling of ferromagnets and antiferromagnets and the influence of the latter on the dynamics. Some important questions addressed in the presented work are:

- Does a coupling between two adjacent layers, one with a ferromagnetic and one with an antiferromagnetic long-range order, influence the ultrafast quench of magnetization in the ferromagnet?
- What are the channels of angular momentum and energy flow in coupled metallic heterostructures?
- What happens at the earliest timescale when the exciting laser pulse arrives at the sample?
- How does the recovery of magnetization evolve in coupled systems?

Not all questions can be answered with certainty, but some essential aspects of ultrafast dynamics in layered systems are successfully identified, and the obtained results are summarized in this thesis.

Additionally, this thesis contains information maybe not so relevant for the reader already familiar with the topics of ultrafast magnetism, namely **chapter 2**, where contemporary methods to measure and observe sub-ps magnetization dynamics are briefly reviewed, and **chapter 3**, in which the currently used models describing magnetization and the observations are discussed in a somewhat chronological fashion. Following the review of the contemporary models of ultrafast magnetism, the experimental results are presented.

An influence of the long-range antiferromagnetic order on the demagnetization time of an adjacent ferromagnetic layer is found and attributed to more efficient spin transport channels compared to a paramagnet. The details of this study are presented in **chapter 4**. Furthermore, it is predicted, and in the frame of this work experimentally verified, that direct electronic excitation by a laser field can lead to transient ferromagnetic spin alignment in an antiferromagnetically ordered system, this is presented in **chapter 5**. The primary experimental technique employed in this work, namely resonant magnetic X-ray reflection, and the consequence of using the related dichroism as an observable of the magnetism is analyzed with scrutiny to rule out misinterpretation of the observed intensities, this is presented in **chapter 6**. A study of ultrafast demagnetization in a system where the antiferromagnetically ordered layer is separated by a spacer layer from the ferromagnetic film is presented in **chapter 7**. Furthermore, we explore the influence of the lateral energy distribution in the probed area on the observed dynamics in experiments employing near-infrared light.

Lastly, **chapter 8** presents a final statement on the observations made in the frame of this work and grants an outlook on possible continuations of this work as well as a general outlook of the field of ultrafast magnetism.



# Chapter 2

## Experimental means to follow sub-ps dynamics

This chapter introduces the most commonly employed experimental techniques to measure ultrafast magnetization dynamics. To track events happening within hundreds of femtoseconds, a scale that is of similar length or preferably shorter is required. Since electronic equipment only provides rise times of nanoseconds or several hundred picoseconds for signal acquisition, ultrafast research is performed almost exclusively with ultrashort light pulses that can be as short as 100 attoseconds, i.e.,  $10^{-16}$  s [5]. Ultrashort laser pulses provide an ideal tool to investigate events happening at the relevant timescales. Therefore, a typical measurement of ultrafast magnetization involves a pump laser pulse, often provided in the infrared (IR) to visible wavelength region, and a probe pulse to detect the induced dynamics. By varying the time delay between pump and probe pulse, both having a width in time of around 100 fs, it is possible to trace the dynamic response of a (magnetic) system after excitation. Although all presented techniques employ a pump-probe scheme, there are important distinctions in how information about the magnetic system is obtained, justifying a closer look at the different experiments. The differences mainly stem from the energy or wavelength of the probe pulse used for the investigations serving in the following as the natural divider between the experiments. At first, schemes using near-IR to visible probes are outlined, and secondly, X-ray probes, which are the primary source of information in this work, are discussed.

### 2.1 Optical probes

It is not the concern of this work to explain or derive ways of creating ultrashort laser pulses in the visible or infrared range from scratch. Nevertheless, a brief overview of pulse generation and manipulation is given at the beginning. The section establishes the language, shows limits, and illustrates the framework under which experiments are performed.

First, the generation of laser pulses, then the amplification and temporal modulation, the reflection and transmission at surfaces, and lastly the application of laser pulses in the experiments is introduced.

## 2.1.1 Light sources

### Ultrashort pulse generation

Ultrashort laser pulses, i.e., for our purposes, pulses with durations shorter than 1 ps, can be achieved routinely in tabletop lab systems. The lab standard and most popular ones are titanium:sapphire (Ti:Al<sub>2</sub>O<sub>3</sub> or Ti:Sa) oscillators pumped by a frequency-doubled pump laser using neodymium-doped yttrium aluminum garnet or Nd:YAG as the gain medium and laser diodes for pumping it. Employing Ti:Sa as a gain medium has the great advantage that it possesses a very broad absorption around 500 nm and an even wider emission profile of more than 200 nm centered around 800 nm [6, 7]. This enables convenient pumping with efficient Nd:YAG lasers that output stable radiation at  $\sim 1064$  nm, which is frequency-doubled to 532 nm. Furthermore, the Al<sub>2</sub>O<sub>3</sub> crystals possess a heat conduction of  $\sim 30 \text{ W m K}^{-1}$  at 300 K [8] close to that of metals<sup>1</sup> enabling continuous wave (cw) pumping powers up to 20 W due to the efficient heat transport away from the crystal. This conversely results in high power, stable cw operation at 800 nm of the Ti:Sa system.

It is surprisingly easy to convert the high-intensity cw radiation into ultrashort laser pulses by self-mode-locking. The general idea is that all spectral modes propagating in the cavity are phase-matched, i.e., mode-locked. They travel together in time and space, leading to a coherent superposition and thus a narrow, high-intensity peak of the electric and magnetic field. The temporal width becomes sharper the more modes are overlapped. Mathematically it is given by the Fourier transform (FT) of the spectral function, which is typically Gaussian and is therefore highly dependent on the spectral bandwidth of the laser. As mentioned before, the Ti:Sa system provides a very large emission window of more than 200 nm, leading to a theoretical transform limit or shortest pulse with a full-width half-maximum (FWHM) of around 5 fs. Many ways to achieve pulsed operation have been identified, active mode-locking by external modulation [10], passive mode-locking by using saturable absorbers [11], and most efficiently and elegantly self-mode-locking by Kerr lensing [12].

Historically, this was apparently observed by accident as a misalignment of the cavity and an additional "mechanical shock" resulted in a stable pulsed operation with a FWHM of 60 fs [12]. Initially, it was labeled "magic mode-locking" since the explanation was delivered later. The high intensity in the Ti:Sa crystal leads to lensing (Kerr lensing) that focuses the high-intensity wavefronts. By simply adding an aperture blocking the low energy cw light behind the Ti:Sa and creating a random wavefront distortion that leads to a sudden high power "pulse", a stable pulsed operation can be established since only the high-intensity pulse is amplified.

Typical times for a mode-locked Ti:Sa system are 10 fs to 150 fs per pulse at 800 nm center wavelength and a repetition rate of 75 MHz, resulting in peak powers of up to 150 kW and 13 nJ per pulse. For experiments, the pulse is focused onto the sample with typical diameters of some micrometers. Using a circular profile one can estimate the incident fluence  $f$  like

$$f = \frac{P_{av}}{R_{rep}} \frac{4}{\pi d^2}. \quad (2.1)$$

With a spot diameter of  $d = 5 \mu\text{m}$ , an average laser power of  $P_{av} = 1 \text{ W}$ , and a repetition rate of  $R_{rep} = 75 \text{ MHz}$ , a fluence of  $f = 60 \text{ mJ cm}^{-2}$  is expected. These parameters vary of course with each system and repetition rates go from 100 Hz to 200 MHz, reasonable spot sizes range from some  $\mu\text{m}$  to several 100  $\mu\text{m}$ , and the average power goes from 1 mW up to several W in

---

<sup>1</sup>For example steel with  $50 \text{ W m K}^{-1}$  [9] at 300 K

amplified systems.

The Ti:Sa system, being the lab standard and the one used in the frame of this work, is, of course, not the only one capable of achieving the required pulses in the near-IR to the visible range for ultrafast investigations. Similarly, mode-locking as a technique is not the only solution to achieve ultrashort laser pulses. Other examples of gain media are chromium-doped Forsterites ( $\text{Cr}^{4+}:\text{Mg}_2\text{SiO}_4$ ) capable of emitting 14 fs laser pulses at  $1.3\ \mu\text{m}$  [13] or ytterbium-doped glass ( $\text{Yb}^{3+}:\text{glass}$ ) where 60 fs pulses at  $1.06\ \mu\text{m}$  have been reported [14]. Pulses of  $<100$  fs duration can also be achieved in diode-pumped (Er or Yb doped) fibers where self-phase modulation in the fiber leads to spectra broadening and consequent pulse compression [15].

## Pulse manipulation

An essential aspect of dealing with ultrashort pulses is maintaining temporal and spatial coherence. It has to be ensured that the pulse that arrives at the sample is sufficiently short and intense to study ultrafast magnetism. For probing, low powers of some mW are usually sufficient for detection, while the pump pulse needs to deliver enough power to excite the system noticeably. Furthermore, control over both pulses' phase, polarization, and frequency is necessary to fully characterize an experiment. In the following, ways of controlling the relevant parameters for visible and near-IR pulses are presented.

The most important aspect is to keep the pulses short at the point of the measurement. Since an ultrashort laser pulse is comprised of a high number of spectral modes, traveling through a medium leads to dephasing due to chromatic dispersion. The refractive index  $n$  is, in general, dependent on the wavelength  $\lambda$  and positive, for example in air. The phase velocity with which a wave travels through a medium is given by  $v_p = \frac{c}{n}$ . Having a wavelength-dependent velocity thus induces a non-constant phase relation and consequently a temporal broadening of the pulse. In air, the refractive index of visible and IR light is monotonically decreasing with the wavelength [16], therefore longer wavelengths will lead the pulse, and shorter ones will trail behind. This is usually termed "chirp" and in the example case, a *positive* chirp, since higher wavelengths lead the pulse. To avoid, or at least reduce, the pulse broadening, a compression by prism or grating pairs is employed. With the gratings or prisms a negative chirp is induced matching the positive chirp acquired during the travel time to the sample. Due to the pulse's wavelength-dependent path in such an arrangement, a certain delay between the modes can be created. By changing the grating (prism) distance and tuning the relative angle, control over the chirp is achieved, and the shortest duration of the pulse is obtained.

Often magnetism is investigated on metal surfaces that possess a high reflectance<sup>2</sup> in the visible to IR region. This is an issue when trying to excite the electronic system strongly. Therefore, to achieve noticeable effects, the pump pulse needs to carry enough power to heat the electronic system at least close to the Curie temperature, the reasons are discussed in chapter 3. An amplification stage can be added to the set-up to ensure that enough power is contained in the pulse. Usually, it is sufficient to amplify the pump pulse and leave the probe unaltered, but in some cases, it is beneficial to obtain the probe later from an amplified source. Generally, a single laser system is used to generate both pump and probe. A beam splitter divides the power into both branches, separating pump and probe, for example, by polarization. The field of pulse amplification easily fills books, therefore only two ways of achieving sufficient pulse power are discussed in the following.

---

<sup>2</sup>For example 70 % for Cu at  $45^\circ$  angle of incidence and unpolarized 800 nm radiation [17].

The most straightforward way to amplify a pulse is to send it repeatedly through the same gain medium while maintaining a high population inversion inside. This is commonly realized in *regenerative* [18] or *multipass* [19] systems, where the seed pulse travels multiple times through the gain medium. One challenge is to keep the gain medium excited by synchronous pumping when the seed pulse is not present. This is realized by synchronizing an active absorber medium (Q-switch) in the pump laser cavity with the round-trip time of the seed laser. By doing so, high-intensity pump pulses of ps duration close to the damage threshold of the gain medium (usually Ti:Sa as stated before) supply the power, which is transferred to the seed pulse. For amplification, it is crucial to consider the high peak power of ultrashort laser pulses, therefore, pulses are stretched in time before being sent into the gain medium and compressed again after amplification. This technique is labeled *chirped pulse amplification* (CPA) [20] and was even awarded a shared Nobel prize in 2018. Using a combination of multipass amplification and pulse stretching, peak powers for focused fs pulses can reach  $>10^{20} \text{ W cm}^{-2}$  [21] - enough to create a plasma on even the shiniest surface. Another challenge is the recompression to ultrashort pulses since all amplification suffers from band narrowing, which reduces the spectral bandwidth and thus the temporal width.

To study magnetic systems, it is sufficient to use focused fs pulses carrying some nJ of energy. From an experimental side it is helpful to have more energy, since focus size and therefore spatial overlap of pump and probe become easier to maintain. Another reason for high intensities is the possibility to frequency-double the light by second harmonic generation either at the sample surface or, for example, within a barium metaborate (BBO) crystal, in order to perform experiments at different wavelengths. Furthermore, it is advantageous to have pump and probe at distinct wavelengths or colors to avoid optical artifacts and to be able to easily remove the pump signal from the detection of the probe pulse.

## 2.1.2 Polarization, magnetization and interfaces

Having established how ultrashort light pulses in the visible to near-IR wavelength can be generated and manipulated, this section is dedicated to the discussion of how this light can be used to investigate a metallic and magnetized sample. Since magnetization is derived from the electronic system, the following is a discussion of the description of light propagation in metals or in the presence of charged particles, i.e., ions or electrons. The description employs a macroscopic approach in the dielectric theory to discuss transmission, absorption, and reflection in the visible to IR region following the derivation of [22–27]. At the end of the section, a brief summary of the understanding in terms of a microscopical theory is presented.

The textbook description of light in metals comes directly from Maxwell's equations using the magnetic induction  $\vec{B}$  and the dielectric displacement  $\vec{D}$

$$\vec{B} = \mu\mu_0\vec{H} = \mu_0(\vec{H} + \vec{M}), \quad \vec{D} = \varepsilon\varepsilon_0\vec{E} = \varepsilon_0\vec{E} + \vec{P} \quad (2.2)$$

with the electric polarization  $\vec{P}$ , which is expressed in terms of the susceptibility  $\chi$  and dielectric function  $\varepsilon$  like

$$\vec{P} = \varepsilon_0\chi\vec{E}, \quad \chi = \varepsilon - 1. \quad (2.3)$$

$\varepsilon_0$  and  $\mu_0$  denote the dielectric function and magnetic permeability in vacuum, respectively. Since the magnetic dipoles can not keep up with the rapidly oscillating fields, we set  $\mu = 1$  for

all purposes, magnetic properties are included as additional terms in  $\epsilon$ . The dielectric function or susceptibility is the response function of the material to the external field. One can express the polarization in terms of the field like

$$\text{instantaneous} \quad \vec{P}(\vec{r}, t) = \epsilon_0 \hat{\chi}(\vec{r}, t) \vec{E}(\vec{r}, t) \quad (2.4)$$

$$\text{non-stationary} \quad \vec{P}(\vec{r}, t) = \epsilon_0 \int_{-\infty}^t \hat{\chi}(t-t') \vec{E}(\vec{r}, t') dt' \quad (2.5)$$

$$\text{non-local} \quad \vec{P}(\vec{r}, t) = \epsilon_0 \int_{-\infty}^t \hat{\chi}(\vec{r}-\vec{r}', t-t') \vec{E}(\vec{r}', t') dt' \quad (2.6)$$

where  $\hat{\chi}$  is indicating that the susceptibility is generally a tensorial function that involves the crystal field symmetries and also contains non-linear higher order off-diagonal terms. A treatment in the Fourier space makes sense to avoid the complexity of the convolution that arises when treating the time- and space-dependent response.

$$\vec{P}(\vec{k}, \omega) = \epsilon_0 \hat{\chi}(\vec{k}, \omega) \vec{E}(\vec{k}, \omega) \quad (2.7)$$

For scattering angles with  $\vec{k} \ll \vec{G}$ , with  $\vec{G}$  being the reciprocal lattice vector in a crystal,  $\chi$  can be treated as independent of  $\vec{k}$ . For X rays this assumption is not valid anymore, though, as will be shown later. Furthermore, one can include the non-locality into local field factors to get rid of the  $k$  dependence in the above equation. Using eq. 2.7 for the expression of the dielectric displacement one finds

$$\vec{D} = \epsilon_0 \vec{E} + \vec{P} = \epsilon_0 (1 + \chi(\omega)) \vec{E}(\omega) = \epsilon_0 \epsilon(\omega) \vec{E}(\omega) \quad (2.8)$$

Finally, using Maxwells equation,s an expression of the response in terms of conductivity and dielectric function can be obtained.

$$\nabla \times \vec{H} = \vec{j} + \frac{\partial \vec{D}}{\partial t} \quad (2.9)$$

where we use  $\vec{j} = \sigma \vec{E}$  for the current density and  $\vec{D} = \epsilon_0 \epsilon \vec{E}$  for the displacement. The equation is evaluated in the frequency spectrum and results in

$$\nabla \times \vec{H} = \sigma(\omega) \vec{E}(\omega) - i\omega \epsilon_0 \epsilon(\omega) \vec{E}(\omega) = \tilde{\sigma}(\omega) \vec{E} \quad (2.10)$$

with the generalized conductivity  $\tilde{\sigma}$ . Expressed in terms of the generalized dielectric function one finds

$$\tilde{\epsilon}(\omega) = \epsilon(\omega) + i \frac{\sigma(\omega)}{\omega \epsilon_0} = \epsilon_1(\omega) + i \epsilon_2(\omega) \quad (2.11)$$

The complex-valued dielectric function can be obtained by having either  $\epsilon_1$  or  $\epsilon_2$ , since by the Kramers-Kronig relation one can calculate one from the other. A prerequisite is that the real part vanishes for larger  $\omega$ . This is the case since the electric dipoles can not keep up anymore with the rapidly oscillating fields for high  $\omega$ .

## Fresnel equations and reflection

At this point it is helpful to introduce the refractive index of a material which is commonly written [22] as

$$\tilde{n}^2 = \tilde{\epsilon}\tilde{\mu} \simeq \tilde{\epsilon}(\omega) \qquad \tilde{n} = n + ik \qquad (2.12)$$

$$\epsilon_1 = n^2 - k^2 \qquad \epsilon_2 = 2nk \qquad (2.13)$$

where we use  $\tilde{\mu} \simeq 1$ . Phenomenologically, the wavelength dependence of the dielectric function and consequently the refractive index can be understood from different electronic excitations. For large wavelengths, thus low energy, excitations happen quasi-continuously within the conduction band, which may be modeled by a quasi-free electron gas. This behavior dominates the optical response at low frequencies. Once a threshold for interband transitions, for example  $h\omega > 2$  eV for s to d bands, is reached, new excitations are possible, and especially in the visible range, this gives rise to the prominent color of copper, gold, and silver, for example [28]. Furthermore, charge density waves (plasmons) or optical active phonon modes (phonon-polaritons) can be excited and influence the optical properties at near-IR and visible wavelengths. With higher excitation energy, core-level transitions become accessible, and sharp absorption edges can be identified, for example around 60 eV for transition metal M edges and higher 2p-to-3d transitions at around 700 eV. Since the latter is investigated experimentally in the thesis, it will be discussed separately in its own section. As mentioned earlier, with even higher energies, once the wavelength becomes comparable to the lattice distance, a description in terms of scattering becomes more useful and is often employed for diffraction experiments resolving the lattice or interfacial structure.

An expression, i.e., the Fresnel equations, for reflection and transmission at an interface can be derived from the Maxwell equations using appropriate boundary conditions, i.e., continuity for the electric and magnetic field. The plane of incidence is set to the xz-plane with the y-axis perpendicular to it. Assuming a propagating electromagnetic field  $\vec{E} \sim e^{-i(\vec{k}\vec{r} - \omega t)}$  in an sp-basis such that  $\vec{E} = \vec{E}\hat{e}_s + \vec{E}\hat{e}_p$ , one finds

$$r_s = \frac{n_i \cos(\theta_i) - n_t \cos(\theta_t)}{n_i \cos(\theta_i) + n_t \cos(\theta_t)}, \qquad r_p = \frac{n_i \cos(\theta_t) - n_t \cos(\theta_i)}{n_i \cos(\theta_i) + n_t \cos(\theta_t)} \qquad (2.14)$$

$$t_s = \frac{2n_i \cos(\theta_i)}{n_i \cos(\theta_i) + n_t \cos(\theta_t)}, \qquad t_p = \frac{2n_i \cos(\theta_i)}{n_t \cos(\theta_i) + n_i \cos(\theta_t)} \qquad (2.15)$$

with the incident angle  $\theta_i$ , angle of the transmitted beam  $\theta_t$ , and refractive indices of the first and second medium  $n_i$  and  $n_t$ , respectively. In the following one usually uses Snell's law which states  $n_i \sin \theta_i = n_t \sin \theta_t$ , to further simplify the equations by eliminating the angle of the transmitted beam. Since the refractive index contains an imaginary part, this only holds for ultrathin films or non-absorptive media [29]. For an interface one should instead write

$$n_i \sin \theta_i = n_t \sin \theta_t = (n_t + ik_t) \sin(\theta_{t,R} + i\theta_{t,I}), \qquad (2.16)$$

which includes the absorptive processes but results in a more complex description. In the derivation of expression 2.15 an isotropic dielectric function is assumed, meaning that there is

no differentiation applied between  $\varepsilon$  for different directions of the E-field vector. This results in a short expression for the reflection  $\vec{E}_r = R\vec{E}_i$  with

$$R = \begin{bmatrix} r_s & 0 \\ 0 & r_p \end{bmatrix} \quad (2.17)$$

as the reflection matrix.

### Magnetic contribution - breaking time reversal symmetry

In the presence of a magnetization  $\vec{m}$  the dielectric function is not isotropic anymore, in terms of a constant isotropic contribution  $\varepsilon_0$  and the off-diagonal terms it might look like

$$\hat{\varepsilon} = \varepsilon_0 + \begin{bmatrix} 0 & i\varepsilon_z & -i\varepsilon_y \\ -i\varepsilon_z & 0 & i\varepsilon_x \\ i\varepsilon_y & -i\varepsilon_x & 0 \end{bmatrix}, \quad \text{where } \varepsilon_{x,y,z} = Qm_{x,y,z}. \quad (2.18)$$

Q (often referred to as Voigt constant), is a proportionality between the magnetization and the dielectric function. The resulting reflectivity matrix R will then have non-zero off-diagonal terms resulting in a change of polarization upon reflection and transmission.

$$R = \begin{bmatrix} r_{ss} & r_{sp} \\ r_{ps} & r_{pp} \end{bmatrix} \quad (2.19)$$

For a single interface the new coefficients can be expressed as

$$r_{ss} = \frac{n_i \cos(\theta_i) - n_t \cos(\theta_t)}{n_i \cos(\theta_i) + n_t \cos(\theta_t)} \quad (2.20)$$

$$r_{sp} = \frac{-in_i n_t^2 Q \cos(\theta_i) (m_z \cos(\theta_t) + m_x \sin(\theta_t))}{n_t \cos(\theta_t) (n_t \cos(\theta_i) + n_i \cos(\theta_t)) (n_t \cos(\theta_t) + n_i \cos(\theta_i))} \quad (2.21)$$

$$r_{ps} = \frac{-in_i n_t^2 Q \cos(\theta_i) (m_z \cos(\theta_t) - m_x \sin(\theta_t))}{n_t \cos(\theta_t) (n_t \cos(\theta_i) + n_i \cos(\theta_t)) (n_t \cos(\theta_t) + n_i \cos(\theta_i))} \quad (2.22)$$

$$r_{pp} = \frac{n_i \cos(\theta_t) - n_t \cos(\theta_i)}{n_i \cos(\theta_t) + n_t \cos(\theta_i)} + \frac{2in_i n_t^2 Q \cos(\theta_i) \sin(\theta_t) m_y}{n_t (n_i \cos(\theta_t) + n_t \cos(\theta_i))^2}. \quad (2.23)$$

Similar expressions can be derived for the transmission. Again the expression can be reduced to the incident angle by using Snell's law. From the equations a rotation of the polarization axis, known as the Kerr rotation  $\theta_K$  and an ellipticity  $\varepsilon_K$  due to the different refractive indices for s- and p-polarization are derived for s- and p-polarized light.

$$\phi_S = \theta_{S,K} + i\varepsilon_{S,K} = \frac{r_{ps}}{r_{ss}} \quad (2.24)$$

$$\phi_P = \theta_{P,K} + i\varepsilon_{P,K} = \frac{r_{sp}}{r_{pp}} \quad (2.25)$$

In case the incident light is along the surface normal, i.e.,  $\theta_i = 0$ , from which  $\theta_t = 0$  follows (Snell's law), the terms  $r_{ss}$  and  $r_{pp}$  become similar and  $r_{sp,ps}$  can be expressed as  $r_{sp,ps} = \alpha m_z$ . Therefore, light that is incident normal to the surface is a probe sensitive to magnetization pointing out of the surface. Conversely, having a large angle of incidence results in a sensitivity to the in-plane magnetization. An example of an air-cobalt interface is shown in Fig. 2.1. Here

$Q = 1$  was used for simplification resulting in quite large Kerr rotations, while in reality  $Q$  values are complex and of the order of  $10^{-2}$  to  $10^{-5}$ , which leads to Kerr rotations of the order of  $<1^\circ$  (Fig. 2.3) to some mrad [23, 25]. By employing p-polarized light at large angles from the surface normal, a sensitivity to magnetization perpendicular to the plane of incidence is found. The effect can be separated into three cases: The first two describe the case where the magnetization is either parallel or perpendicular to the plane of incidence for grazing incidence. The third case describes the case where the incidence is normal, and the magnetization is parallel to the surface normal. The three different cases result in distinguished set-ups of the same experiment, namely longitudinal (L-), transversal (T-), and polar (P-) magneto-optical Kerr effect (MOKE) experiments, in the respective order. Measuring MOKE is one of the most prominent tools magnetism research since it is comparably easy to set up and provides a very high accuracy local probe. A more detailed description of the experimental realization of measuring MOKE is given in the next section, where also its applicability to investigate magnetization on an ultrafast timescale is discussed. Similar to the reflected light, the transmitted light changes in terms of rotation and ellipticity, this is usually referred to as the Farady effect. Experiments performed in transmission are not further discussed in this work, but it should be mentioned that they also provide a very prominent and handy tool for the investigation of magnetic samples. Unfortunately, it requires either very thin or transparent samples, an obstacle that can sometimes not be overcome. The change in ellipticity can be understood from differences in attenuation and refraction for s- and p-polarization. The resulting wave is generally a superposition of an s- and p-state. This is expressed as elliptical, or circular polarization, and the eigenmodes of linear magneto-optical problems are left and right circular polarization. The change in polarization due to the two distinct refractive indices due to magnetization is termed magnetic birefringence, and changes in the intensity of the transmitted or reflected light due to different damping (absorption) of circularly polarized light are called magnetic circular dichroism or MCD.

Microscopically, this result can be understood intuitively since a driving circular electric field will pull electrons onto a circular trajectory. From electrodynamics, it is evident that with a circular electronic motion, a magnetic moment can be associated<sup>3</sup>. Without a magnetic field, the direction of circular motion and, therefore, the direction of the magnetic moment is degenerate, left or right circular polarization can be treated equally. In case something breaks the (time-reversal) symmetry, e.g., a magnetic field is present, the two helicities will be attenuated differently, inducing a change of polarization and ellipticity.

So far, only linear terms in  $\vec{\epsilon}$  are considered. When including higher-order terms, contributions that scale with  $\vec{M}^2$  can be identified, leading to additional changes in ellipticity and rotation. The effects that scale with the square of  $\vec{M}$  are termed Voigt effect, Q- (quadratic) MOKE, and linear dichroism. Since those contributions are typically much smaller, it is justified to focus on the linear terms for MOKE, but in some instances, for example, in magnetic insulators, the effects can be quite considerable, e.g., [30]. More importantly, the  $\vec{M}^2$  dependence allows a measurement of antiferromagnetic structures where the moments are aligned oppositely, leading to  $\langle \vec{m} \rangle^2 = 0$  but  $\langle \vec{m}^2 \rangle \neq 0$ , employed for example in [31]. This has great relevance in X-ray studies, where the X-ray version of the linear dichroism is commonly used to investigate antiferromagnetic structures. The topic will be touched on again in the respective section.

---

<sup>3</sup>A more thorough treatment follows from spin-orbit coupling, this is meant only as a heuristic

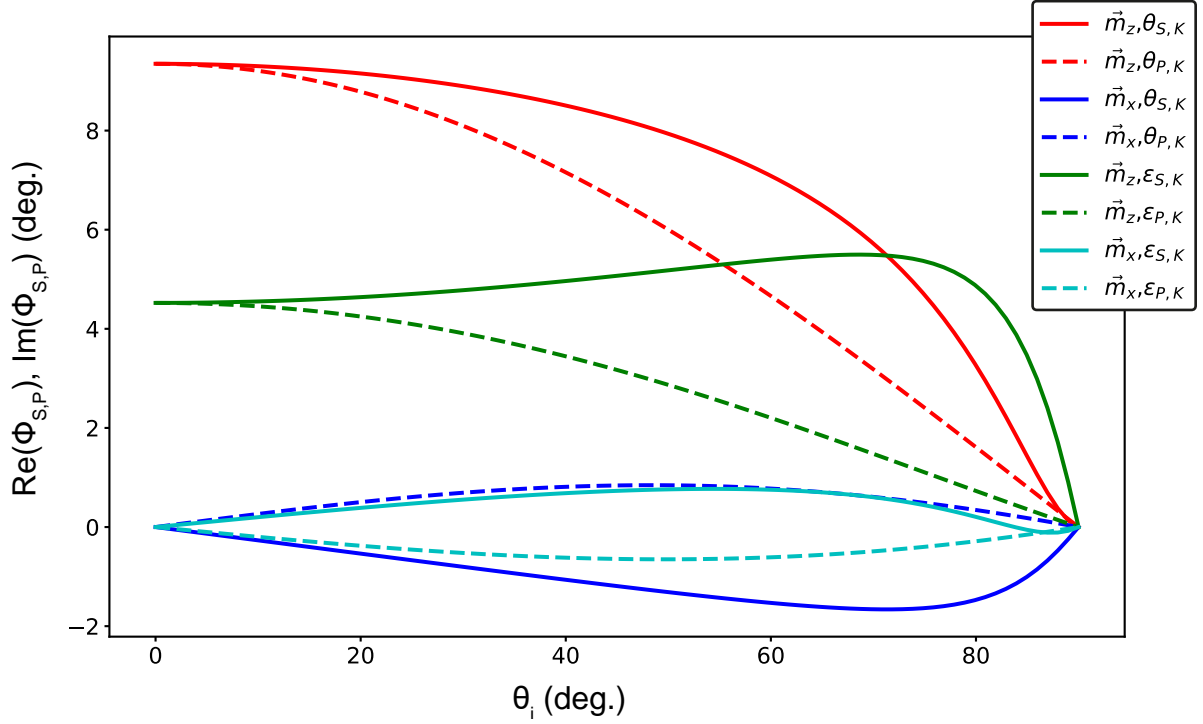


**Figure 2.1:** Calculation of the Kerr rotation and ellipticity for an air-cobalt interface over the incident angle  $\theta_i$  with respect to the surface normal. Two of the three scenarios as described in the text are depicted, namely with the Co magnetization pointing in x-, or in z-direction. Dashed lines are used for p-polarized light and solid lines show the case of s-polarized light. A  $180^\circ$  reversal of the magnetization leads to a sign change of the respective signal.

### Multilayer reflection

The description above is only valid for a single interface. The authors of [23–25, 32–34] present solutions on how to expand this to multilayers and even thick films. A solution of the multilayer reflection poses a quite important result for ultrathin multilayers similar to those investigated in this study. A better understanding of the Kerr effect is obtained and furthermore insight about layerwise absorbed power is gained. The penetration depth of light in metals is typically calculated using the wave equation for light coming from Maxwell equations [22] where we assume a propagation in z-direction

$$\nabla^2 \vec{E} = \mu_0 \epsilon \frac{\partial^2 \vec{E}}{\partial t^2} + \mu_0 \sigma \frac{\partial \vec{E}}{\partial t} \quad (2.26)$$

which is solved by a damped wave travelling in z-direction like

$$\vec{E} = \vec{E}_0 \cos(\omega(t - n_R \frac{z}{c})) e^{-\omega n_I z/c} \quad (2.27)$$

with the complex index of refraction  $\tilde{n} = n_R + in_I$  and the speed of light  $c$ . Since the intensity scales with  $\vec{E}^2$ , an exponential decrease of the intensity with the typical decay constant  $\delta$  for a decrease by  $1/e$  is given by

$$\delta = \frac{c}{2\omega n_I} = \frac{\lambda}{4\pi n_I} \quad (2.28)$$

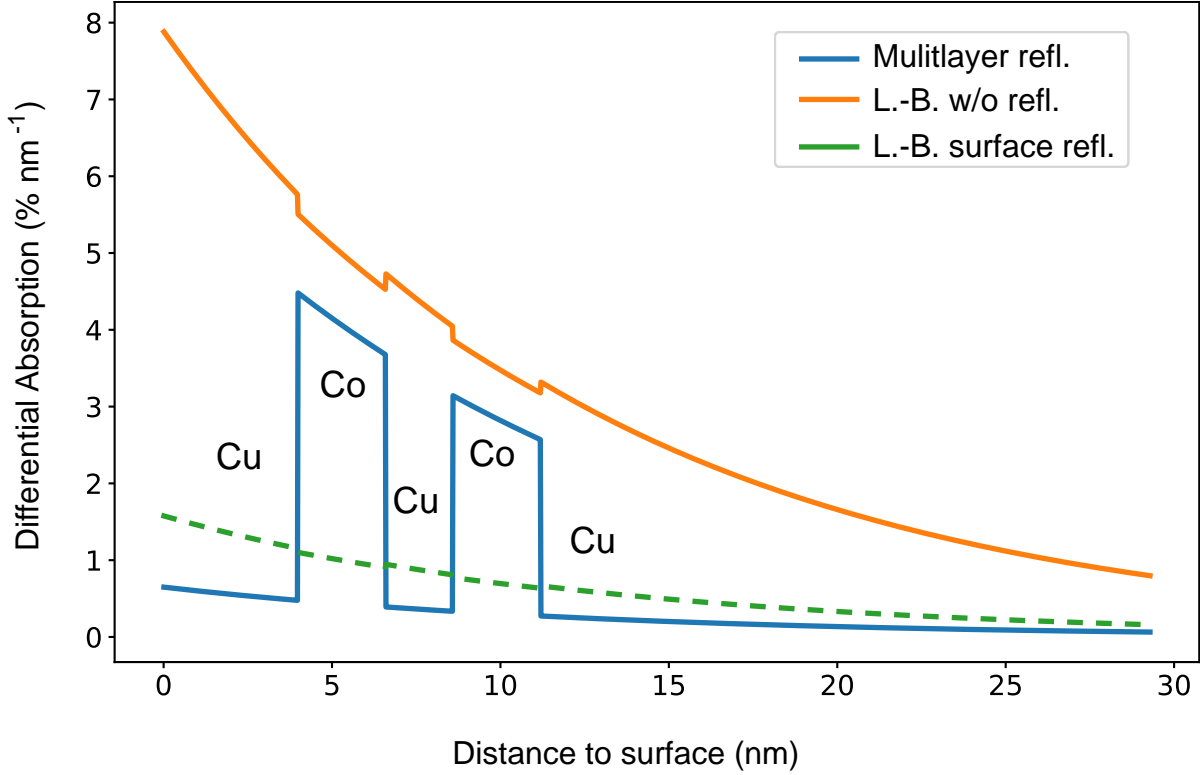


**Figure 2.2:** Differential absorption in case of a simple exponential without reflection (solid orange line), with 80% reflection at the surface (dashed green line) and a multilayer calculation using the extended formalism of [25] for a Cu(4.0 nm)/Co(2.6 nm)/Cu(2.0 nm)/Co(2.6 nm)/Cu(18 nm) stack and p-polarized light of 800 nm. According to the multilayer calculation about 80% of the light is reflected. The dashed green line is the exponential decay rescaled 20% of the orange line. All three curves are calculated using *udkm1Dsim* [36].

with the wavelength  $\lambda$ . Using  $\lambda = 800$  nm and  $n_{Co} = 2.488 + 4.803i$  [17] one finds a decay constant, also called the optical penetration depth, of only  $\sim 13.3$  nm. This neglects reflection at interfaces in multilayer structures. To actually calculate the depth-resolved absorbed laser power, it is necessary to carry out the full field propagation as described in [22] or [23]. A comparison of absorbed laser power in a Cu/Co-multilayer thin film sample using the Lambert-Beer-like exponential decay and a multilayer reflection calculation is presented in Fig. 2.2. The calculations are performed using a script called *udkm1Dsim* developed by D. Schick in the group of Mathias Bargheer [35, 36], in which both calculations are implemented. Most importantly, due to interface reflections the majority of the laser power per nm is absorbed in the Co layers and significantly less in Cu. The calculations are carried out for 800 nm light incident at  $45^\circ$  to the surface normal using  $n_{Co}$  as stated above and  $n_{Cu} = 0.254 + 5.013i$  [28].

### 2.1.3 Time-resolved MOKE

The previous section introduced a description of the magneto-optical effect for reflected light from a magnetic surface. This section deals with the experimental realization of a MOKE setup and the extension thereof to the ultrafast regime. In the last couple of months of this thesis, a time-resolved (TR-)MOKE was built from scratch and is used in the following to describe the

technical details of the experiment. Further measurements recorded at an established set-up are presented in section 8.

### Experimental set-up

In Fig. 2.1 it is observed that the highest magnetic signal can be measured for the Kerr rotation under a small angle of incidence with respect to the surface normal and the magnetic field aligned parallel to it, i.e., polar MOKE. Often the set-up is realized such that the light is incident under almost  $45^\circ$  where still a high rotation for out-of-plane fields is measured but at the same time, a sensitivity to in-plane fields is achieved. This has the advantage that the optics do not need to change. Simply turning a magnetic coil to magnetize the sample in the desired direction is sufficient. The Kerr rotation is then measured by (almost as in [23]) crossing two polarizers, one in front of and the second one behind the sample. The change of polarization of the reflected light is converted into a change of the detected signal intensity after the second polarizer (analyzer). The change in intensity is then proportional to the magnetization of the sample, and by ramping an external field, hysteresis loops are recorded. Generally, since  $\epsilon$  depends on  $\omega$ , the rotation is wavelength-dependent. An example is shown in Fig. 2.3 where an FeGd sample is characterized for time-resolved experiments.

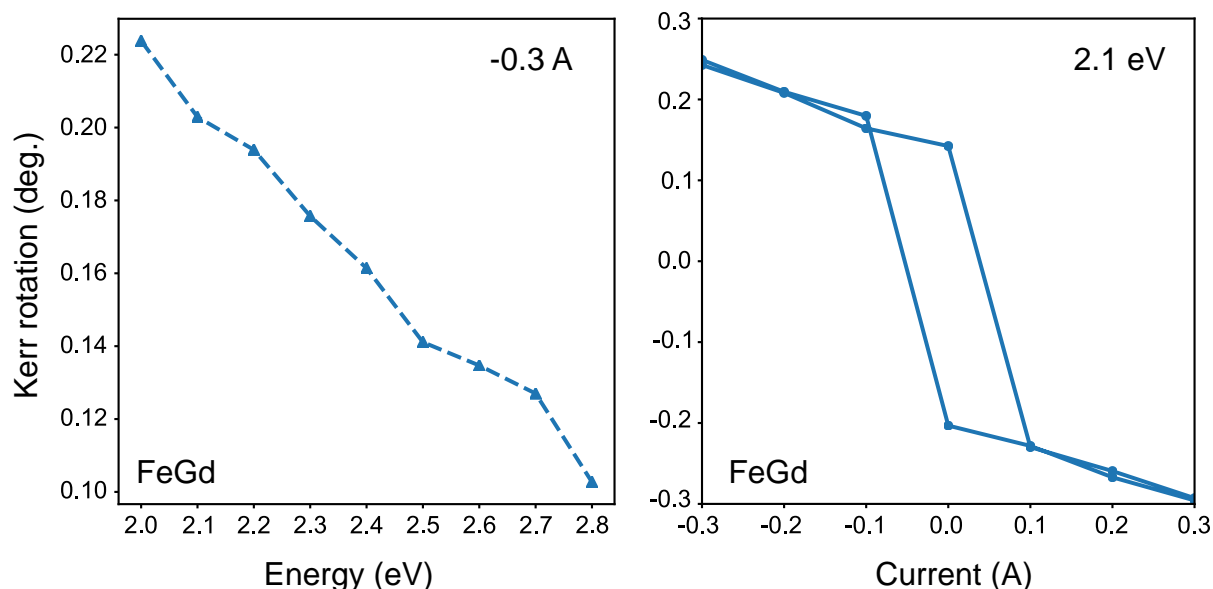


**Figure 2.3:** Left: Energy dependence of the polar Kerr rotation measured in an FeGd alloy thin film sample [37]. With higher energy the rotation and therefore the contrast between the two magnetization directions decreases. Right: Hysteresis loop recorded in the same sample using a photon energy of 2.1 eV as indicated in the plot. The magnetic field can be calculated from the applied current denoted on the x-axis.

Static characterization is typically done with continuous-wave (cw) light sources. When investigating dynamic changes at ultrafast timescales, a pump-probe scheme is employed. A pulsed light source like a Ti:Sa laser is necessary for that purpose. A single pulse is split into two that travel in different directions while maintaining an ultrashort temporal width. The power each pulse carries can either be fixed, e.g., 90 % to 10 %, or adjusted when employing a beamsplitter that splits into s- and p-components of the light, for example. The pulse which carries little power is used as a probe since the system is not noticeably disturbed by it, and the other should

carry enough power to excite the system and is therefore called pump. Changing the time delay between the arrival of pump and probe allows the system to be investigated at different moments in its excited state. For this to work, the repetition rate has to be low enough to ensure that the system reaches the same static state after excitation before the next pulse arrives.

For the TR-MOKE built here, a Ti:Sa, *Femtosource compact* by *Femtolasers*, system is used to create pulses at 76 MHz repetition rate, 350 mW average power, and pulse durations of 70 fs FWHM with a center wavelength at 805 nm. When investigating a copper surface, for example, at 70° incidence angle, around 90% of the light will be reflected [38]. If a 90-10 beamsplitter is used, and the light is focused into a spot of 100 μm FWHM, only around 6 nJ cm<sup>-2</sup> are absorbed. Using a constant electronic heat capacity<sup>4</sup> of 21 kJ m<sup>-3</sup> [39] and around 20 nm penetration depth, this results in an increase of the electronic temperature of less than 1 K. To measure the full range of excitation, a multipass amplifier, *ODIN-C* by *Quantronix*, is used to amplify the 76 MHz, 350 mW pulse train to around 200 mW at 1 kHz. Even though the average power is now lower, it is contained in fewer pulses while maintaining a temporal width of about 130 fs of the amplified pulses. Using the same parameters as before, one finds an absorbed fluence of 230 mJ cm<sup>-2</sup>, which would result in an electronic temperature increase of  $\sim 7 \times 10^6$  K, again using a constant heat capacity. This is, of course, not physical but highlights that in the amplified light is enough power to measure demagnetization phenomena.

A schematic of the set-up is presented in Fig. 2.6. The multipass amplifier works by chirped pulse amplification (CPA) fashion in combination with a Pockels cell pulse picker to let a seed pulse through at the desired time. The gain medium is a Ti:Sa crystal pumped by a frequency-doubled Q-switched Nd:YAG lamp. The seed pulse selected by the Pockels cell does eight roundtrips before entering the compressor stage and leaving the cavity. Both spatial and temporal chirps are compensated in the compressor, and a pin-hole mask is used to block unwanted self-lasing modes propagating in the same beam path.

### Pulse characterization by FROG

To ensure that the pulses are truly short at the sample position, a second-harmonic generation frequency-resolved optical gating (SHG-FROG) set-up was assembled [40]. The SHG-FROG consists of a beamsplitter here, an s-p splitter is used to separate a pulse into two branches, a delay stage model *M505.6PD* by *PI*, to change the time delay between the pulses at the point of arrival, a BBO crystal which facilitates second harmonic generation once the pulses are overlapped in space and time, and a spectrometer to monitor the second harmonic spectrum.

FROG relies on using one of the pulses as the 'gate' to measure the other. In our case, the pulses are identical and only delayed by  $\tau$ , which reduces the issue to an autocorrelation, and the detected spectral intensity follows

$$I_{FROG}(\omega, \tau) = \left| \int_{-\infty}^{\infty} E(t - \tau)E(t)e^{i\omega t} d\tau \right|^2 = |\tilde{E}(\omega, \tau)|^2 \quad (2.29)$$

The spectral intensity  $I(\omega)$  for a given  $\tau$ , therefore, depends on the full field  $E(\omega)$  including its spectral phase. This allows a mathematical retrieval of the spectral amplitudes and their absolute phase, which is required to reconstruct the temporal pulse shape. For pulse retrieval, an implementation called *Python for pulse retrieval (pypret)* written by N. C. Geib at the Friedrich

---

<sup>4</sup>This is not a good assumption and is only used to judge the temperature change roughly. Commonly a heat capacity linear in T is used.

Schiller University in Jena [41], originally designed for simulations, was changed to be used for actual data and successfully employed. An example is shown in Fig. 2.4. By changing the compressor grating distance and angle, we can shorten the amplified pulses to about 130 fs FWHM with an almost flat phase function as shown in 2.5. The results are cross-checked with a commercial autocorrelator system *pulseCheck* by *APE* yielding even shorter times of around 100 fs FWHM.

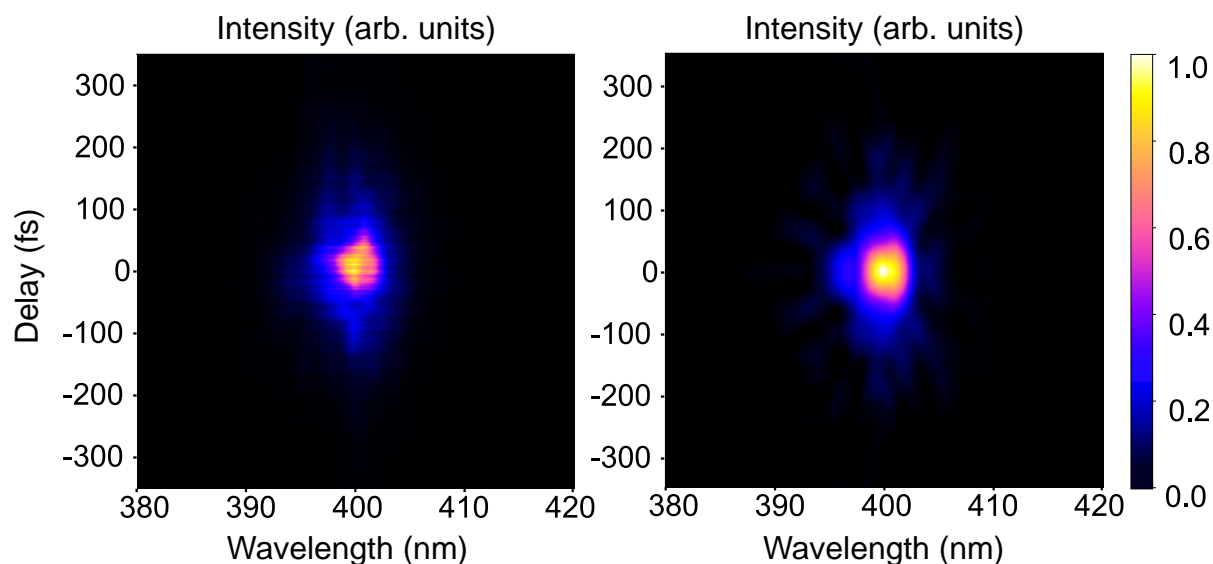


**Figure 2.4:** Retrieval of a FROG trace. The y-axis shows the delay time between the two pulses and the x-axis denotes the wavelength. The color-coded intensity is normalized to one. Left: Measured SHG spectrum after overlapping pump and probe in a BBO crystal. Right: The spectrogram (FROG trace) retrieved by *pypret*. For the retrieval an initial Gaussian distribution is assumed and the final pulse is subsequently calculated by gradient-descent in order to match the SHG trace.

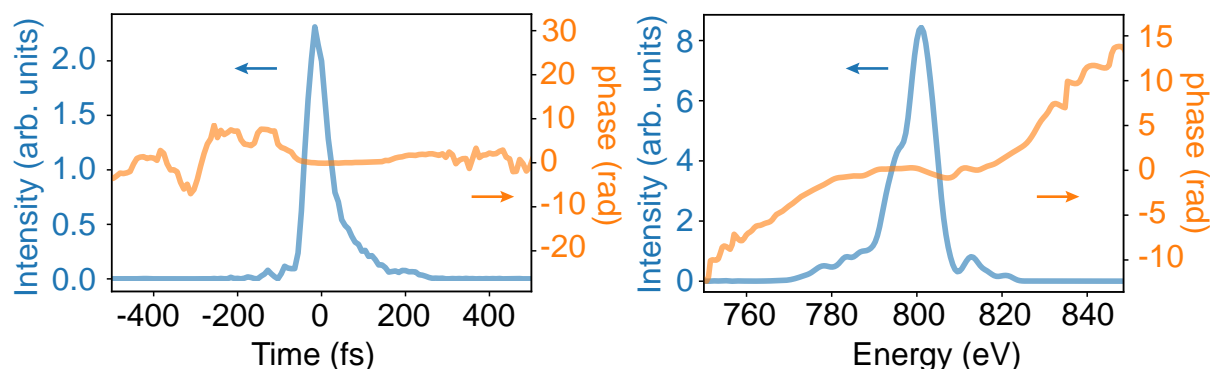


**Figure 2.5:** Time (left) and spectral (right) domain of the retrieved pulse shown in 2.4. The initial time duration of the seed pulse of around 70 fs is not recovered, due to band-narrowing a temporal width of around 130 fs FWHM is achieved. The flat temporal phase shown in orange indicates that the pulse is close to the minimum in temporal width.

Since the autocorrelation is symmetric in time, the retrieved field  $E(t)$  is ambiguous. This means that the direction in time is not clear, for our purpose this ambiguity is negligible since a

small leading (or trailing) flank does not change the overall dynamics. In principle the direction of time can be identified by adding a dispersive element in the beam path to induce a positive chirp. Then by checking the altered pulse shape one can determine the sign of the time axis.

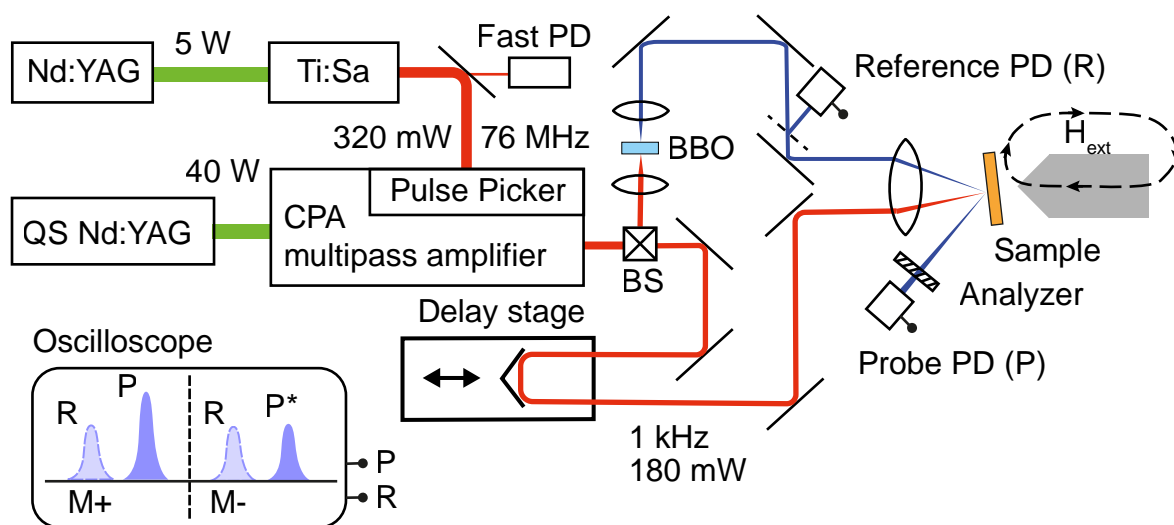


**Figure 2.6:** Schematics of pulse generation and consecutive pump-probe measurement of the Kerr rotation. The initial pulse is generated in a Ti:Sa oscillator by self mode-locking. The frequency is monitored by a fast photodiode (PD) behind the first mirror and used to trigger the pulse picker and the Q-switch (QS) inside the amplifier. Once the pulse enters the amplifier, it is stretched to almost 1 ns before entering the pulse picker and then the multipass stage. After eight round trips, the pulse is coupled out and compressed again. The beam is further separated into pump and probe. The power ratio is adjusted by a  $\lambda/2$  plate (not shown) in front of the beamsplitter (BS). The probe is frequency-doubled to 400 nm by a BBO pass. The probe intensity is monitored by a reference diode (R) and passes a polarizer to ensure s-polarization. After the sample, the reflection is guided through color filters (not shown) and the analyzer, and the intensity is detected by a second photodiode (P). The pump path can be adjusted by a delay stage which allows for a maximum time delay of  $\Delta t = 1$  ns. Both R and P are detected in an oscilloscope where the area under the curve is integrated. The change of area is considered proportional to the change in magnetization.

### Delay-time traces

The transition from a FROG measurement to the TR-MOKE measurement is considerably easy, simply exchanging the BBO with a magnetic sample already provides knowledge of the temporal and guarantees spatial overlap on the sample. In the experiment assembled here, the BBO is further used for SHG of the probe pulse. Additionally, the pump focus is widened to avoid burning the surface too easily and to facilitate a stable pump-probe overlap. Overall the probe, now at 400 nm center wavelength, is focused to about 100  $\mu\text{m}$  diameter carrying only  $<10$  mW average power. The pump is focused to about 500  $\mu\text{m}$  diameter with the power adjusted between 20 mW and 100 mW. For detection, a photodiode, behind a red color filter to avoid stray light from the pump, is used in combination with a reference diode before the sample to detect both the incoming intensity  $I_0$  and the intensity  $I_K$  after the analyzer. By normalizing  $I_K$  to

$I_0$  the noise is reduced due to intensity variations of the light. The magnetic field is supplied by a coil with an iron core, and the current is ramped by a bipolar *KEPCO* power supply. A maximum field of 80 mT is achieved at the sample position with the current settings, simply turning the magnet will change from out-of-plane to in-plane fields. Usually, MOKE is measured in combination with a lock-in technique using either a photoelastic modulator (PEM) or chopper or both at the same time to modulate the signal. This technique is extremely powerful and enables typical sensitivity of some mdeg. down to  $10^{-8}$  mdeg. [42].

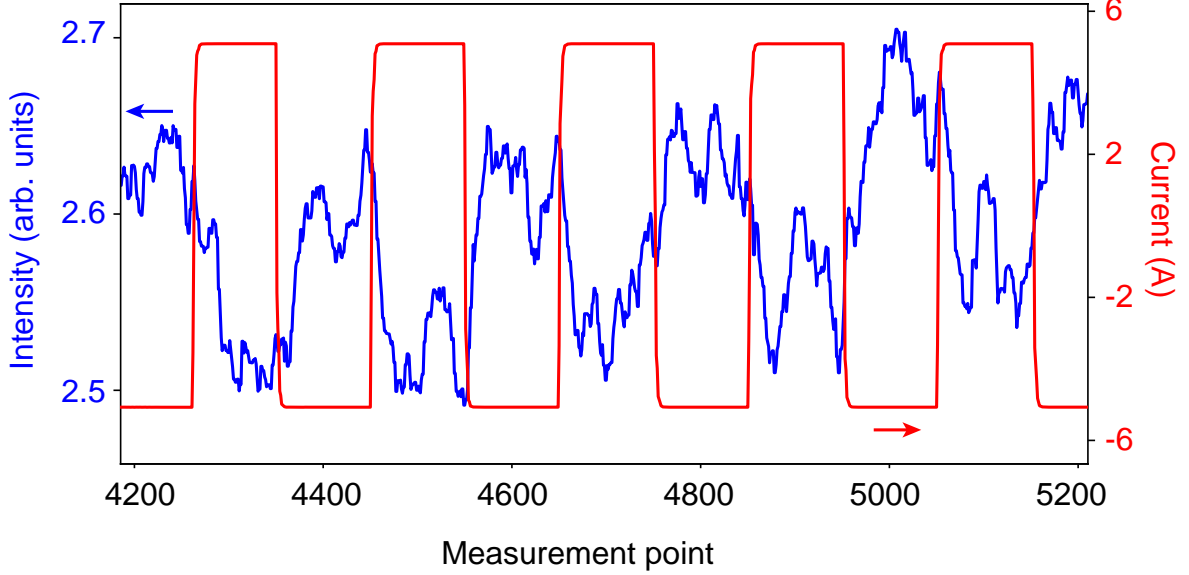


**Figure 2.7:** Integrated photodiode intensity in blue for different delay steps and reversed magnetic field (current shown in red). The magnetic contrast is evaluated from the difference in intensity when changing the magnetic field direction and thus turning the magnetization in the sample. Not shown here is the position of the delay stage that was moved after recording each magnetization direction twice.

In its current state, no modulation is employed. Instead of reading the photovoltage by a lock-in amplifier, an oscilloscope is used in which the signal is integrated over a small gating window of around 2 ns. This is averaged over a typical acquisition time of some seconds before the field is changed. For time-dependent measurements, the sample is successively saturated magnetically in each direction when recording before advancing the delay stage to the next position in time. An example of such a measurement, recorded on a Co/Pt sample with an out-of-plane easy axis of magnetization, is presented in Fig. 2.7. For each magnetization direction, the signal is accumulated for several seconds and averaged. The contrast is calculated by the asymmetry as  $A = 2 \frac{I_+ - I_-}{I_+ + I_-}$ , where  $I_+$  and  $I_-$  denote the averaged intensity for each field direction, respectively. An example of the contrast obtained in that fashion is shown in Fig. 2.8. A sharp drop can be identified, which we attribute to the coincidence of pump and probe in time. The dynamic is typically fitted with a double exponential function of the form

$$\begin{aligned}
 A(t) &= g(t) * f(t) \\
 f(t) &= \Theta(t) \left( a \left( e^{-\frac{t}{\tau_{de}}} - 1 \right) - b \left( e^{-\frac{t}{\tau_{ee}}} - 1 \right) \right) + A_0
 \end{aligned} \tag{2.30}$$

where  $g(t) * f(t)$  describes a convolution of the fit function with the probe pulse since it has a finite width in time. For  $g(t)$  a Gaussian of 100 fs to 200 fs FWHM is used. The phenomenological function  $f(t)$  is described by a double exponential, one describing the demagnetization on the timescale  $\tau_{de}$  and one for the recovery of magnetization labeled  $\tau_{re}$ . The arrival of the pump pulse is modeled by a stepfunction  $\Theta(t)$ .

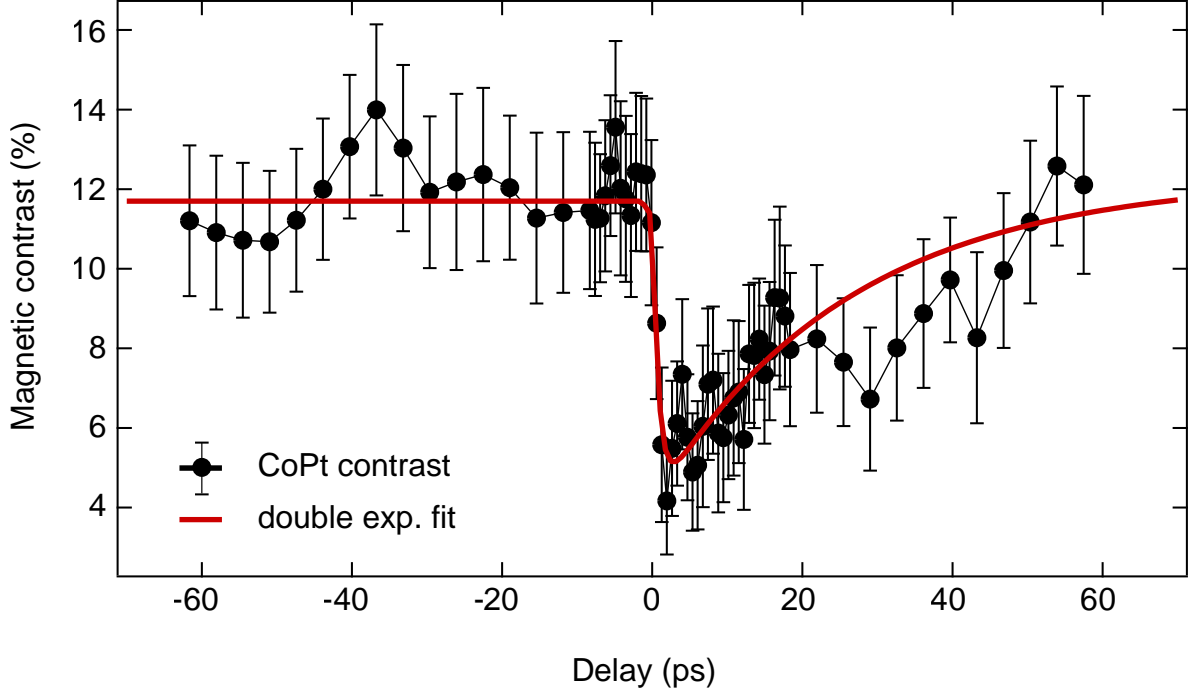


**Figure 2.8:** Magnetic contrast recorded on Co/Pt over delay time. The contrast or asymmetry is obtained as described in the text and shows a sub-ps decrease when pump and probe coincide. The solid red line denotes a double exponential fit as described by eq. (2.30). A demagnetization time  $\tau_{de} = (0.8 \pm 0.1)$  ps is found by fitting. Time zero is set using the signal change. It falls in the same range as measured in FROG traces. The error is estimated from the standard deviation at each delay step.

### What is really probed?

Intuitively the fast signal change is interpreted as an ultrafast quench of the magnetization since the contrast of the signals vanishes or at least reduces. The first measurements of ultrafast demagnetization in Ni were recorded and interpreted more or less in this fashion, the only difference being that both pump and probe were centered at 800 nm and complete hysteresis loops were recorded and evaluated [43]. Although the measurement was subsequently confirmed employing a wide variety of different techniques [39, 44–48], the results sparked a discussion as to what is really probed in such a time-resolved measurement of the Kerr rotation and ellipticity [45, 49–51].

At the heart of the issue lies the fact that the observable measured is only *proportional* to the magnetization. In other words, the signal change can not unambiguously be attributed to a change in the magnetization. If one recalls that the change  $\theta_{S,P}$  depends on  $\epsilon(\omega)$  which describes all the optical properties of the system, it is evident that there can also be other mechanisms at work, influenced by the ultrashort heat- or laser pulse. This is discussed in terms of

a thermal dependence of  $\varepsilon(T, \omega)$  (or  $\chi(T, \omega)$ ) in [49]. Microscopically the issue arises when considering the excitations in a single particle picture where the transitions excited by the optical probe are already blocked by the photoelectrons of the pump (called optical 'bleaching') investigated in [50] and [51]. And lastly, all models agree that around the presence of the light field, i.e., up to 50 fs delay time, the electrons have not reached a thermal equilibrium required for any thermomagnetic model, preventing statements about ensemble properties at the earliest timescales.

It is agreed upon that the conclusions drawn from TR-MOKE are largely valid, e.g., [1, 51–54]. Mainly due to the coherent image transported by the multitude of different ways, the same or at least similar results are achieved. Magnetization is also probed by second-harmonic generation (MSHG) at the surface or at an interface. Since the intensity  $I(2\omega) \propto (\chi_{ij}E(\omega)_iE(\omega)_j)^2$  depends on  $\chi$ , it also provides a measure of  $\vec{M}$  [55] which can be utilized in pump-probe measurements [47, 56–58] confirming the findings by MOKE and extending the research to anti-ferromagnets. MSHG is still an optical probe and suffers from similar ambiguities as MOKE and Faraday measurements. A more direct tool to investigate magnetic properties is obtained by time- and angle-resolved photoemission (TR-ARPES) or two-photon photoemission (2PPE) studies, where a near-IR pulse is applied to heat the system, and a probe at  $\sim 6$  eV to 30 eV is used to extract electrons from the surface. By detecting their energy, momentum, and spin character, conclusions about spin polarization and thus magnetization is gained [58–61]. The last two examples use probes already far beyond the visible range only accessible by elaborate higher-harmonic generation sources. Measuring at even higher photon energies introduces some of the most powerful techniques that directly probe the magnetic system by measuring element-specific core-level transitions, further confirming the ultrafast magnetization quench. All techniques can not be discussed in the scope of this thesis, which is why the middle ground between visible light and X-rays is not reviewed, and the next chapter deals directly with soft X-ray spectroscopy.

## 2.2 X-rays to investigate magnetism

Pump-probe techniques in the visible range access the electronic population close to the chemical potential, whereas higher energy photons can directly excite transitions from a core level into the valence band. The resonant excitation probability or photon absorption depends strongly on the photon polarization, wave vector, energy, electron initial, and final state. Excitations probed with a high energy resolution allow to resolve transition probabilities while changing parameters such as sample magnetization, light helicity, or photon energy. This is successfully employed in magnetic studies of the 3p-3d ( $M_{2,3}$ -edge<sup>5</sup>) transitions of rare-earth and transition metals. For these investigations photon energies in the extreme ultraviolet (XUV) region, e.g., 50 eV to 80 eV, are sufficient and can be coherently generated in higher-harmonic generation (HHG) processes, for example in gas jets. Since the XUV light is generated by ultrashort laser pulses the, extension into an XUV-MOKE or -Faraday experiment is natural and can be assembled on an optical table [62–65]. The contribution of time-resolved XUV studies to the research of ultrafast magnetization is invaluable and the results allow for precise identification of magnetic contributions which helped rule out doubts about the nature of the observables described

<sup>5</sup>Absorption edges are labeled according to the *IUPAC* notation describing the initial state. From inner to outer shell, the letters K,L,M,N. are used, and numbers denote the spin-orbit split level.

in the previous section and expand the understanding of femtomagnetism, e.g., [66–70]. Even higher photon energies allow to probe transition from the inner shell, e.g., 2p-3d ( $L_{2,3}$ -edge) transition at around 500 eV to 1 keV for transition metals. Before discussing the details of how magnetization can be probed by X-rays, a short survey on (almost) coherent X-ray generation is presented.

## 2.2.1 Pulsed X-rays

### Light sources

Unlike radiation in the visible to XUV region, tabletop set-ups for (time-resolved) soft X-ray experiments are not readily available. Even though coherent ultrashort pulses at energies up to 2 keV [71] can be achieved in HHG sources, the number of photons is not sufficient for experiments. There are some advances, for example, using dense-plasma radiation to do spectroscopy [72], which has been successfully employed also in ultrafast time-resolved studies [73]. Despite these efforts to improve lab systems, synchrotron radiation still prevails in soft X-ray spectroscopy due to the high photon flux of around  $10^{10-14}$  photons  $s^{-1}$  (compared to just below  $10^9$  photons  $s^{-1}$  in [73]). The principles of synchrotron radiation are readily described in textbooks, for example in [74–77] and are not repeated here. The summary presented here aims to introduce the idea of how fs X-ray pulses are generated in a synchrotron light source using the example of the slicing facility at BESSY II in Berlin.

Generally, synchrotron, a term coined by Ed McMillan [78], radiation is generated by accelerated electron bunches kept in a storage "ring". Electrons are bunched together by an RF-field that *synchronizes* the kinetic energy of the electrons. The actual storage facility is not ring-shaped but consists of linear acceleration stages and bending magnets, the latter are responsible for curving the electrons path and thereby generating light. Kinetic energies stored in a synchrotron facility are in the order of 1.7 GeV (BESSY II, Germany) to 8 GeV (Spring8, Japan) with a circumference of 240 m (BESSY II) to 1436 m (Spring8) and typical RF-fields of 500 MHz. The standard measure to compare synchrotron radiation is the brilliance, defining the number of photons per unit bandwidth (BW) and areal emission, which is typically around  $10^{18}$  (BESSY II) to  $10^{21}$  (Spring8) photons  $s^{-1} \text{ mm}^{-2} \text{ mrad}^{-2} (0.1 \% \text{ BW})^{-1}$ . Massive increases in brilliance have been achieved over the last decades, mainly by introducing new insertion devices, i.e., wigglers and undulators. The brilliance is still expected to increase some orders of magnitude for high-energy regions with increasing the number of dipoles for the bending magnets in so-called diffraction-limited storage rings.

The electrons are forced onto a circular orbit in a bending magnet and emit radiation in a cone tangentially to the radius. This gives rise to a broad emission spectrum, typically from 0.001 keV to 20 keV with a reasonable number of photons. By using monochromator gratings or zone plates, the experimentalist can choose the energy required for the experiment. The bending magnet radiation suffers from low brilliance due to the large emission cone. This issue is targeted in a wiggler or undulator, which consists of dipoles arranged in a linearly alternating fashion to force electrons onto an oscillating path. Again, due to the acceleration the electrons experience in the dipole array, radiation is emitted, in this case in the direction of the original path. By tuning the field, a specific energy is radiated. In a wiggler, the electrons deviate strongly from their original path, and the radiation is a simple sum of the photons emitted at each turn inside the wiggler. In an undulator, the magnetic field is adjusted to match the kinetic energy of the electrons in such a way that the phase between each turning of the electrons matches a distinct wavelength. This leads to constructive interference of the light field of the

desired wavelength and, therefore, to a much narrower emittance angle and thus higher brilliance. Together with control over wavelength, the undulator arrangement facilitates changes in the polarization by shifting the dipole arrays relative to each other. Different polarizations can also be accessed by spatially selecting parts of the light in the radiation cone of a bending magnet, but since this involves mechanical motion of mirrors and gratings, changing the polarization in an undulator is much faster and far more stable.

Typical electron bunch lengths are in the order of some mms, which corresponds to 20 ps to 100 ps in time while being separated by a few ns. This gives direct access to time-resolved measurements by synchronizing an excitation and detection scheme to the frequency of the synchrotron. If special measures are undertaken, the pulse duration can be further reduced down to  $<10$  ps and, in the future, perhaps even below one ps by exploiting different electron orbits and shortening the bunch length [79]. While this provides sub-nanosecond time resolution, currently, it is not short enough to track magnetization at femtosecond timescales.

### Femtosing

One way to achieve femtosecond soft X-ray pulses is realized in the *FemtoSpeX* facility at BESSY II [80, 81]. Comparable facilities have been assembled at the Advanced Light Source [82, 83] where the technique was pioneered, the Swiss Light Source [84], and SOLEIL [85]. The technique is termed *slicing* and was first proposed by Zholents and Zolotarev [86]. A schematic of the working principle is presented in Fig. 2.9. It relies on superimposing an ultrashort laser field on an electron bunch inside a wiggler or undulator tuned to emit the central laser wavelength. The electron bunch and the light pulse, typically a Ti:Sa source centered at 800 nm with  $<50$  fs FWHM, are synchronized to create a leading (or trailing depending on the phase) tail of electrons. The temporal width of the leading tail is as short as 100 fs in time due to acceleration (or deceleration) in the presence of the light field. After this *modulator* stage, the main bunch and the sliced electrons are spatially separated by a dipole bending magnet. Since the tail has a different energy than the main bunch, the electrons will be deflected onto a different trajectory. The energy difference is only about 1 %, and the separation is in the order of  $\sim 1$  mrad. Therefore, both the 100 fs electron bunch and the 50 ps main bunch are guided downstream together into an undulator or *radiator* where the ultrashort X-ray pulse is generated. The light emitted by the main bunch is typically dumped by apertures, but since the 50 fs and 100 fs pulses are close to each other, one can switch between the two by slightly changing the electron orbit in the storage ring (*femtobump* at BESSY) to alter the initial kinetic energy. Since the modulation is performed only on some electron bunches already flying a special orbit and the main bunch is basically unaffected, the storage ring's normal operation remains undisturbed.

A significant advantage of the slicing facilities is the inherent synchronization of the X-ray pulse generation with the driving NIR pulse. At BESSY II, one Ti:Sa oscillator supplies two amplifier stages, one operating at 6 kHz and one at 3 kHz. The former is used to slice the electron bunch, and the latter is used to pump the sample. Since both are seeded by the same system, both pump and probe are inherently synchronized and a simple optical delay line is sufficient to access different pump-probe delays without losing temporal overlap over time. The system is pumped with 3 kHz to enable a pumped/unpumped detection. The detection is performed by integrating gated currents on an avalanche photodiode (APD) positioned behind the sample to detect transmission or moving together with the sample-beam angle to measure

reflection.

One challenge of slicing is to achieve both high energy resolution and very short temporal width of the pulses simultaneously. To meet this end, the FemtoSpex facility is fitted with tailored zoneplate monochromators, one for each transition metal absorption edge, employed to obtain a good focus and energy resolution while maintaining ultrashort pulses.

Another important approach to achieving ultrashort X-ray pulses is using light generated in X-ray free electron laser (XFEL) facilities. Light generation in XFELs is technically similar to the one in synchrotron undulators. The difference mainly stems from the length of the undulator. While a typical undulator length in a synchrotron is about 3 m to 4 m, the XFEL undulators extend to and beyond 130 m (LCLS Stanford) [87, 88]. On such lengthscales, the phase-matched light emission of the electrons creates a feedback effect, bunching the electrons further together. This leads to self-amplified spontaneous emission (SASE) that facilitates tunable X-ray pulses from atto- to  $>100$  fs pulses with a very high number of photons per pulse. This property makes XFEL light a great source for ultrafast experiments. Downsides are reduced repetition rates of typically around 100 Hz and fixed linear polarization, both issues are challenged, and improvements to existing facilities are planned to target specifically these issues [88].

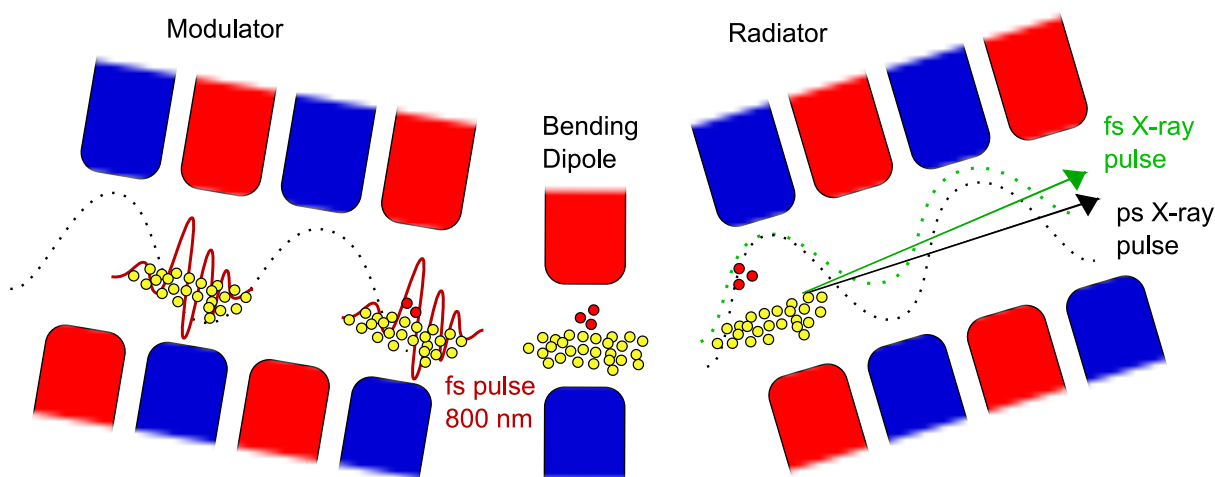


**Figure 2.9:** Slicing principle using two rows of alternating magnetic dipoles called wiggler or in more advanced geometries (not depicted) undulator used for the radiator. First the electron bunch is synchronized with a fs laser pulse inside the modulator. This introduces an energy shift of a small proportion of electrons (indicated by a different coloring) which translates into a different trajectory after a bending magnet stage. Due to the different path of the slice and the main bunch the light generated in the downstream undulator (or radiator) is spatially separated and the fs X-ray pulse (green) can be isolated from the main light (black).

## 2.2.2 Magnetic interaction

This section aims to introduce the idea of a microscopic understanding of X-ray absorption and its resulting sensitivity to magnetization. The true nature of the absorption process is quite involved and the presented equations and assumptions are only a drop of the vast ocean that is

electron-photon interaction. The derivation follows closely the formulations by Y. Joly in [89, 90] and arguments of [91, 92] with the goal of introducing symmetry arguments to justify the measurement geometries in the next chapter. Similar to reflection and absorption in the visible range, the X-ray magnetic circular dichroism (XMCD) can be described by dielectric theory and its expansion to very high frequencies. This is used to describe scattering experiments discussed in the respective section.

### Photon absorption

To treat light-matter interaction, it is beneficial to describe the electromagnetic wave in terms of the vector potential  $\mathbf{A}$ <sup>6</sup> which is parallel to the electric field vector  $\mathbf{E}$  and perpendicular to the magnetic flux density  $\mathbf{B}$  and connected to both as  $\mathbf{E} = -i\omega\mathbf{A}$  and  $\mathbf{B} = -i\mathbf{k} \times \mathbf{A}$  with the frequency  $\omega$  and the wave vector  $\mathbf{k}$ . The interaction Hamiltonian for a single electron in a potential  $V$  without relativistic contributions can be formulated as

$$H = \frac{1}{2m_e}(\mathbf{p} + e\mathbf{A})^2 - eV - ig_l \frac{e}{2m_e} \mathbf{s}(\mathbf{k} \times \mathbf{A}) + H_A \quad (2.31)$$

where  $m_e$  denotes the electron mass,  $e$  the elementary charge,  $\mathbf{p}$  the momentum,  $g_l$  the Landé factor,  $\mathbf{s}$  the spin, and  $H_A$  is the number operator reflecting the number of photons or classically the intensity. By separating the non-interacting parts from the rest, one can apply an approach from perturbation theory to arrive at an expression for the transition operator  $T$  from an initial into a final state. The interacting  $H_1$  and non-interacting  $H_0$  are separated like:

$$H_0 = \frac{p^2}{2m_e} - eV + H_A \quad (2.32)$$

$$H_1 = \frac{e}{2m_e} (2\mathbf{p}\mathbf{A} + e\mathbf{A}^2 - ig_l \mathbf{s}(\mathbf{k} \times \mathbf{A})) = \alpha V_1 \quad (2.33)$$

with  $\alpha = \frac{e}{2m_e}$  and the perturbation  $V_1$ . According to Fermi's golden rule the probability of a transition  $w_{fi}$  from an initial  $|\phi_i\rangle$  into a final state  $|\phi_f\rangle$  can be formulated as

$$w_{fi} = \frac{2\pi}{\hbar} |\langle \phi_f | T | \phi_i \rangle|^2 \rho_f \quad (2.34)$$

with the density of states  $\rho_f$  instead of a single localized final state. The transition operator  $T$  can be expanded in orders of  $\alpha V_1$

$$T = \alpha V_1 + \alpha^2 V_1 G_0 V_1 + \mathcal{O}(\alpha^3) \quad (2.35)$$

where  $G_0$  denotes the Green's function. For the discussion here only the linear term is considered, furthermore we neglect the  $\mathbf{A}^2$  term since it deals with two photon processes. The reduced transition can then be written only containing linear terms in  $\mathbf{A}$ . For an absorption process one photon is annihilated in the vector field  $\mathbf{A}$  which is best described in terms of second quantization. The field is generally written as

$$\mathbf{A}(\mathbf{r}, t) = \sum_{\epsilon, \mathbf{k}} \mathbf{A}_{0, \mathbf{k}} \left[ a_{\epsilon, \mathbf{k}} e^{i(\mathbf{k}\mathbf{r} - \omega t)} \boldsymbol{\epsilon} + a_{\epsilon, \mathbf{k}}^\dagger e^{-i(\mathbf{k}\mathbf{r} - \omega t)} \boldsymbol{\epsilon}^* \right] \quad (2.36)$$

---

<sup>6</sup>For better readability vectors are denoted in bold font throughout the chapter.

using the photon raising (creation) and lowering (annihilation) operators  $a_{\epsilon,\mathbf{k}}$  and  $a_{\epsilon,\mathbf{k}}^\dagger$  and the polarization  $\epsilon$ . Since only absorption is considered, one can rewrite  $T$  into

$$T = \alpha V_1' = \alpha \sum_{\epsilon,\mathbf{k}} A_{0,\mathbf{k}} a_{\epsilon,\mathbf{k}} (\epsilon \mathbf{p} - i \mathbf{s} \mathbf{k} \times \epsilon) e^{i(\mathbf{k}\mathbf{r} - \omega t)} \quad (2.37)$$

The states  $|\phi_{i,f}\rangle$  consist of electron  $|\psi\rangle$  and photon states  $|\mathbf{k}, \epsilon\rangle$  with  $|\psi_{i,f}; \mathbf{k}_{i,f}, \epsilon_{i,f}\rangle$ . Evaluating 2.37 in 2.34 leads to

$$w_{f,i} \propto |\langle \psi_f | \hat{T} | \psi_i \rangle|^2 \rho_f(E_f) \quad (2.38)$$

with the density of states  $\rho_f$  at  $E_f = E_g + \hbar\omega$ . The new transition operator  $\hat{T}$  reduces to

$$\hat{T} = (\epsilon \mathbf{p} - i \mathbf{s} \mathbf{k} \times \epsilon) e^{i\mathbf{k}\mathbf{r}} \simeq (\epsilon \mathbf{p} - i \mathbf{s} \mathbf{k} \times \epsilon) \left(1 + i\mathbf{k}\mathbf{r} - \frac{1}{2}(\mathbf{k}\mathbf{r})^2 \dots\right) \quad (2.39)$$

where the exponential is approximated by an expansion. Neglecting non-linear processes a surprisingly simple expression for the electric and magnetic (dipole-) transition is obtained.

$$\hat{T}_e = \epsilon \mathbf{p} \qquad \hat{T}_m = -i \mathbf{s} \mathbf{k} \times \epsilon \quad (2.40)$$

Using commutator rules<sup>7</sup> and only considering electric dipole transitions one can express 2.38 as

$$w_{i,f} \propto (E_f - E_g)^2 |\langle \psi_f | \epsilon \mathbf{r} | \psi_i \rangle|^2 \rho_f(E_f) \quad (2.41)$$

which can be evaluated for single-electron systems. The intensity can be calculated by integrating the differential scattering cross section [91]. The details of the evaluation can be found in textbooks, e.g., [89, 91, 92]. The integration of the angular part leads to the well-known dipole selection rules. Even without considering the magnetic term  $\hat{T}_m$ , this gives rise to the X-ray magnetic circular dichroism when comparing absorption intensities for circular left and circular right polarized light in a magnetic medium. It turns out that one helicity predominantly excites one spin species and once there is a spin-dependent difference in the density of states (DOS) of the final state  $\rho_f$ , this difference directly translates into differences in the absorption. Experimentally this can be realized by either changing the helicity from left to right circular (or vice-versa) or magnetizing the sample in the opposite direction. An important characteristic of XMCD is that the *final* density of states is probed, i.e., the empty states at the valence band. This motivates geometries where a Stoner-like exchange splitting is observed along  $\mathbf{k}$  when using circular polarization. J. Stöjir and H.C. Siegmann reduce the formalism to

$$I_{XMCD} \propto p_{circ} \mathbf{m} \mathbf{L}_{ph} \quad (2.42)$$

with the degree of circular polarization  $p_{circ}$ , the photon angular momentum vector  $L_{ph}$ , and the magnetization vector  $\mathbf{m}$  [91]. Similar to MOKE in the visible range, out-of plane magnetization is best probed by normal incidence and in-plane magnetization is detected in grazing incidence. The second-order term of  $\hat{T}_e$  in  $\mathbf{k}$  describes quadrupole transitions and adds a contribution linear in  $\mathbf{s}$ , which is why it is often combined into the first magnetic term. While

---

<sup>7</sup> $\epsilon \mathbf{p} = \frac{m}{\hbar} [\epsilon \mathbf{r}, H_0]$

the electric quadrupole transition leads to noticeable differences, all higher electrical terms and similarly all magnetic terms compare to the dipole one with magnitudes of only about  $10^{-3}$  and can therefore usually be ignored [90]. Not discussed in this short review is the class of phenomena that can be measured by linearly polarized X rays. When employing linearly polarized photons, specific dipole geometries can be targeted and asymmetries, for example due to structure or magnetization, are revealed. Similar to the quadratic MOKE this effect is sensitive to  $\langle \mathbf{m}^2 \rangle$  and can thus be employed for the study of antiferromagnets. Further complication in the description arises once the final levels are not well separated anymore, which is the case for transition metal L edges [91], where final-state effects have to be considered. This is treated in the multiplett analysis [89, 91].

XMCD has been established as one of the most powerful tools to investigate magnetism directly due to the immediate connection of the observable to the magnetic state of the system. A careful analysis even allows quantitative analysis of the unoccupied states or holes in a system. In many magnetic systems this can be expanded to an analysis of the elemental magnetic moments, anisotropies, and spin- and orbital moments separately [91, 93–95].

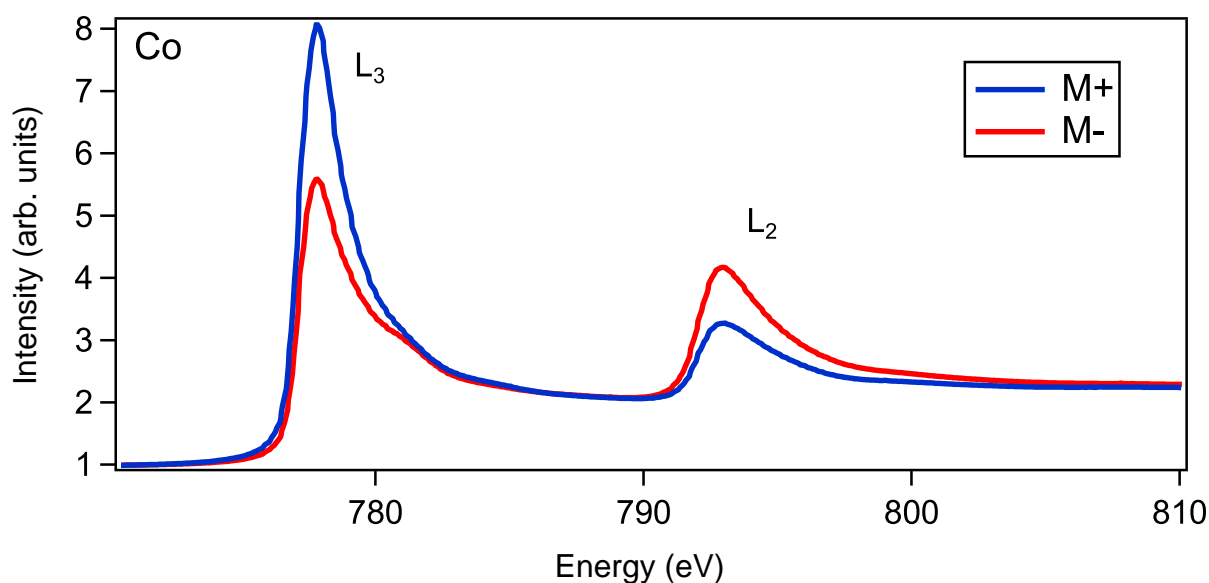


**Figure 2.10:** Recording of the TEY in a Co/Mn-multilayer sample at the Co  $L_{3,2}$  resonance using circular polarized light. The intensity at the resonances depends on the direction of the sample magnetization. In case the sample is magnetized in the direction of the beam (blue, M+) the TEY signal at the  $L_3$  edge is increased compared to a magnetization anti-parallel to the beam (red, M-).

For X rays and XUV photons, instead of measuring a polarization change, recording the intensity of the reflected or transmitted beam thus provides an accurate way of determining the magnetic state of a sample. Not all specimen can be investigated in a transmission geometry and X-ray reflection under certain angles contains not only absorptive but also reflective features of the sample. Experimentally it is therefore often easier to detect the absorption directly as a current coming to the sample, usually referred to as total electron yield (TEY) signal. An example TEY measurement on Co is presented in Fig. 2.10. A similar energy scan performed in reflection under a certain angle is presented in Fig. 2.11. Since the current is a direct measure of

the photo-excited electrons leaving the sample, it contains the same information as the absorbed light. It only requires a good contact and conductive samples. Depending on the material investigated TEY is only sensitive up to 10 nm depth. Unfortunately ultrafast measurements cannot be directly performed in TEY, since current read-out is too slow. In a pump-probe scheme the TEY can be used to record the delay-time dependent absorption. Time-resolved studies typically employ a detection of the light either in transmission or in reflection using a fast avalanche photodiode (APD). The results presented in this thesis rely on measurements performed in a scattering geometry, i.e., the reflected intensity at a specific energy on the resonance is recorded with an APD. As mentioned before, the reflected angle-resolved intensity contains more information than the absorption, which motivates a more thorough treatment of X-ray scattering in the context of transition metal L-edges. This is presented in the next section.

### 2.2.3 Resonant X-ray scattering and reflectivity

In the previously presented quantum-mechanical treatment of the interaction between photon and electron, the terms for scattering factors and cross section can be obtained [90, 91]. In this section a semiclassical approach is chosen to derive the expressions useful for diffraction experiments following the derivations of [75, 93].

First an expression for the equation of motion for a bound electron in the presence of a driving light field is derived to express the current density in Maxwell's equations. From the expression of the scattered field, an expression of the atomic scattering factor  $f(\Delta\mathbf{k}, \omega)$ , which links the radiated or scattered field to the incoming one, can be derived.

$$f(\Delta\mathbf{k}, \omega) = \sum_s^Z \frac{\omega^2 e^{-i\Delta\mathbf{k}\Delta\mathbf{r}_s}}{\omega^2 - \omega_s^2 + i\gamma\omega} \quad (2.43)$$

Where  $\Delta\mathbf{k} = \mathbf{k}_{in} - \mathbf{k}_{out}$  denotes the scattering vector and  $\mathbf{r}_s$  describes the displacement of the charge. In terms of scattering angle the change in wave vector is expressed by

$$|\Delta\mathbf{k}| = \frac{4\pi}{\lambda} \sin \theta \quad (2.44)$$

with the wavelength  $\lambda$  and the scattering angle  $\theta$ . The displacement of the electron  $\mathbf{r}_s$  is typically isotropically confined to the Bohr radius  $a_0$  [75] which can be used in combination with 2.44 to get an upper limit for  $\Delta\mathbf{k}\Delta\mathbf{r}_s$ .

$$\Delta\mathbf{k}\Delta\mathbf{r}_s \leq a_0 \frac{4\pi}{\lambda} \sin \theta \quad (2.45)$$

Thus for  $\theta \simeq 0$  or  $\lambda \gg a_0$  in the expression 2.43, the  $\Delta\mathbf{k}$  dependence can be omitted. Since we are dealing with X rays, the first case of  $\theta \simeq 0$  or  $\mathbf{k}_{in} \simeq \mathbf{k}_{out}$  is treated in the following. Since not all electrons contribute to the same amount, a phenomenon that is readily understood in the context of the transition probabilities described in the previous chapter, a weighting factor  $g_s$  is introduced to the scattering factor. This weighting or *oscillator strength* is normalized to the total number of charges and follows

$$\sum_s g_s = Z \quad (2.46)$$

and can in principle be calculated by the transition probabilities. Using 2.46 and  $\mathbf{k}_{in} \simeq \mathbf{k}_{out}$ , eq. 2.43 is rewritten into

$$f(\omega) = \sum_s \frac{g_s \omega^2}{\omega^2 - \omega_s^2 + i\gamma\omega} \quad (2.47)$$

Coming back to Maxwell's equation, one can subsequently identify by rearrangement the refractive index  $n$  in the wave equation, shown for example in chapter 3 of [75] or 9 of [91]. From this derivation the refractive index is expressed as [75]

$$n(\omega) = 1 - \frac{e^2 n_a}{2m_e \epsilon_0} \sum_s \frac{g_s}{\omega^2 - \omega_s^2 + i\gamma\omega} \quad (2.48)$$

with the average density of atoms  $n_a$ , the electron mass  $m_e$ , the resonance frequency  $\omega_s$ , and a spectral weighting factor  $g_s$ . The sum can be written in terms of the form factor  $f(\omega)$ <sup>8</sup>

$$f(\omega) = \sum_s \frac{g_s \omega^2}{\omega^2 - \omega_s^2 + i\gamma\omega} = f'(\omega) - i f''(\omega) \quad (2.49)$$

where imaginary and real part are separated into  $f''(\omega)$  and  $f'(\omega)$ , respectively. Using this notation the refractive index is expressed

$$n(\omega) = 1 - \frac{n_a r_e \lambda^2}{2\pi} (f'(\omega) - i f''(\omega)) \quad (2.50)$$

or commonly expressed as

$$n = 1 - \delta + i\beta \quad (2.51)$$

which is closer to the expression from low frequencies where  $n$  is expressed as  $\tilde{n} = n + ik$ . It is useful to rewrite 2.49 in terms of energy using  $\hbar\omega = E$  and  $\hbar\omega_s = E_n$  to number the resonances. The damping is rewritten in terms of a resonance line width  $\Delta_n$ . Using the notation of Siegmann and Stöhr [91] one finds

$$f(E) = Z + F'(E) - iF''(E) \quad (2.52)$$

$$F'(E) = \frac{(E^2 - E_n^2)E_n^2}{(E^2 - E_n^2)^2 + (E\Delta_n)^2} \quad (2.53)$$

$$F''(E) = \frac{E_n}{\Delta_n} \frac{(\Delta_n/2)^2}{(E - E_n)^2 + (\Delta_n/2)^2} \quad (2.54)$$

where the sum over  $g_s$  is separated (see footnote 8). Once a magnetic system is investigated, additional scattering terms will contribute to the refractive index. They can be included additively as

<sup>8</sup>This is also expressed as  $f(\omega) = Z + F'(\omega) - iF''$  [91] for forward scattering, e.g., in eq. 2.52 with the atomic scattering factors  $F(\omega)$  and total number of electrons  $Z$ . For  $\omega \gg \omega_s$  and  $\gamma \ll \omega$ , the sum approaches  $f(\omega) = \sum_s g_s = Z$ , which is treated as an offset in this expression. The often referenced Henke-factors [96] are defined exactly in this way.

$$n = 1 - (\delta + \Delta\delta) + i(\beta + \Delta\beta) \quad (2.55)$$

where  $\Delta\delta$  denotes the magnetic change in the real part and  $\Delta\beta$  the change in absorption due to magnetism. Again it is sufficient to know either  $f'$  or  $f''$ , since they are related by the Kramers-Kronig relation (KKR). The imaginary part  $f''$  can be obtained by X-ray absorption measurements, since they are proportional. Experimentally one can find the scattering factors by rescaling experimental data to the tabulated off-resonant values of  $f''$  and then by KKR find  $f'$ . Having obtained an expression for the refractive index it is now possible to employ the same formalism as described in 2.1.2 to calculate reflected and transmitted intensities within the limits of the approximations, done in [97] for example. This can be employed to calculate the scan presented in Fig. 2.11 using the experimental data obtained in Fig. 2.10.

The soft X-ray wavelength is typically of the order of a few nm, too large to resolve atomic positions but quite sensitive to thin film spacings where interfaces are typically separated by some nanometers. Next to the magnetism, this is employed to recover film thickness, surface roughness, and chemical composition from a diffraction scan [98, 99]. In the scope of this work, this approach is used to calculate reflected intensities in excited systems using time-dependent optical constants and lattice spacings.

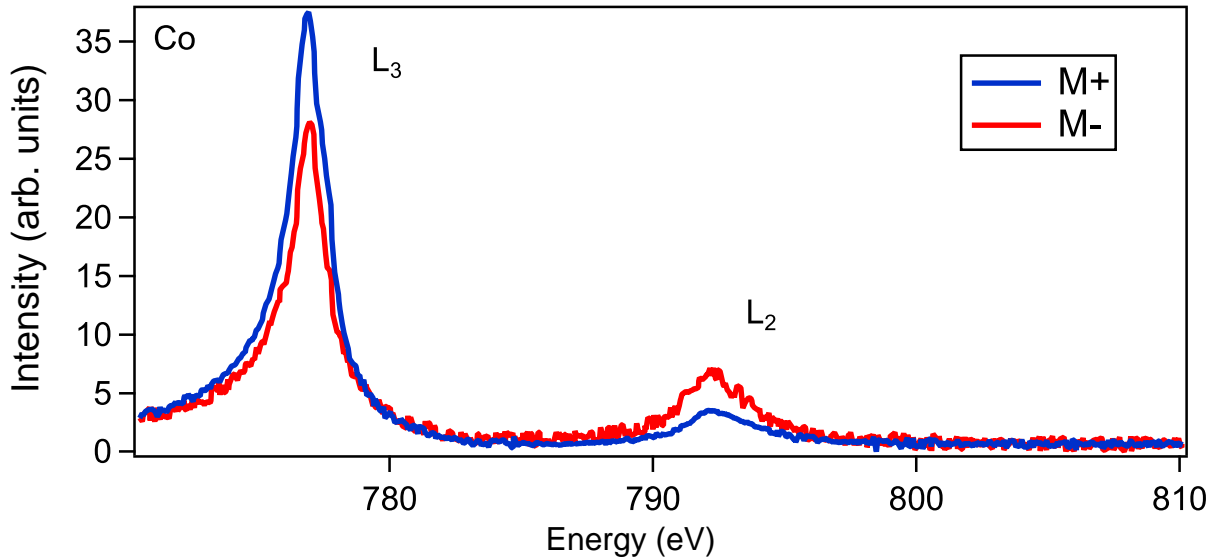


**Figure 2.11:** Recording of the reflected intensity of a the same Co/Mn-multilayer sample as in Fig. 2.10 measured at  $40^\circ$  to the beam and with  $20^\circ$  between sample surface and beam using circular polarized light. The intensity at the resonances still depends on the direction of the sample magnetization. In case the sample is magnetized in the direction of the beam (blue, M+), the TEY signal at the  $L_3$  edge is increased compared to a magnetization anti-parallel to the beam (red, M-).

## 2.3 Very low and high frequencies and other notable techniques

The previous sections cover the employed techniques in this study. For completeness and to highlight the plethora of experiments that can be used to probe magnetism at early excited

states, this section includes a short discussion on even lower wavelengths and what has not yet been discussed, very high wavelength (IR) radiation. Additionally, some experiments which do not rely on an all-optical pump-probe scheme are introduced.

When increasing the photon energy even more to wavelengths short as 1 Å, the scattering discussed before becomes highly sensitive to the position of the scattering atoms, thereby allowing to resolve the atomic lattice. Similar to approaches in the soft-X-ray range, recording the angle-resolved hard X-ray diffraction can be used to calculate back lattice distortion, i.e., strain, stress, and, more generally, phononic excitations. This provides an indirect means to study the effects of magnetization by observing changes coming from magnetostriction and transport, e.g., [100, 101]. Hard X-ray pulses are either incoherently generated from a plasma as discussed before [72, 102] or quasi-coherently in XFELs like the LCLS in the US or SACLA in Japan [87, 103]. XFEL hard X-ray pulses can also be used in resonant experiments similar to soft X-ray absorption to measure XMCD on absorption edges that lie above the typical threshold of 2 keV, for example, in Pt at 11.6 keV [104], revealing the dynamics of induced magnetic moments in elements other than the 3d TMs. Or non-resonantly in time-resolved studies of the inelastic scattering [105], revealing intrinsic coupling strengths in an AFM and resolving time-dependent changes of the long-range magnetic order. The list of experiments investigating ultrafast magnetism with X-rays is still growing, and this summary is, of course, not comprehensive but intended to introduce the methodology. On the high-energy side, we stop at energies of the order of tens of keV used as probe light and continue with a brief discussion on probes almost ten orders of magnitude smaller or around some meV.

In the low-energy region, the radiation is commonly referred to by the frequency as THz radiation. THz radiation has successfully been employed in the study of ultrafast magnetism either for pumping a magnetic system, for example in [106, 107], or as a radiative signature of magnetization change, e.g., [108–110]. Using THz frequencies allows direct coupling to charges and spin waves, for example in NiO, where direct control of magnons by THz pulses has been demonstrated [107]. The first experiment presented here that deviates from the all-optical pump-probe scheme is the recording of THz radiation generated by optically pumping a ferromagnet/heavy metal (HM) layer stack. The optical pulse drives ultrafast spin currents flowing from the FM to the HM (or vice-versa) resulting in perpendicular charge currents. The charge currents can be viewed as a source of dipole radiation which emits light in the THz region. The ultrashort large-bandwidth THz pulse is subsequently measured by electro-optical sampling<sup>9</sup> since it contains information about ultrafast carriers and the magnetization quench and therefore also provides a tool to investigate magnetic interfaces and thin films [110]. The field of THz studies is quite recent and growing fast since the pulses generated are a promising tool that may find applications far beyond magnetism research [4].

Lastly, after already deviating from the all-optical pump-probe scheme, another tool employed to investigate ultrafast phenomena linked to magnetization is electron diffraction. Similar to hard X-rays, the electrons have a wavelength that allows resolving the reciprocal lattice. In combination with an optical pump, electron diffraction by ultrashort electron pulses can therefore also provide a measure of the energy present in the lattice. When investigating magnetic samples, additional contributions attributed to the spin system are identified [111].

Spatially resolving experiments are not yet mentioned but of course there are also advances that promote both time and spatial resolution of magnetic systems exploiting MOKE in microscopy

---

<sup>9</sup>It does end up being a pump-probe experiment. However, the probe is not overlapped with the pump on the sample but is co-propagating with the THz pulse behind the sample at different time delays. It is used to measure the effect of the THz pulse in a birefringent crystal, which allows the reconstruction of the THz electric field.

[112, 113], MCD for photo-electron emission (PEEM) [114], and also THz-STM studies [115] are examples. Spatial imaging has proven to be very successful even without fs time resolution in discovering ultrafast magnetism phenomena like all-optical switching (AOS) [116, 117].

## 2.4 Summary

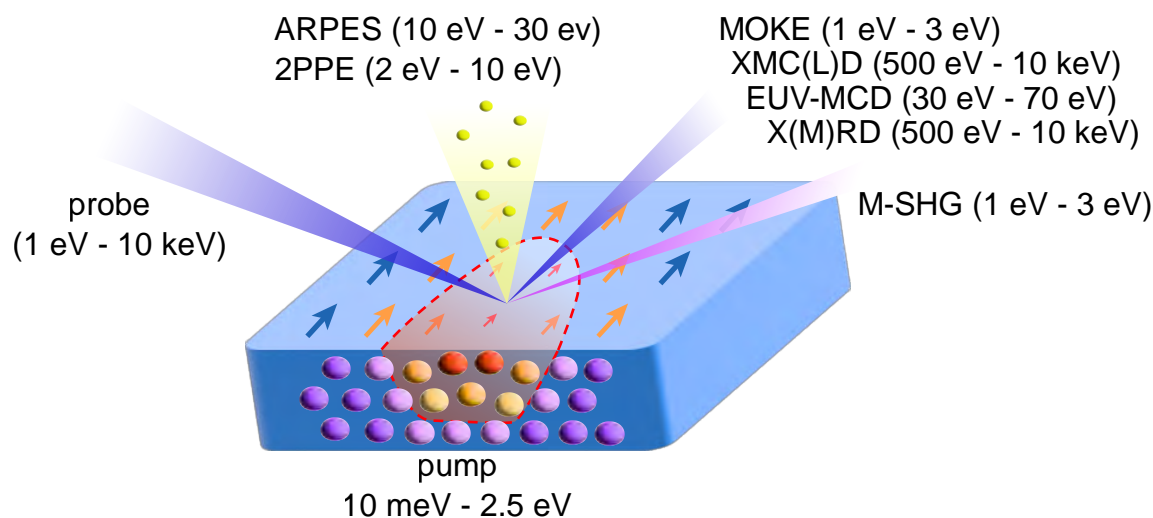


**Figure 2.12:** Overview of the experimental techniques covered in the chapter. The fundamental principle is the pump-probe technique. Depending on the experiment, different excitation but most importantly different probing energies are used, this is indicated by the energy range next to the respective technique. Some techniques use the same photon energy but vastly different intensities to exploit non-linear effects, for example MOKE and M-SHG, and are therefore separated in the discussion. Not shown are THz magnetometry and electron diffraction. Within this work, XMCD and MOKE are used in time-resolving experiments to answer the research question posed initially.

The chapter introduces the experimental methods employed in this work, goes beyond that, and presents a brief survey of the many experiments used in ultrafast magnetism research. A summary of the most important aspects like the magneto-optical Kerr effect, the Faraday effect, and the linear, and circular X-ray magnetic dichroism is presented. A rigorous treatment in terms of derivations of the phenomena is not given, but the interested reader can find the relevant formalisms in the referenced literature. The results presented in chapters 4, 5, and 6, which are obtained in this work, are readily understandable with the background of the experimental means MOKE and XMCD provided within the chapter, in combination with the discussion of magnetization models discussed in the next chapter.

The research on ultrafast time-resolved phenomena relies heavily on advances made in the field of optics and has benefited greatly from affordable fs laser pulse table-top sources. Since the field is still advancing, many research questions are still being discussed. The practical means to study ultrafast magnetism have multiplied in the past 25 years since the first curve recorded by Beaupaire et al. was published. Initially, research was dominated by MOKE and ARPES measurements, then HHG sources and pulsed synchrotron or XFEL radiation opened new avenues of successful research. A short summary of the most important techniques is presented in Fig. 2.12 together with the relevant probing energies. The current image of ul-

trafast magnetization dynamics is further solidified by experiments observing magnetization indirectly, for example, via magnetostriction acting on the lattice, resolved in hard X-ray and electron diffraction studies. Similarly, transport phenomena that are also directly linked to the observation of ultrafast demagnetization are experimentally investigated in THz emission and absorption experiments. Finally, a comprehensive picture of magnetism at femtosecond timescales is achieved by combining the information obtained by all different methods and avenues. What this picture contains and how it connects to the existing models of magnetism is the topic of the next chapter.



## Chapter 3

# Emergence and treatment of ultrafast magnetization

The following chapter is concerned with the models and descriptions of magnetism at ultrafast timescales. It intends to establish the relevant physical processes and material parameters employed in the theory to interpret and reproduce observations. Furthermore, it introduces the explanations of the underlying microscopic origin of the observed effects. This is done in an effort to connect the observations of the experiments to the interpretations presented. Lastly, the concepts introduced here are applied to explain the findings presented within this work.

The subject of ultrafast magnetism is still developing and adjustments to existing models expanding them to more complex systems like multilayers and antiferromagnets are constantly being pushed. Therefore, it is not in the scope of this review to offer a complete description of all processes but rather several important concepts that are mostly connected to each other are highlighted.

The first section covers the phenomenological description of ultrafast magnetism in terms of a rate model using different reservoirs of heat and therefore, energy. The extension of the heat models to a microscopic description is presented afterwards. The subject of ultrafast magnetism is commonly approached from many angles, which is why the third section is concerned with non-local effects in terms of the semi-ballistic hot electrons mediated spin transport. Lastly, a brief insight into an example of coherent electron and spin dynamics, existing only in the duration of the excitation, is given. To avoid a boring enumeration of the key factors and most prominent magnetism models, the theoretical explanations are presented along with the experimental observation in a somewhat chronological fashion. This does again stretch the scope of this literature survey and the more hasty reader might prefer to directly go to the references, for example [53, 54, 118–120] for a more concise explanation of the employed models.

### 3.1 Ultrafast quench and temperature models

Over the past 40 years the motivation for time-resolved research in magnetism hardly changed. Due to the importance of magnetic bits in data storage media and the ever increasing demand for higher recording densities, light-induced effects are being explored. Early works, in the late 80s and early 90s, employing ps laser pulses found that a pulse can switch the magnetization in rare earth alloys [121] kicking off the research of all-optical switching (AOS). At the same

time, transition metal ferromagnets, i.e., Ni and Fe thin films, were investigated to understand spin-lattice coupling [122, 123]. Some investigations concluded that, "[.] Fe<sup>1</sup> cannot be demagnetized within the duration of a 30 ps laser pulse [...]" [122], from data recorded in streak camera experiments of reflectivity. That this is not the case and indeed Ni, Fe, Co, and many of their alloys can be demagnetized faster was first reported six years later by Beaurepaire et al. [43] employing fs laser pulses in a TR-MOKE setup. Why a reduction of the magnetization was not observed in the works employing ps laser pulses is a quite intriguing question which we will be able to answer partly in the scope of ultrafast spin transport. The results in [43] contradicted the previous works and started an interesting discussion around the applicability of MOKE for ultrafast investigations which is to some extent still ongoing. As stated before, many of the doubts could be rebutted by using different techniques that all showed the same findings. The earliest works are summarized in Fig. 3.1. The common property in all the measurements is that already in the first 500 fs after excitation a strong reduction of the magnetic contrast is found.

### 3.1.1 The three-temperature model (3TM)

The authors of [43] offer a phenomenological description of the observations in terms of three coupled heat reservoirs, the electrons, the lattice, and the spins. It is a natural extension of the already present two-temperature model employed in the description of electron-phonon interactions in light-induced experiments, e.g. [124]. The three-temperature model (3TM) includes the spin reservoir with its own heat capacity, spin-lattice, and electron-spin coupling terms. By modeling the laser excitation as a heat source term in the electron temperature and assuming a magnetization dependent on the spin temperature the model can reproduce the findings quite well. The 3TM is summarized in three coupled equations

$$\begin{aligned}
c_e(T_e) \frac{dT_e}{dt} &= -G_{el}(T_e - T_l) - G_{es}(T_e - T_s) + S(t) \\
c_l(T_l) \frac{dT_l}{dt} &= -G_{el}(T_l - T_e) - G_{ls}(T_l - T_s) \\
c_s(T_s) \frac{dT_s}{dt} &= -G_{es}(T_s - T_e) - G_{ls}(T_s - T_l)
\end{aligned} \tag{3.1}$$

with the specific heat of the electrons  $c_e$ , the lattice  $c_l$ , and the spin system  $c_s$  and the laser source term  $S$ . The coupling constant  $G_{el}$  between electrons and lattice can be estimated by experiments of reflectivity [124]. The coupling between lattice and spin  $G_{ls}$  was initially sought after in the experiments by Vaterlaus et al. and the coupling term between electron and spin  $G_{es}$  has to be considered purely phenomenologically. The early picture condensed from the results of [43, 46, 56] can be briefly summarized as follows: the optical laser pulse acting only on the electron system creates a non-equilibrium electron distribution that thermalizes within  $\sim 100$ -300 fs. In the time below 100 fs the model therefore does not apply. Afterwards, the electron temperature governs the magnetization dynamics by heat dissipation into the spin system. The coupling parameters of the system are extracted from fits to the data and the overall dynamic can be described well. There are, however, several downsides to the model, first of all it does

---

<sup>1</sup>Similarly Ni [123].

not offer an explanation in terms of the underlying processes, it assumes instantaneous internal thermalization of the reservoirs, it neglects angular momentum, and it artificially separates electrons and spins. The coupling parameters are fitted from the experiment and especially for the electron spin temperature a solid physical meaning is difficult to reason. Explanations of the processes are suggested in [46] in an effort to unify the observations of [43, 56] and [122]. At the early times, that is up to 300 fs, Stoner excitations, i.e., electron-electron spin exchange scattering, which scales with the electron temperature, reduces the local atomic moment and thereby the magnetization. After thermalization, the excitations decay into magnons which are slowly dampened by magnon-phonon scattering and finally the magnetization relaxes back into equilibrium after several 100s ps.

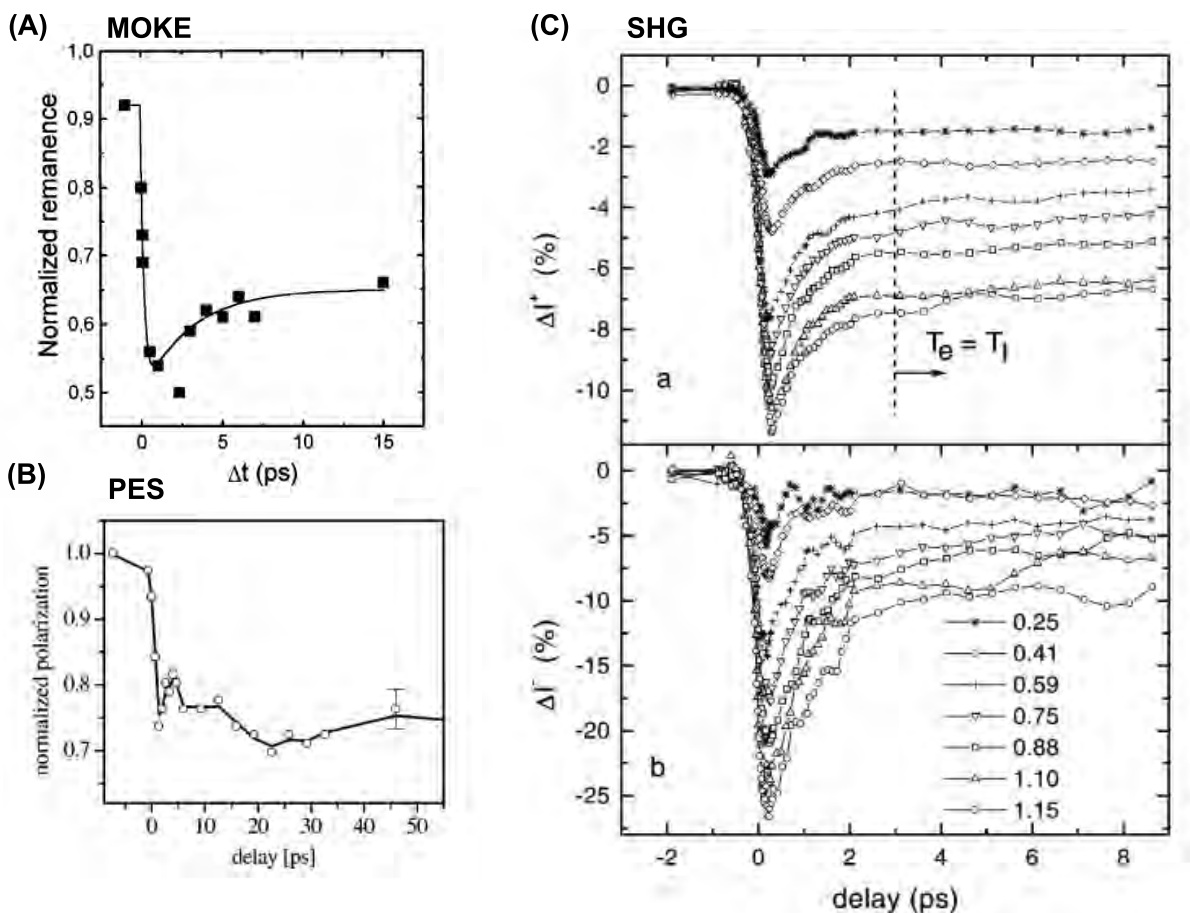


**Figure 3.1:** First measurements of the ultrafast quench of magnetization. (A) Ultrafast reduction of the remanence in Ni, measured by Beaupaire et al. in TR-MOKE, published in '96. The curve sparked an ongoing discussion about the true observable in TR-MOKE experiments. (B) Normalized spin polarization recorded in a pump-probe photoemission experiment on Ni published in '97. The curve reproduces the findings of [43], further establishing the ultrafast quench from an electronic point of view. (C) Delay-time-dependent second harmonic signal on Ni, also published in '97. The top panel shows the sum signal and the bottom one the difference assumed to be proportional to the magnetization. The curves shown in (A),(B), and (C) are reprinted with permission from Ref. [43, 46, 56], respectively. Copyright (2021) by the American Physical Society.

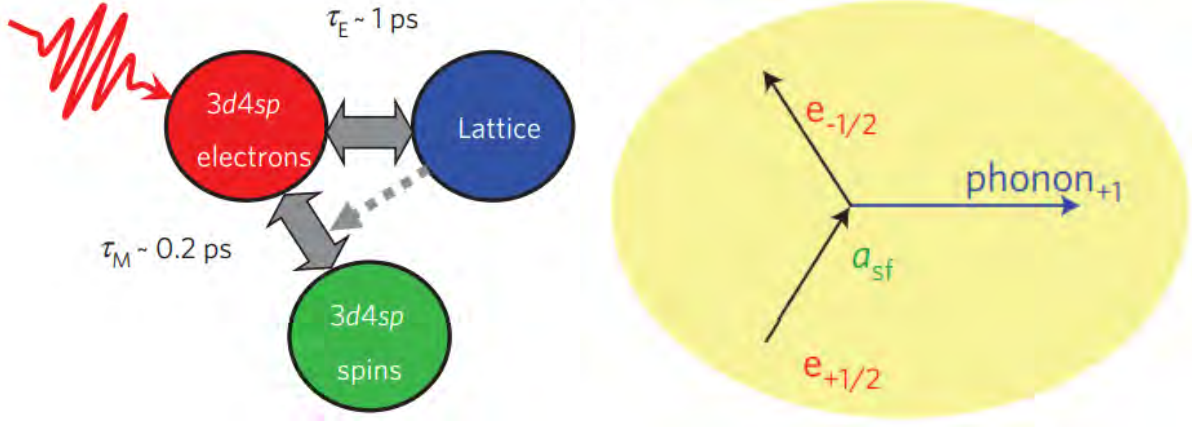


**Figure 3.2:** Assumptions of the microscopic 3TM. The systems (left) are not in equilibrium at early timescales and energy flows from the electronic reservoir to the lattice via electron-phonon scattering. Each scattering event is associated with a spin-flip probability  $a_{sf}$ , depicted on the right. Statistically more majority spins will undergo a spin-flip which reduces the magnetization of the system. Reprinted with permission from Ref. [54]. Copyright (2009) by the Nature Publishing Group.

### 3.1.2 The microscopic 3TM

Since the 3TM, although applicable to the observation, lacks predictive character, efforts were undertaken to put it on a solid physical basis [53, 54]. About 9 years after the publication of [43], Koopmans et al. arrived at a model describing both the early demagnetization in terms of electron-phonon spin-flip scattering and the longer times in terms of the Landau-Lifshitz-Gilbert (LLG) equation [53]. Within this description the authors manage to link the magnetic timescale  $\tau_{de}$  of the demagnetization<sup>2</sup> to meaningful electronic parameters

$$\tau_{de} = \frac{\hbar}{4\alpha k_B T_C} \quad (3.2)$$

with the Curie-Temperature  $T_C$ , the Boltzmann constant  $k_B$ , the reduced Planck constant  $\hbar$ , and an effective electron-phonon scattering probability  $\alpha^3$ . This approach was further refined and merged with the 3TM [54]. The new model referred to as the microscopic-3TM (m3TM), the Koopmans, or Elliot-Yafet (E.-Y.) model, since the E.-Y. approach is used to model the scattering, does not treat the spin as an independent heat reservoir anymore but the magnetization  $m$  is directly coupled to the lattice and electron temperature. Instead of the last line in eq. 3.1 Koopmans et al. suggest to use

$$\frac{dm}{dt} = mR \frac{T_l}{T_C} \left(1 - m \coth\left(m \frac{T_C}{T_e}\right)\right) \quad (3.3)$$

with a material constant  $R$  given by the electronic properties. The spin reservoir is thus not attributed with a temperature anymore.

<sup>2</sup>In the sense employed in the formulation of eq. 2.30.

<sup>3</sup>The scattering probability  $\alpha$  is also interpreted as the Gilbert damping factor in the LLG equation.

The Koopmans model therefore solves several important aspects that were lacking in the 3TM. First of all spin-flip electron-phonon scattering is identified as a microscopic origin of the demagnetization. This allows to compare experiments performed on different samples systematically. Additionally, a channel for angular momentum dissipation, namely the phonons, is found. Furthermore, the model manages to incorporate observations in rare-earth elements and their alloys, which show different behavior than the transition metals due to their localized 4f moments.

At the same time Koopmans et al. presented their model based on Elliot-Yafet scattering Battiato, Carva, and Oppeneer proposed a different model based on superdiffusive transport. This is the subject of the next sections where transport phenomena, which are especially relevant for multilayer systems, like the ones investigated in this thesis, are discussed as a channel for demagnetization.

## 3.2 Spin transport

The picture of local demagnetization and spin dissipation is challenged by investigations on half metallic samples [125, 126], for example, where only one spin channel posses empty states around the chemical potential. Consequently, a direct spin-flip channel by Elliot-Yafet scattering is not present. Nevertheless, demagnetization is still observed, although with a larger demagnetization time of more than 100 ps. Given the large timescale of demagnetization the authors of [125, 126] suggest that first the energy is distributed to the lattice which leads to an altered bandstructure due to a new crystal field. Then an effective spin-flip scattering can take place. Furthermore, investigation of demagnetization in multilayer samples [127] revealed that transport channels have to be considered paving the way for an alternative explanation. In the work of [127] two FM layers separated by either an insulating or a metallic spacer layer are investigated after excitation by a laser pulse. When using an insulating spacer layer the measured demagnetization time is independent of the direction of magnetization in each layer, i.e., parallel or antiparallel alignment. When using a metallic spacer layer the timescales for parallel and antiparallel alignment change. The observations are can be explained in the transport model by Battiato et al. [128, 129].

The superdiffusive transport model conceptually accounts for hot non-equilibrium electrons induced by the laser pulse which are semi-ballistically transported away from the stimulus. The concept has been employed before in the description of pump-probe reflectivity measurements [130] where a mixture of diffusive and ballistic electrons is assumed to describe the experiment. The basis for demagnetization arises from distinct carrier lifetimes for spin majority and minority electrons. The model employs a higher spin lifetime for majority carriers, which encompasses a longer mean free path and thus a reduction of magnetization since majority spins are carried away more efficiently. Since a charge depletion is screened very quickly in a metal<sup>4</sup>, the transport, although consisting of free charges, is a net spin current. The model is commonly referred to as "superdiffusive" since the numerical mean displacement of hot electrons, obtained by solving the transport equation given in [128, 129], in the relevant timescale for demagnetization, lies between the diffusive and the ballistic regime. The transport model offers an alternative explanation of ultrafast demagnetization without the need of local spin and angular momentum dissipation channels. Angular moment is conserved and magnetization is distributed away from the region of interest.

---

<sup>4</sup>The authors of [131] assume less than 2 fs for screening in transition metals.

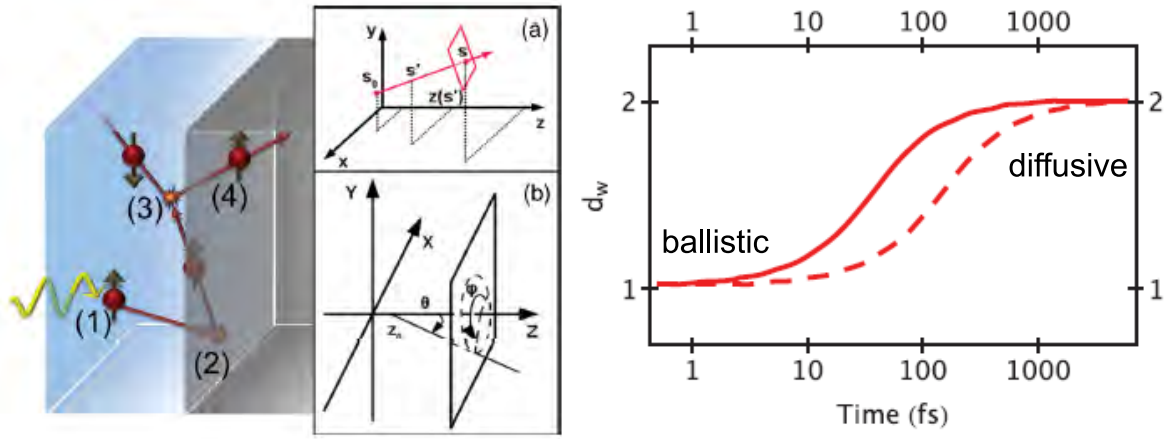


**Figure 3.3:** Left: Sketch of the superdiffusive transport mechanism. Laser excitation (1) induces hot spin-polarized carriers that are uniformly transported away. Scattering events at interfaces (2) or with other electrons (3) mix the ballistic nature with the diffusive transport. Eventually spin polarization is carried away from the top layer (4). (a) and (b) illustrate the geometry employed in the calculation. Right: Diffusion parameter  $d_w$  as defined in [129], initially the electrons are ballistically transported away from the hot region and with increasing time approach a thermal diffusion behavior due to scattering. The solid line represents the values obtained assuming an elastic lifetime of  $\tau = 10$  fs and the dashed one is calculated for  $\tau = 40$  fs. Reprinted with permission from Ref. [129]. Copyright (2021) by the American Physical Society.

The approach is further validated by more recent experimental studies measuring the increase in spin polarization after laser heating in a Au layer adjacent to Fe [132], and by further investigating the spin injection in parallel and antiparallel multilayer stacks [133]. An indirect validation is reported in an investigation of Ni demagnetization through a Au layer mediated by hot electron transport after laser excitation [134]. It also offers an explanation for the apparent absence of demagnetization in the early experiments which employed pulses of durations  $>30$  ps. The superdiffusive current in case of a fs-excitation is driven by the large number of carriers excited at the same time in the excitation region. Their successive cascading leads to a depletion of majority spin carriers in the laser spot region. However, using pulses with long durations allows the sample to heat-up uniformly and the electron motion will simply be described by heat diffusion. The elastic lifetimes, of around 10 fs to 100 fs [131], is orders of magnitude smaller than the stimulus. Superdiffusive carriers are therefore not invoked in these experiments.

That transport plays an important role is established, the question as to what is the dominant contribution, local or non-local, is a difficult one to assess. The authors of [128, 129] calculated that the contribution of spin-flip scattering could only account for  $\sim 3\%$  of demagnetization [135, 136] and concluded that transport should be the dominant contribution to demagnetization. At the same time, comparisons of measurements of demagnetization in FM layers coupled to insulators to demagnetization in FM layers coupled to conductive layers performed by the authors of [53, 54] showed no significant difference [137] leading to the assumption that transport plays only a minor role, at least in single layers. A middle ground is found by the authors of [138] who claim from depth-dependent analysis that in the first  $\sim 200$  fs spin transport dominates and then spin-flip scattering takes over. Most authors agree that both channels are

important and will give rise to a sizable effect. The role of each is most likely determined by the system investigated.

Despite this discussion, the transport theory offers explanations for spin injection in multilayer systems, accounts for effects of insulators and thereby also the dielectrics investigated in [125, 126], explains observations of the long demagnetization time in rare earth elements due to the localized nature of the 4f-electrons, and crucially explains the generation of THz signals in multilayers following ultrafast demagnetization.

### 3.3 Optically induced spin transfer

While the models discussed to this point aim to capture thermal processes that follow the initial electronic excitation leading to demagnetization, they do not include a coherent coupling between the laser field, the electrons and their spin. It has been reasoned in early theoretical works aiming to describe ultrafast demagnetization that a coherent electronic excitation following the temporal laser pulse profile alters the exchange interaction already in the presence of the laser pulse [139]. Since this timescale is difficult to access experimentally, the first investigation revealing a coherent electron dynamic in the presence of the photon field [140] was published 11 years after [139], about the same time as the m3TM. In Ref. [140] a coupling between the laser field and the magnetic and electronic dynamic is revealed in Ni and CoPt<sub>3</sub>. These coherent dynamics are not the result of the inverse Faraday effect, i.e., a direct angular momentum transfer of the photons to the magnetic system, which has been argued to be a driving mechanism in ultrafast magnetization experiments [141], but was found to be orders of magnitude smaller than thermal effects in metallic films<sup>5</sup> by investigations of helicity-dependent all optical switching [144–148].

A microscopic picture of one coherent excitation in the presence of the light field is offered by [120] in terms of an optically induced (inter-site) spin transfer (OISTR). The authors of [120] find by time-dependent density functional (TD-DFT) calculations that optical transitions are driven between neighboring atomic sites. In case the neighboring sites, for example at an interface, at the surface, or in an alloy possess a different density of states in the energy reached by the optical excitation, an exchange of carriers and therefore spin happens. While charge neutrality is always fulfilled, since the electronic transfer is considered an exchange of electrons in more favorable states, the local atomic moment is not conserved. An example between neighboring Mn atoms is calculated in [120] and the sketch is shown here in Fig. 3.4 (A). The two Mn sites, in the following referred to as A and B, are AFM ordered and thus have a mirrored spin-resolved DOS. A majority electron of A possess a high probability for a transition into the B site where a higher unoccupied number of states will be available since spin is conserved in the optical transition.

The OISTR predicts an enhancement of the demagnetization process at earliest times in NiPt which has been observed experimentally in XUV absorption studies using 300 as pulses [149] to resolve the early dynamics. Further confirmation is achieved in time-resolved XUV absorption experiments using 60 fs pulses [150] revealing an increase of the demagnetization in CoPt compared to Co. An investigation of half-Heusler compounds in XUV experiments revealed a significant OISTR effect at early times [151]. In M-SHG experiments a back-transfer of spins in Co on Cu(001) has been identified and also attribute to the OISTR effect [152]. Along with

---

<sup>5</sup>In garnets the inverse Faraday effect is significant and coherent magnetization dynamics can be triggered by light in this fashion [142, 143].

the ultrafast decrease of the local atomic moments in AFM Mn layers, the authors of [120] predict a spin exchange at the interface of Co and Mn that leads to an enhancement of the local moment for one spin species of the Mn atoms thereby resulting in a net moment of the Mn layer. The latter is investigated in this thesis experimentally by time-resolved X-ray reflectivity in Co/Mn multilayers. The results are shown and discussed in chapter 5.

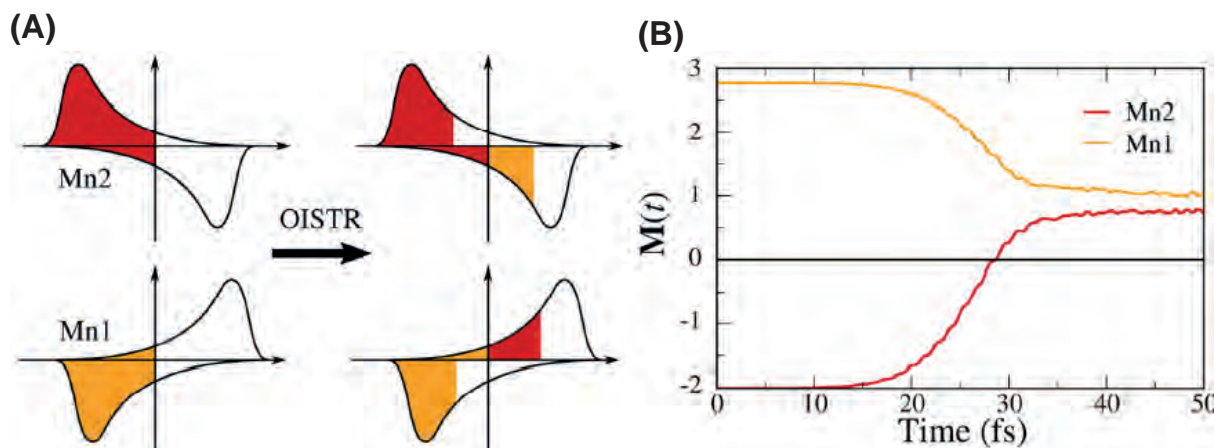


**Figure 3.4:** (A) Sketch of the OISTR process from [120]. Two AFM-ordered Mn atoms adjacent to a Co layer with mirrored spin-resolved DOS offer an efficient OISTR channel which results in charge and thus spin exchange between the atomic sites. While no net charge transfer happens, the local atomic moment is reduced by now having a net increase in minority spin carriers. The calculated time evolution of the local atomic moments of Mn is plotted in (B). Due to the surplus of majority carriers in Co both Mn moments align ferromagnetically. Reprinted with permission from Ref. [120]. Copyright (2021) by the American Physical Society.

### 3.4 Summary

The description of ultrafast demagnetization remains a challenge to this day since there is still a unifying model missing which accounts for all processes induced by the pump light. This chapter aims to provide a brief overview of the most relevant theoretical models for the investigations performed in the scope of this thesis. In summary three models are presented, the (microscopic) three temperature model, super-diffusive transport, and optically induced spin transfer. The models offer a description of the light-induced dynamics from the time of arrival of the laser pump up to several ns when the system has reached equilibrium again. The OISTR process offers a fast channel for spin-exchange in heterogeneous systems that leads to an enhancement of demagnetization in alloys, and even magnetization (reversal) at AFM/FM interfaces. Then thermal processes take over and spin and angular-momentum are dissipated by scattering with phonons and defects in the excitation region. At the same time almost ballistic carriers transport magnetization away from the excitation region leading to a further quench of the magnetic system and can even induce transient magnetization in adjacent films.

There are more descriptions available, not reviewed here, that manage to incorporate other experiments. A prominent example is the  $\mu T$ -model [153–155] which offers an explanation to resolve the conflict between the theoretical prediction of the magnetic quench induced by local scattering mechanisms and the experiments. This is done by including a dynamic exchange interaction and chemical potential in the calculations. Another example is an alternative transport

model based on spin-dependent resistivity and chemical potentials in the heat gradient of the excitation region [156]. Furthermore, not discussed are atomistic and micro magnetic models [157–159] which play an important role also for the ultrafast community, especially in the description of all-optical switching, where it is possible to predict the switching of GdCo alloys for example [160, 161].



# Chapter 4

## Accelerated demagnetization in a FM/AFM bilayer

In this section, the results of the investigation of light-induced sub-ps demagnetization in a ferromagnetic/antiferromagnetic (FM/AFM) bilayer are presented. The aim of the investigation is to explore the possibility to tailor the timescale and/or magnitude of the quench of magnetization in the FM by placing an AFM adjacent to it. The system chosen for this study is Co(Ni)/Ni<sub>40</sub>Mn<sub>60</sub> grown on a Cu(001) single crystal surface.

The investigation is performed in two temperature regimes, one where the NiMn layer is ordered antiferromagnetically and one where it is paramagnetic. By comparing the two temperature regimes we can relate changes in the demagnetization dynamics directly to the different magnetic order of the NiMn film. When NiMn is in the paramagnetic state the Co layer demagnetizes slower compared to the demagnetization with NiMn in the AFM state. The results are summarized and published in [162]. The following will provide a more detailed description of the results and start with the sample growth and characterization process. Then the experimental results are displayed and discussed. Lastly, an interpretation of the findings and an explanation of the accelerated demagnetization due to the AFM state is provided by arguments of super-diffusive transport.

### 4.1 The Co/NiMn/Cu(001) system

The investigation is driven by the idea of having a tunable AFM next to a FM layer. The Ni<sub>x</sub>Mn<sub>100-x</sub> alloy is an excellent choice in this regard since it has a Néel temperature  $T_N$  in the vicinity of room temperature (RT) depending on the film thickness and Ni concentration  $x$  [163–165]. Although Tieg et al. suggested that  $T_N$  does not change significantly with concentration from the bulk value of 1070 K [163]<sup>1</sup>, Khan et al. showed that on Cu<sub>3</sub>Au(001) the critical temperature can be tuned between 200 K to 400 K [164, 165] by changing  $x$  from 40 to 20 in thin films. Judging from those previous investigations we aim for a Ni concentration of around 30 % and a layer thickness of about 20 monolayers (ML) which guarantees a strong coupling to a Co(Ni) top layer [163, 166] in combination with the critical temperature around 300 K to 400 K. The choice of the Cu(001) surface is pragmatic since it offers a small lattice mismatch (about 2 %) with the fcc phase of Co. Both Co and Ni can be grown layer-by-layer

---

<sup>1</sup>Only a concentration variation of 5 % which resulted in a change of 60 K was investigated.

on a Cu(001) surface resulting in interesting magnetic and structural properties of the thin films and both systems have been studied extensively. The Co growth after the two initial MLs is smooth and uniform on a clean Cu(001) surface [167–172]. Similarly, Ni can be grown in a layer-by-layer fashion on Cu(001) and shows a spin-reorientation transition from in-plane to out-of-plane between 7 ML and 20 ML [173–177]. And lastly, it has been shown that also NiMn can be grown epitaxially on Cu(001) and that a top layer of Co or Ni is strongly influenced by the AFM ordered NiMn film through interfacial coupling [163, 166].

### 4.1.1 Thin film deposition

#### Cu(001) surface and material evaporation

Sample preparation is carried out in a UHV system at a base pressure of  $6 \times 10^{-10}$  mbar to avoid contamination of the thin films. The Cu(001) crystal surface is cleaned and smoothed by repeated Ar-ion sputter and anneal cycles. The Ar-ion bombardment removes surface contaminants and provides a pure Cu surface at the cost of surface smoothness. To reconstruct the surface, minimize terraces, and reduce islands the crystal is annealed after sputtering at 800 K for 20 minutes. Repeating this cycle yields an oxygen-free pristine Cu(001) surface with a high degree of smoothness. The chemical composition of the surface is checked by Auger electron spectroscopy (AES, system and instrumentation by *PHI*, model 15-155) which locally probes the surface composition down to 3 nm. The surface reconstruction is checked by low energy electron diffraction (LEED, system and instrumentation by *Omicron*, model *SPECTALEED NGL 10*) to ensure that the surface is smooth.

The elements of the thin films are thermally evaporated by electron bombardment from metallic rods, and in the case of Mn from a crucible. The rods, purchased from *Alfa Aesar* with 99.995 % purity, are evaporated in a commercial evaporator, EFM3 by *FOCUS GmbH*, which is water-cooled during heating to guarantee a pressure  $< 1 \times 10^{-9}$  mbar at all times. Elemental Mn, purchased in irregular pieces of 99.95 % purity, is evaporated in the same system from a tungsten crucible which allows a very controlled evaporation rate and purity of the deposited Mn films. To form a desired  $\text{Ni}_x\text{Mn}_{100-x}$  alloy, Ni and Mn are co-evaporated from the EFM3 which offers a flat circular focus of about 1 cm diameter of all three evaporation pockets at a 9 cm distance. All materials are subject to pre-heating, and evaporation was performed initially with the shutter closed to ensure oxide-free and stable deposition of the evaporants. In the evaporator, the material is heated by running a current, between 2.6 A and 3 A depending on the material, through a 0.125 mm diameter tungsten wire and applying a high voltage (HV) between filament and evaporant to accelerate the thermally emitted electrons to the material. Typical emission currents from the filament are about 10 mA with 1 kV applied, this results in a heating power of 10 W, enough to heat the material to 1400 K [178]. Typical evaporation rates for the materials are in the range of 20 s to 300 s to form a monolayer. By varying filament current and high voltage (HV), the deposition rate is adjusted to form an alloy of the desired stoichiometry.

#### Layer-by-layer growth

During growth, information about the surface is obtained by recording the specular medium energy electron diffraction (MEED) intensity. In MEED, conceptually similar to reflection high

energy electron diffraction (RHEED) [179], the electrons, which carry energies around 2 keV to 4 keV, are scattered in grazing incidence at the top layers of the thin film during growth. Continuous MEED intensity oscillations can be used as a proof of layer-by-layer growth and furthermore directly yield information about the film thickness [163, 166, 179, 180]. To record the MEED intensity, the phosphorous screen of the LEED system is used in combination with the electron gun of the AES system. The LEED system and the Auger system are mounted opposite of each other in the UHV chamber which allows collecting the focused electron beam of the AES system on the phosphorous screen. The sample is placed in the center of the two with the surface aligned almost parallel to the LEED-AES-vertical plane. Slightly turning the sample angle out of the parallel plane guides the specular MEED reflection onto the LEED screen where recording with the help of a CCD camera is performed.

The AES system is used to detect the elemental composition at the top 3 nm of the sample. In combination with MEED, AES is used to measure the film thickness after growth by measuring relative changes in the intensity of the elemental Auger electron peaks, shown in Fig. 4.1. Furthermore, AES is used to determine the stoichiometry in alloys by estimating the fraction of each element in the layers. An overview of the monitoring data during and after growth is presented in Fig. 4.4 where data of the first sample used in this investigation is shown.

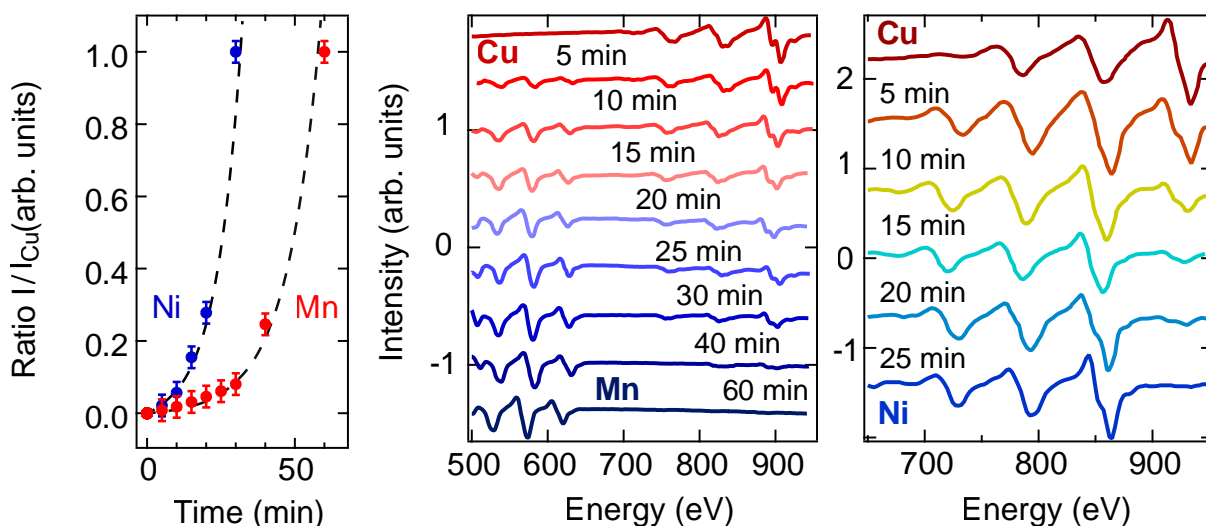


**Figure 4.1:** Characterization of the deposition rate of Mn and Ni on Cu(001) by AES. The ratio of the peak intensity of Mn (or Ni) and Cu changes over time as more material is deposited, visible in the Auger spectra for Mn (center graph) and for Ni (right graph). The normalized ratio of the elemental peaks, 589 eV in Mn, 716 eV for Ni, and 920 eV for Cu is shown in the left graph. The ratios are normalized to the highest intensity for better side-by-side comparison. The ratio is fitted with the exponential given in eq. (4.1) to find the sensitivity factor as well as the deposition rate in Mn. For Ni, additional MEED oscillations allow a precise calibration of the film thickness. The error of the ratio is estimated from the standard deviation of the Auger system from a timescan at constant energy. The error in time from opening and closing the shutter is too small to be visible here.

The ratio between the heights of the elemental peaks  $r$  obtained by AES for varying film thickness  $d$  can be described by

$$r = \frac{I_{film}}{I_{sub}} = S \frac{1 - e^{-d/\lambda_{film}}}{e^{-d/\lambda_{sub}}} \quad (4.1)$$

with the intensity of the peak of the deposited film  $I_{film}$ , the intensity of the substrate  $I_{sub}$ , the sensitivity factor  $S$ , and the energy-dependent inelastic mean free path  $\lambda_{film}$  and  $\lambda_{sub}$  corrected for the acceptance angle of the Auger system, of the electrons [181, 182]. Employing eq. (4.1) for different sets of depositions the calibration parameters of Ni, Mn, and Co are found. In the case of Co and Ni the evaporation is mainly calibrated by MEED oscillations, example curves for Co are shown in Fig. 4.2. The parameters for the thickness analysis using Auger spectra are summarized in Table 4.1. The parameters are crucial to evaluate the alloy stoichiometry using the spectra recorded after deposition.

Element	$S (S_x/S_{Cu})$	$\lambda$ (ML)	Energy (eV)
Mn	$0.88 \pm 0.06$	$4.0^1$	589
Co	$0.69 \pm 0.03$	$4.1 \pm 0.2$	656
Ni	$0.34 \pm 0.02$	$4.2^1$	716
Cu	1	$4.8^1$	920

**Table 4.1:** Material parameters for AES found for Co, Ni, and Mn. <sup>1</sup> Taken from the PhD Thesis of Yasser Shokr, [183].

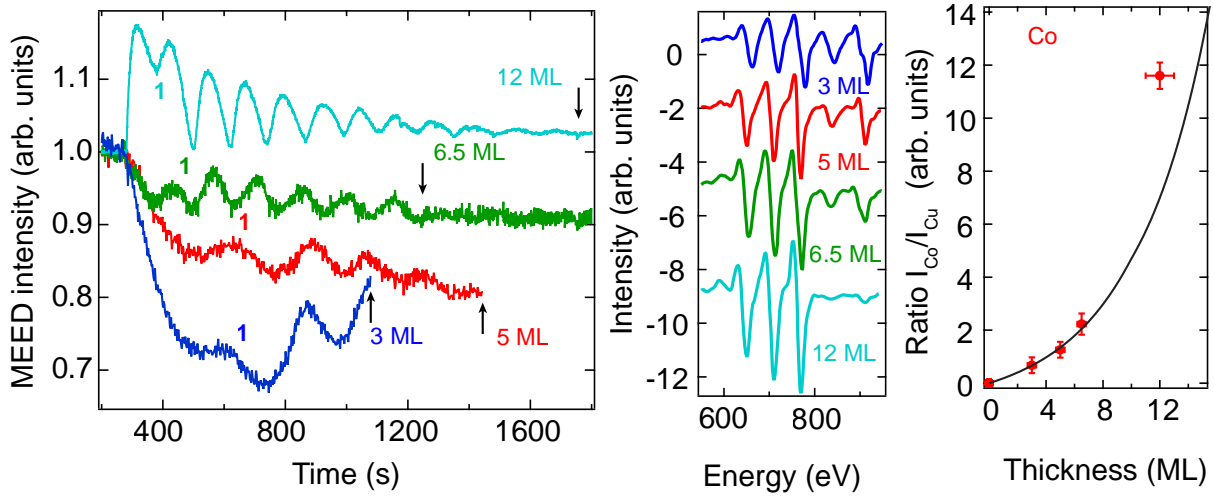


**Figure 4.2:** Calibration of the Co growth parameters by MEED intensity and AES. During thin film growth of Co on Cu(001) the specular MEED intensity is recorded and used as an indication of film thickness. The first deposited layer is denoted with a "1" in the graph and the moment the shutter was closed is indicated by an arrow. The MEED oscillations for four different Co films are shown in the left panel. The oscillations for the 12 ML film behaves reversely, indicating that in this deposition the recording was set to the minimum intensity. The corresponding Auger spectra are shown in the center panel. Each spectrum is recorded after deposition in the center of the sample. The ratio evaluated from the spectra comparing the intensity of the 656 eV and 920 eV lines is plotted on the right.

The alloy composition can be evaluated from the relative peak height of the constituent atoms in the Auger spectra. Assuming that the Auger electrons are attenuated by the same thickness

of the film one finds for the ratio of the alloy materials and sufficiently thick coverages (above 10 ML)

$$r = I_1/I_2 = \frac{S_1}{S_2} \frac{x}{1-x} \frac{1 - e^{-d/\lambda_1}}{1 - e^{-d/\lambda_2}} \quad (4.2)$$

with the total film thickness  $d$ , the concentration  $x$  of material 1, the peak-to-peak intensities  $I$ , the sensitivity factors  $S$ , and the mean free path  $\lambda$  for the Auger electrons from the respective materials 1 and 2. Using the parameters for Ni and Mn listed in Table 4.1 to interpret AES spectra in combination with MEED to directly monitor film thickness the growth of the NiMn alloy is calibrated, shown in Fig. 4.3.

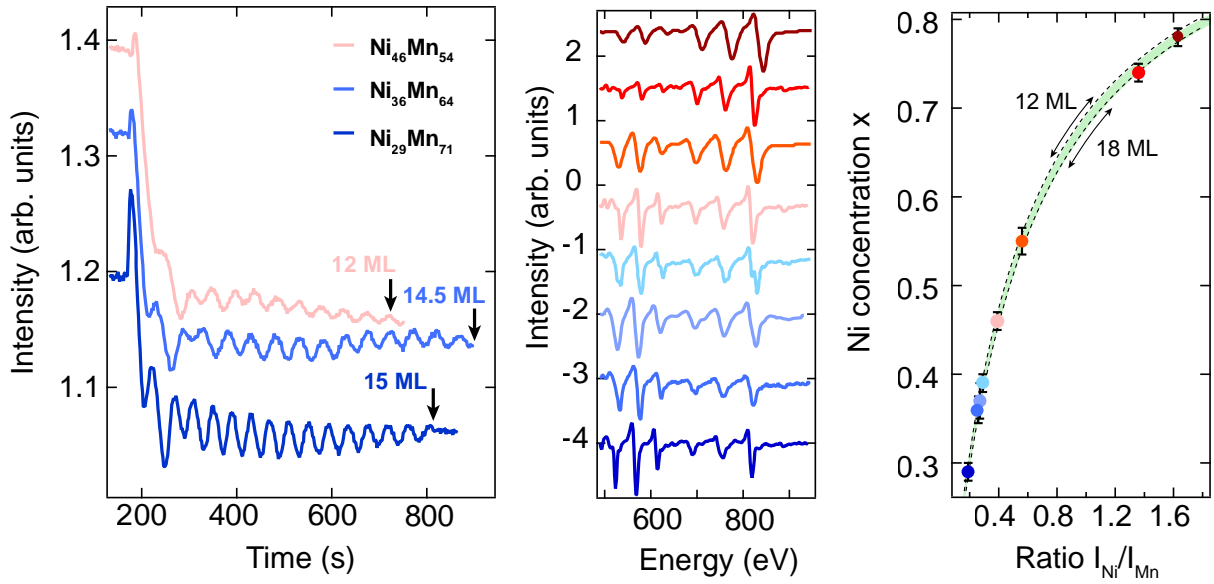


**Figure 4.3:** Evaluation of the  $\text{Ni}_x\text{Mn}_{1-x}$  alloy concentration. Using MEED intensity oscillations and timing based on the evaporation rates to calibrate the thickness, NiMn alloys of different stoichiometry were grown. MEED oscillations, shown in the left panel, were not recorded during every growth. To characterize the chemical composition of the alloy, Auger spectra are recorded after deposition, shown in the center panel. Using the thickness, obtained either by MEED or from the time of deposition, and the ratio of peak intensities of Mn and Ni, the concentration according to eq. (4.2) is evaluated. The dependence of the Ni concentration  $x$  on the ratio of the intensities of the deposited films is plotted in the right panel. The colors always denote the same deposition. The two dashed black lines indicate the concentration vs. ratio dependence for a 12 ML thick and an 18 ML thick film. The highest error in this estimation most likely comes from the uncertainty of the true film thickness. Fortunately, the concentration can still be assessed quite well even with a large uncertainty of the film thickness, as indicated by the green shaded area, covering the range between 12 ML and 18 ML.

## 4.1.2 Sample characterization

Having established the parameters for evaporation of the relevant elements, two samples are grown for the investigation. First a 15 ML Co film on a 20 ML  $\text{Ni}_{31}\text{Mn}_{69}$  film deposited on Cu(001) and capped with 20 ML copper is prepared (S1). The growth is monitored by MEED and AES is used to check the surface composition after each deposition. The corresponding spectra and the MEED curves are shown in Fig. 4.4.

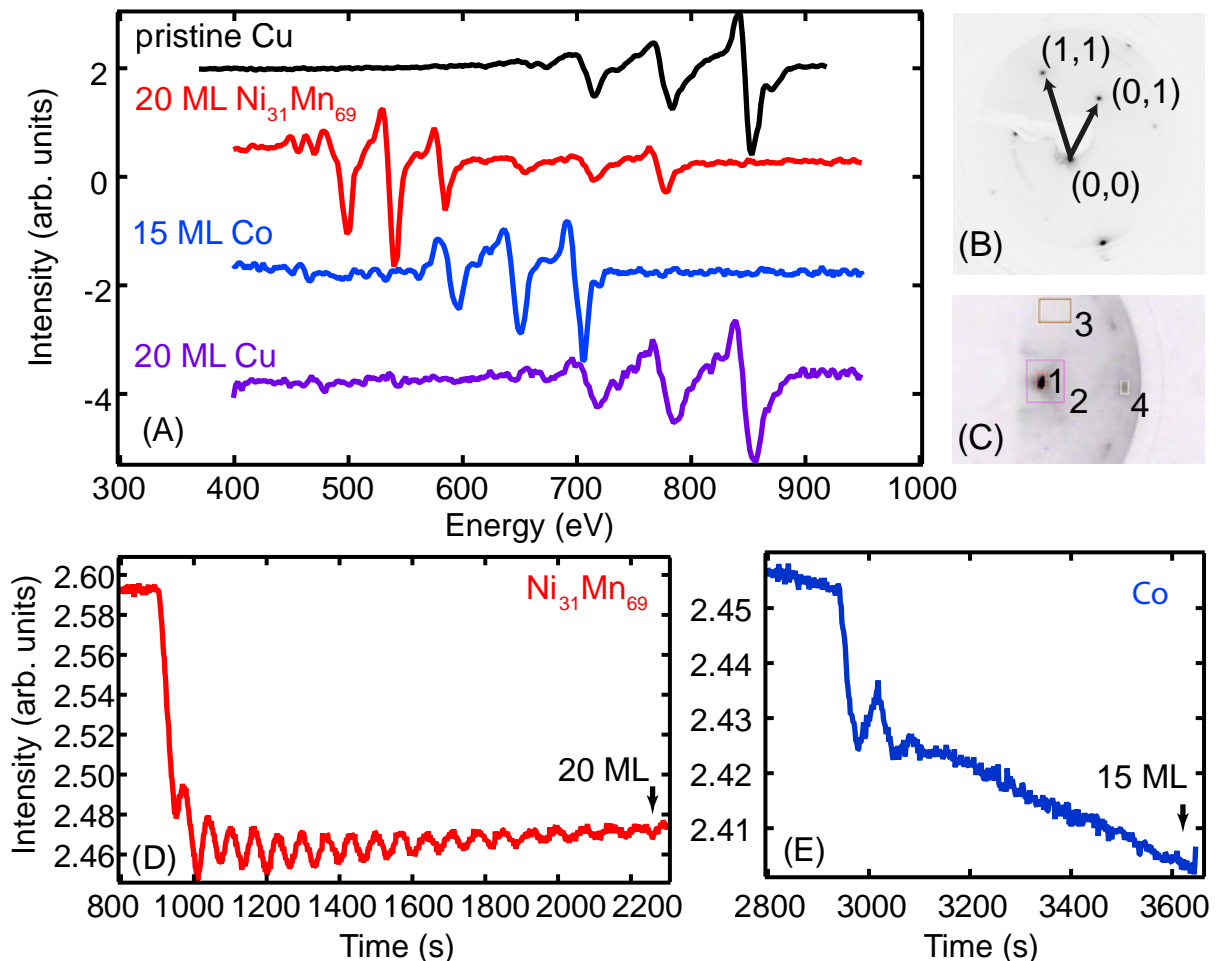


**Figure 4.4:** Overview of the growth characteristics for the Cu (20 ML)/Co (15 ML)/ $\text{Ni}_{31}\text{Mn}_{69}$  (20 ML)/Cu(001) sample. After each deposition step an Auger spectrum is recorded (A) to check for the presence of oxygen and to confirm the desired alloy composition for NiMn. The spectra in (A) are shifted vertically for better distinction. The LEED image of the pristine Cu(001) surface (B) is recorded prior to evaporation to confirm film smoothness after the sputter and anneal cycles. The growth of the  $\text{Ni}_{31}\text{Mn}_{69}$  layer and the Co layer is monitored by MEED intensity oscillations. The specular MEED reflection visible in (C) is recorded on a phosphorous screen with a CCD camera. The rectangles indicate the integration area of the images recorded during growth. To evaluate the intensity, multiple spots are recorded as denoted in (C). The intensities shown in (D) and (E) are evaluated by taking the ratio of the mean intensity of the rectangles 1 and 3. The  $\text{Ni}_{31}\text{Mn}_{69}$  film grows layer-by-layer, but the roughness increases significantly. The successive Co layer oscillates only twice, the evaporation time is adjusted according to the evaporation rate.

A second sample (S2) comprised of 12 ML Ni grown on 14 ML Ni<sub>38</sub>Mn<sub>62</sub> deposited on Cu(001) and capped with 20 ML copper is prepared. The growth is monitored in the same fashion as the previous sample and the data is displayed in Fig. 4.5. Both samples have a magnetic in-plane easy axis and before collecting time-dependent dynamics the magnetic properties are recorded in-situ in the growth chamber.

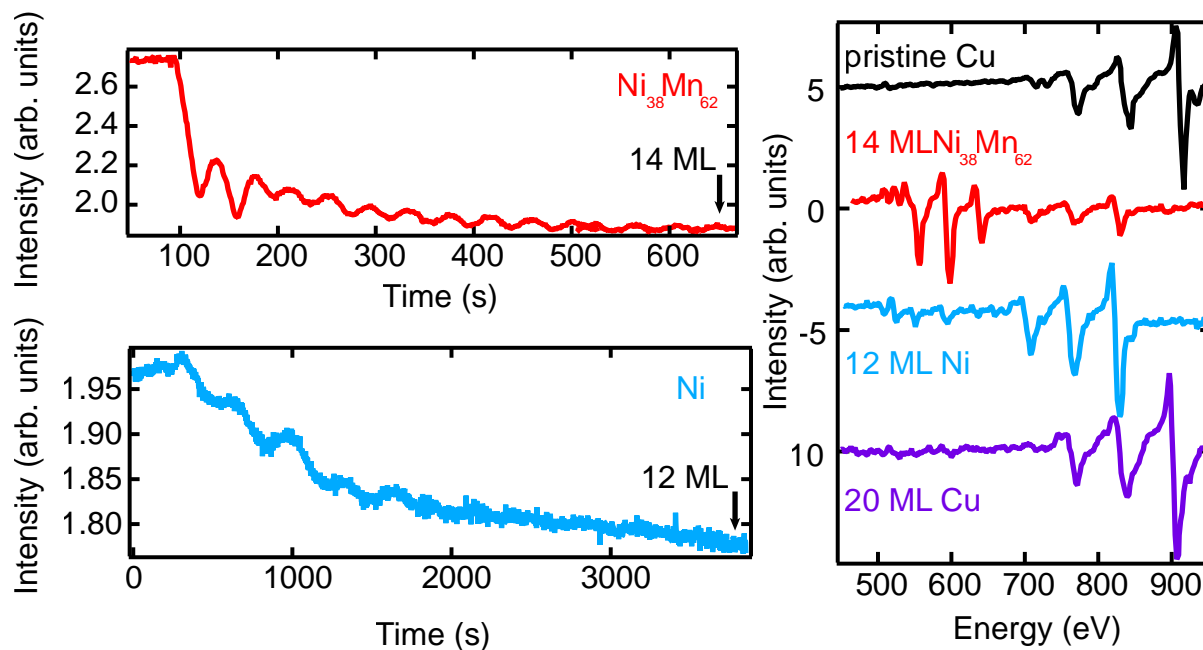


**Figure 4.5:** MEED oscillations recorded during the growth of the Cu/Ni/NiMn/Cu(001) sample shown on the left panels. The oscillations during the growth of the NiMn alloy are shown in the top left panel and the oscillations during the growth of the top Ni layer are shown at the bottom left panel. The corresponding Auger spectra recorded after each deposition step are shown on the right side.

### Static magnetic properties

Static magnetic characterization is performed in the growth chamber by moving the sample on the holder into a quartz-glass tube extruding into the center between two coils. By applying a current to the coils, fields up to 150 mT can be applied uniformly over the sample area. The transparent quartz tube enables the detection of magnetization by detecting the MOKE of the reflected CW light of a laser diode. The incoming light is linearly polarized by passing through a polarizer, it is then reflected from the sample surface and the Kerr angle is detected by placing a second polarizer acting as an analyzer in front of a photodiode detecting the intensity at the end of the beam path. To reduce noise, a photo-elastic modulator is placed in front of the analyzer enabling the detection of the signal change with a lock-in amplifier. Both in-plane and out-of-plane magnetization can be detected by simply turning the sample angle and realigning the beam path. For both samples S1 and S2, the magnetic easy-axis lies in the surface plane. A strong interface coupling in the samples is established by first heating to 400 K and then cooling to liquid nitrogen temperatures (around 100 K is reached) while applying an external magnetic field of  $-100$  mT. This field-cooling procedure orients the interface spins of NiMn along the direction of the ferromagnetic spins which are directed by the external magnetic field. At elevated temperatures, the NiMn spins possess some freedom to align themselves and the

successive cooling "freezes" the spins in the alignment along the axis of the FM. Preparing the FM/AFM system in this manner leads to enhanced coercive fields and exchange bias fields coming from pinned moments at the interface or in deeper layers of the AFM [184–187]. The magnetic properties after field-cooling are checked by in-situ MOKE at different temperatures. The temperature-dependent scans are presented in Fig. 4.7 for both samples. The coercive field together with the exchange bias field is evaluated by analyzing the maxima of the derivative curves of the recorded magnetization loops. Temperature-dependent hysteresis and derivative curves are presented in Fig. 4.6.

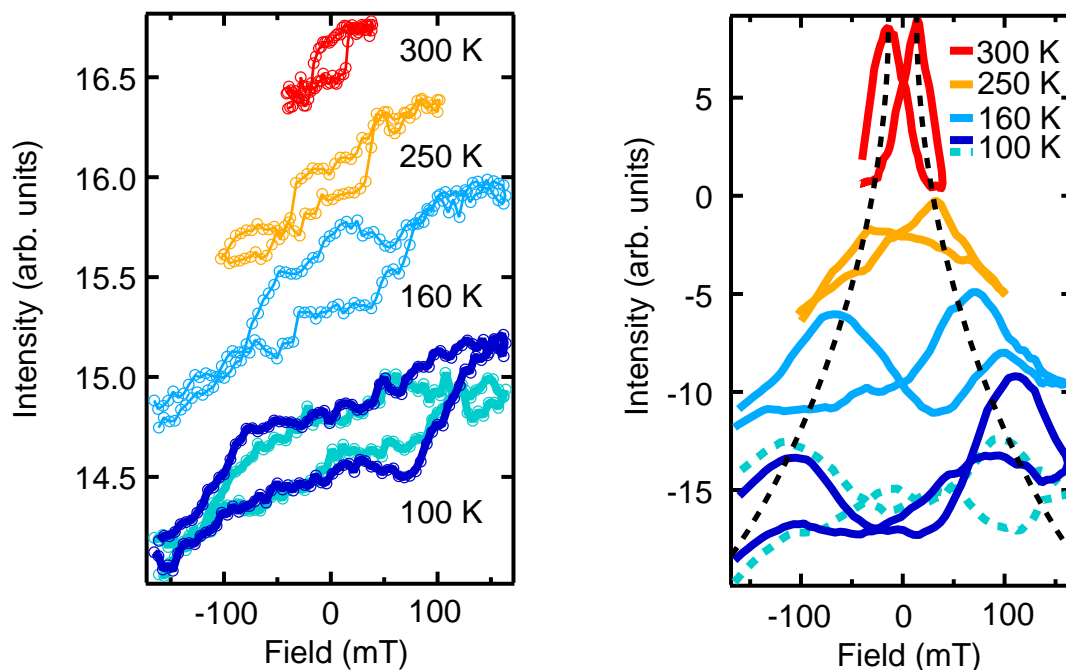


**Figure 4.6:** Example hysteresis loops detected by in-situ MOKE at different temperatures of the second sample S2 (left) and the respective derivative curves (right). The hysteresis loops are acquired with a "flying" temperature leading to deviations of the temperature of around 3 K while scanning. Sample holder vibrations due to boiling liquid nitrogen lead to noisy scans at low temperatures. The paramagnetism of the quartz glass introduces a linear slope in all scans. For the evaluation of the derivative curves, all loops are slope-corrected and interpolated to achieve a sufficient point density to accurately define the maximum in the derivative curve. Furthermore, the derivative curves are smoothed by a Savitzky-Golay filter, using a 9 point window and third power polynomial, to avoid errors coming from outliers. The two black dashed lines are a guide to the eye of the evolution of the maxima with temperature. All displayed curves are shifted vertically for better visibility.

Since the cooling rate in this setup is not precisely controllable, it is challenging to acquire a stable temperature over longer times, motivating many fast scans taken with a slowly changing temperature instead of having long precise scans at a fixed temperature. Single recorded scans are presented in Fig. 4.6 where an additional second scan at 100 K is presented to display the relatively high scan-to-scan deviation leading to the high error bars in Fig. 4.7. The strong scan-to-scan deviation mainly comes from vibrations of the sample holder while cooling which introduces a significant degree of noise that is not canceled by the lock-in amplification.

Furthermore, it becomes challenging to accurately determine the presence of an exchange bias field at low temperatures. Nevertheless, in both curves, a kink in the coercive field can be identified, around 300 K in S2 and around 200 K in S1, which might indicate the onset of the antiferromagnetic phase in the NiMn layer by a modified coupling at the interface. Based on the magnetic properties and the measured blocking temperatures in Ref. [164], we conclude that by changing the temperature well below 300 K and slightly above we indeed cross a transition in the magnetic phase of the NiMn layer, which is the desired property for this investigation.

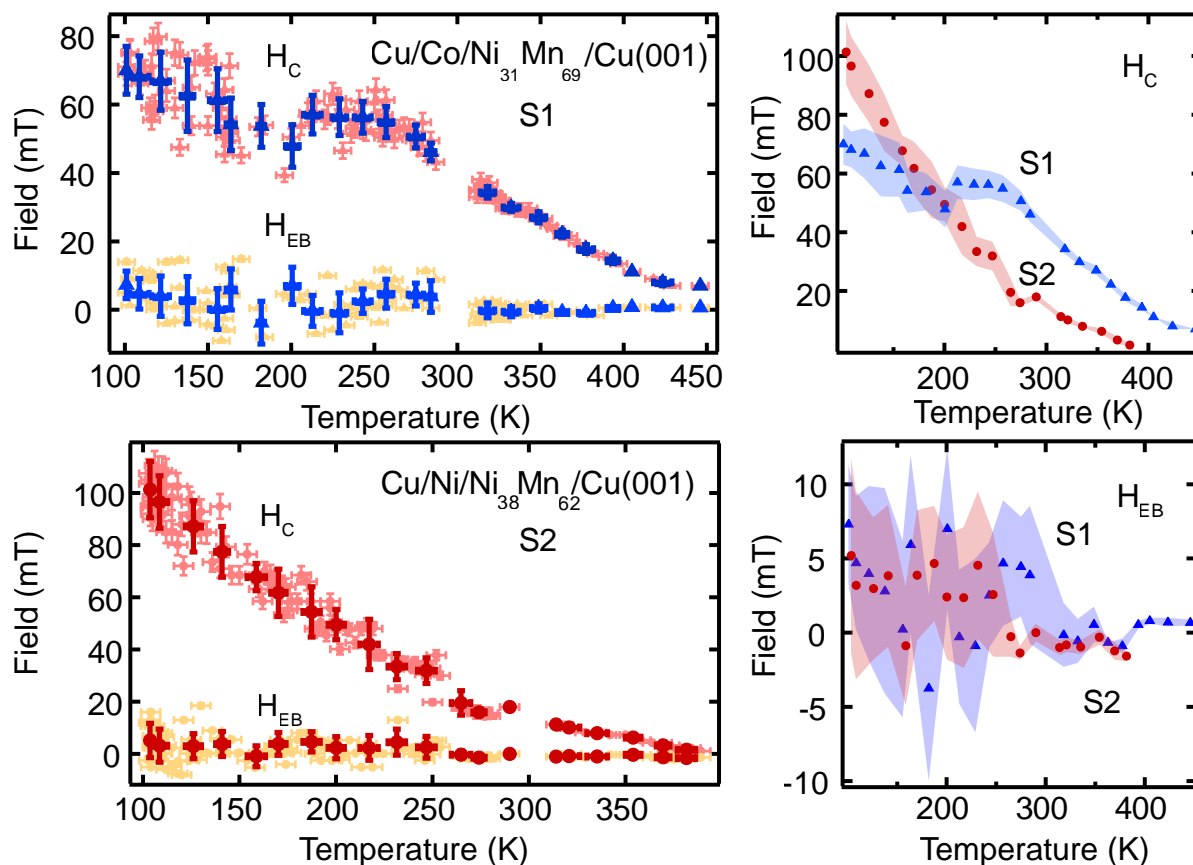


**Figure 4.7:** Coercive field ( $H_C$ ) and exchange bias field ( $H_{EB}$ ) for both samples S1 and S2. The evaluated coercive fields from all recorded scans are indicated by the light red markers and the exchange bias fields are denoted by the light yellow markers in the top and bottom left panels. The coercive fields are binned in a reduced field vs temperature curve indicated by the dark blue (S1) and dark red (S2) markers overlaying the light markers. The error is evaluated from the mean deviation of the binned points in addition to the error that is attributed to each point coming from the estimation of the maxima in the deviation curves. Similarly, the exchange bias fields are binned in a reduced curve. The binned curves are displayed on the right side to allow a better comparison between the two samples. In the top right panel the coercive fields of S1 and S2 are compared and the shaded area indicates the uncertainty. In the bottom right panel the binned exchange bias fields are displayed. Given the large uncertainty no clear exchange bias is identified.

## 4.2 X-ray magnetic circular dichroism in reflectivity

The following section presents the results obtained at the synchrotron radiation facility BESSY II in Berlin where energy-, angle-, and time-dependent soft X-ray reflectivity is recorded. First an evaluation of the energy- and angle-dependent dichroism in reflectivity is presented. This characterization is of great importance for time-dependent scans since they are quite time consuming and the measurement geometry has to be optimized to facilitate meaningful measurements in the short amount of time available in a beamtime. In the second part the results of the time-resolved measurements carried out at the slicing facility will be presented.

### 4.2.1 Angle- and energy-resolved magnetic reflectivity

The reflectivity characterization is carried out at the scattering endstation at the PM3 beamline at BESSY II, schematically displayed in Fig. 4.8. The samples are first magnetized by applying an external field of  $\pm 100$  mT along the sample plane. The reflectivity scans are then performed in remanence in a  $\theta$ - $2\theta$  geometry, i.e., the sample is turned to an angle  $\theta$  and the reflected light is detected at  $2\theta$  with respect to the incoming beam. In this fashion the sample is turned from  $0^\circ$  to  $15^\circ$  and the X-ray energy is ramped over the range of the  $L_3$  absorption edge of Ni and Co in the respective sample.

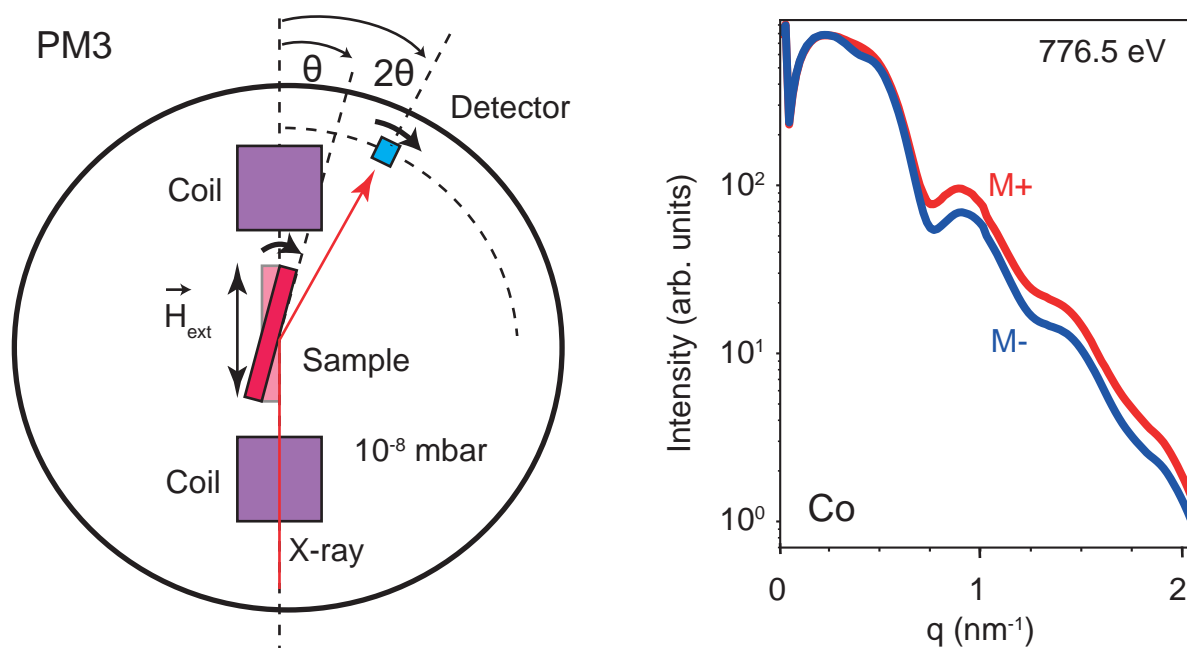


**Figure 4.8:** Schematics of the measurement geometry at the PM3 scattering station (left) and a corresponding example measurement (right) of the resonant X-ray reflectivity. The sample angle is turned to an angle  $\theta$  and the detector to  $2\theta$  to measure the specular reflectivity. The intensity is plotted against the momentum-scattering vector  $q$  instead of the angle  $\theta$ . In this investigation the sample is initially magnetized parallel or anti-parallel to the beam and the reflectivity is measured in remanence. Later measurements are performed with a new coil arrangement where we measured under an applied field.

For a better comparison between different energies the reflected intensity is often plotted against the momentum-scattering vector  $q$

$$q = \frac{4\pi}{\lambda} \sin \theta \quad (4.3)$$

determined by the X-ray wavelength  $\lambda$  and the angle of incidence  $\theta$ . The intensity of the reflected X-rays varies strongly with the angle of reflection, displayed in Fig. 4.8. This can be understood if one recalls the dependence of the scattering factor on the scattering vector in (2.43) in section 2.2.3. Additionally a multilayer system with different material-dependent scattering factors is probed. Together this leads to an interference pattern of the intensity resulting from the layer wise reflection. In general this signal can be used to extract structural information about film thickness, interfaces roughness, material parameters, and layer resolved magnetization [98, 99]. To the best of my knowledge there is no analytical way to directly extract this information from the data and numerical simulations are used to reproduce the scattered intensity and benchmark the underlying expectations about the sample properties. Here we employ two different realizations of such calculations in an effort to reproduce the X-ray reflectivity. The authors of [98, 99] provide a software tool, titled *ReMagX*, to simulate the X-ray reflectivity in a multilayer system. Another solver for the energy- and angle-dependent scattering is published by D. Schick et al. [188] in a python package called *udkm1dsim*. Both solve the layer wise field propagation and reflection at the interfaces. As an input they require the sample geometry, the magneto-optical material constants, and the properties of the incoming light. An analysis of the involved constants and the means to simulate the X-ray reflectivity together with the results of reproducing the experimental data is provided in section 6.

The aim of the investigation presented here is to find the best combination of angle of incidence and energy to optimize the product of reflected intensity and square of the magnetic contrast. This is expressed in a figure of merit (FOM). Following the derivation by N. Pontius [189], the measurement time  $t_{meas}$  required for a scan can be expressed in terms of the FOM as

$$FOM = n_{ph} c_{mag}^2, \quad t_{meas} = 4 \frac{r_{sig}^2 M_{chan}}{FOM} \frac{1 + (1 + p_{pump})^2}{p_{pump}^2} \quad (4.4)$$

where  $r_{sig}$  is the desired degree of significance,  $M_{chan}$  is the number of channels,  $n_{ph}$  denotes the number of photons, and  $c_{mag}$  is the magnetic contrast. The number  $p_{pump}$  is the relative pump-induced signal change that has to be estimated in advance. The experimental significance is defined here as  $r = \frac{p}{\Delta p}$  and indicates how well the value  $p$  is measured compared to its error  $\Delta p$ . The channels refer to the number of acquisitions recorded sequentially in the experiment. For all our purposes these are four, the two dichroic pumped and the two dichroic unpumped channels.

### Co/NiMn sample

First the energy- and angle-dependent scattering at around the  $L_3$ -edge of Co is presented. The reflected intensity for different energies and angles, shown in the left panel of Fig. 4.9, is evaluated with an energy-dependent factor to convert it into the expected number of photons for the evaluation of the FOM according to eq. (4.4). Together with the angle- and energy-dependent contrast, shown in the center panel, an expected measurement time for a pumped-unpumped dichroic scan with a degree of significance of 10, 50 points, and a pump-induced change of 50 % of just below one hour is found at 778 eV and  $5^\circ$  (right panel). The final

evaluation of the best measurement conditions is done at the slicing facility where only a narrow energy- and angle-range is checked a second time.

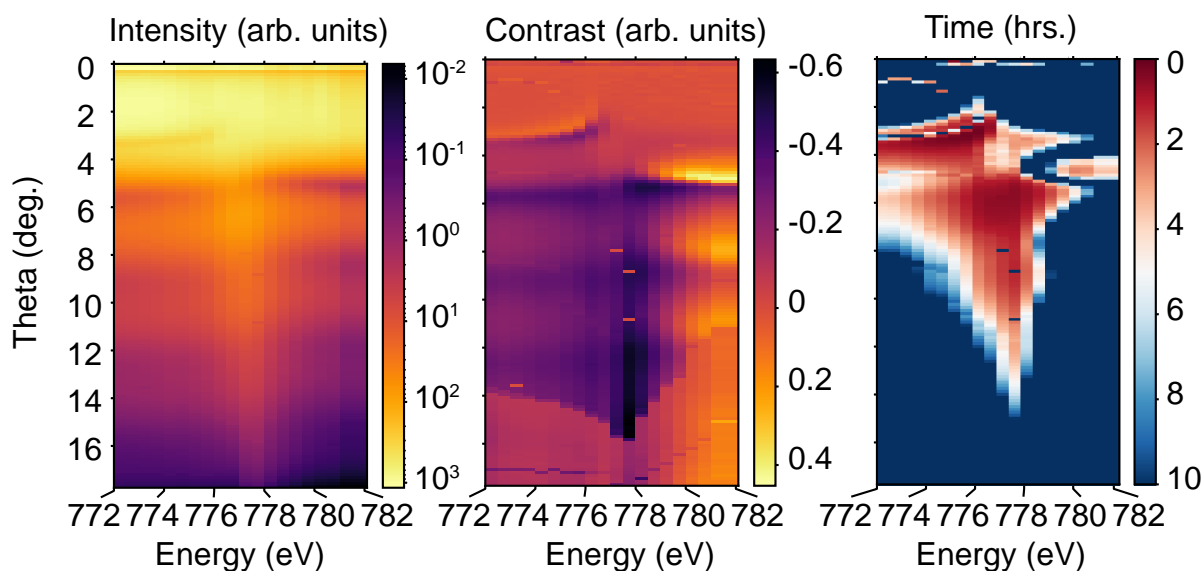


**Figure 4.9:** Reflected X-ray intensity (left), magnetic contrast thereof (center), and evaluated measurement time (right) for Co. The intensity is plotted as the average between the two reflectivities for the oppositely magnetized sample. The contrast is evaluated as the ratio of the difference and the average intensity plotted on the left. The measurement time is evaluated according to eq. (4.4) using the parameters as described in the text.

### Ni/NiMn sample

The energy- and angle-dependent scattering at around the  $L_3$ -edge of Ni measured in the second sample is presented. The FOM is evaluated in the same fashion as in Co in Fig. 4.9. Using the same parameter set for the measurement conditions, a minimal time-per-scan of around one hour is found at 855 eV and  $8^\circ$ . In this sample the contrast is quite narrow in energy, visible in the center panel of Fig. 4.10, which is smeared out with the high energy width at the slicing facility. The estimation for the acquisition time is likely to be too optimistic and the final estimation at the slicing endstation yielded higher acquisition times than anticipated. Therefore, in the Ni/NiMn sample fewer different time-dependent scans were recorded since we wanted to have the same degree of significance in all scans.

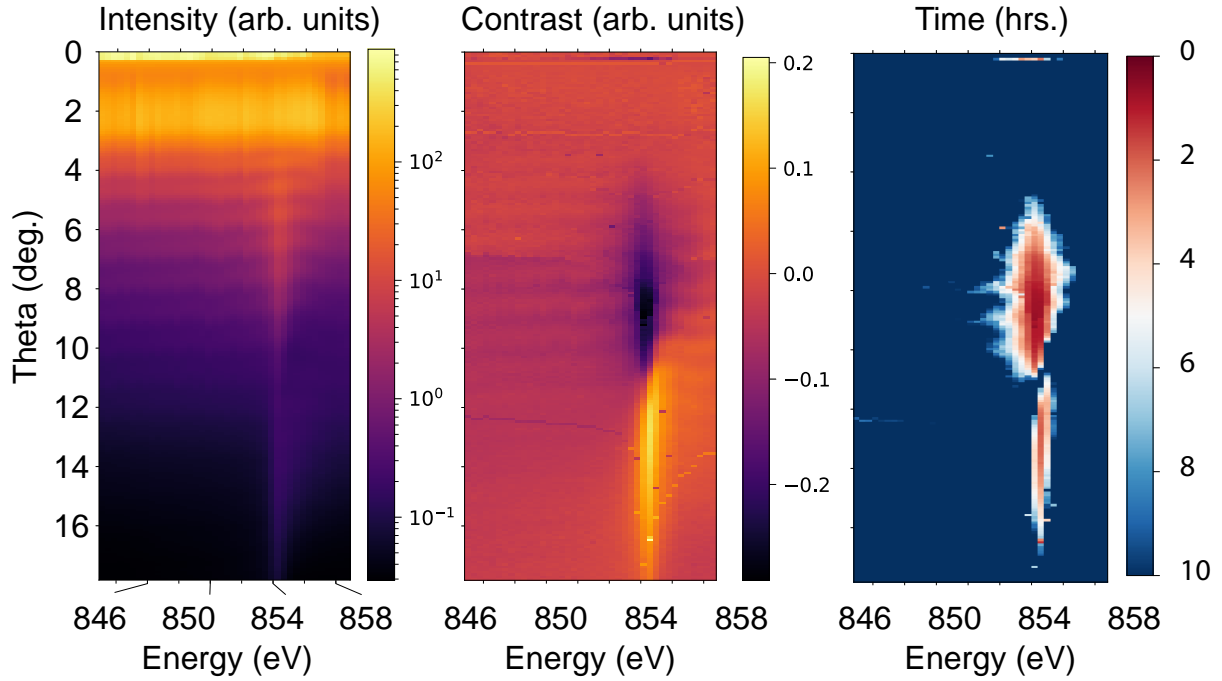


**Figure 4.10:** Reflected X-ray intensity (left), magnetic contrast thereof (center), and evaluated measurement time (right) for Ni. The intensity is plotted as the average between the two reflectivities for the oppositely magnetized sample. The contrast is evaluated as the ratio of the difference and the average intensity plotted on the left. The measurement time is evaluated according to eq. (4.4) using the parameters as described in the text.

## 4.2.2 Time-resolved dynamics

With the evaluation of the optimal measurement geometry, presented in the previous chapter, time-resolved measurements are performed at the slicing endstation of the UE-56\1 beamline at BESSY II. The final measurement geometry as evaluated again at the slicing endstation and optimal conditions for measurements were found at  $\theta = 7^\circ$  and  $E = 777.8$  eV for Co and  $\theta = 6.5^\circ$  and  $E = 854$  eV for Ni. The results of the investigation resolving the effect of the AFM order on the demagnetization are presented together with an interpretation in the next section. Here a brief summary of the time-resolved measurements is given and example curves are presented. The curves are analyzed using a double-exponential fit function motivated by the m3TM to extract de- and remagnetization times. The equation is already introduced for TR-MOKE measurements in eq. (2.30) and contains the sum of two exponentials which describe a decay and a recovery term. The onset of the dynamics is modeled by a step-function and the finite time resolution of the set-up is considered by a convolution of the dynamics with a gaussian function describing the instrumental bandwidth in time. Both samples are investigated systematically for fluence and base temperature dependence.

An example scan recorded at the Co resonance is presented in Fig. 4.11 and consists of four datasets, pumped and unpumped intensity for parallel and anti-parallel alignment of the field with respect to the X rays. To evaluate the dynamic magnetic information, we take the asymmetry of the pumped signal, which we call XMCD. Furthermore, the pumped signals are normalized by the unpumped data to remove drifts and reduce noise. For display, the data is then normalized to the XMCD signal at negative delay times to allow easy comparisons between timescales for different temperatures and energies.

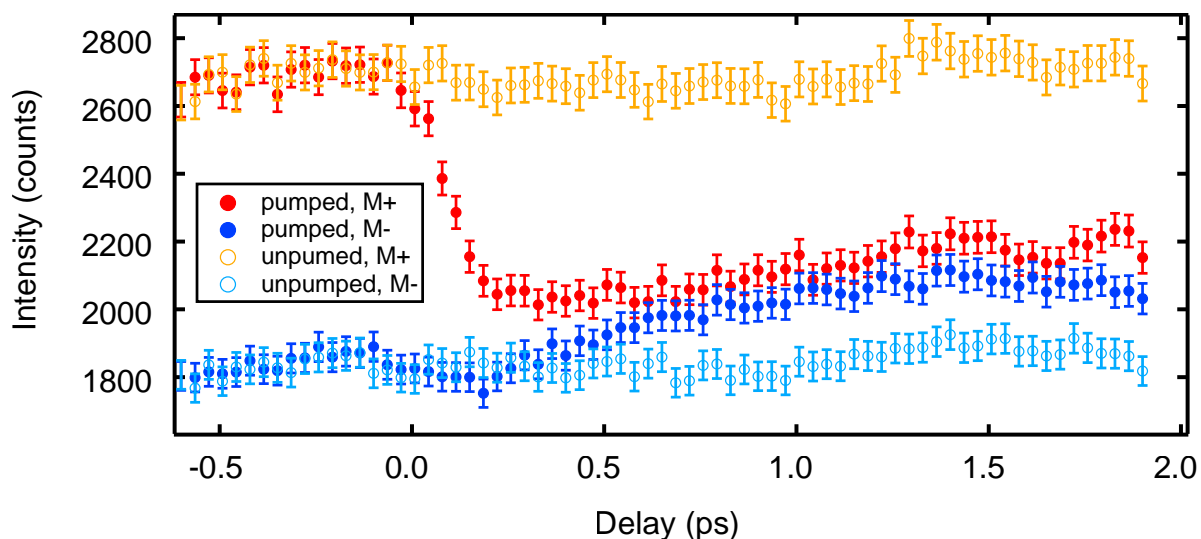


**Figure 4.11:** Reflected X-ray intensity vs delay time recorded at the Co  $L_3$  absorption edge, with (pumped) and without 800 nm pump (unpumped), for magnetization along the beam direction (M+) and anti-parallel to the beam (M-). The measurement is performed with  $40 \text{ mJ cm}^{-2}$  incident fluence and at a sample temperature of 390 K. The scan is recorded at a sample temperature of 390 K. To evaluate the magnetic information, the pumped signal is divided by the unpumped channel and the asymmetry between M+ and M- is evaluated. The error is estimated from the counting statistics as  $\sqrt{N}$  with the number of counts  $N$ .

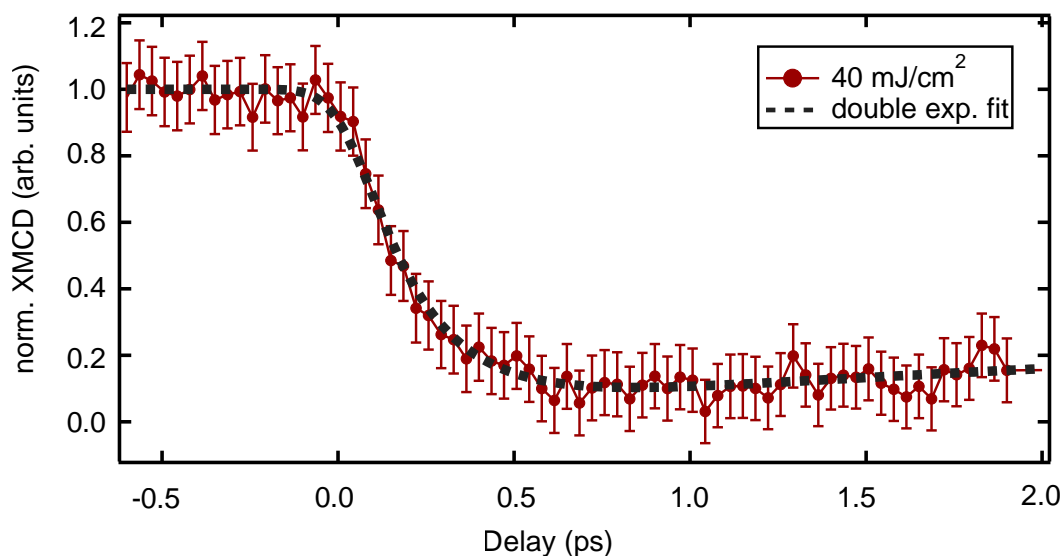


**Figure 4.12:** Evaluated XMCD signal from the data presented in Fig. 4.11. To evaluate the magnetic information, the pumped signal is divided by the unpumped channel and the asymmetry between M+ and M- is evaluated. The dotted line represents the double-exponential fit used to extract the time constants from the data.

The normalized XMCD acquired in the described fashion from the data of Fig. 4.11 is displayed in Fig. 4.12. The magnetic contrast and therefore the magnetization is quenched by about 90 % within 500 fs. The time constants of the exponential decay are extracted from the fit also

displayed in the figure. In this measurement a demagnetization time of  $\tau_{de} = 188 \pm 19$  fs is found. The comparison for all recorded fluences at 390 K sample temperature is presented in Fig. 4.13 and the data recorded at 80 K is presented in Fig. 4.14. The overall dynamics remain quite similar at both sample temperatures. An ultrafast quench of the magnetization followed by a slower recovery is recorded at all fluences and mainly the magnitude of the quench varies with the laser intensity. In Co the absolute change of magnetic contrast is almost similar in both investigated temperatures since the XMCD signal evaluated at negative delay times hardly changes, a decrease from 0.41 to 0.39 when increasing the temperature is recorded. An example recorded at  $30 \text{ mJ cm}^{-2}$  incident fluence is presented in Fig. 4.18. More subtle changes are observed for the intermediate fluences  $20 \text{ mJ cm}^{-2}$  and  $30 \text{ mJ cm}^{-2}$  where the slope of demagnetization is visibly different for the two sample temperatures, also visible in Fig. 4.18. The evaluated time constants are presented in Table 4.2.

The data recorded in the Ni/NiMn sample is analyzed in the same fashion. In this sample lower temperatures and fluences are investigated since Ni shows a lower  $T_C$  and therefore demagnetizes more effectively already at lower fluences. In the same fashion, the saturation magnetization reduces significantly already close to 400 K. For this reason the Ni/NiMn sample is investigated for 80 K and 360 K and only up to  $45 \text{ mJ cm}^{-2}$ . For time reasons only two fluences are recorded with decent statistics,  $15 \text{ mJ cm}^{-2}$ , and  $45 \text{ mJ cm}^{-2}$ . In Ni, a greater change of the static XMCD is recorded and the contrast at negative delay times reduces from 0.32 to 0.19 when increasing the temperature from 80 K to 360 K. Two example curves are shown in Fig. 4.17.

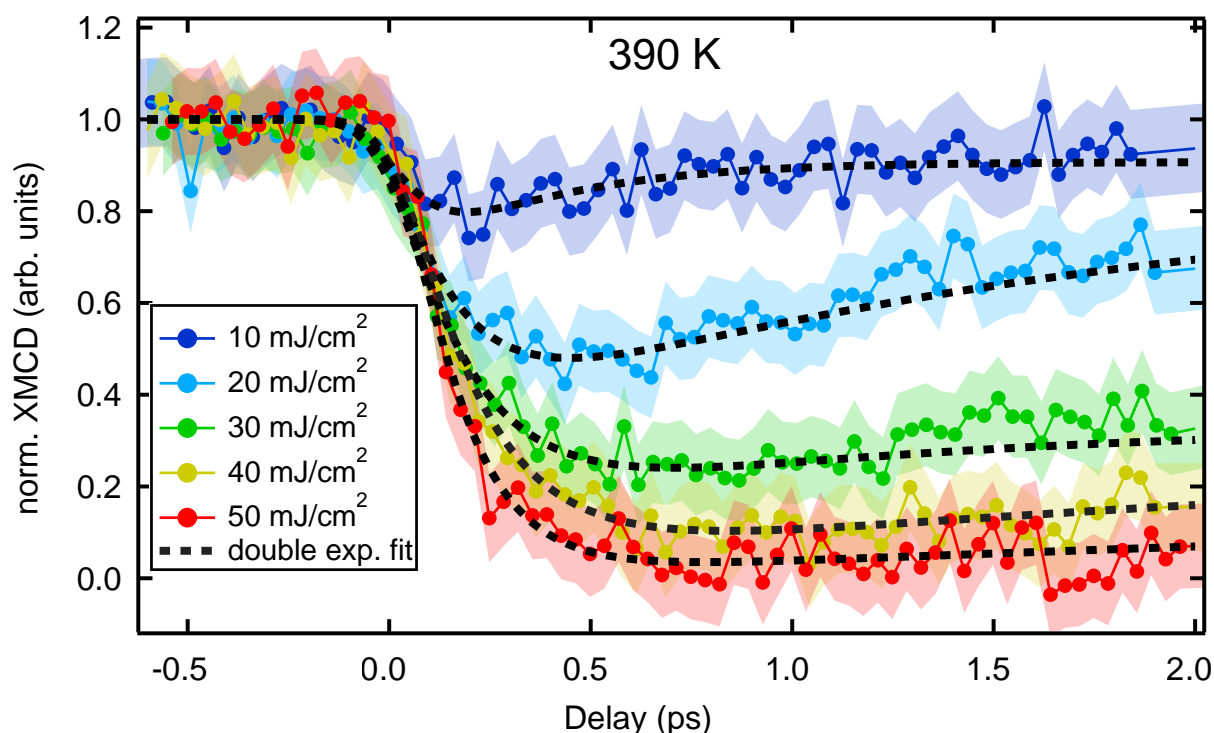


**Figure 4.13:** Normalized time-resolved XMCD evaluated at the Co  $L_3$ -edge recorded for different pump fluences as indicated in the legend. Each scan is fitted in a 2 ps window using the double-exponential fit described in the text. Time zero of each scan is evaluated using the fitting and the scans are shifted to the same time zero. The shaded area indicates the uncertainty evaluated from the counting statistics.

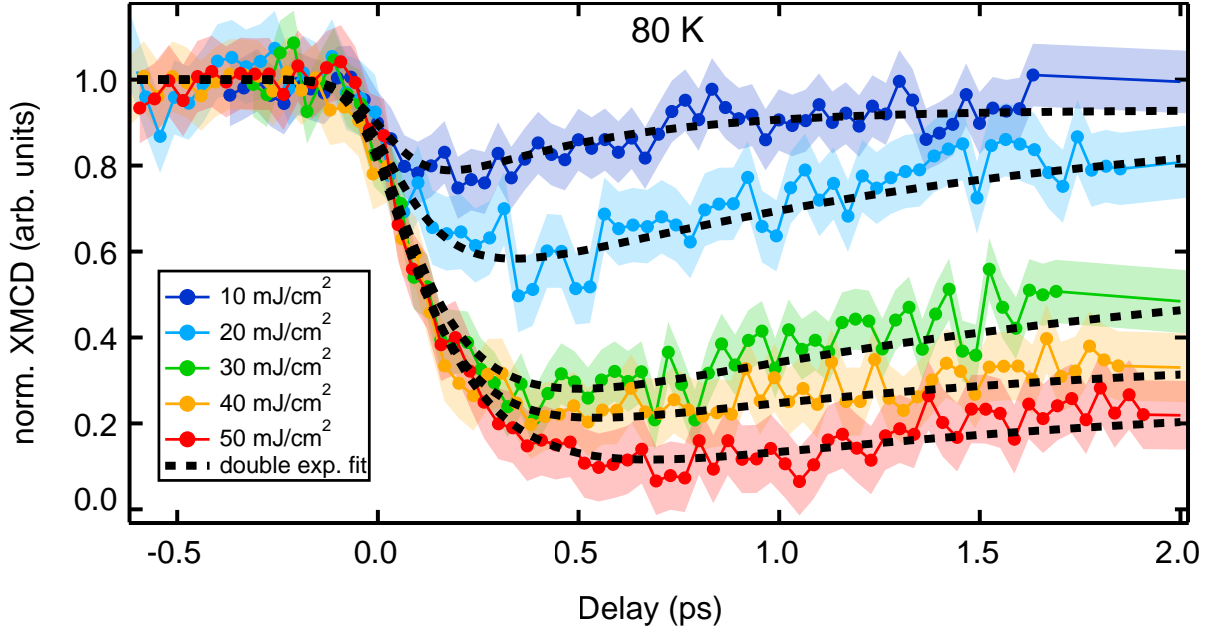


**Figure 4.14:** Normalized time-resolved XMCD evaluated at the Co  $L_3$ -edge recorded for different pump fluences as indicated in the legend at 80 K sample temperature. The curves are evaluated in the same fashion as in Fig. 4.13.

Co	fl. ( $\text{mJ}/\text{cm}^2$ )	demag. amplitude	$\tau_{de}$ (fs)	$\tau_{re}$ (ps)
390 K	10	$0.37 \pm 0.03$	$82 \pm 12$	$0.4 \pm 0.2$
	20	$0.69 \pm 0.02$	$147 \pm 16$	$1.6 \pm 0.4$
	30	$0.90 \pm 0.03$	$179 \pm 20$	$1.0 \pm 0.6$
	40	$0.96 \pm 0.05$	$181 \pm 19$	$3.2 \pm 1.1$
	50	$0.99 \pm 0.03$	$140 \pm 17$	$11.1 \pm 2.9$
80 K	10	$0.36 \pm 0.02$	$74 \pm 12$	$0.4 \pm 0.2$
	20	$0.58 \pm 0.02$	$119 \pm 12$	$1.3 \pm 0.4$
	30	$0.78 \pm 0.03$	$135 \pm 18$	$1.7 \pm 0.4$
	40	$0.81 \pm 0.04$	$142 \pm 16$	$1.2 \pm 0.5$
	50	$0.95 \pm 0.03$	$159 \pm 21$	$1.4 \pm 0.4$

**Table 4.2:** Time constants evaluated from fitting the demagnetization traces of the Co/NiMn sample.

In the Ni/NiMn sample, the effect of a different sample temperature on the relative demagnetization is quite pronounced in the remagnetization. The relative change of the XMCD signal is only affected slightly with an increase in magnitude with increased sample temperature. The time constants obtained by fitting are displayed in Table 4.3.

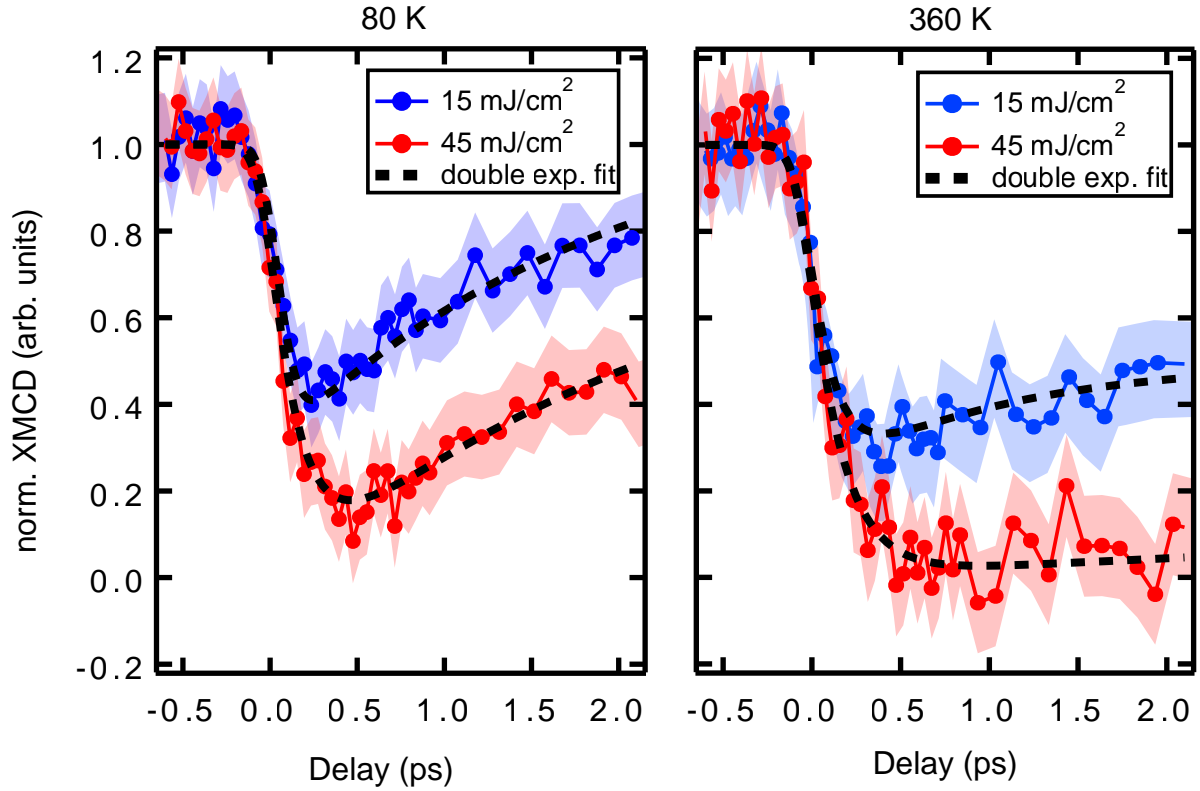


**Figure 4.15:** Normalized time-resolved XMCD recorded at the Ni  $L_3$ -edge for different pump fluences as indicated in the legend. The curves are evaluated in the same fashion as the Co data. The data recorded at 80 K is displayed in the left panel and the data recorded at 360 K is displayed in the right panel.

Ni	fl. ( $\text{mJ}/\text{cm}^2$ )	demag. amplitude	$\tau_{de}$ (fs)	$\tau_{re}$ (ps)
360 K	15	$0.80 \pm 0.10$	$130 \pm 24$	$1.0 \pm 0.4$
	45	$0.99 \pm 0.07$	$182 \pm 18$	$13 \pm 2$
80 K	15	$0.79 \pm 0.09$	$52 \pm 14$	$1.1 \pm 0.3$
	45	$0.91 \pm 0.12$	$161 \pm 20$	$1.6 \pm 0.7$

**Table 4.3:** Time constants evaluated from fitting the demagnetization traces of the Ni/NiMn sample.

To estimate the transient temperature in Co reached during and after the excitation, calculations in the frame of the m3TM are carried out. The results of the calculation are presented in Fig. 4.16 together with a comparison to the data. The material parameters for Co are taken from [54] and the fluence is fitted to reproduce the experimental curve of the 390-K Co measurement done with  $30 \text{ mJ}/\text{cm}^2$  incident fluence. The lattice heat capacity used is reduced to reach a better agreement with the experiment. The model predicts that transiently an electron temperature of up to 1450 K is reached after excitation from a base temperature of 390 K. The lattice in the model heats up by about 500 K for both ambient temperatures after 1 ps. In the calculation, no heat dissipation is included and the true temperature reached is probably slightly lower. It is

interesting to note that due to the linear scaling of the electronic heat capacity with temperature the difference in the electronic temperature reached between the two cases reduces to about 100 K. Transiently the difference is therefore not as great anymore. This does not reflect in the predicted magnetization in the model. Although the 390 K data is reproduced nicely, changing the ambient temperature in the model results in a drastic reduction of the quench, slower dynamics, and a faster remagnetization. That this is indeed an overestimation of the lower temperature effect within the m3TM model and not a miscalibration of the fluence in the measurement is confirmed in [190] where exactly this behavior is also reported in Ni data. A more detailed discussion on the temperature dependence of the magnetization dynamics in the scope of the m3TM is done in the next section.

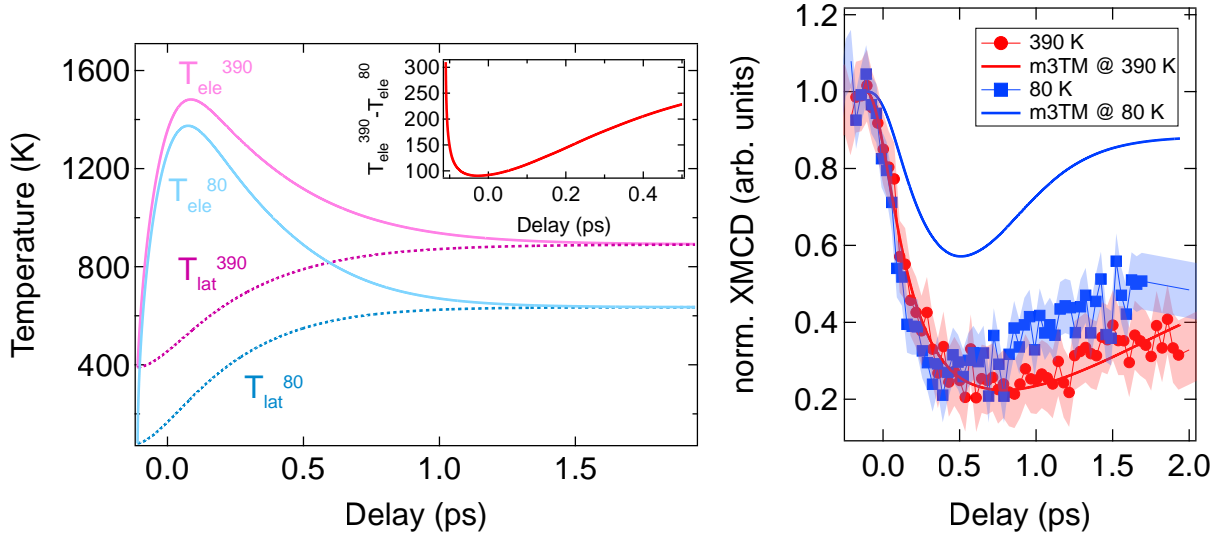


**Figure 4.16:** Left: Electron and lattice temperature of Co, denoted as  $T_{ele}$  and  $T_{lat}$  respectively, after excitation by a 100 fs pulse at an ambient temperature of 80 K and 390 K. The transient electron temperature exceeds  $T_C$  of cobalt at the higher ambient temperature. Overall, an increase of about 300 K is estimated after 1 ps. No heat dissipation is included in this estimation and the true temperatures are likely to be lower. The inset shows the difference in electronic temperature reached between the two cases. Since the electronic heat capacity scales linear with temperature the initial temperature difference of 310 K reduces to just about 100 K. Right: The m3TM reproduces the 390-K measurement in Co surprisingly well using the material parameters taken from [54], only the lattice heat capacity had to be reduced by 22 % to more accurately match the dynamics. The fluence is matched to the experimental curve. The model drastically overestimates the effect of the sample base temperature change.

At this point, it is important to consider the effect of the sample temperature on the saturation magnetization when approaching  $T_C$ . Generally, the change in magnetization is better expressed in the absolute change of the dichroic signal instead of the normalized XMCD. Since a higher sample temperature leads to a lower saturation magnetization, the same energy introduced in the sample will bring the magnetic system to a different final state, this is illustrated in Fig. 4.17. The dissipation of magnetization depends on both the fluence and the initial temperature. On the one hand, the change in temperature  $\Delta T$  is smaller for higher base temperatures since the electronic heat capacity scales approximately linear with temperature. On the other hand, the change in magnetization can be significantly higher due to the power scaling of mag-

netization with temperature. Generally, a higher base temperature should lead to an equal or higher quench of the magnetization when not demagnetizing entirely.

In the following, the data is analyzed with respect to the time required to quench a certain amount of magnetization. Assuming that the dissipation channels of magnetization are only insignificantly affected by the base temperature and having the context of the discussion above in mind it follows that at higher sample temperatures, i.e., when more magnetization is quenched, longer overall demagnetization times are measured.

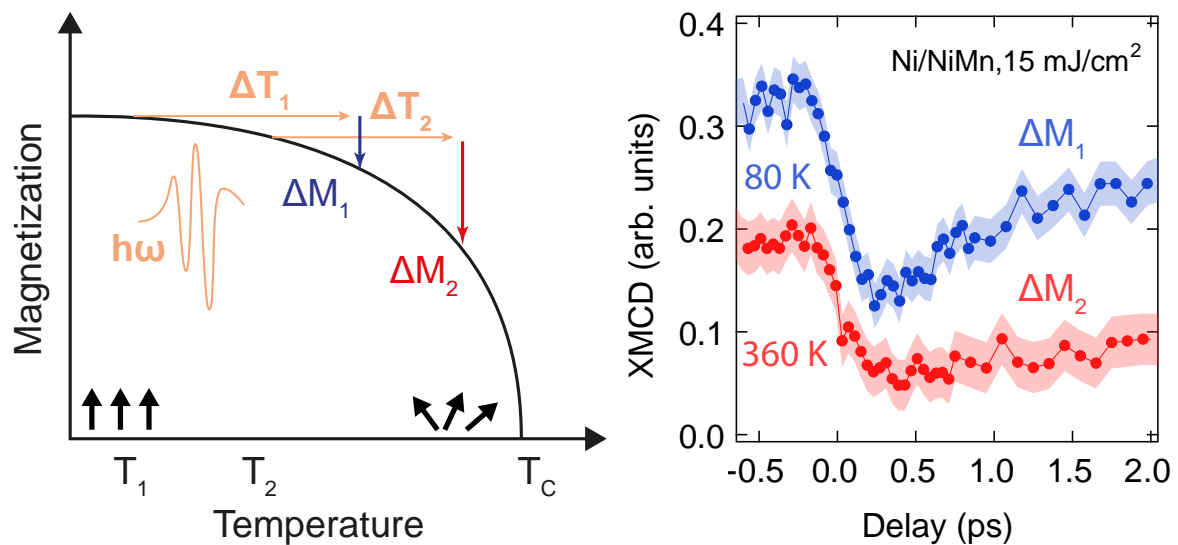


**Figure 4.17:** Left: Illustration of the magnetization vs temperature profile of a ferromagnetic thin film heated by a laser pulse of fixed fluence. The laser pulse energy increases the sample temperature by  $\Delta T$ .  $\Delta T$  depends on the starting temperature since the electronic heat capacity scales approximately linear with temperature. The change in magnetization  $\Delta M$  thus also depends on the initial sample temperature and the change in magnetization might be significantly higher in the vicinity of  $T_C$ . Right: A comparison of the Ni data. A laser pulse of  $15 \text{ mJ/cm}^2$  incident fluence is used to heat the Ni/NiMn sample. The curves show the change from 80 K and 360 K sample base temperature. The change in magnetization is plotted in absolute XMCD signal against delay time.

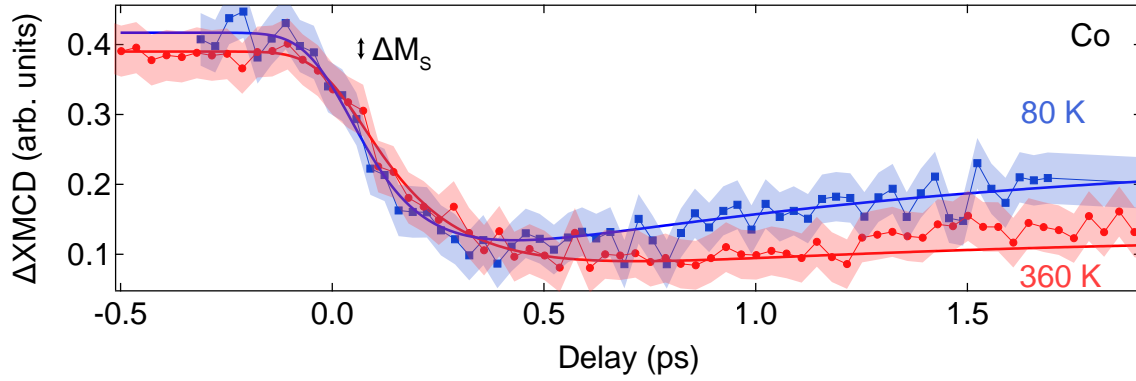


**Figure 4.18:** Delay-time traces recorded in Co at a sample base temperature of 80 K and 390 K. The demagnetization is measured in both cases with an incident fluence of  $30 \text{ mJ cm}^{-2}$ . Reducing the temperature to 80 K results in an increased XMCD signal at negative delay times. The change is only about 0.03 in absolute units of XMCD or 7.5 % contrast change.

### 4.3 Accelerated demagnetization due to ultrafast transport

The effect of the different sample base temperatures on the demagnetization dynamics is examined in the following in terms of the rate of magnetization dissipation, i.e., the time required to dissipate magnetization vs the amount of magnetization quenched. The findings are summarized and published in [162] and parts of the following section are paraphrased from the publication.

The observations described in the previous section are summarized in Figure 4.19 where the demagnetization time and the magnetic quench are plotted against the employed laser fluence. The overall increase of the demagnetization time constants with fluence agrees with the results published in the literature, for example [54, 155, 190]. In [54] even the drop in the demagnetization time when demagnetizing entirely is predicted, e.g., Figure 3 in the publication. Similarly, the almost linear increase of the quench with higher fluence is reported in the same references. Here, we focus on the differences observed for the two investigated sample temperatures. At lower sample temperature, the Co film demagnetizes faster when applying the same fluence, at the same time a reduced quench of the magnetization is observed. For us this raises the question - is this a temperature effect explained by a higher saturation magnetization and lower heat capacity at reduced temperature or is this an effect of the magnetic phase change in NiMn at low temperatures?

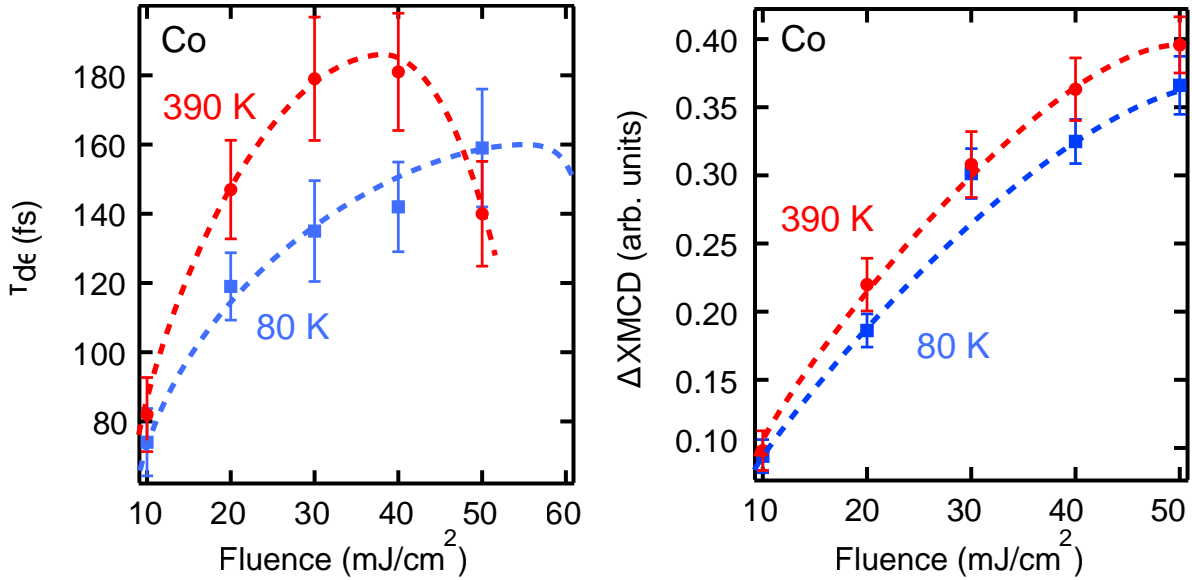


**Figure 4.19:** Left: Demagnetization times for the recorded fluences in Co evaluated by fitting as described in the text. With increasing fluence the demagnetization time constant increases significantly for both sample base temperatures. At 390 K (red circles) the time constant decreases when demagnetizing the film entirely. At 80 K sample temperature (blue squares) this drop is not yet observed. The dashed lines are a guide to the eye motivated by the calculations in [54] where similar dynamics are observed in Co and Ni. Right: Change in XMCD or magnetic quench for the recorded fluences. For both sample temperatures the magnitude increases monotonically with fluence. The dashed lines serve as a guide to the eye.

To answer the question we recall the illustration in Fig. 4.17 which highlights that at different sample temperatures the same fluence will result in a different magnetic quench. For a better comparison it is therefore necessary to compare the rate of demagnetization in terms of the absolute change of the magnetic signal. The comparison of the demagnetization times in Co and Ni by relative units of XMCD and by absolute XMCD quench is presented in Fig. 4.20. When comparing the timescale for a similar amount of magnetization dissipated for both sample temperatures, a gap remains between the time constants of the cold and the hot sample. This is observed in Co and even more significantly in Ni although only two data points are really comparable in the investigated fluences. Having established that the rate of demagnetization is indeed different in the observed temperature range, it is now important to discuss the mechanisms of demagnetization and their scaling with temperature.

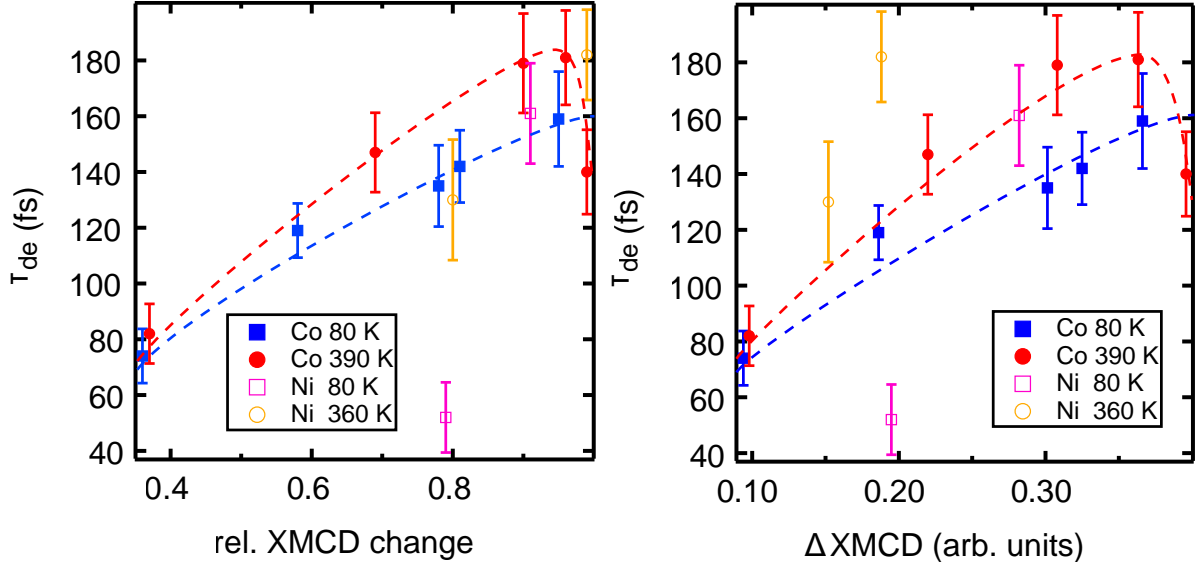


**Figure 4.20:** Left: Demagnetization time plotted against relative magnetization change in Co and Ni for the recorded sample temperatures. The rate of demagnetization is different for the two temperatures indicating that more magnetization is quenched in the same time interval at lower temperatures. The dashed lines are a guide-to-the-eye. Right: Demagnetization time plotted against absolute XMCD change. The same conclusion as in the relative comparison is drawn. When plotted against the absolute XMCD change, a similar rate of magnetization dissipation is expected assuming that the dissipation channels, like the Elliot-Yafet scattering, are only insignificantly temperature-dependent at the investigated temperatures. Comparing the timescale against the actual magnetic quench allows to compare also the Ni data, which indicate an even stronger effect than what is observed in Co. The dashed lines are guides to the eye.

We start with discussing the temperature dependence of local mechanisms quenching the magnetization on the ultrafast timescale. Most prominently the Elliot-Yafet spin-flip scattering, acting between electrons and phonons, is argued as the driving mechanism, redistributing angular momentum from the magnetic into the atomic lattice [54]. The m3TM, introduced in section 3.1.2, has no explicit temperature dependence. The beauty of the model lies in the fact that all parameters are defined by the material investigated. The ambient temperature is reflected in the spin-flip probability  $\alpha_{sf}$ , the electron-phonon coupling strength  $G_{ep}$ , and the final temperature reached.

The spin-flip probability  $\alpha_{sf}$  has been calculated from first principles to estimate the magnitude of magnetic quench induced by local electron-phonon scattering events [135]. Solving the spin-flip Eliashberg function for Ni apparently yields only slightly modified spin-flip rates for different temperatures. Although the ambient temperature is not explicitly taken into account in [135], the calculated spin-flip rates at elevated electron temperatures can be used to estimate the induced change. In Ni, it is calculated that an increase in the electron temperature from  $<300$  K to 1500 K results in an increase by a factor of about 1.25. For Co, the spin-flip rate is estimated to increase by about a factor of 2.5 in the temperature range estimated in Fig. 4.16. However, it is important to note that in all calculations an increase of the spin-flip scattering rate is found. This will effectively drive a faster and stronger demagnetization. This temperature dependence is at the heart of the argument of the Elliot-Yafet mechanism. In addition to enhanced spin-

mixing at elevated temperatures, the higher spin-flip rate drives the demagnetization, since the electron temperature is transiently significantly higher than the lattice temperature. In total it follows that a stronger quench and a higher rate of demagnetization should be observed at an elevated sample temperature. This is not what is found in the data presented here. Although a higher quench is observed for the same fluence, comparing the rates shows that at the reduced ambient temperatures a higher rate is found.

The electron-phonon coupling  $G_{ep}$  is generally temperature-dependent [191, 192]. The temperature scaling is strongly influenced by the DOS and the shift of the chemical potential with temperature of the element. In Ni,  $G_{ep}$  is found to scale inversely with temperature [192] due to the high density of states at the Fermi edge. For Co, to the best of my knowledge, no conclusive experimental report on the scaling of the coupling with temperature is published. In case the coupling increases with temperature, as suggested in [193, 194] the demagnetization rate is expected to increase as well. This follows directly from the derivation of the m3TM since a higher coupling strength leads to a more efficient spin redistribution. This would result again in a contradiction to the observation. In any case, in the relevant transient electron temperature region, only a small deviation is found. We argue that this alone does not suffice to explain the measured difference in rates. Together with the higher rate due to spin mixing and a higher spin-flip probability, a significantly reduced coupling is necessary to explain the effect. Moreover, with a reduced coupling, the heat-capacity deviates from a linear scaling [192] and a reduced heat-capacity conversely leads to a higher temperature reached and thus an even higher spin-flip probability.

An investigation of the influence of the ambient temperature on the demagnetization dynamics in Ni employing the m3TM in an attempt to reproduce the dynamics shows precisely the feature mentioned before, i.e., a higher quench and rate at elevated ambient temperature [190]. The authors of [190] do not elaborate on the details of the refined m3TM used to include the ambient temperature dependence but state the importance of the reduced exchange splitting when nearing  $T_C$  at higher temperatures. A significant slow-down of the dynamics, especially of the remagnetization is reached in the model once the temperature is sufficiently high. A significant reduction of the exchange splitting that would also result in reduced overall magnetization and therefore reduced XMCD signal is not observed in Co in the investigated temperatures. Therefore, we exclude that in Co, with a  $T_C$  of about 1300 K, reduced compared to the bulk value due to finite size scaling, the findings are explained by a break-down of the exchange splitting close to  $T_C$ . In Ni, where the Curie temperature is estimated to be only around 600 K, this effect might contribute and could help to explain the vastly different rates.

In conclusion, we do not expect that the temperature dependence of local effects in the terms of the m3TM can explain the offset observed in the demagnetization rates in Co. The spin-flip rate at a higher temperature would lead to the opposite effect. A reduced electron-phonon coupling is most likely compensated by the increase in scattering rates and spin mixing which is also suggested in calculations in [190]. Lastly, a break-down of the exchange splitting in the vicinity of  $T_C$  is not likely due to the relatively high value of  $T_C$  in Co.

In the following, the temperature dependence of non-local effects is discussed. For transport phenomena, it is elementary to establish first an understanding of the gradients and excitation regions involved. To confirm that carriers are mainly excited in Co and NiMn, calculations of the differential optical absorption are carried out. The layer-wise optical absorption, evaluated with an implementation of the formalism described in section 2.1.2 written by E. Golias, reveals that most of the absorption happens in the Co and the NiMn layer. The result of the calculation is presented in Fig. 4.21. We expect that there is a heat gradient to Cu with the hot

side being the Co and NiMn layers. Both layers are expected to absorb the 800 nm pump light almost equally.

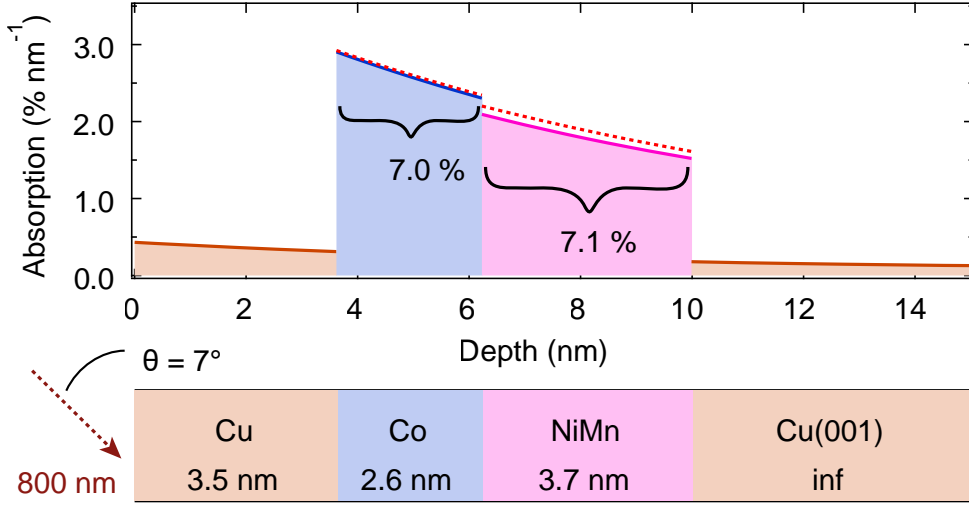


**Figure 4.21:** Differential absorption calculated for the Co/NiMn sample for 800 nm p-polarized light. The calculation is performed following the formalism of [195] as described in section 2.1.2. The Co and the NiMn layer absorb almost the same magnitude of the light, 7 % and 7.1 %, respectively, as indicated in the plot. A schematic of the sample is shown below the graph indicating the thickness of each layer. The calculation is performed for p-polarized 800 nm light, incident at  $7^\circ$  with respect to the surface. The optical constants for Co, Ni, and Mn at 800 nm are taken from [28]. We use  $n_{Cu} = 0.2533 + 5.013i$ ,  $n_{Co} = 2.488 + 4.803i$ , and  $n_{NiMn} = n_{Ni} = 2.218 + 4.893i$  or  $n_{NiMn} = n_{Mn} = 2.788 + 3.998i$ . Since the value for NiMn is not known, we perform the calculation for  $n_{NiMn} = n_{Ni}$  leading to the colored differential absorption and for  $n_{NiMn} = n_{Mn}$  indicated by the dashed red line. The vertical lattice distances  $d$  used are  $d_{Cu} = 1.81 \text{ \AA}$ ,  $d_{Co} = 1.74 \text{ \AA}$  [167], and  $d_{NiMn} = 1.88 \text{ \AA}$  [163].

With the excited regions established, we focus again on the temperature dependence of the non-local phenomena. The concept of ultrafast superdiffusive transport [128], introduced in section 3.2, is the most prominent candidate to explain the ultrafast quench of magnetization from a transport perspective. Alternatively, ultrafast magnon generation leads to spin transport away from the region of excitation. While ultrafast magnons have been reasoned to play a role in the early demagnetization [196, 197], their role and timescale are not yet established definitely. Although we expect an influence of magnon transport on the dynamics recorded in our experiment, their effect is more pronounced on longer timescales. Since spin waves or transversal spin excitations are secondary processes, generated by the electronic thermalization and spin equilibration mechanisms, the other angular momentum channels are more likely responsible for effects seen at the timescales investigated here. The discussion of transport phenomena is therefore limited to the discussion of hot-electron transport away from the excited region.

Similar to the m3TM, the superdiffusive transport model does not contain an explicit temperature dependence and a detailed investigation of the temperature scaling has not been carried out. The model is based on different effective velocities for electrons carrying majority or minority spins. The lifetime and velocity of the excited electrons are temperature-dependent properties. A general reduction of the spin lifetime at elevated temperature is symmetric for both minority and majority carriers. Since superdiffusive transport considers a net spin current, only asym-

metric effects for minority and majority carriers, or changes in the relative carrier lifetimes and velocities play a role. An overall reduction of the spin polarization already described before happens at higher temperatures. This is either described in terms of a reduction of the exchange splitting or by transversal excitations. Following the argument of the temperature dependence in the m3TM, such a reduction is not observed here in Co since the XMCD at negative delays hardly changes. In Ni, it is likely that due to the reduced magnetization and therefore reduced asymmetry of carrier lifetime and velocity the temperature difference already results in a sizeable effect on the demagnetization rates. A more subtle effect is induced by temperature due to an altered band structure which might lead to either an increase or decrease of the velocities, depending on the slope at the excited transitions. This change is considered to be insignificant in the range of temperature investigated here since no phase change in the Co or Ni layer is expected to occur. Most of the energy is dissipated by electron-electron scattering events which are almost temperature-independent.

To summarize, the strongest temperature effect is expected to arise from a change of the spin asymmetry mediated by either a reduced exchange splitting or spin mixing. Although this would decrease the rate as observed in the experiment, the mechanism is not likely to be responsible for the different rates in Co since the static XMCD remains virtually unchanged at the two temperatures. The effect might be more pronounced in Ni where a reduction of the static XMCD by almost 1/3 is observed. Weaker effects like differences in the bandstructure and spin-dependent scattering cross-sections are ruled out as the cause for the different rates since their temperature dependence is not sufficient in the interval investigated here.

In conclusion, we rule out that the effect is caused by the temperature change alone. In the m3TM, describing local effects, an opposite behavior is expected. This is in line with calculations in a scenario where  $\alpha_{sf}$  and  $G_{ep}$  are temperature independent, but according to [190] even with a refined model considering the ambient temperature change of the involved parameters the observations are not expected. In case local mechanisms are the dominant mechanisms for angular momentum dissipation, the observation can not be explained. In the superdiffusive transport model, only slight changes in the demagnetization rate with the investigated temperatures are expected. They become considerably larger when approaching  $T_C$ . Since the static XMCD hardly changes in Co the observed effect is too large to be explained by a reduction of the carrier asymmetry.

Since the temperature alone is not responsible for the observed difference in the rates, we argue that it is caused by the long-range antiferromagnetic order in NiMn which disappears at elevated temperatures. It is difficult to argue which process of demagnetization, local scattering or transport, generally dominates in experiments. However, it is established that ultrafast carriers play a significant role in the magnetization dynamics as elaborated in section 3.2. Here, ultrafast carriers are excited over the entire sample region and transport between the Cu, Co, and NiMn layers contributes to the observed dynamics. A sketch of the expected spin transport away from Co is presented in Fig. 4.22. Superdiffusive carriers, excited in Co, transport the majority spin polarization away from the excited region into Cu and NiMn. Similarly in NiMn hot electrons are excited and transported into the Co layer and the Cu substrate. Since Cu is not magnetic, both the cap layer and the substrate are expected to act as an efficient spin sink at both ambient temperatures. At low temperature, the NiMn layer is antiferromagnetically ordered with the sublattice magnetization collinear to the magnetization in Co. In this state polarized superdiffusive carriers coming from Co are injected into empty states of the same spin character leading to an efficient transport away from the FM layer [198]. Once the NiMn layer is not magnetically ordered anymore, i.e. at higher ambient temperature, the spin-state

matching is lifted and the disorder leads to a significantly enhanced carrier reflection at the interface and a reduced spin-penetration depth [199]. In total, this leads to the conclusion that the ordered AFM will act as a much better spin-sink for the majority electrons coming from Co compared to a disordered paramagnetic state. At the same time, with the AFM order present, polarized hot electrons from the NiMn layer are injected into the Co film. Since there are more unoccupied minority states available in Co, carriers of this type are preferentially entering the FM layer. This superdiffusive current further accelerates the demagnetization in the FM layer. In the case of a magnetically disordered paramagnetic NiMn layer, i.e., at higher ambient temperature, the number of polarized electrons carrying spin of the same state is reduced. Both effects together lead to a sizeable difference in the demagnetization rate of the Co FM-layer between an adjacent AFM-ordered layer and a disordered one.

## 4.4 Summary and conclusion

This section covers the investigation of ultrafast laser-induced demagnetization in Co and Ni coupled to a Ni<sub>30</sub>Mn<sub>70</sub> layer. The antiferromagnetic long-range order in NiMn can be switched on or off by ramping the temperature well below 300 K or heating it up close to 400 K, respectively. The calibration of the MBE growth parameters is described. Precise knowledge of deposition rates and instrument sensitivity is necessary to fabricate the NiMn alloy in the desired stoichiometry. Both parameters are obtained by recording datasets of evaporations for all materials involved and correlating the AES intensities with MEED intensity oscillations obtained during growth, as presented. Static temperature-dependent magnetic characterization is carried out in-situ after growth to estimate the onset of the AFM order in NiMn. Further characterization of the reflectivity properties is done at the scattering end-station at the PM-3 beamline at BESSY II. The information about the angle- and energy-dependent scattering intensity and magnetic contrast are vital for successful time-resolved measurements in the limited time window granted to users of the slicing facility. The time-resolved reflectivity recorded at the slicing facility Femtospex at BESSY II is presented for the early timescales up to 2 ps. All curves are analyzed with respect to their demagnetization dynamics, which is evaluated from the X-ray magnetic circular dichroism. The time constants are obtained by fitting a two-exponential model to the early dynamics, yielding the speed and magnitude of the light-induced quench of the magnetic asymmetry. The aim of the experiment is to identify effects induced by changing the ambient temperature of the sample from 80 K to 390 K, thus covering the magnetic order phase change in NiMn from AFM to PM. The evaluation of the obtained timescales shows that at 80 K higher demagnetization rates are found for Co and Ni. While in Ni no systematic study is possible due to the low number of recorded scans, the findings in Co show a clear trend. The observation of the increased demagnetization rates at low temperatures contradicts predictions of the temperature scaling in the m3TM, which treats local scattering events as the driving source for demagnetization. In the investigated temperature range a simple temperature scaling of the superdiffusive transport is ruled out since the static magnetization in Co is virtually unchanged. Therefore we attribute the observed difference to enhanced spin transport through an ordered AFM layer compared to a disordered PM layer. A larger spin penetration depth together with a lower reflection at the interface of the ordered AFM, compared to the disordered state, is responsible for the difference observed in the Co rates. The process is illustrated in Fig. 4.22. Although we tentatively reason that the same mechanism is responsible for the even

larger effect in Ni, the interpretation is more difficult due to the low number of data points. In Ni, the temperature change already reduces the static magnetization significantly, which results in temperature effects on transport and local scattering that can be ruled out for cobalt. This scaling further adds to the observed difference and might explain the vastly higher change in the rates.

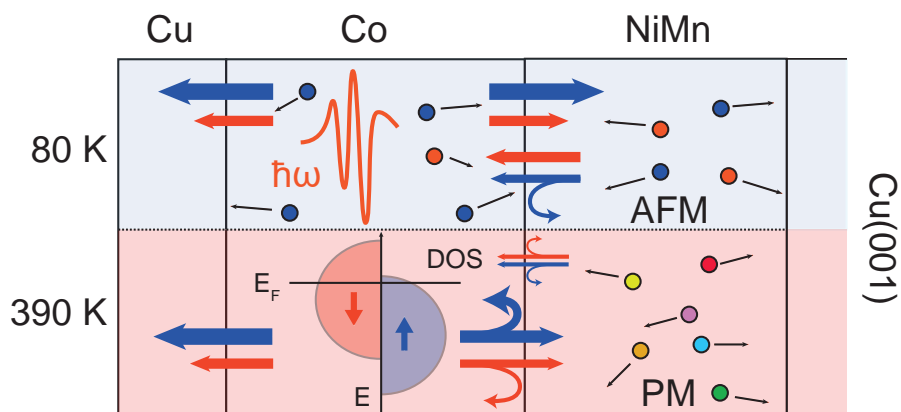


**Figure 4.22:** Illustration of the transport processes responsible for the different demagnetization rates observed at the two investigated temperatures. The Co layers remains FM ordered in both temperature regimes. At 390 K a higher reflection at Co/NiMn interface is expected due to the spin mismatch of the Co and the NiMn spins. Conversely at low temperatures an efficient spin transport through the AFM interface is expected due to the high degree of collinear spin alignment. At the same time a higher minority spin transport into Co coming from the AFM ordered NiMn layer is expected compared to the paramagnetically aligned case. Transport strength and spin character are indicated by the arrows' thickness and color, respectively. An illustration of the electrons is given by the colored circles where the color indicates the spin character according to the DOS schematics. Note that in the PM case the spin character is mixed.

This finding provides us at least with a partial answer to the first research question of this work: Does the coupling between two adjacent layers, one a FM and one an AFM, influence the ultrafast quench of magnetization?

An indication that the proximity of the AFM layer to the FM in ultrafast experiments alters the observed demagnetization dynamics is found. In the FM an acceleration of the demagnetization due to the adjacent AFM layer is observed [162]. This change is introduced purely by the long-range order in the material since no other parameters but the temperature are changed and the other temperature-induced effects can be ruled out efficiently. That ultrafast (superdiffusive) transport plays an important role in the demagnetization of heterostructures is further validated. The findings highlight the potential to influence magnetization dynamics not only in the layers adjacent to the ferromagnet but also the other way around. The combination of AFM and FM materials has historically been quite fruitful and both new physical understanding and novel technologies have been acquired. From a dynamical perspective, this is still new territory and further interesting properties can be expected to be observed in future experiments. For example, next to the finding in this work, the combination of an artificial AFM with a magnetic layer in all-optical switching experiments is found to be useful due to the spin exchange be-

tween the FM layer and the two layers of the synthetic AFM [200]. Combining a tunable AFM in a multilayer stack opens opportunities to tailor the dynamic magnetic response to a light stimulus in the adjacent layers. In the next chapter another light-induced phenomenon arising at the interface of a FM and an AFM, happening at even shorter times, is presented.

# Chapter 5

## Magnetization in the presence of the laser field

In the last chapter, the investigation into the effect of an AFM layer adjacent to a FM layer on the demagnetization is described. The following chapter covers an investigation on a similarly structured sample, an FM Co film adjacent to an AFM Mn film. This time the focus of the investigation is the magnetization dynamics at the very early timescale, i.e., in the presence of the exciting laser pulse. We grow the model system calculated in [120], and already introduced in section 3.3, to study light-induced dynamics at the interface of Co and Mn. Since we expect the effect described in [120] to be only present at the interface, a multilayer sample with alternating Co and Mn layers is grown. The time-dependent magnetization is traced by element-sensitive X-ray reflectivity. We observe the signature of a light-induced AFM to FM transition in Mn. The FM state in Mn is deduced from an ultrafast increase in magnetic contrast evaluated at the Mn edge. The contrast enhancement lives for the duration of the excitation. The findings are explained by the optically induced spin transfer between Mn and Co sites at the interface. The results of the investigation are published in [201] and parts of the following are paraphrased from the publication.

### 5.1 The Co/Mn system

The investigation is performed on a Co/Mn-multilayer system grown on a Cu(001) single crystal surface. Why this system is investigated, and the aim of this study is elaborated in the following. The motivation is to look for experimental verification of the OISTR phenomenon, predicted in time-dependent density-functional theory (TD-DFT) calculations. The idea of the OISTR is introduced in section 3.3. The authors of [120] have identified a coherent light-induced mechanism driven by the excitation laser pulse that rearranges the electrons of different neighboring atomic sites. In those inter-atomic transitions, the charge remains neutral, but the local atomic moment changes since the electrons are of a distinct spin character. Dewhurst et al. [120] predict different dynamics for Mn/Co systems depending on the number of layers in each film. For example, in a 2 ML Mn film adjacent to a 4 ML Co film, the average moment on Mn is expected to increase by almost a factor of two. In case 3 ML Mn are coupled to 3 ML Co, the calculations predict a contrast reversal in Mn. If only 2 ML of Mn are adjacent to 3 ML Co, the same scenario as for 4 ML of Co is predicted. The relevant graphics of [120] are reprinted

in Fig. 5.1 for clarity.

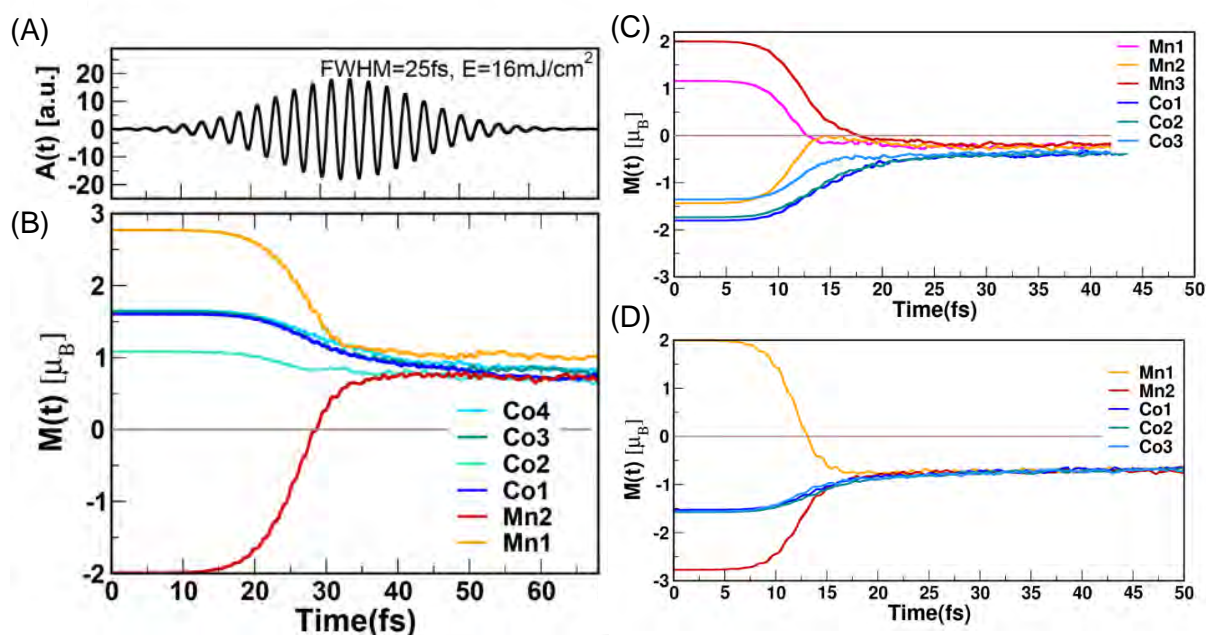


**Figure 5.1:** Predictions of the layerwise atomic moment evolution in Mn and Co during optical excitation by 800 nm taken from [120]. The time-dependent optical field is presented in (A). In (B), the evolution of the atomic moments in Co and Mn is plotted. The numbering refers to the layer of the element. It is assumed that Mn and Co couple antiferromagnetically such that the interface between Mn2 and Co1 is a  $180^\circ$  spin reversal. During excitation, carriers from Co are excited into Mn sites, and the sum of all Mn moments increases by ferromagnetic alignment with the Co moment. In (C), the scenario for 3 ML Mn is shown. It is predicted that all Mn layers align ferromagnetically, resulting in an overall contrast reversal of the Mn moments. In (D), 2 ML of Mn are put on top of 3 ML of Co. The resulting dynamics are similar to (B) only with a reversed total moment due to the FM being aligned in the opposite direction which is arbitrary. Reprinted with permission from Ref. [120]. Copyright (2021) by the American Physical Society.

We aim to investigate the OISTR predictions experimentally by time-resolved resonant magnetic X-ray reflectivity (RMXR). For this purpose, different multilayer systems of Co and Mn are grown, and the coupling between Co and Mn is investigated. Since only one system can be measured time-resolved in a reasonable amount of time, we first benchmark the contrast in some systems to find the most promising one to study. First, a system comprised of 2 ML Mn/4 ML Co (2/4) with several repetitions is grown. We compare the static characteristics to a 3 ML Mn/3 ML Co (3/3) system, also grown with several repetitions. Ultimately, we expect that in the (3/3) system, the time-dependent magnetic contrast in Mn reverses during excitation, whereas in the 2/4 system, it should increase, based on the predictions of [120].

The growth of the samples on Cu(001) is monitored by recording the specular MEED reflection intensity during deposition. The evaporation parameters for this system are already known due to the calibration performed for the earlier works and are chosen according to the description given in section 4.1.1. The sample surface is cleaned by sputtering and annealing, similar to the process explained in section 4.1.1. Example MEED curves of the growth are shown in Fig.

5.2. Both samples start with a small Co coverage on which repetitions of the 3/3 or 2/4 system are grown. For the time-resolved investigation at the ZPM scattering chamber, a 3/3 system is grown. The characterization of this sample is presented in Fig. 5.5.

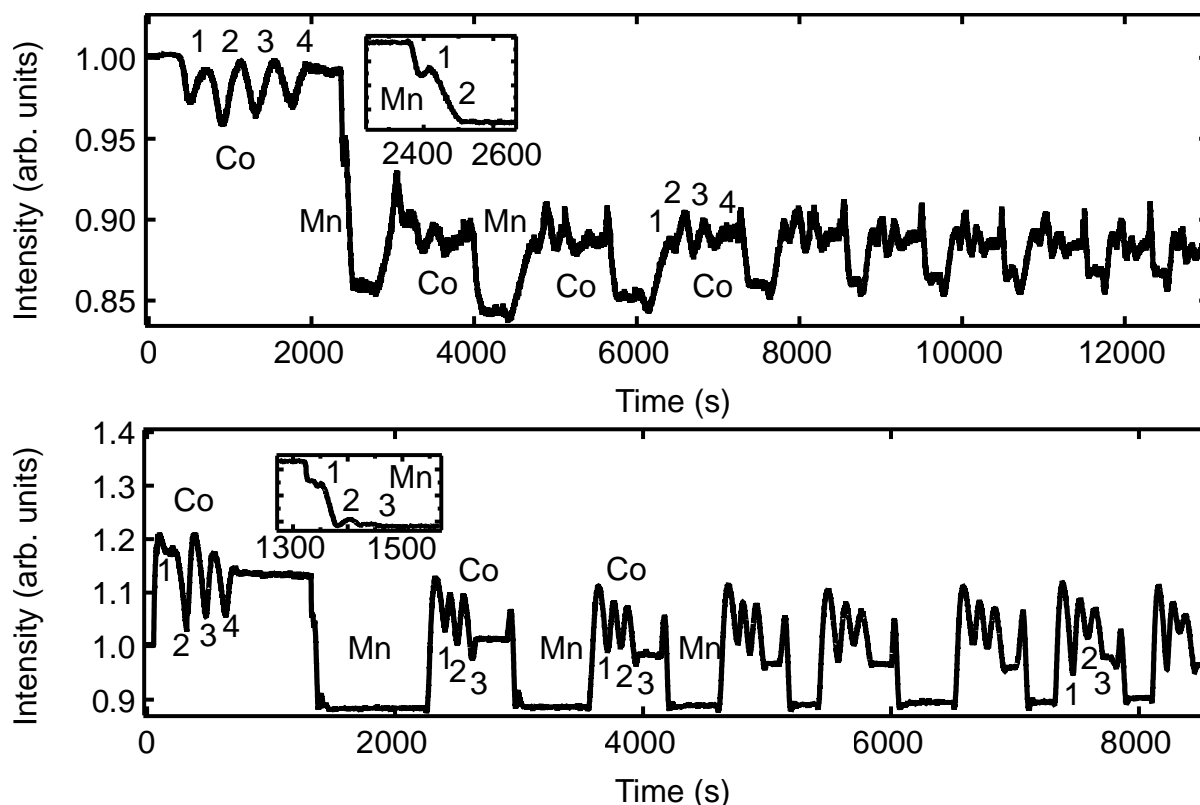


**Figure 5.2:** MEED intensity recorded during growth of the Co/Mn multilayer samples. The numbers indicate the layer number in the respective deposition step. For clarity, the deposited element is denoted in some parts of the recorded intensity. The top panel shows the repeated growth of 2 ML Mn/4 ML Co on 4 ML Co on Cu(001). The inset shows the MEED intensity during Mn evaporation. Only the first recovery of intensity is visible. Due to the absence of a second oscillation, the time for Mn evaporation is based on the rates and calibration of the deposition. During the growth of the successive Co layers, the MEED intensity recovers, and oscillations for the Co layers are visible up to 10 repetitions of the 2/4 system. At the end of the evaporation the timings decrease due to an increase in the evaporation rate. The lower panel shows the growth of a 3/3 system on 4.5 ML Co on Cu(001). Here the MEED intensity is not recorded at the maximum, which results in the initial increase of the intensity, and a full layer is formed at the minimum. The inset shows the MEED intensity evolution during the deposition of the first 3 ML Mn. A small bump is visible in the Mn deposition coming from filling first the half-layer. The next Co layers recover some of the intensity again by creating a smooth surface. Initially, the timings are slightly off, and more than 3 MLs of Co are grown during each deposition. Nevertheless, static characterization was carried out to test the sample.

The samples are investigated statically at the VEK MAG and the PM3 endstation at BESSY to identify the magnetic ordering by employing element-sensitive soft-X-ray scattering and absorption spectroscopy. Similar to the process described in section 4.2.1, an evaluation of the expected measurement time is carried out. This is again done by recording the reflected X-ray

intensity for a set of angles and energies while employing circular polarization and changing the sample magnetization, similar to the description in section 4.2.1. Based on the estimations of the measurement time, we decided to perform the time-resolved experiment on the 3/3 system. The growth characteristics of the sample are shown in Fig. 5.5.

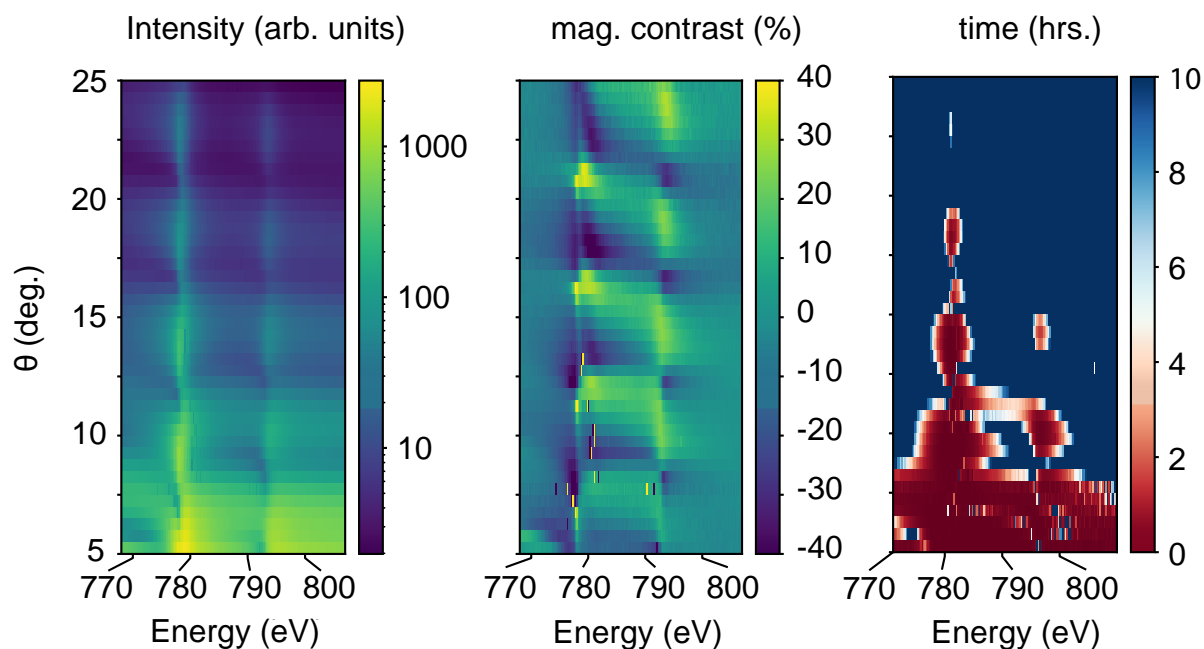


**Figure 5.3:** From left to right: Recorded X-ray reflectivity, magnetic contrast, and expected measurement time evaluated according to eq. (4.4) for Co in the 3/3 sample.

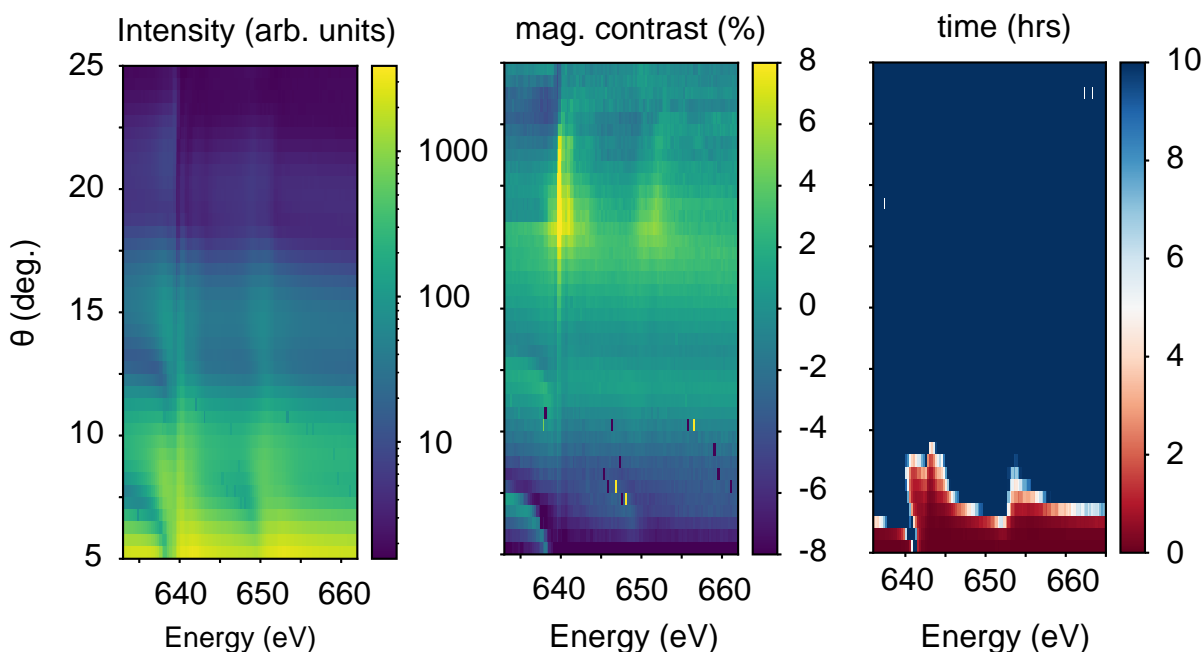


**Figure 5.4:** From left to right: Recorded X-ray reflectivity, magnetic contrast, and expected measurement time evaluated according to eq. (4.4) for Mn in the 3/3 sample.

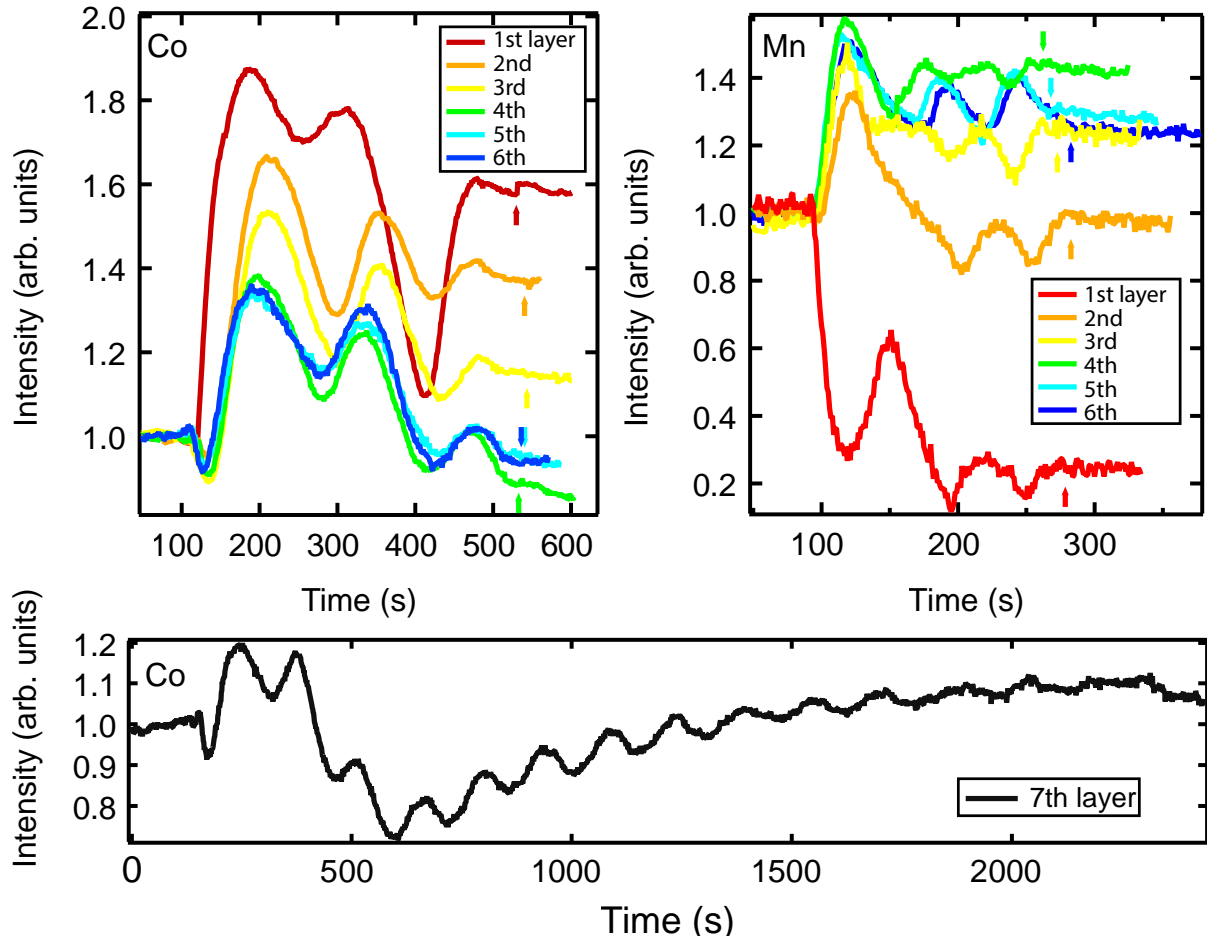


**Figure 5.5:** MEED intensity recorded during growth of the Co/Mn multilayer sample. The sample is grown alternating between Co and Mn depositions. The sample starts with the first layer of Co, and then the first layer of Mn is deposited on top. The MEED intensity is recorded at the minimum for Co. A complete layer is formed in each minimum. The arrows indicate the moment the shutter is closed to stop the deposition. In Mn, the intensity is first recorded at the maximum and after the first layer in the minimum. After alternating between 3 ML Co and 3 ML Mn six times, the sample is capped with 14 ML Co. Data by courtesy of I. Gelen, who prepared the sample.

## 5.2 Light-induced magnetism in an AFM

The time-resolved X-ray reflectivity (XRR) measurements on the 3/3 system are carried out at the ZPM endstation at BESSY II employing 100 fs X-ray pulses. The X-ray energy is tuned to record the dynamics resonantly at the Mn or Co  $L_3$  absorption edge. Two dichroic scans, measured at the slicing endstation in ps time resolution, of the reflected intensity across the resonance edge of Co and Mn, are shown in Fig. 5.6. A change in contrast across the Mn  $L_3$  edge is observed. In Co, the contrast remains constant across the absorption edge. The highest figure of merit, in the sense of eq. (4.4), is found at 636 eV, at the maximum positive contrast in Mn. In Co, the best conditions are found at 778 eV, at the energy where the peak intensity is recorded in reflectivity. The energy resolution of the ultrashort X-ray pulses is around 3 eV. This will not lead to a significant change in the recorded dichroism in Co since the contrast is

almost constant across the reflectivity peak. In Mn, we choose a slightly lower energy in the slicing operation to not "average" across the contrast change.

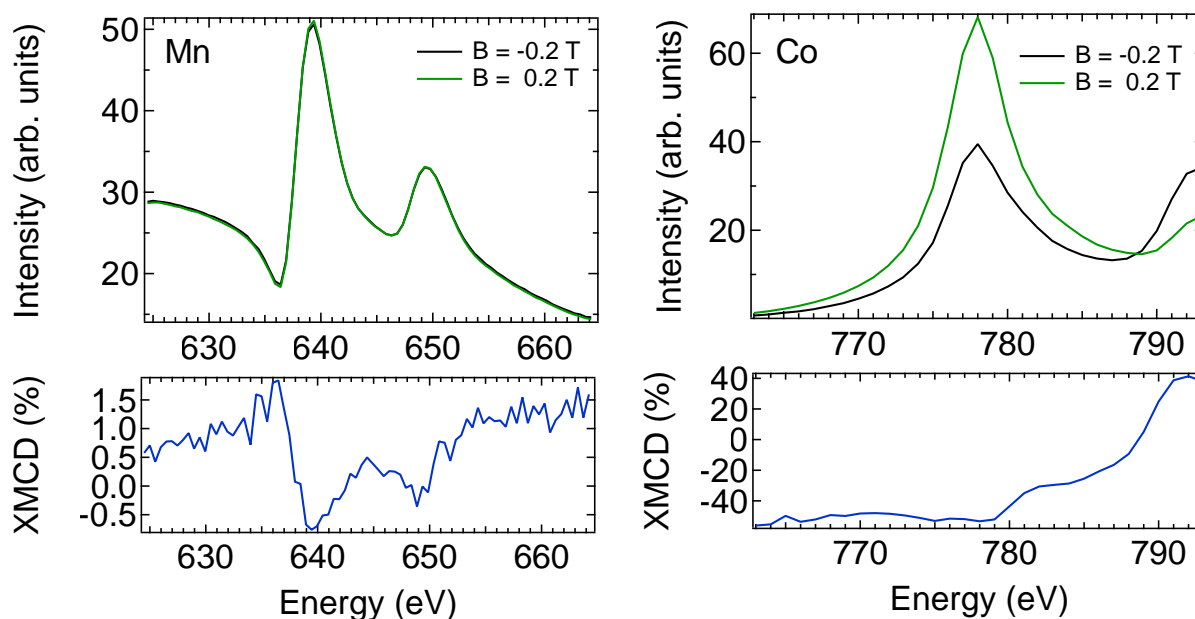


**Figure 5.6:** Spectra recorded over the  $L_3$  absorption edge of Mn (left) and Co (right) at the slicing facility in reflectivity under  $\theta = 8.75^\circ$ . The magnetic contrast evaluated from the spectra is shown below. In Co the magnetic contrast is almost constant across the absorption edge. In Mn a contrast reversal around the peak close to 640 eV is measured.

Using the combination of angle and energy, already established from preliminary measurements, shown in Fig. 5.3, we start by recording the time evolution of the magnetic contrast after laser excitation at the Co  $L_3$  absorption edge in reflectivity. The experiment is carried out at an angle of  $\theta = 8.75^\circ$  under which a decent magnetic contrast, a sufficient photon yield, and enough laser absorption is registered. For the excitation, 60 fs linearly polarized laser pulses are employed with an incident fluence of  $12 \text{ mJ/cm}^2$ . The dynamics are presented in Fig. 5.7. The Co dynamics show a demagnetization similar to the one observed in the measurements in the last chapter, e.g., see Fig. 4.18. The experimental error is deduced from the photon counting statistics, and for fitting the data, an experimental resolution of 120 fs is used. The magnetic contrast reduces to about 30 % of the initial value, and a time constant of around 160 fs is found for the demagnetization. This is slightly faster than what is observed at 390 K in the previous chapter. Here, all measurements are carried out at room temperature.

The dynamics recorded in Mn are presented in Fig. 5.8. A quite different evolution of the pumped signals is found in Mn compared to Co. In the channels recording the evolution of the XRR after excitation, an increase in intensity around zero delay time is observed. At the same time, a magnetic contrast in the channels is visible. After normalization by the unpumped channels, only a sharp rise of the contrast around time zero remains. A successive dynamic sets in after 500 fs, where both signals start to increase in intensity. A comparison of the XMCD evaluated from the time-resolved data is presented in Fig. 5.9.

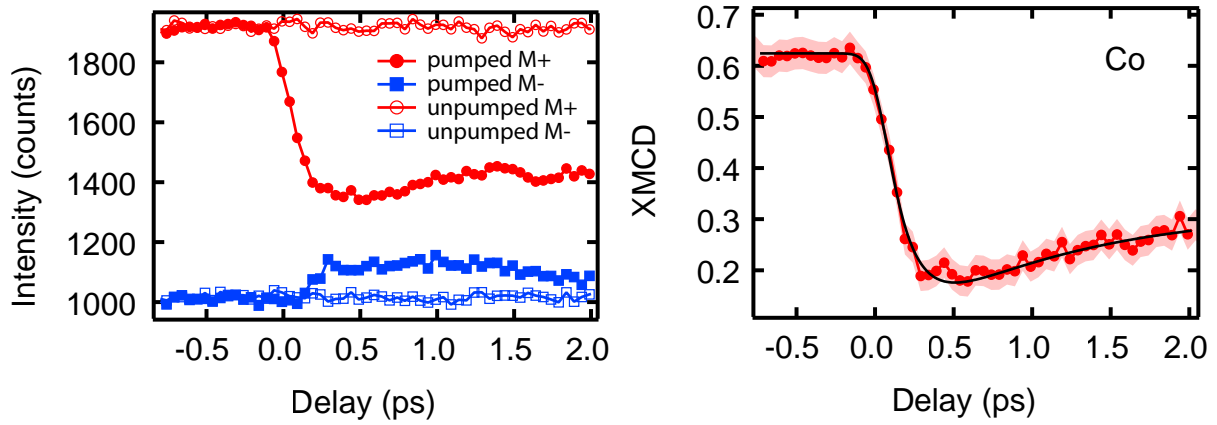


**Figure 5.7:** Left: Measured pumped (filled symbols) and unpumped (open symbols) channels for two opposite directions of magnetization (circles and squares). The difference between the two signals is the magnetic contrast which reduces after excitation. Right: Calculated XMCD from the data shown of the left side. A double exponential fit, using eq. 2.30, and a demagnetization time of  $\tau_{De} = (155 \pm 29)$  fs and a remagnetization time of  $\tau_{Re} = (1.0 \pm 0.2)$  ps is plotted together with the data. The data is recorded at 778 eV.

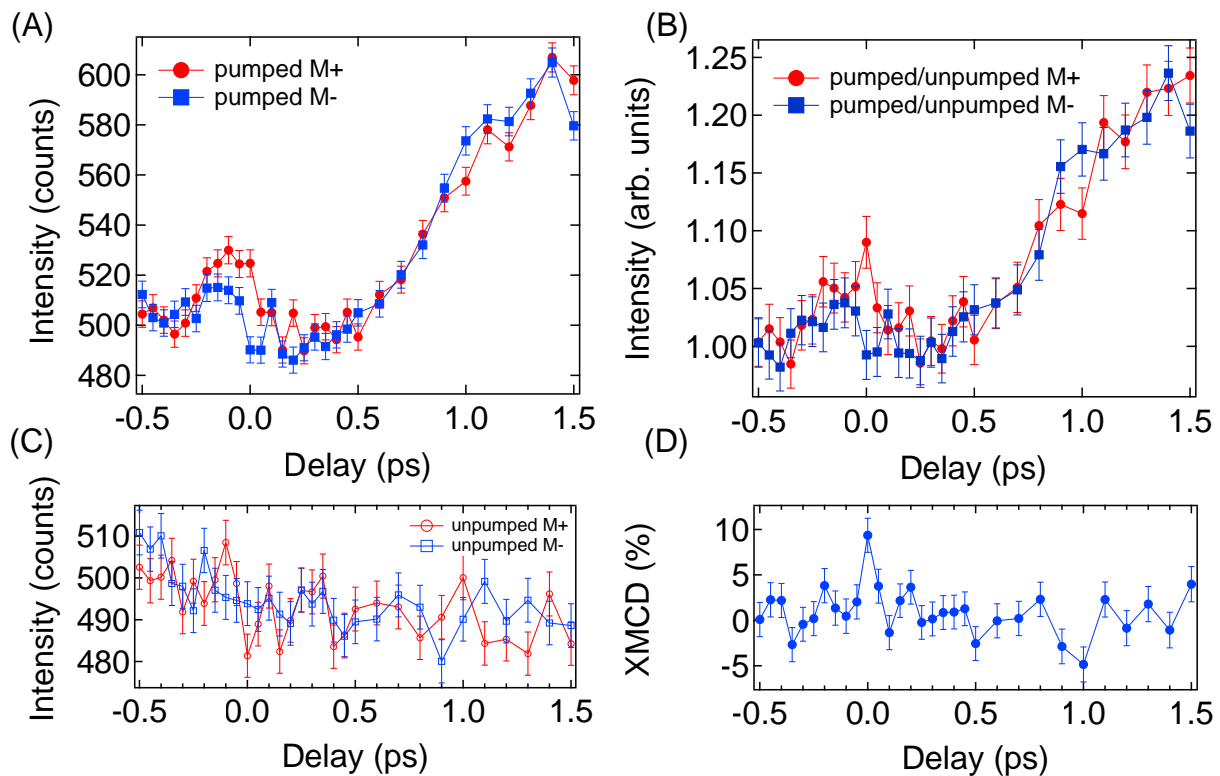


**Figure 5.8:** (A) Pumped channels for applied fields of  $\pm 0.2$  T, recorded at 636 eV after excitation. Around zero delay time, a rise in both channels and a magnetic contrast are visible. After 500 fs, a combined increase of both channels is visible. (B) The recorded dynamics after normalizing to the unpumped channels. The rise in intensity and the apparent change in contrast around time zero are still observed. (C) Unpumped XRR in Mn, recorded at the same time as the data in (A). Under slicing conditions, no static contrast is observed. (D) Resulting XMCD of the normalized channels. At time zero, a sharp increase of the Mn contrast is visible.

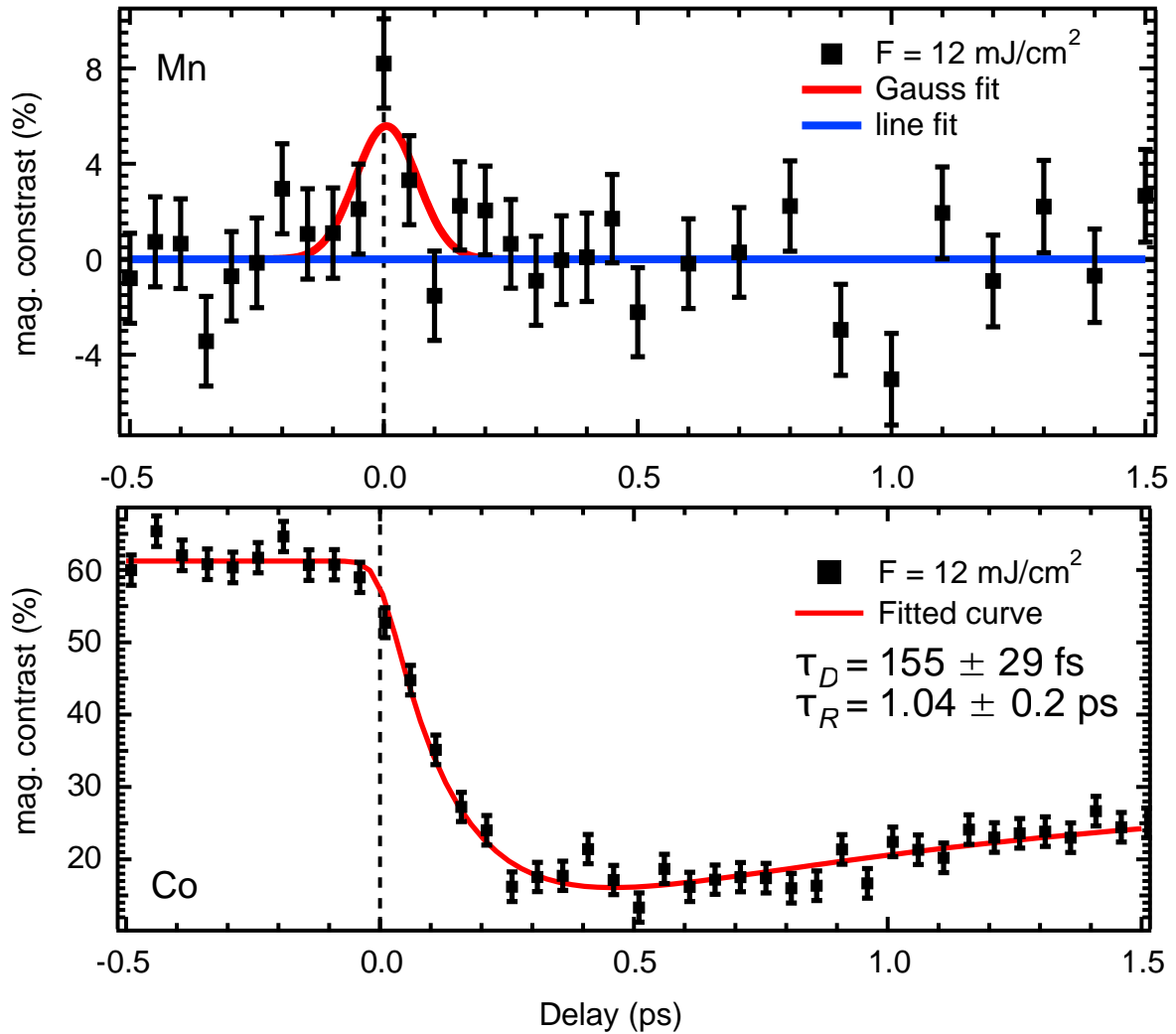


**Figure 5.9:** Top: Time-resolved XMCD recorded at the Mn  $L_3$  absorption edge. At time zero a sharp rise of the contrast to about 8 % is observed. The evolution is fitted with a Gaussian (red) and its likelihood is compared to a baseline fit (blue). Bottom: Time-resolved XMCD recorded at the Co  $L_3$  absorption edge. The dynamics are fitted with a double exponential function (solid line).

We interpret the short-lived appearance of a magnetic contrast in Mn as a sign of coherent spin dynamics resulting in a ferromagnetic alignment of the Mn spins. During the excitation by the laser pulse, the majority spin alignment in Co drives the reorientation of the interfacial Mn spins in the same direction. This reasoning is supported by calculations performed in [120] where exactly this observation is predicted.

A perfect image of the time evolution of the contrast is not obtained in the XMCD due to the low statistics. Nevertheless, the change in contrast is reflected in the data around time zero. The likelihood of an underlying Gaussian profile, as shown in Fig. 5.9 is 3400 times higher compared to a line fit. Using only the peak value at time zero, "only" a 108 times higher likelihood is found for a Gaussian compared to a baseline. Together with the excited dynamics presented in Fig. 5.8, a confident assignment of the contrast is possible, and it is ruled out that the point is an artifact of the measurement. Judging from the pumped channels in Fig. 5.8 the ferromagnetic alignment is present longer and the lifetime estimation of the excited

state from the XMCD is a lower bound. However, the estimation of the lifetime, that the state lives only for the duration of the excitation, is in agreement with the timescale for decoherence due to spin-orbit coupling [202], the theoretical predictions in [120], and the observation of OISTR in Ni/Pt [149]. A negative contrast change in the Mn XMCD is observed around 1 ps delay time which the OISTR mechanism can not explain. Comparing the dynamics of the individual channels to the evaluated XMCD, it is apparent that this contrast change happens during a time when electronic and also phononic excitation are already visible. We argue that the appearance of the contrast at 1 ps is distinctly different from the one at 0 ps due to the longer delay time. While phononic modes can not be excited within 100 fs, they might act at 1 ps by magnetostriction on the observed dichroism and can result in such a change of the contrast. The rise in overall intensity is an indication of layer expansion or compression, resulting in an overall changed reflectivity profile [203, 204] therefore implying the existence of (coherent) phonons in the system. The initial rise in magnetic contrast is also accompanied by a rise in intensity in both channels. However, this cannot be explained by phonons. The initial increase is described by state-blocking effects that alter the X-ray scattering properties and lead to an overall increase in the signals. This increase is a result of the electronic transitions driven by the excitation. Therefore, this is precisely the timescale of the OISTR, which treats the electronic transitions between atomic sites. This excitation decays quickly as the electronic population in the system reacts to the strongly non-equilibrium state.

The underlying mechanism is explored by TDDFT calculations, carried out by S. Sharma, where the system is compared to a 3 ML Co/2 ML Mn system [201]. We chose to compare the observation to this system due to the absence of a recognizable XMCD at negative delay times. Statically, a small dichroism of around 1.5 % is observed, which is below the resolution of the time-resolved measurements. In a perfect layerwise antiparallel orientation of the three-layer system, a larger XMCD in Mn is expected. However, surface roughness and intermixing at the interface reduce the net magnetization in the Mn layers. Therefore, a better agreement with the 2 ML Mn system is found. The calculations support the mechanism already introduced in section 3.3 and the result shown in Fig. 5.1 for the 2 ML Mn system. The optical excitation by the laser pulse drives a charge transfer between neighboring Mn and Co sites. While no net charge is transferred, a net spin transfer is present due to the oppositely occupied density of states in the Mn atoms and the heavy imbalance of electrons of majority spin character in Co. The spin injection from Co leads to a change of the local atomic moment in the Mn atoms, thereby reversing their alignment at the interface if the initial spin alignment was antiparallel with respect to Co. In the two-layer system, this results in an appearance of a magnetic contrast in Mn due to the transient ferromagnetic spin alignment. An illustration of the process is reprinted from [201] in Fig. 5.10. This is similar to what is observed in the experiment and shown in Fig. 5.9. The appearance of the magnetic contrast in Mn happens at a timescale where no sizable change of the magnetization in Co is observed. The demagnetization channels like Elliot-Yafet scattering [54] and superdiffusive transport [119] happen on longer timescales during the thermalization and relaxation of the excited electrons.

### 5.3 Summary and Conclusion

To investigate the OISTR effect in a Co/Mn system like the ones calculated in [120], multilayer Co/Mn samples are grown with alternating Co and Mn layers. The sample investigated is a (3 ML Co/3 ML Mn) $\times$ 6 sample grown on Cu(001) and capped with 14 ML of Co to prevent ox-

idation in the Mn layers. Time-resolved resonant magnetic X-ray reflectivity is recorded on the Co and Mn  $L_3$  edge before and after excitation by a 60 fs laser pulse. While in Co, the magnetic contrast reduces after excitation, a sharp rise in magnetic contrast at time zero is measured in Mn. We attribute this increase in magnetic contrast to the OISTR effect leading to a transient realignment of the Mn spins. During the presence of the light field, spin is injected into the interface Mn layers from Co by direct optical transitions of majority carriers from Co. This intersite spin-transfer results in a transient ferromagnetic alignment of Mn illustrated in Fig. 5.10. The recorded data, albeit with low statistics, reveals a mechanism changing the magnetic alignment of an elemental antiferromagnet into a transient ferromagnet. The results are published in [201].

This finding is a verification of the importance of coherent photon-electron dynamics acting at the earliest timescale, the timescale of the exchange interaction itself, in light-induced magnetization dynamics. The OISTR process, also experimentally studied in [149–152], is further validated by our results. Lastly, the identification of the OISTR process in heteromaterials such as AFM/FM multilayers might lead to novel device concepts like ultrafast spin-valves.

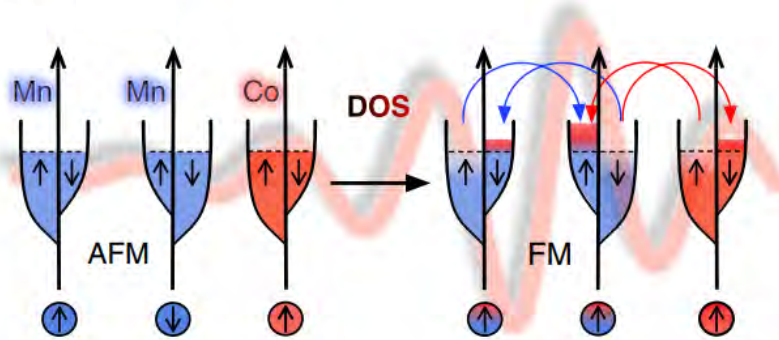


**Figure 5.10:** Schematics of the OISTR process in the 2 ML Mn system coupled to Co. The light-induced transitions between opposite Mn sites lead to an equilibration of the spin population in the oppositely aligned Mn atoms. The Co atoms lead to a surplus of majority carriers, creating an imbalance in the population, and therefore to a transient ferromagnetic state in Mn. Reprinted with permission from Ref. [201]. Copyright (2021) by the American Physical Society.

The conclusion about the magnetic state in Mn and Co, presented in this chapter, relies on information obtained resonantly in XRR. The magnetic contrast measured in time-resolved experiments is not always unambiguous, see section 2.1.3. For that reason, the next chapter is dedicated to the discussion of the extent RMXR can be employed to derive the magnetic state of a system.

## Chapter 6

# Light-induced magneto-optics in the soft X-ray range

So far, the experimental investigations presented in this thesis employ resonant magnetic X-ray reflectivity (RMXR) as the primary tool to trace the magnetization dynamics in ferromagnets after excitation by light. Using synchrotron radiation to generate fs X-ray pulses offers the unique possibility to address the information about the magnetic state in each involved element selectively by tuning the energy to the respective absorption edge. In this photon-electron interaction, information about the magnetic state of the system is contained, see section 2.2.3. However, in X-ray reflectivity, where not only the absorptive features are detected, the magnetic contrast, recorded as an intensity change of the reflected light, depends significantly on the angle and the energy employed. Using the same energy but different angles can lead to a vanishing of the contrast or a reversal in sign thereof, for example, at 778 eV in Fig. 5.3. Similarly, using the same angle but tuning the energy across the absorption edge can lead to the same result, see Fig. 5.6.

This dependence complicates the interpretation of RMXR especially concerning conclusions about the absolute magnetic state of a system, and comparisons between measurements have to be carried out with care. The issue is further complicated in time-resolved measurements where the intrinsic properties that govern reflection and absorption, i.e., the magneto-optical constants introduced in section 2.2.3, also change upon excitation. Of course, this is also true in absorption experiments. However, it is easier to disentangle magnetic and electronic properties by directly correlating transient changes in the absorption to the electron population after excitation. A complete picture of the electronic and magnetic state could be obtained in XRR, for example, by recording complete transient spectra to calculate back the magnetic and electronic properties. The condition of the complete spectra is somewhat relaxed in time-resolved measurements due to the considerable energy broadening of the ultrashort pulses that entail that the recorded intensity is already representative for large parts of the spectrum. Since the required time to record a complete spectrum for each delay step is too large, we simulate the sum and difference signals obtained at the finite energy window in the time-resolved measurements. In the following, numerical simulations of the reflectivity spectra in static and non-equilibrium conditions are presented. The chapter aims to obtain an understanding of the intensity changes in dichroic time-resolved experiments.

## 6.1 Simulations of the X-ray reflectivity

We start the chapter by looking at examples of the recorded XRR spectra presented so far. The aim is to simulate the reflected spectra recorded in static dichroic X-ray measurements. We have obtained spectra for Co, Mn, and Ni in the discussed experiments from several angles. The spectra are calculated by *udkm1Dsim*, using the sample geometries and magneto-optical constants evaluated from dichroic X-ray absorption spectra. First, the magneto-optical constants  $\delta + \Delta\delta$  and  $\beta + \Delta\beta$ , see eq. (2.55), are presented.

The imaginary part of the magneto-optical constants, i.e.,  $\beta + \Delta\beta$ , describes the wavelength-dependent absorption. Its value is evaluated using spectra obtained by recording the TEY for opposite magnetization directions in the Co samples investigated at the VEKMAG endstation. An example for Co recorded in the Co/Mn multilayer sample is shown in Fig. 6.1.

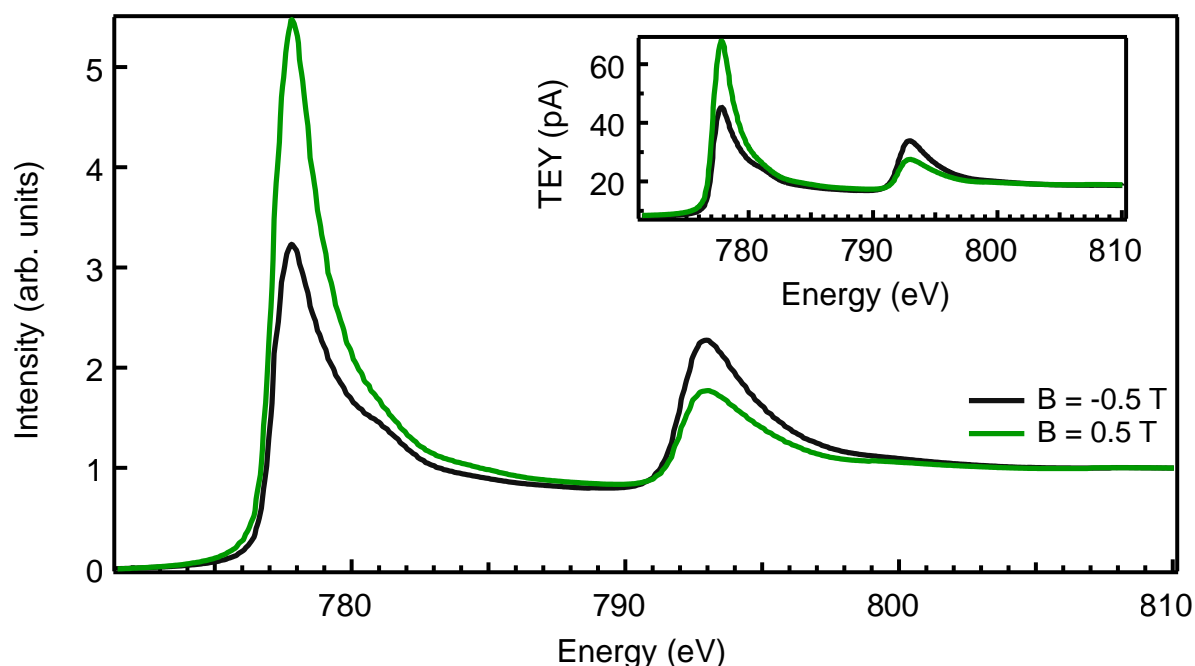


**Figure 6.1:** X-ray absorption signal over photon energy, recorded in the Co/Mn multilayer sample described in the previous chapter. The signal is obtained from TEY, shown in the inset, by normalizing the signal to the edge jump.

Since the measurement does not yield the absolute value of  $\beta$  or  $\Delta\beta$ , the curves are compared to the X-ray attenuation values tabulated in the literature. First the atomic form factors  $f_1$  and  $f_2$  (called  $F'$  and  $F''$  in section 2.2.3) are evaluated by scaling the edge jump of the spectra to that recorded in the literature. Here, we use the values by C.T. Chantler [205] made available by S. Seltzer [206]. Furthermore, we use the Henke values [207] that are made easily accessible by E. Gullikson [208] to compare the optical constants. The edge jump, measured in TEY, is scaled to the tabulated values of the atomic form factor, shown in Fig. 6.2. The real part is obtained from the form factor, shown in Fig. 6.2 on the left side by calculating the KKR. It should be noted here that the Henke convention for the definition of the form factors is employed, i.e.,  $f_1 = Z + F_1(E)$  and  $f_2 = F_2(E)$  with the atomic number  $Z$ .

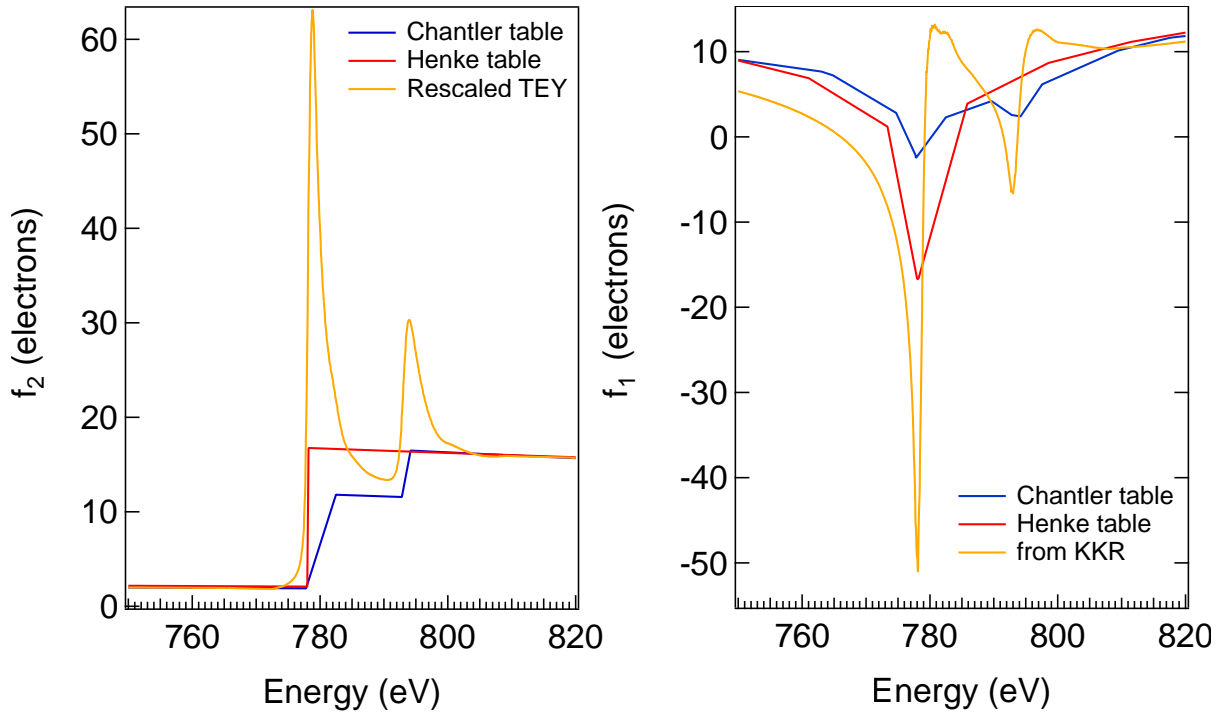


**Figure 6.2:** Recorded absorption scaled to the tabulated attenuation of [205]. By merging the experimental curve with the tabulated values the form factor covering a large energy window around the resonance is obtained (left). This is necessary to calculate the real part from the KKR (right). For comparison, the values contained in the Henke tables [207] are shown, too.

The magnetic contribution is calculated as the difference  $\Delta$  when performing the abovementioned steps for the spectra with opposite magnetization. The non-magnetic part is considered to be the average between the two. Furthermore, the magnetic contribution is affected by the incident angle and the degree of polarization of the X rays. This is taken into account by scaling the difference with  $\Delta = \Delta_0(\cos(\theta)\sigma)^{-1}$  for in-plane magnetized samples, with the angle of incidence  $\theta$  with respect to the surface, and the degree of polarization  $\sigma$ . The magneto-optical constants  $\delta$  and  $\beta$  are calculated from the form factors, see eq. (2.50). The constants obtained for Co are presented in Fig. 6.3. For Mn, two sets of constants are used, one for the case where a small dichroism is observed and one where Mn is completely antiferromagnetic and no XMCD is observed. The resulting magneto-optical constants for Co, Ni, and Mn are presented in Fig. 6.3, 6.4, 6.5, respectively. Since the optical constants and the form factors are only different by a factor, both descriptions are equal. The programs used in the following employ either the magneto-optical constants or the form factors as inputs, which is why both are evaluated here. We now calculate the X-ray reflectivity for different angles at fixed energy using the optical constants. We use *udkm1Dsim* [188] to simulate the reflected intensities. The software calculates the magneto-optical field propagation described in [24, 33] or specifically for X-rays in [34], with the sample geometry, the light properties, and the magneto-optical constants as inputs. The results are presented in Fig. 6.6.

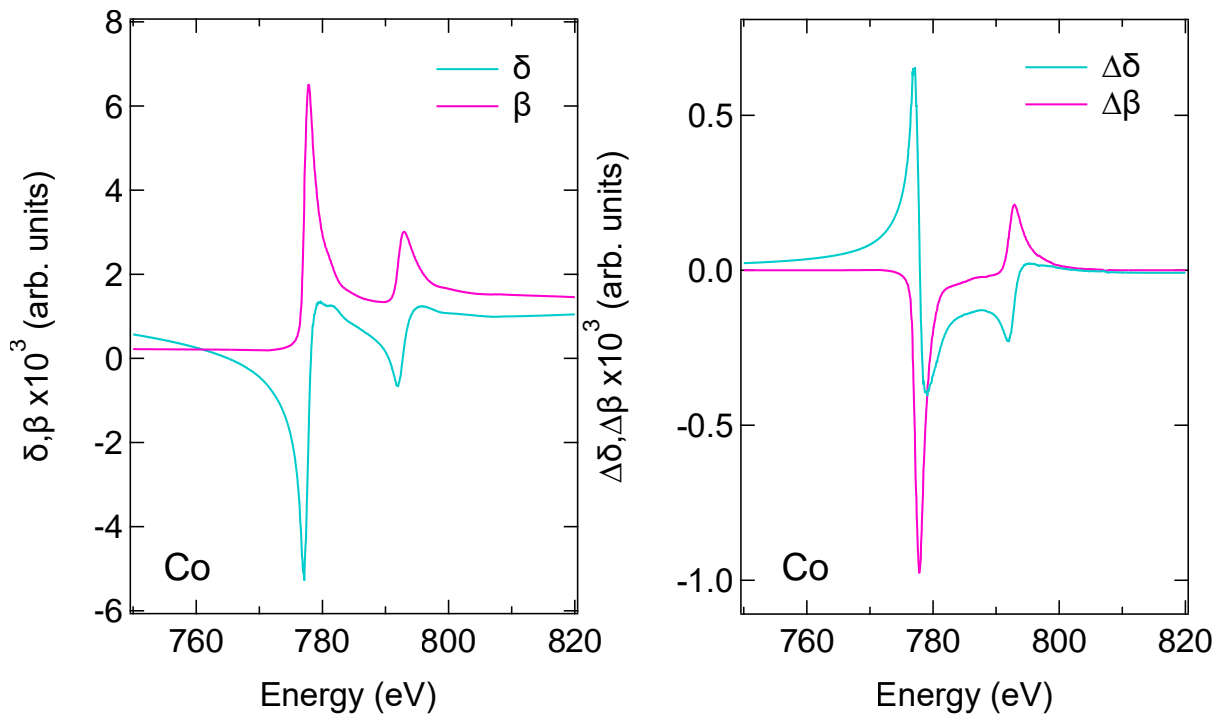


**Figure 6.3:** Left: Evaluated  $\delta$  and  $\beta$  for the Co L<sub>3,2</sub> resonance. Right: Evaluated  $\Delta\delta$  and  $\Delta\beta$  for the Co L<sub>3,2</sub> resonance.

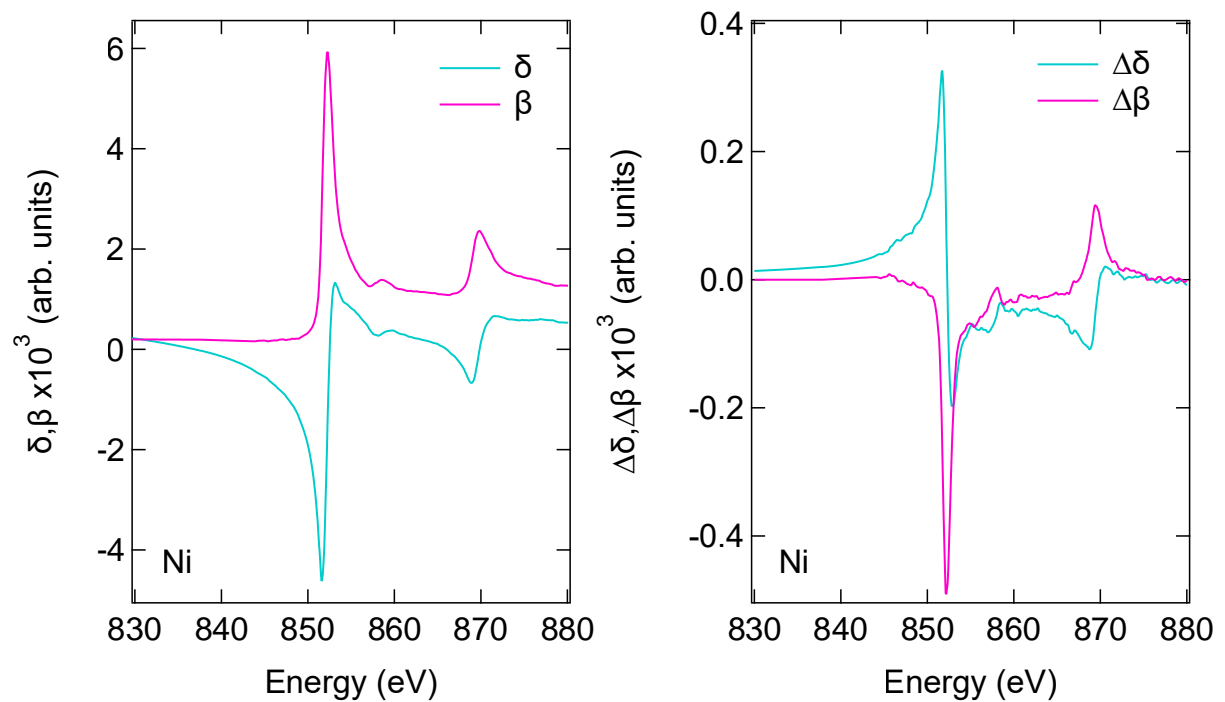


**Figure 6.4:** Left: Evaluated  $\delta$  and  $\beta$  for the Ni L<sub>3,2</sub> resonance. Right: Evaluated  $\Delta\delta$  and  $\Delta\beta$  for the Ni L<sub>3,2</sub> resonance.

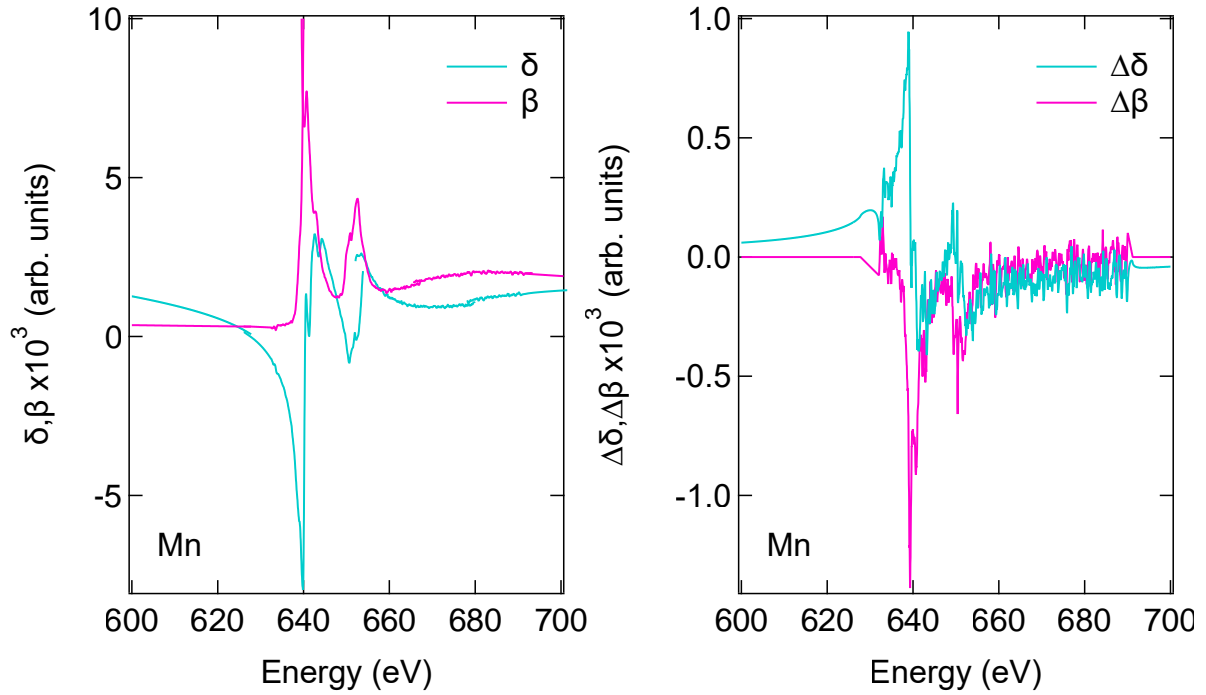


**Figure 6.5:** Left: Evaluated  $\delta$  and  $\beta$  for the Mn  $L_{3,2}$  resonance. Right: Evaluated  $\Delta\delta$  and  $\Delta\beta$  for the Mn  $L_{3,2}$  resonance.

The layer distances in the simulation are slightly adjusted for better agreement with the experimentally recorded reflectivity scans. The OISTR sample is simulated satisfactorily using the layer thickness expected from the growth and calibration. A slight increase in the layer thickness in Co from 3.0 ML to 3.3 ML and in Mn from 3.0 ML to 3.2 ML further improves the agreement with the recorded data. In the reflectivity curves presented in Fig. 6.6 for the OISTR sample, the recorded intensity oscillations are less pronounced compared to the simulations. Individual layer changes are not considered, i.e., all Co layers are treated equally, and similarly, all Mn layers are considered to be the same. An excellent agreement is achieved if one allows for individual changes and surface roughness. Since we have no means to double-check the parameters, we do not fine-tune the layer thicknesses and interface roughness. The simulation of the bilayer sample reveals that a much higher cap layer thickness than expected is needed to reproduce the reflectivity curves. The best agreement for the Cu/Co/NiMn sample is obtained for 60 ML Cu instead of the expected 20 ML. The result is most likely accurate since we do not have the means to monitor the Cu deposition directly. Furthermore, the Cu layer acts as the capping layer and has probably oxidized during transport resulting in a larger lattice spacing of the CuO layer. The same is true for the Cu/Ni/NiMn sample, where 160 ML of Cu are needed for a decent fit of the reflectivity.

Having the simulated reflectivity scans used to clarify the sample geometry, we calculate the spectra across the  $L_{3,2}$  resonance of the materials employed. The spectra are now calculated for the dichroic case, i.e., for opposite light helicity, to compare the measured and simulated magnetic contrast. Example spectra in Co and Mn, recorded and simulated in the OISTR sample, are shown in Fig. 6.7. Although the simulated spectra do not consistently reproduce the recorded ones perfectly, an excellent qualitative agreement is achieved. It can already be judged from Fig. 6.6 that under several angles the intensity is not described perfectly. Nevertheless, the overall intensity change with the angle and the energy, at least at an incident angle range

between  $7^\circ$  and  $15^\circ$ , is reproduced.

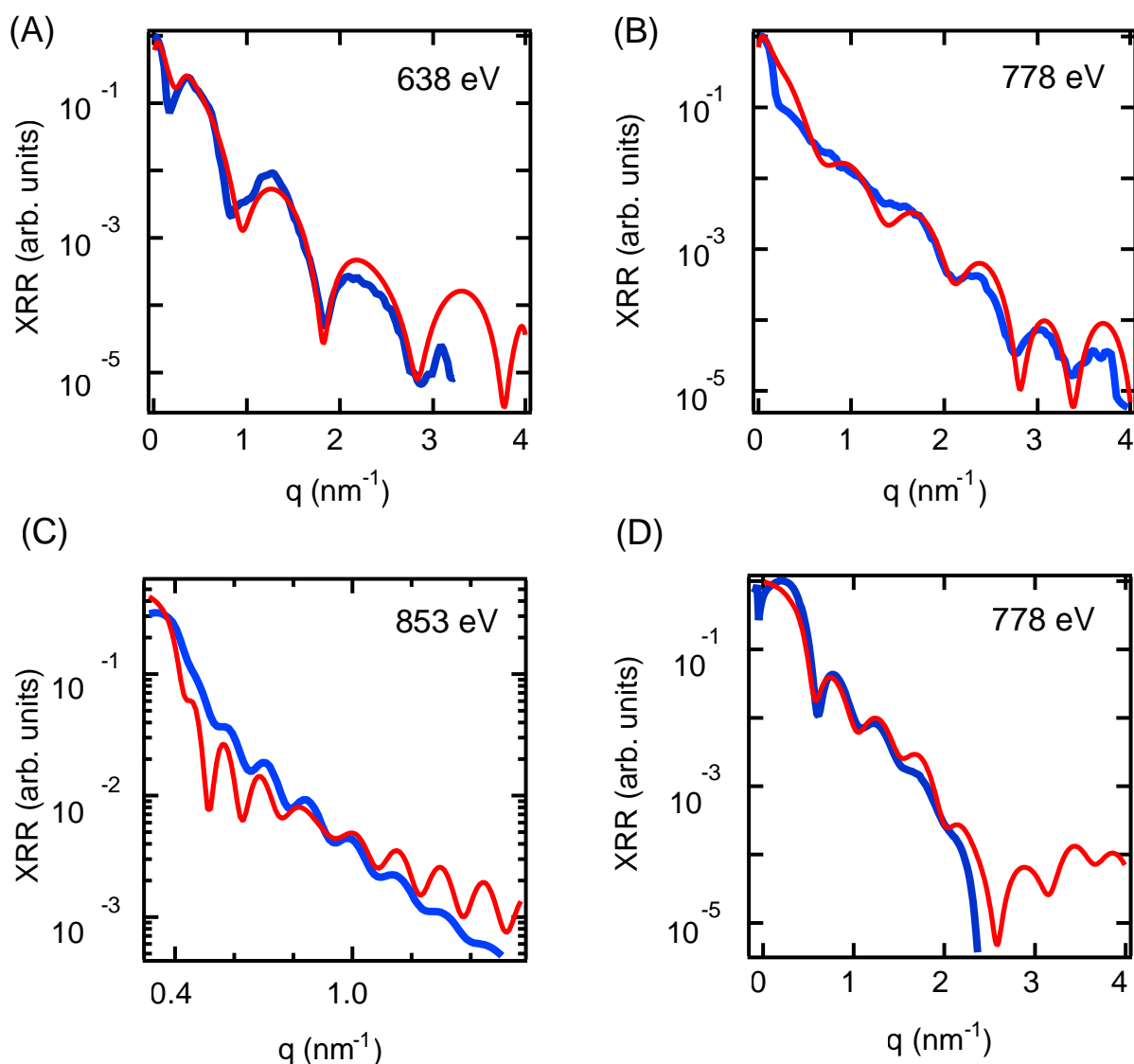


**Figure 6.6:** (A) Recorded (blue) and simulated reflectivity (red) at 638 eV in the OISTR sample. The recorded intensity is recovered in the simulation using the optical constants obtained from TEY spectra and a slightly increased layer thickness of 3.3 ML and 3.2 ML for Co and Mn, respectively. (B) Experiment (blue) and simulation (red) of the reflectivity at 778 eV of the same sample as in (A). The same parameters are used for the simulations as in (A), only a different photon energy is employed. (C) Experiment and fit for the reflectivity in Ni, recorded in the Ni/NiMn bilayer sample described in section 4.1.1. The simulation shows that the cap layer is larger than expected, and a thickness of about 160 ML leads to a decent agreement with the experimental curve. (D) Measured reflectivity (blue) and simulation (red) at 778 eV in the Co/NiMn bilayer sample described in section 4.1.1. The top Cu layer thickness is increased to 60 ML to reach a decent match.

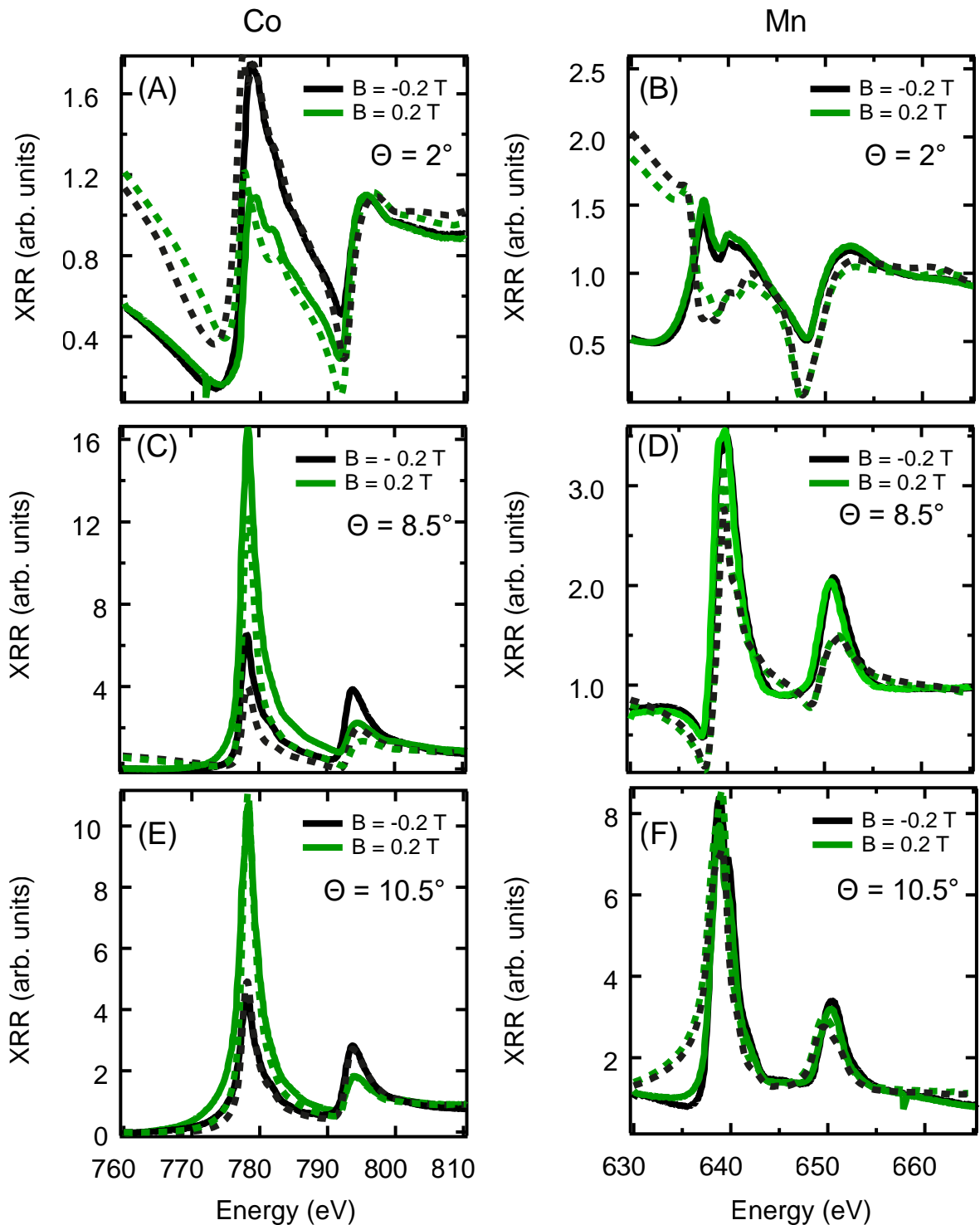


**Figure 6.7:** Recorded (solid lines) and simulated dichroic spectra (dashed lines) measured at the Co and Mn  $L_{2,3}$  resonance in the OISTR sample. (A), (C) and (E) show the measured and the simulated spectra under  $\theta = 2^\circ$ ,  $\theta = 8.5^\circ$ , and  $\theta = 10.5^\circ$ , respectively. All curves are normalized to the post-edge intensity. In (B), (D), and (F) the spectra recorded and simulated on the Mn edge are presented. Although the curves are not perfectly matched, a decent qualitative agreement between the simulation and the experimental spectra is obtained. The spectra recorded at  $\theta = 2^\circ$  seem to be affected the most by inaccuracies in the optical constants or the measurement geometry.

The recorded and simulated reflectivity spectra do not always resemble the recorded absorption spectra. The real part of the refractive index alters the overall energy dependence of the reflected intensities. We estimate the contribution of the real and the imaginary part of the refractive index to the reflected intensity by simulating spectra with either one set to zero. The spectra using the magneto-optical constants evaluated from the experiment as described before are compared to the two extreme cases of  $\delta = 0$  and  $\beta = 0$ . The spectra for several arbitrarily chosen angles are shown in Fig. 6.8, the same calculation for selected energies and an angle range from  $2^\circ$  to  $15^\circ$  is shown in Fig. 6.9. 2D images of the spectral evolution with the angle of incidence are shown in Fig. 6.10.

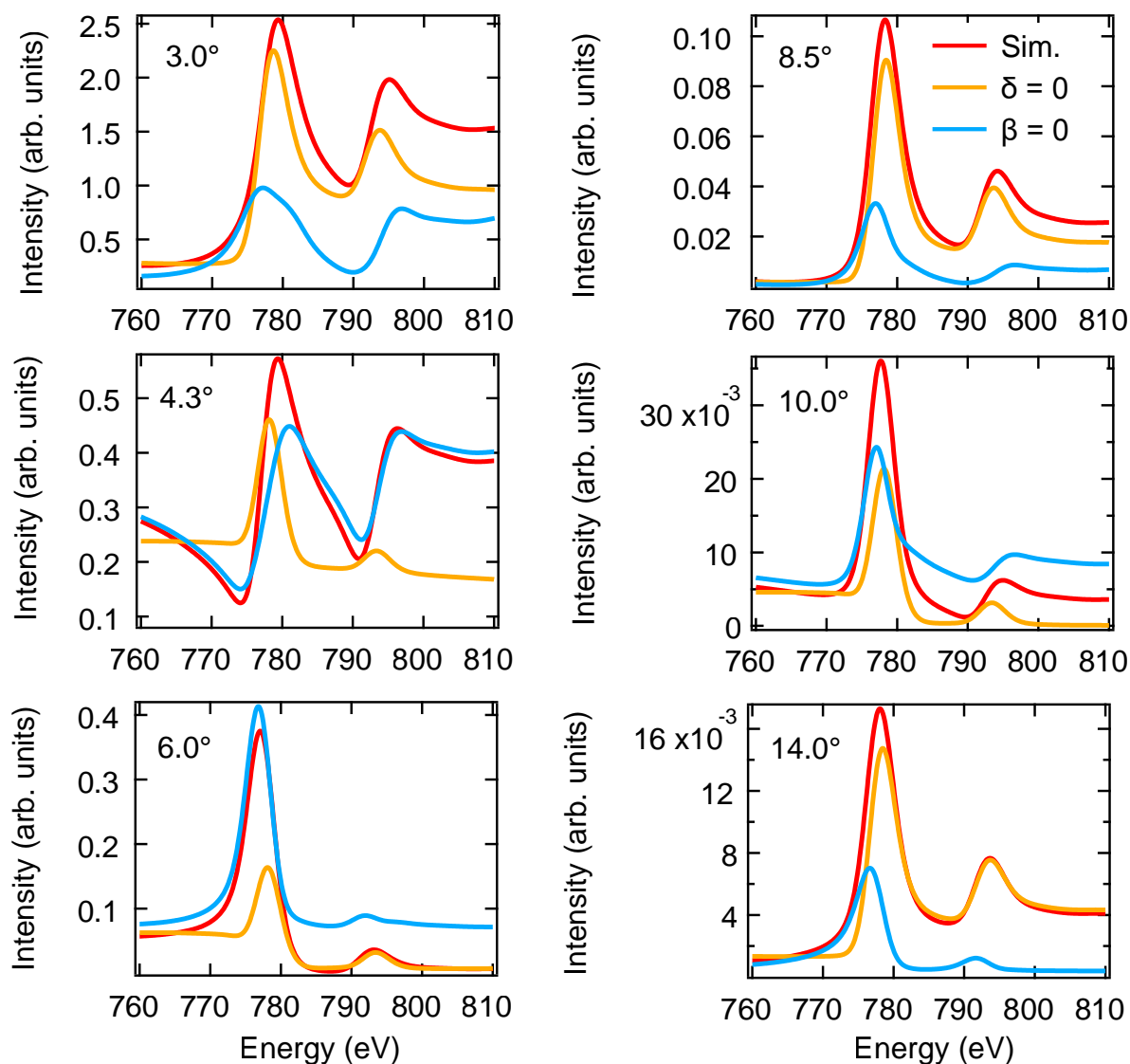


**Figure 6.8:** Simulated reflectivity spectra for different angles of incidence as indicated in the panels. At each angle, the simulated spectrum (red) is compared to a simulation with the imaginary part of the optical constants set to zero ( $\beta = 0$ , blue), and one with the real part set to zero ( $\delta = 0$ , orange). Only considering  $\beta$  or  $\delta$  does not reproduce the spectral reflectivity for any angle. However, at certain angles, for example,  $3.0^\circ$  and  $8.5^\circ$ , shown here, the absorption dominates the spectrum. At other angles, for example,  $4.3^\circ$  and  $6.0^\circ$ , the real part describes the resonance well.

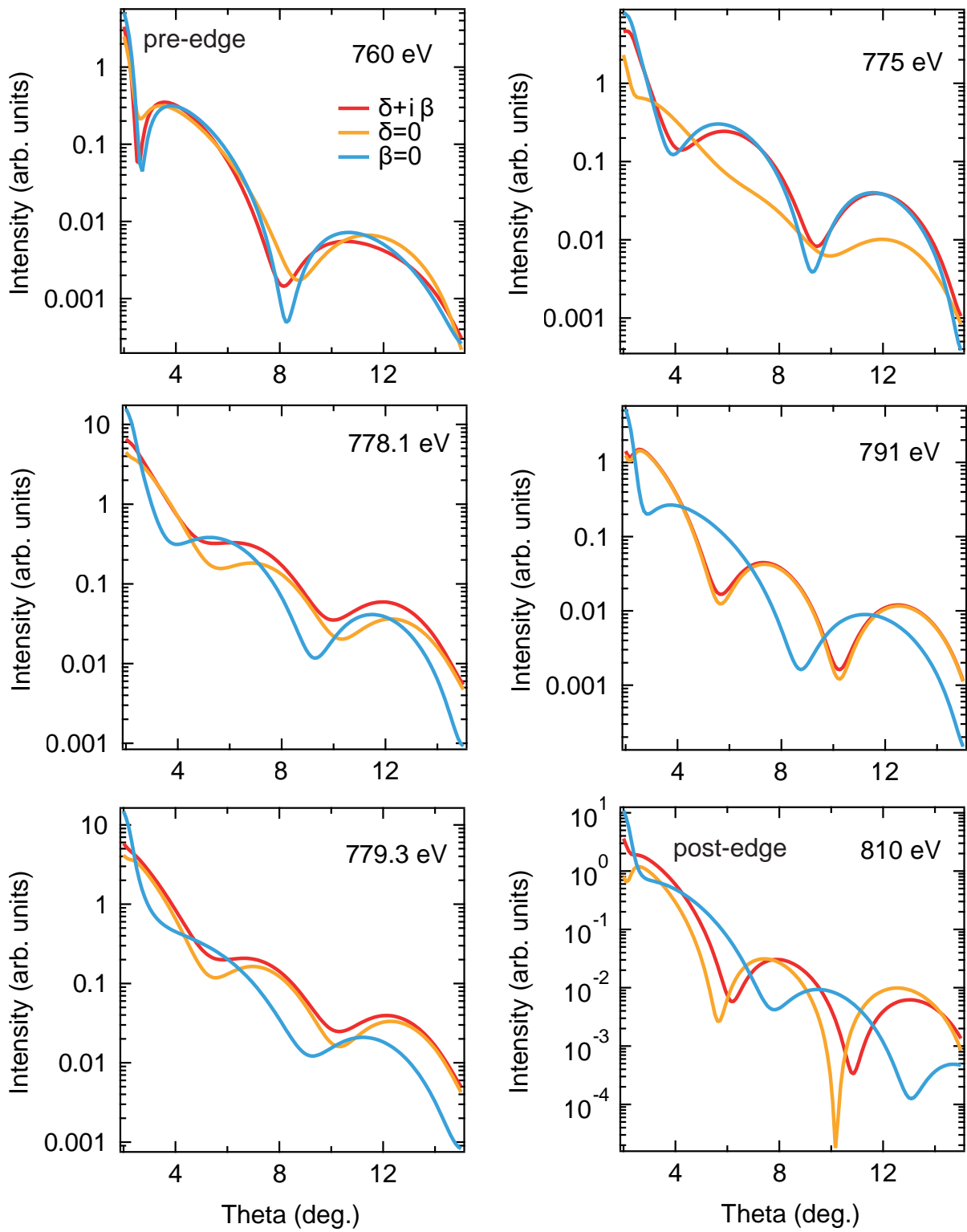


**Figure 6.9:** Simulated reflected intensity for selected energies across the Co  $L_{3,2}$  absorption edges from  $2^\circ$  to  $15^\circ$ . The reflected intensity is calculated with only the real part (blue), only the imaginary part (orange), and compared to the complete calculation (red).

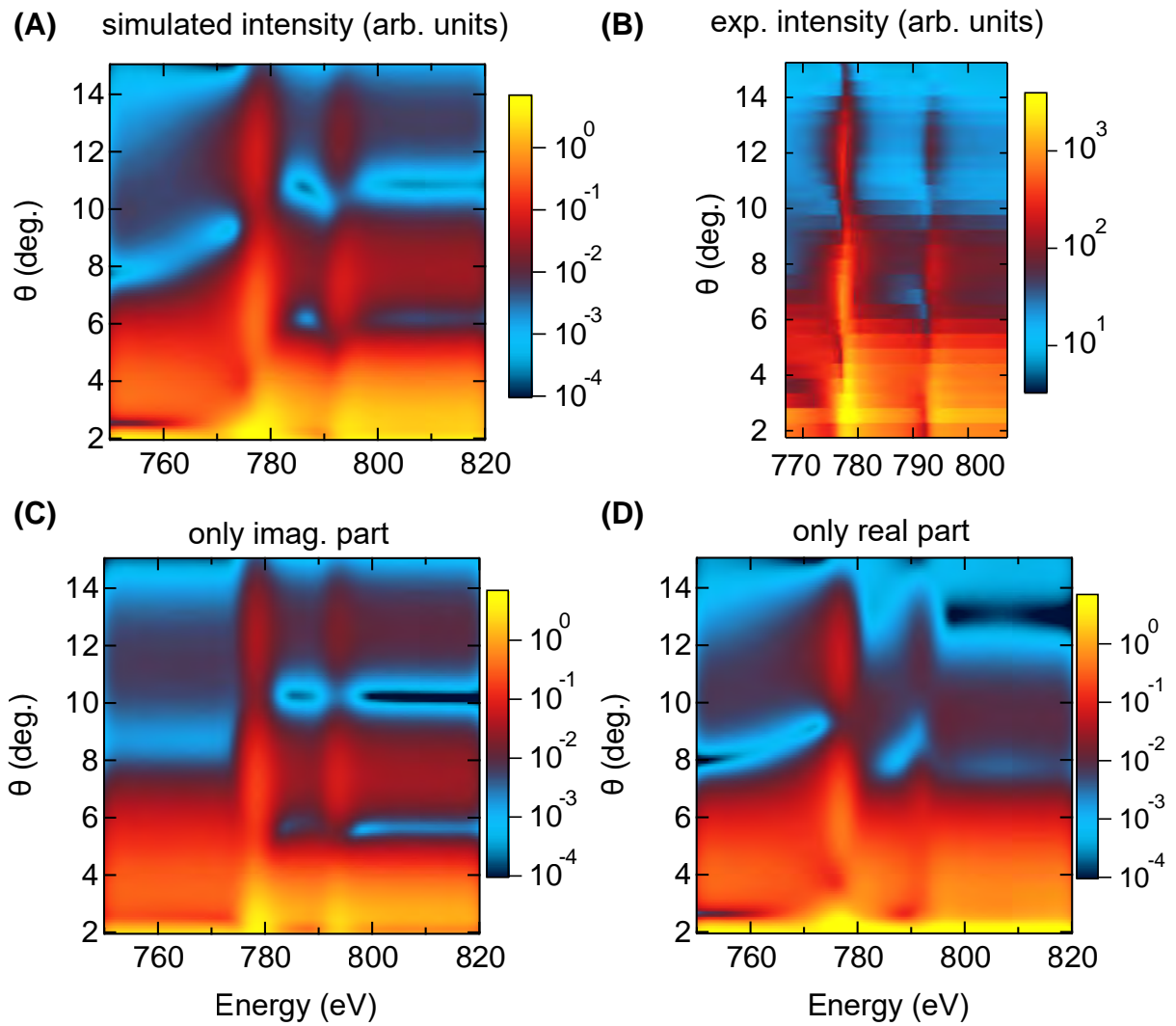


**Figure 6.10:** (A) Simulated reflected intensity for energies around the Co  $L_{3,2}$  absorption edges. (B) Measured reflectivity across the Co  $L_{3,2}$  absorption edges. (C) Simulated partial reflectivity with the real part of the optical constants set to zero. (D) Simulated partial reflectivity with the imaginary part of the optical constants set to zero.

At some angles,  $\theta = 4.3^\circ$ , for example, as shown in Fig. 6.8, setting the imaginary part to zero does not result in a significant qualitative difference between the simulated spectra when compared to the spectrum simulated with the complete refractive index. We interpret this as an indication that the spectrum is largely described by the real part of the optical constants. At  $\theta = 8.5^\circ$ , the difference in the simulated spectra using the full refractive index and using  $\delta = 0$  is quite small. This is interpreted as a sign that the imaginary part dominates the spectrum under this angle. Therefore, an estimation of the contribution of either constant is difficult and strongly depends on the angle of interest. However, a general trend toward a more absorption-dominated reflectivity with higher incident angles is observed in the simulations. This is still very much dependent on the angle, and, for example, at  $10^\circ$ , which is already a relatively high angle of incidence, the spectrum is still largely influenced by the real part. Nevertheless, an estimation derived from comparing the spectra, and the examples presented in Fig. 6.8, is possible. In the range between  $3^\circ$  and  $14^\circ$ , we derive the following rule: If the pre- to post-edge intensity ratio is greater than one, the spectrum is largely dominated by the real part. In

case the pre- to post-edge ratio is smaller than one, as it is in absorption spectroscopy, the absorption features dominate the reflected intensity. The angles at which either part dominates depend on the sample structure and the photon energy employed for probing. Judging by the angle dependence of the intensities shown in Fig. 6.9 and the 2D log plots of the reflected intensity in Fig. 6.10, the pre-edge energies are largely accounted for using only the real part of the optical constants whereas for post-edge energies the intensity across the simulated angle range is reasonably well described using only the imaginary part. Furthermore, the angles where a decent simulation of the reflectivity is found using only the imaginary part, e.g.,  $3.0^\circ$  and  $8.5^\circ$ , are found close to a maximum of the reflected intensity with respect to the angle. And the spectra dominated by the real part, e.g., at angles  $4.3^\circ$ ,  $6.0^\circ$ , and  $10.0^\circ$ , are located near a minimum of the reflected intensity. Lastly, it should be mentioned that the presented comparison is only an estimation of the contributions in the sense of a local derivative, and the actual reflectivity is, of course, not simply the sum of the two boundary cases.

The distinction between reflection and absorption features is important since it allows a better understanding of the transient features. In case the spectra are dominated by the imaginary part, an interpretation of the pump-induced optical changes derived from the transient reflected intensities in terms of absorption and electronic redistribution is possible. At other angles, i.e., when the real part has a significant influence, the optical response is better interpreted in terms of transient reflection changes.

With a better understanding of the features of the reflected intensities, we want to look at how the simulated spectra change upon excitation by light. The calculated transient spectra are subsequently used to model the recorded time-resolved intensities.

## 6.2 Time-dependent optical refraction

In the description of the simulated light-induced changes, we will, initially, focus on the discussion of thermal processes. The thermal processes encompass the reduction of a macroscopic magnetization by temperature and lattice strain due to thermal expansion and (coherent) phonon population. The first directly addresses the magnetic contrast change, which is ultimately the observable we are interested in. The latter affects the vertical lattice distances and layer thickness and, therefore, the reflectivity properties of the underlying sample. Additional mechanisms induced by electronic transitions that influence the optical response are discussed in the next section.

We work with the already written script in *udkm1Dsim* which calculates the depth-resolved optical absorption for a given laser pulse. Furthermore, a temporal grid is introduced, with which thermal transport over time and, in combination with the already existing underlying spatial grid, sample space is calculated. Furthermore, since ultimately we are interested in the magnetic contrast, a temperature-dependent magnetization is added. The calculation of the magnetization is based on the m3TM, and the simulation is summarized in a set of 3 coupled differential equations containing transport and magnetization. The equations are similar to the ones in [54]. Nevertheless, we repeat them here to ease the discussion about the constants employed.

$$c_e(T_e)\rho \frac{\partial T_e}{\partial t} = \frac{\partial}{\partial z} \left( k_e(T_e) \frac{\partial T_e}{\partial z} \right) - g_{ep}(T_e - T_l) + S(z,t) \quad (6.1)$$

$$c_l(T_l)\rho \frac{\partial T_l}{\partial t} = \frac{\partial}{\partial z} \left( k_l(T_l) \frac{\partial T_l}{\partial z} \right) - g_{ep}(T_l - T_e) \quad (6.2)$$

$$\frac{\partial m}{\partial t} = Rm \frac{T_l}{T_C} \left( 1 - m \coth\left(m \frac{T_C}{T_e}\right) \right) \quad (6.3)$$

The parameters used are the electron heat capacity  $c_e$ , the lattice heat capacity  $c_l$ , the material density  $\rho$ , the thermal conductivity of the electrons  $k_e$  and the lattice  $k_l$ , the electron-phonon coupling  $g_{ep}$ , a material-dependent parameter  $R$  that links the magnitude of magnetization change to the material properties, and the Curie temperature  $T_C$ . The equations couple the electron temperature  $T_e$ , the lattice or phonon temperature  $T_l$ , and the magnetization  $m$ . In the implementation, the coupled differential equations are solved for all  $N$  layers. Therefore, in total  $3N$  equations are solved. The source term  $S(z,t)$ , as mentioned before, depends on the temporal profile of the laser pulse and the layer depth  $z$ .

Most of the parameters are temperature-dependent. Nevertheless, we approximate them as constant or linearly scaling with temperature since their exact dependence is, in most cases, not known. For example, the heat capacity is approximated by a linear function for the most part. In the last section, a more refined heat capacity model is used. Similarly, the electron-phonon coupling is assumed constant for the most part. Again a temperature scaling is evaluated in the last paragraph of this section. Furthermore, the simulation requires the sound velocities, vertical layer distance, and linear expansion coefficients of the materials employed. The parameters used for the simulations are presented in Table 6.1.

Using an 800 nm, 60 fs temporal FWHM, and 48 mJcm<sup>-2</sup> laser pulse, incident at 7° on the OISTR sample, we reproduce the experimental conditions to explore the details of the demagnetization in Co. An illustration of the OISTR sample geometry and the calculated differential

optical absorption is presented in Fig. 6.11. The depth- and delay-resolved electron and lattice temperature is presented in Fig. 6.12. The corresponding magnetization map is presented in Fig. 6.13.

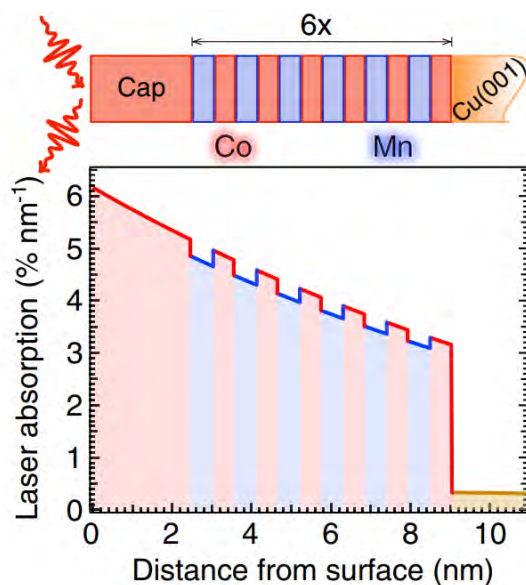


**Figure 6.11:** Schematic of the OISTR sample and calculated optical differential absorption. The optical power is mainly absorbed in the top Co layer and slightly less in Mn compared to the thinner Co layers. Reprinted with permission from Ref. [201]. Copyright (2021) by the American Physical Society.

The calculation reveals that different transient electron and lattice temperatures are reached for the individual Co layers, see Fig. 6.12. Since the source term directly couples to the electron temperature, an initial ultrafast increase in  $T_e$  is seen, and the lattice temperature  $T_l$  lags behind. In Co, the electron-phonon coupling is not as strong as in Ni at ambient conditions [193]. Therefore both temperatures require more than 2 ps to converge, see (C) in Fig. 6.12. The simulation reveals that the lattice in the center of the multilayer system initially heats up faster than the rest. After about 0.7 ps, the top layer becomes the hottest part of the sample in both the electron and the lattice temperature, see (D) in Fig. 6.12. A maximum electron temperature of about 1600 K is reached in the simulation using  $48 \text{ mJ cm}^{-2}$ . The lattice reaches about 900 K in 2 ps. This temperature is likely slightly higher than in reality since we approximate the heat capacity by a linear function. In Co, this will underestimate the required amount of energy for heating, as can be seen in Fig. 6.16. Overall, we expect a transient thermal gradient in the sample in the vertical direction of up to almost  $75 \text{ K nm}^{-1}$ , derived from Fig. 6.12. This thermal gradient translates into a difference in the magnetization across the vertical axis of the sample.

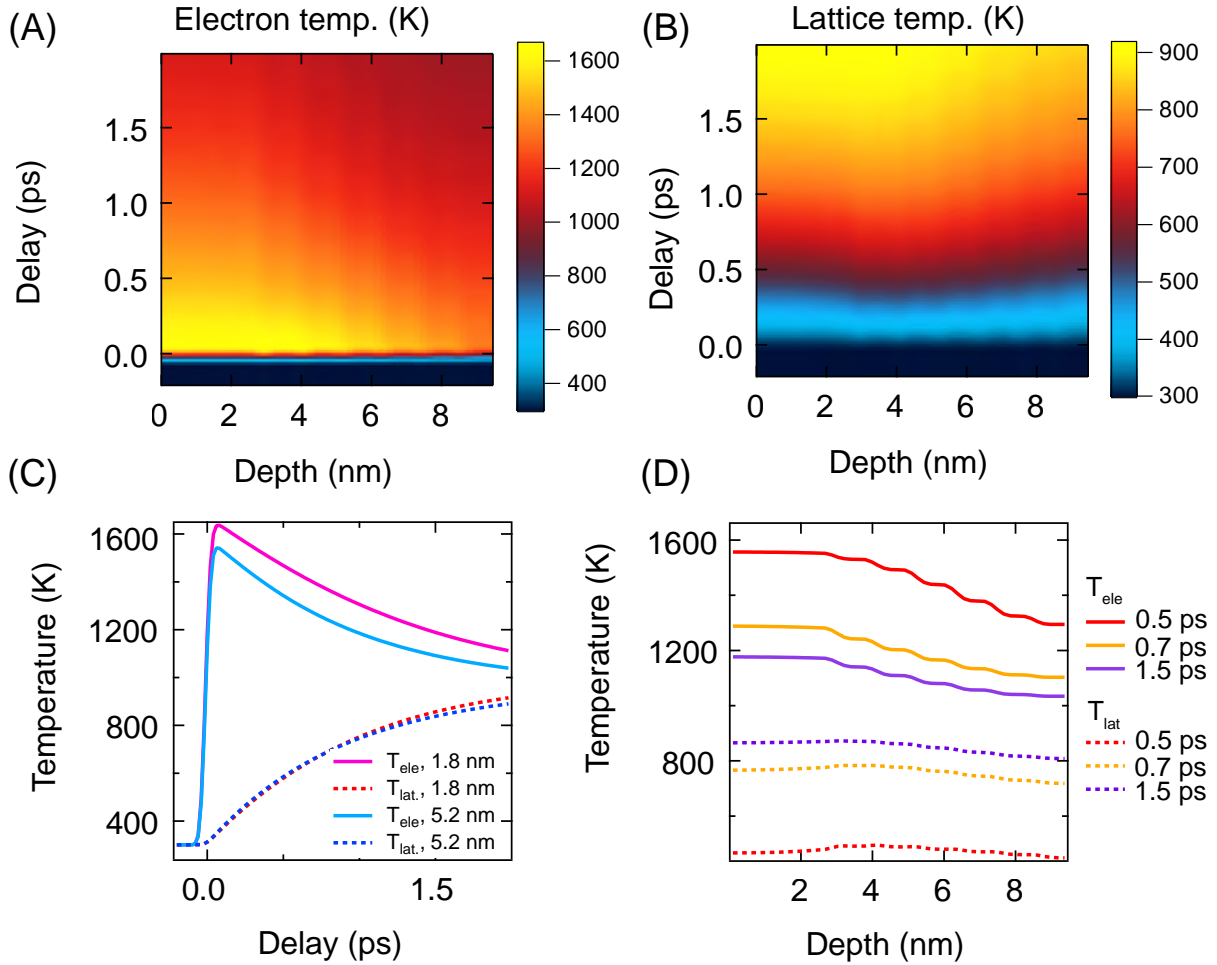


**Figure 6.12:** (A) Electron temperature evolution after excitation with an 800 nm, 60 fs, and  $48 \text{ mJ cm}^{-2}$  laser pulse. The initial temperature change is calculated based on the multilayer absorption profile of the OISTR sample. The maximum temperature increase is found in the top layer, where most of the light is absorbed. Due to heat diffusion, the temperature equilibrates over time. (B) Lattice temperature after excitation. The electron-phonon coupling mediates the temperature exchange between the electron temperature (A) and the lattice. A small difference at early times in the lattice temperature of the Mn and the Co layers is predicted. (C) Example temperature vs. delay time curves, highlighting the difference between the top and the buried layers. (D) Time evolution of the vertically resolved electron and lattice temperature. While the electron and lattice temperatures are initially different, they thermalize after 2 ps.

The demagnetization predominantly happens in the thicker top layer while the buried layers remain in a more strongly magnetized state. Since the magnetization dynamics in Mn, investigated in the previous chapter, happen on much shorter timescales, we exclude the Mn magnetization at this point. This is done artificially by setting its Curie temperature to  $10^5 \text{ K}$ . This effectively leads to no net magnetization change in Mn but allows a fast and easy initialization of the system for computation. Mn remains magnetized, as can be observed in Fig. 6.13. However, this is of no relevance to the simulated dynamics in Co. In the simulation, the magnetization in Co is mainly determined by the temperature of the layer, see eq. (6.3). Of course, the induced demagnetization and thus temperature change depends strongly on the laser fluence. Estimating the fluence employed in the simulation is tricky because the only useful

observable that we have at this point is the magnetic contrast. Therefore, the fluence is adjusted until a decent agreement to the experimental demagnetization is achieved.

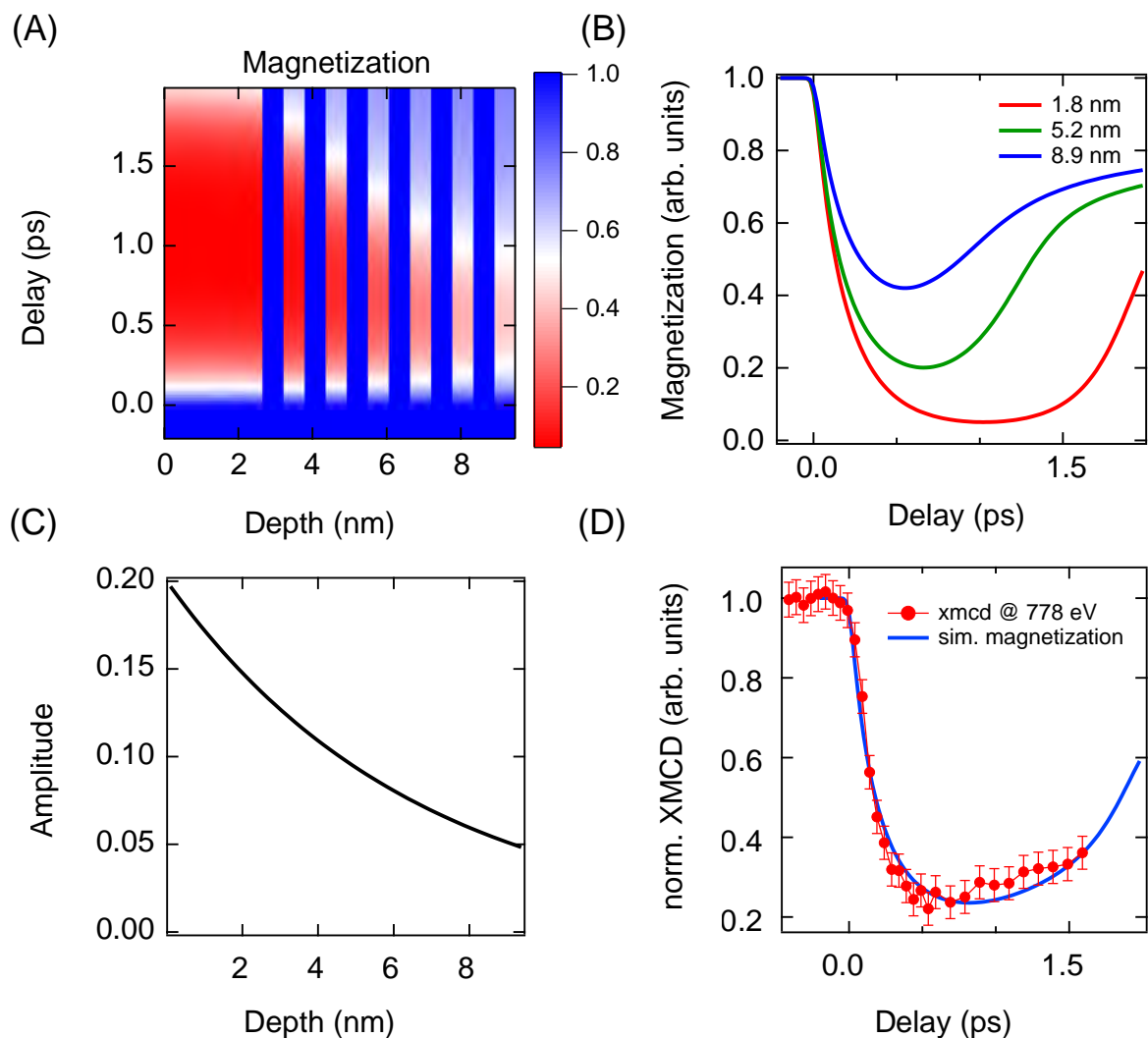


**Figure 6.13:** (A) Magnetization map calculated with the m3TM model using the temperature evolution presented in Fig. 6.12. The Mn layers remain magnetized in the simulation for simplicity. The magnetization in Co is mostly affected in the top layer. (B) Magnetization evolution in different Co layers at a distance to the surface, as indicated in the legend. While the capping layer completely demagnetizes, the buried layers remain magnetized, although with a reduced magnetization, at all times. (C) The exponential weighting used to calculate a magnetization profile of Co that is comparable to the experiment. (D) Simulated demagnetization in Co compared to the experimental curve. Each Co-layer magnetization (A) is summed and weighted by the exponential decay (C) to mimic the reflected X-ray intensity contribution of the top and the buried layers.

However, adjusting the fluence in the simulation to the experiment is not straightforward since the observed X-ray intensity is a combination of reflection and absorption in all present layers. To consider the depth-dependent contributions, an exponential weighting, mimicking the finite X-ray penetration depth in Co, shown in Fig. 6.13, is used. An attenuation length of 6.6 nm

based on the resonant energy is employed, and we normalize the weighting function to be equal to one when summed across the sample distance. A decent agreement of the simulation with the experiment is achieved at a fluence of  $48 \text{ mJcm}^{-2}$  compared to  $12 \text{ mJcm}^{-2}$  used in the experiment. That we have to use a four times higher fluence in the simulation has many possible reasons. Most likely, the actual sample possesses different reflection properties than the calculated ideal surface. Furthermore, the exchange coupling and, therefore,  $T_C$  might be reduced in the thin multilayer films leading to an enhanced demagnetization. Additionally, if the contribution from the surface Co layer dominates the reflected magnetic contrast even more than anticipated, lower fluences also reproduce the experiment satisfactorily.

In the simulation, the magnetization is a function of both space and time, whereas only one intensity over time is measured in the experiment. To resolve the issue of the comparability of the simulation to the experiment, we now calculate the time-dependent spectra of the reflectivity. We employ the same procedure as in the static case and calculate the change in the wavelength-dependent intensity based on the temperature. As mentioned in the beginning, the transient temperature has two effects in the simulation. One is the induced lattice strain which affects the overall reflection. The other is the magnetization change which influences the magnetic contrast in the dichroic calculations.

To illustrate the change in reflectivity induced by lattice strain, the transient angle-resolved intensity, simulated at 778 eV, is shown in Fig. 6.14. Here, the magnetization is held constant to highlight the effect of the lattice expansion. Initially, the thin Co layers are compressed by laser heating and a strain builds from both ends of the multilayer, where either the Co-vacuum or Co-Cu substrate interface is located. After about 1 ps, the strain waves reach the center, and the sample expands. This is followed by damped compression and expansion cycles that persist for several tens of ps. This is not shown in the Figure since we focus on the early times. Following the lattice's coherent expansion (or compression), the X-ray reflection changes. During the expansion cycle, for example, after 2 ps, the reflectivity curve shifts towards lower q-vectors qualitatively, see (B) and (C) in Fig. 6.14. When probing at fixed energy and angle, this results in an overall reduction (or increase) of the intensity depending on the scattering vector employed. The scattering vector in the experiment is about  $1.16 \text{ nm}^{-1}$ . Judging by the close-up shown in (C) in the same figure, the strain should therefore reduce the recorded X-ray intensity. That this is indeed the case is shown and discussed later in Fig. 6.15. The difference in XRR after 2 ps delay time is shown in panel (D) in Fig. 6.14. The strain follows the temperature of the lattice and is, therefore, slower than the magnetization dynamics, which are also affected by the electron temperature. A significant difference in the intensity of the reflected X rays is simulated only after about 2 ps.

Considering this sample change, we now calculate the XRR spectra. Since both angle and energy affect the scattering vector, we approximate the precise scattering vectors in the following calculations of the transient spectra. In other words, we calculate a high point density in the energy, i.e., 1 meV steps, but to save computation time, the scattering vectors are only calculated in  $0.01 \text{ nm}^{-1}$  steps. Compared to a test spectrum with a higher density of points in the q-vectors, no differences are observed from this approximation. To account for the energy broadening of the fs X-ray pulse the spectra are convoluted with a Gaussian of 3.2 eV FWHM.

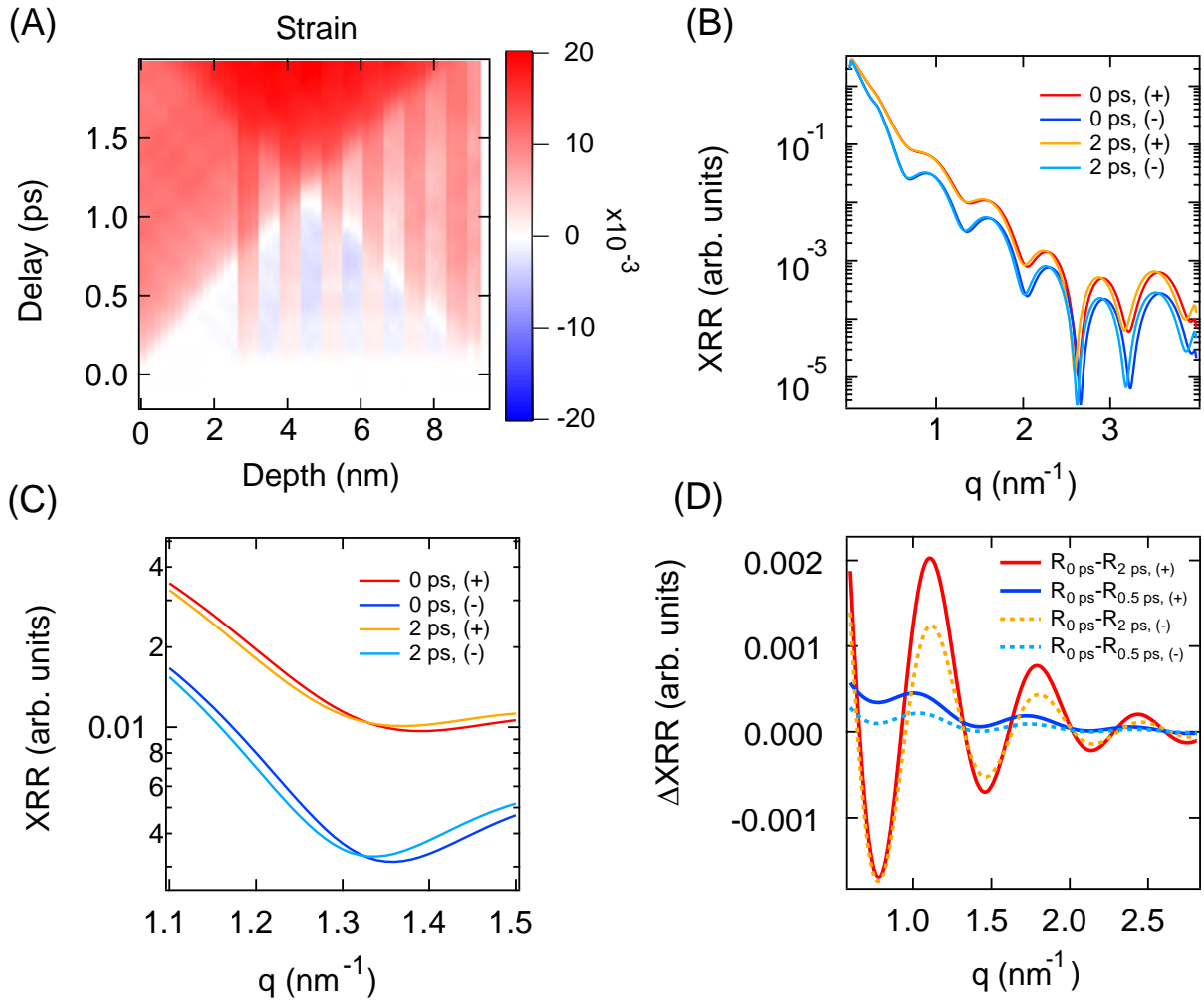


**Figure 6.14:** (A) Strain map calculated from the linear expansion induced by the temperature increase. A positive strain wave is launched from the top and bottom interface of the multilayer stack. On longer timescales, not shown here, the center of the system undergoes alternative phases of contraction and expansion with a period of about 2 ps. (B) X-ray reflectivity at time zero and 2 ps after excitation. No dramatic changes across the reasonable scattering vector range are observed. For a better visibility, the experimentally investigated  $q$ -range is shown in (C). (C) Close-up of the XRR in the vicinity of the investigated energy and angle combination, which spans  $1.12 \text{ nm}^{-1}$  to  $1.22 \text{ nm}^{-1}$ . The minimum in the reflection is shifted towards lower scattering vectors due to thermal expansion. (D) Difference of the XRR at different times compared to time zero.

The evaluated transient XRR spectra are presented in Fig. 6.15. The intensity at the energy of interest is evaluated for each delay point for both helicities to evaluate the magnetic contrast. Consequently, the contrast is evaluated as the asymmetry between the intensities for both helicities. Calculating the XRR directly from the spectra as described reveals that the observed dichroism is dominated even more strongly by the top Co layers, compared to the estimation shown in Fig. 6.13. Using the simulated spectra and calculating the resulting contrast change leads to a better agreement of the simulation with the experiment at  $40 \text{ mJ cm}^{-2}$ . It should be noted that the remagnetization in the simulation is quicker than the one recorded in the experiment.

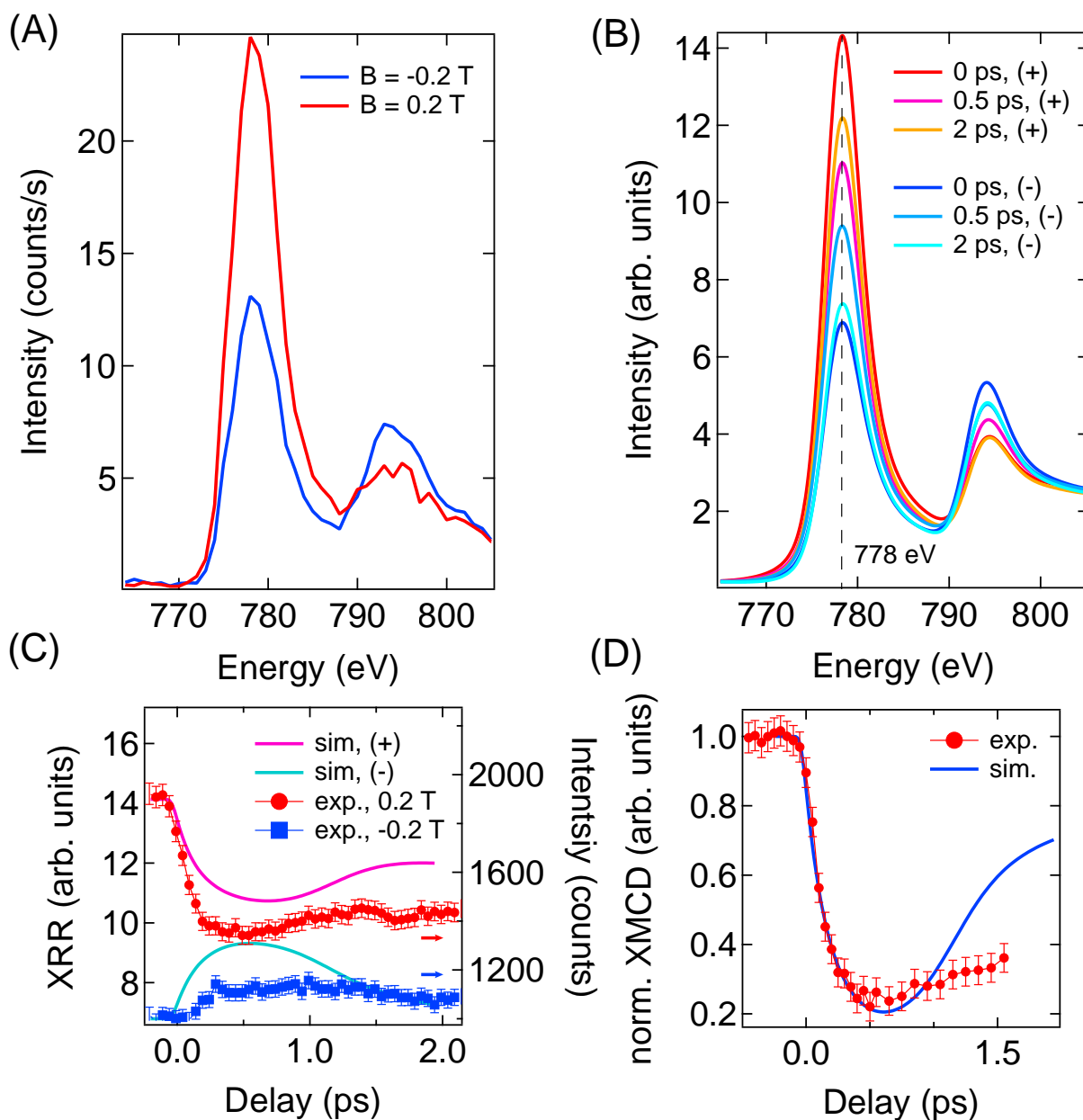


**Figure 6.15:** (A) Dichroic spectrum recorded in reflectivity at an incident angle of  $8.75^\circ$  at the slicing endstation. The ultrashort X-ray pulses are broad in energy which leads to a larger FWHM of the peak compared to the spectra shown in Fig. 6.7. (B) Simulated dichroic spectrum using a fluence of  $40 \text{ mJ cm}^{-2}$ . The spectra change over time due to layer expansion leading to different scattering intensities, see Fig. 6.14, and due to the vanishing magnetization resulting in a quench of the magnetic contrast. The dashed line indicates the 778 eV position. (C) Simulated (lines) and recorded (markers) intensity at 778 eV for the (+) and (-) spectrum over delay time. (D) Evaluated and normalized magnetic contrast of the experiment and the simulation. The magnetic contrast appears to reflect the magnetization of the upper Co layers. A much quicker remagnetization is observed in the simulation compared to the experiment.

For the simulation, we employ parameters found in the literature, see Table 6.1, and only the fluence is adjusted until the simulation matches the experimental demagnetization. For example, a slower remagnetization is simulated when reducing the material-dependent parameter  $R$ .

For the calculations here we employ a value of  $R_{Co} = 19.1 \text{ ps}^{-1}$  compared to  $R_{Co} = 25.3 \text{ ps}^{-1}$  in [54]. This is derived from the lower electron-phonon coupling in Co compared to Ni. In [54]  $g_{ep}^{Co} = g_{ep}^{Ni}$  is used. Reducing  $R_{Co}$  even further results in a significant slow-down also of the demagnetization dynamics, which does not match the experiment anymore. Therefore, the R value employed here is adjusted to match the simulation to the experiment.

The change of reflectivity due to strain and the reduction of the magnetic contrast due to the quench of magnetization lead to an overall reduction of the reflected intensity in the recorded energy range. The non-magnetic change is presented in Fig. 6.14 where the magnetization is fixed, and only temperature-induced strain affects the XRR. The combination of 778 eV and  $8.75^\circ$  correspond to a scattering vector of  $q = 1.16 \text{ nm}^{-1}$ . It is noteworthy that this reduction of the overall X-ray reflectivity due to lattice expansion is not enough to model the observed drop in signal intensity. A comparison between the simulated dichroic time-dependent intensity and the recorded one is shown in Fig. 6.15 in panel (C).

The quench of the magnetic contrast is modeled accurately. However, the simulated channel-dependent signals remain more intense compared to the experiment, see panel (C) in Fig. 6.15 again. This manifests as a sharper drop in the upper signal and a less pronounced one in the less intense channel. Furthermore, an apparent delay is visible in the experimental (-) channel. This delay is not a time delay between start of the dynamics in the two dichroic channels but a result of the competing gain (magnetic quench) and simultaneous loss (lattice expansion) in intensity.

In summary, the experimental demagnetization is reproduced well, as highlighted in Fig. 6.15 (D), while the reduction in both channels, described by the sum of the two channels, is not sufficiently captured. A possible explanation is that the expansion coefficients employed for the simulation are not suited for the ultrafast timescale. However, the temperature change leads to a significant drop in the intensity using the parameters employed, but it is effective only after about 2 ps, see Fig. 6.14 (D). In the experiment, the sum signal decreases simultaneously with the magnetic contrast, leading to the channel dynamics as presented in Fig. 6.15 (C). At delay times longer than 1 ps, the magnetization in the model recovers faster than in the experiment. Since we do not fit most of the parameters, apart from the fluence and, to some extent, the R value, a possible solution is the inclusion of other mechanisms. For example, a temperature-dependent electron-phonon coupling or a better representation of the heat capacity, including the spin heat capacity. The heat capacity of the spin system becomes significant for Co around  $T_C$ . The heat capacity of Cu, Mn, and Co is shown in Fig. 6.16.

In an attempt to improve the simulated magnetization dynamics, we approximate the heat capacity in Co using the sum of a Gaussian and a sigmoid function on a linear background. The approximation, also the linear one, is based on the values in [209]. Furthermore, as mentioned before, we implement a scaling of the electron-phonon coupling with temperature. Since the remagnetization happens too fast in the simulation, the coupling parameter should be reduced at high temperatures. This is most likely the case for Ni [192, 193]. There have not yet been enough studies on Co to have a definite answer on the scaling. The authors of [193] suggest an increase with temperature in the low-temperature regime. However, they also calculate the same scaling in Ni, whereas several other studies cited in the same reference arrive at a different conclusion. Noting this uncertainty, we introduce a linear scaling with the electron temperature to reduce the coupling at high temperatures, leading to a slower magnetic change at elevated temperatures.

Parameter	Mn	Co	Cu
vertical layer distance ( $\text{\AA}$ )	1.71 [210, 211]	1.74 [167]	1.81 [212]
sound velocity (nm/ps)	5.150 [213]	4.720 [213]	3.570 [214]
density $\rho$ (kg/m <sup>3</sup> )	7210 [214]	8860 [214]	8960 [214]
thermal expansion ( $10^{-6}/\text{K}$ )	15 [215]	12 [216]	17 [216]
el. therm. conductivity $k_e$ (W/(m K))	4.8 [194]	78 [194]	361 [194]
lat. therm. conductivity $k_l$ (W/(m K))	3.0 [194]	12 [194]	18 [194]
el. heat capacity $c_e$ (J/(kg K <sup>2</sup> ))	$0.28 \times T$ [209]	$0.6 \times T$ [209]	$0.11 \times T$ [209]
lat. heat capacity $c_l$ (J/(kg K))	495 [209]	693 [209]	350 [209]
el.-ph. coupling $g_{ep}$ ( $10^{18}\text{J}/(\text{s K m}^3)$ )	0.5 [194]	1.2 [193, 194]	0.14 [194]
$R$ (1/ps)	0	19.1	0

**Table 6.1:** Parameters employed for the simulation of the light-induced heating and the coupled magnetization dynamics using udkm1Dsim. The heat capacity employed is derived from [209], made available by *NIST* in [217]. We use a linear approximation for the electronic heat capacity. The electron-phonon coupling for Co is approximated using the theoretical predictions of [193, 194] and the fitted values from [54]. A constant electron-phonon coupling is used since the employed elements' exact temperature dependence is unknown. The material parameter  $R$  should be lower by comparison to [54], given the reduced electron-phonon coupling. However, a too small  $R$  value slows down the dynamics, which does not describe the experiment anymore. Therefore, the parameter  $R$  is estimated by fitting the demagnetization.

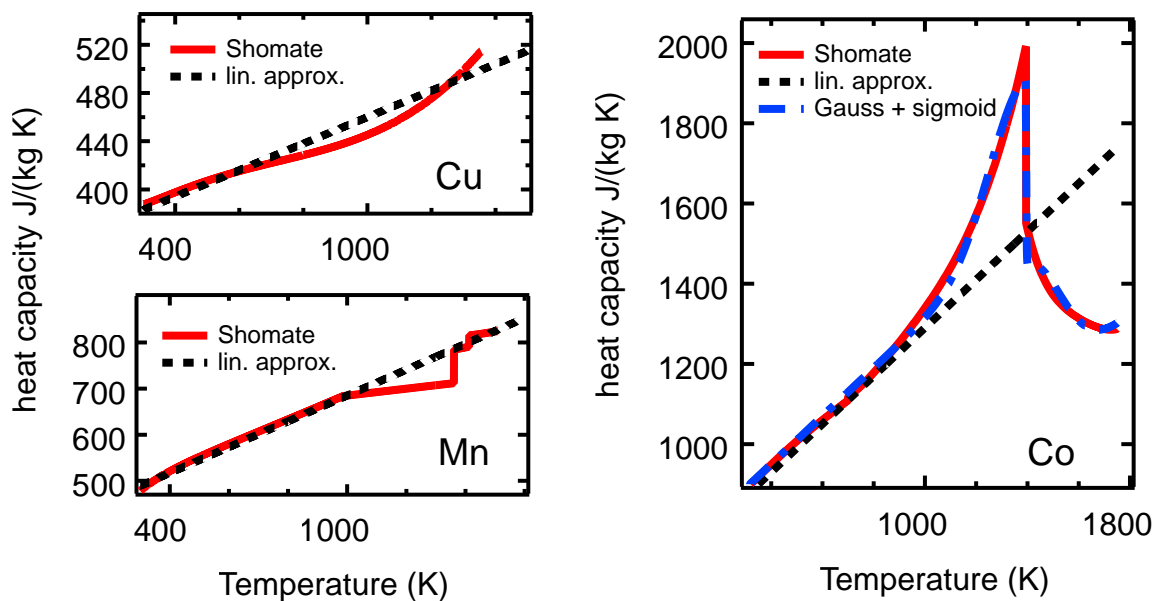


**Figure 6.16:** Heat capacity scaling with temperature for Cu, Mn, and Co. The Shomate equation refers to the polynomial step-wise approximation given by *NIST* [217] based on the experimental values in [209]. The black dashed lines denote the linear approximation used in the equations. Since Co is an elemental magnet, the magnetic phase transition around 1388 K contributes significantly to the heat capacity. To approximate the heat capacity in Co with a continuous function, we use the sum of a Gaussian and a sigmoid on a linear background. The approximation, including the spin heat capacity, is shown as the blue dashed-dotted line, and the details are mentioned in the text.

Using a temperature-dependent  $g_{ep}$  and  $R$ , together with the refined magnetic heat capacity, does not result in a significantly improved matching of the simulation and the experiment. The resulting magnetization dynamics are presented in Fig. 6.17. The coupling is approximated by  $g_{ep} = g_{ep}^0 \pm \gamma T_{el}$ , with  $g_{ep}^0$  being the value noted in Table 6.1 and  $\gamma = 2 \times 10^{15} \text{ Js}^{-1} \text{ K}^{-2} \text{ m}^{-3}$ . We use  $\pm$  here since the scaling of the coupling is not known and both cases are tested. The new electron heat capacity of Co is approximated by  $C_{el} = C_{el}^0 + Ae^{-((T_{el}-B)/C)^2} - D/(1 + e^{-(T_{el}-E)}) + F$ , again  $C_{el}^0$  refers to the value given in Table 6.1, to include the magnetic heat capacity. The parameters that best describe the heat capacity in [209] are  $A = 365 \text{ Jkg}^{-1} \text{ K}^{-1}$ ,  $B = 1387 \text{ K}$ ,  $C = 192 \text{ K}$ ,  $D = 468 \text{ Jkg}^{-1} \text{ K}^{-1}$ ,  $E = 1395 \text{ K}$  and  $F = 20 \text{ Jkg}^{-1} \text{ K}^{-1}$ . We simulate the dynamics for both scalings of the electron-phonon coupling since the true temperature dependence is not known. The fluence is not adjusted and is fixed to  $40 \text{ mJ cm}^{-2}$  in both cases.

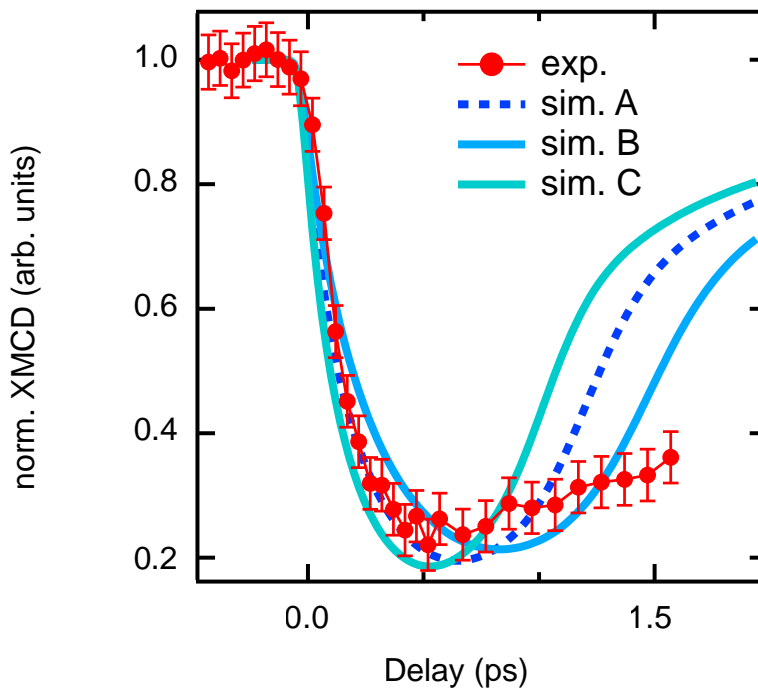


**Figure 6.17:** Experimental and simulated XMCD at 778 eV in Co on the multilayer OISTR sample. The simulation with a constant electron-phonon coupling and a linear heat capacity is labeled as sim. A. For sim. B, an electron-phonon coupling that decreases with temperature as described in the text is used. In sim. C an increasing electron-phonon coupling is employed with the same scaling as in sim. B. Using a better-matching heat capacity for Co in sim. B and sim. C mainly leads to lower final temperatures, and the magnetization dynamics are not affected significantly by including the specific heat of the spins.

The experimental curves are still not described flawlessly, despite having a decent agreement between the observed demagnetization and the simulated ones. The dichroic sum signal does not reduce sufficiently in the simulation. One possibility, as mentioned before, is that in the investigated regime, the expansion and compression are not described by the parameters used

in the simulation. Another approach tackles the issue from a very different point of view. During the optical excitation by the pump pulse, electrons transition into excited states and initially assume a non-thermal distribution above  $E_F$ . Their thermalization leads to a population of the states probed by the X-ray pulse. Since these states are now occupied, and the core levels are very narrow in energy, the new electronic population leads to state-blocking effects, reducing the X-ray absorption. The effect of the electronic redistribution in Ni on the dichroic XAS has been investigated theoretically in [218]. The results of [218] are in-line with experimental reports of a reduction and shift of the transient X-ray absorption recorded in Ni [219, 220]. That the results are equally applicable for reflectivity experiments is not guaranteed since the XRR signals combine absorption and reflection. To investigate the effects of the excited electron distribution on the reflectivity spectra, the transient optical response function or, in other words, the magneto-optical constants at all times, is required. In the following section, we use time-dependent optical constants calculated by TDDFT to estimate the influence of the altered electron population on the reflectivity spectra.

### 6.3 Effects of electronic redistribution

The optical excitation at 800 nm drives electronic transitions around the Fermi edge, i.e., from about 1.5 eV below to 1.5 eV above  $E_F$ . Since the X-ray reflectivity measures the unoccupied density of states around  $E_F$ , a significant light-induced change in the X-ray absorption at this fixed energy is expected. We employ *ab initio* TDDFT calculations of the transient electronic occupation in Co and the corresponding optical response function to evaluate this change, at least qualitatively. The calculations are carried out by S. Sharma using a fully noncollinear version of the ELK code considering relativistic dynamics [221, 222]. The approach includes spin and charge effects, spin-orbit mediated spin-flips, and electron-electron scattering. In the simulation, the Born-Oppenheimer approximation is employed, i.e., the nuclei are considered static. Long timescales are computationally heavy, and therefore only a small time window, up to 180 fs delay time, is simulated. Furthermore, to obtain noticeable dynamics in this short period, calculations are carried out using a 20 fs FWHM pulse of  $24 \text{ mJ cm}^{-2}$  incident fluence. The occupied partial density of states before and after excitation is presented in Fig. 6.18 together with the evaluated spin-resolved change after 150 fs. The resulting magneto-optical response function in terms of the atomic and the magnetic form factor is presented in Fig. 6.19. The simulation in Co indeed reveals that after excitation, more states are occupied at and above  $E_F$  than before. For the calculations, we employ p-polarized light. Nevertheless, slightly more transitions of the minority spin species are excited, as seen in the difference image in Fig. 6.18. A significant increase of occupation at the Fermi energy is recognized, whereas new free states become available for the X-ray-excited core level electrons only at about 1 eV below  $E_F$ . The transient electron distribution leads to a new energy-dependent response to the X-ray excitation described by the atomic and magnetic form factors.

The comparison to the experimentally obtained form factors reveals that the magnetic contribution is overestimated in the simulations, especially at the  $L_2$  absorption edge. Similarly, the absorption is slightly overestimated, and consequently, the real part is estimated to be too low. Nevertheless, the optical response, the atomic and the magnetic one, is described qualitatively well. Upon excitation, the absorption reduces at both edges, and similarly, the magnetic part reduces. This is true for both the imaginary and the real part. Since the optical response at the  $L_2$  edge does not match the experimental curve well, we focus on the dynamics of the  $L_3$  edge

in the following.

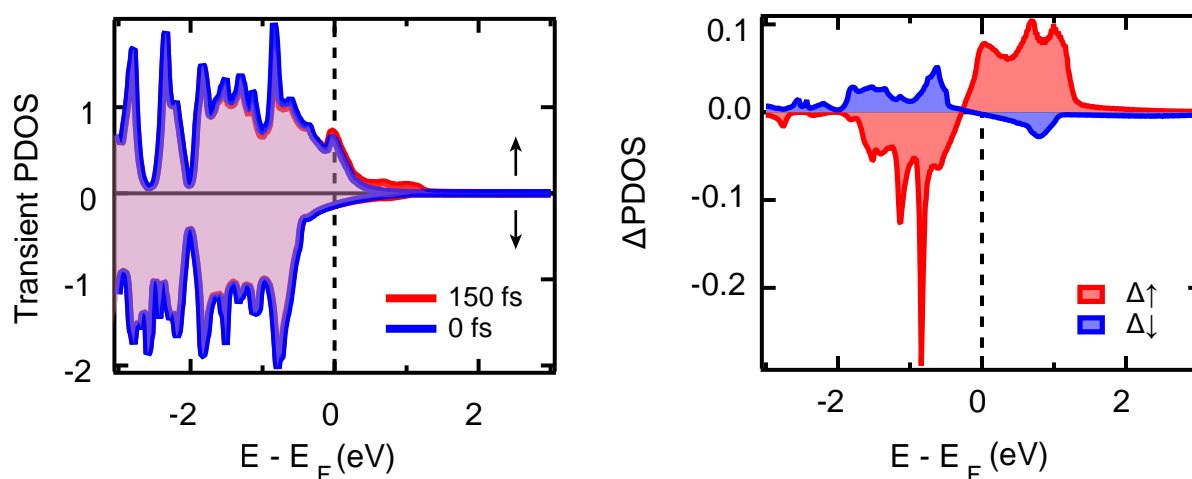


**Figure 6.18:** Left: Simulated occupied DOS (PDOS) at 0 fs and at 150 fs around the Fermi energy  $E_F$ . Right: Evaluated change in occupation after 150 fs for both spin species. The sign of the occupation is arbitrary, the up- and down-states are plotted with opposite sign.

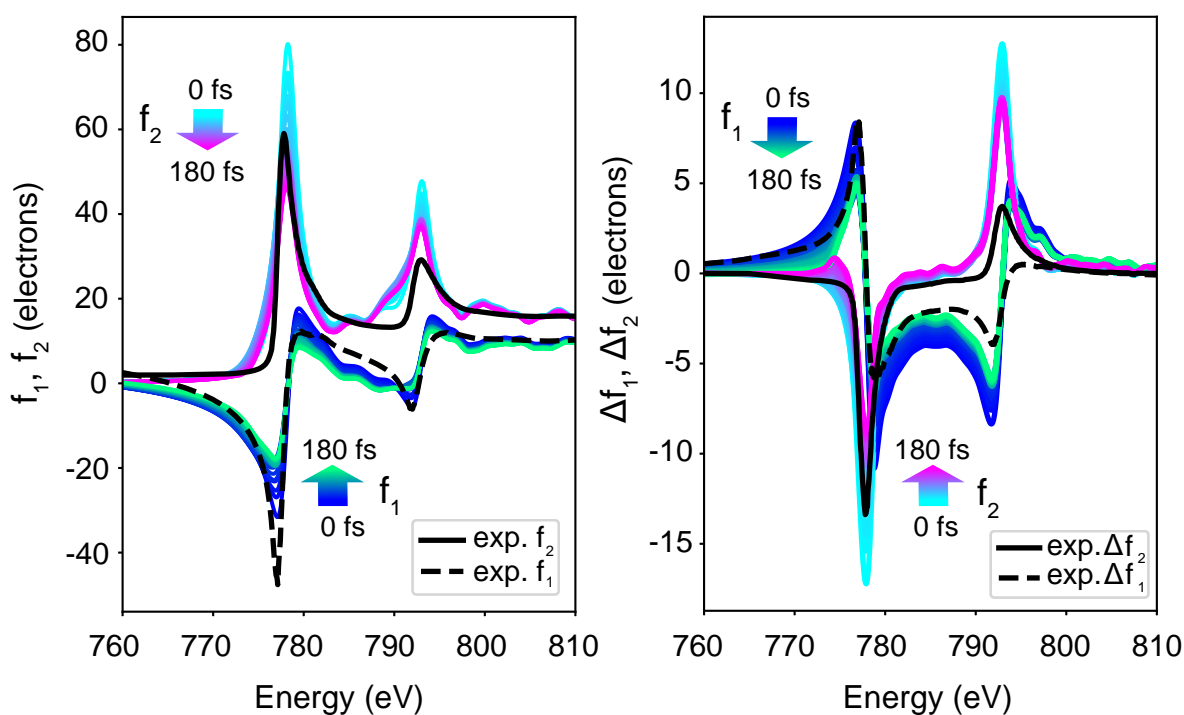


**Figure 6.19:** Left: Simulated transient atomic form factors  $f_1$  and  $f_2$  in Co from 0 fs to 180 fs after excitation, shown as the colored solid lines. The color scale indicates the time passed after the excitation. The calculated form factor follows the static experimental one, shown in black, with a high qualitative agreement. Right: The magnetic contribution to the atomic form factor. Again the calculated values are shown with the color scales, and the experimental curves recorded statically are shown in black. The DFT calculation overestimates the magnetic contrast at the  $L_2$  edge by almost a factor of two.

We simulate XRR spectra at different delay times under the investigated angle to evaluate the influence of the transient optical response function on the reflectivity signals. This time, no heat-induced changes are considered. The sample is considered static, i.e., no phononic modes are excited, and also no depth-dependent excitation profile is taken into account. The transient reflectivity is calculated by using the optical response, shown in Fig. 6.19, at the corresponding time delay and keeping the temperature and strain stationary. The simulated transient spectra, obtained by using the calculated optical response, are compared to the experimental ones in Fig. 6.20. Most notable is the reduction of the intensity over the resonance edges. At the same time, the magnetic contrast reduces slightly. The reduction of intensity and magnetic contrast happens already within 180 fs after excitation. The simulated dynamics are faster than what is observed in the experiment since a much shorter excitation is used in the calculations. As mentioned before, the reflectivity at the  $L_2$  edge is overestimated and does not match well with the experimentally observed reflected intensity shown in the left panel of Fig. 6.20.

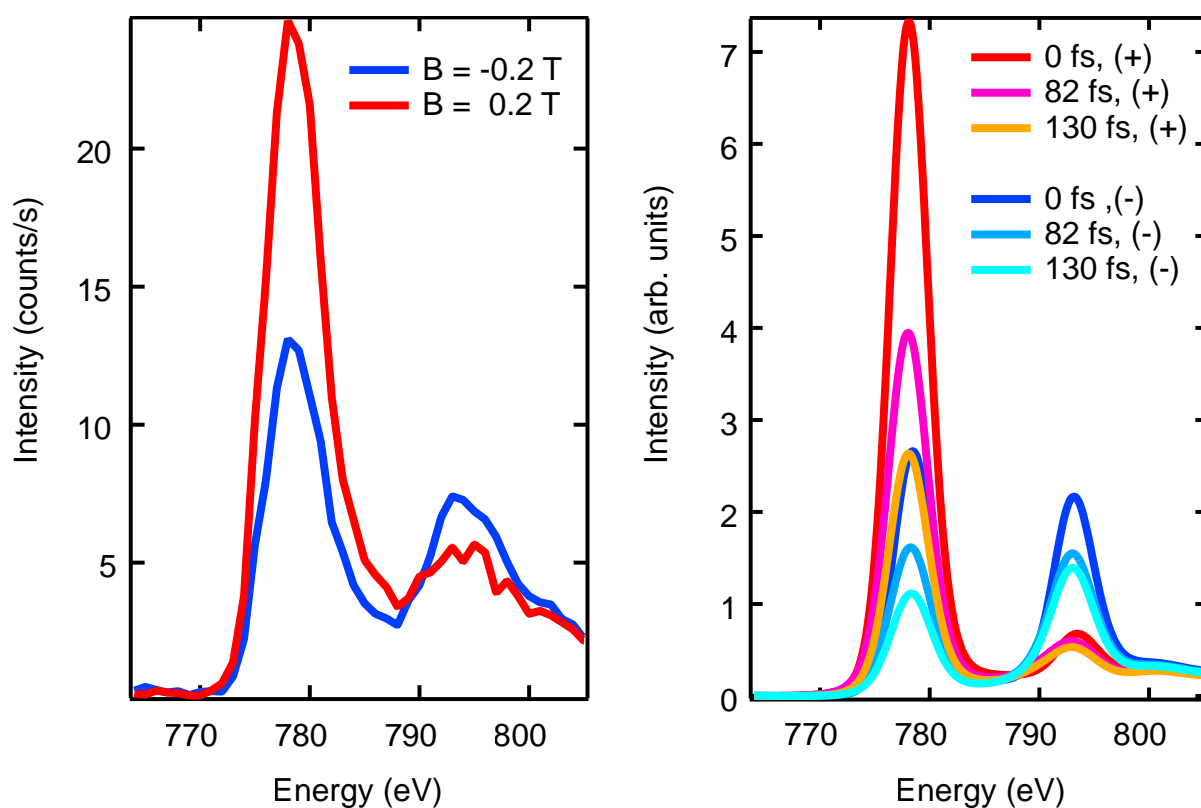


**Figure 6.20:** Left: Static XRR spectra recorded under  $8.75^\circ$  incident angle over the  $L_{3,2}$  absorption edge energies for opposite saturation magnetizations. The spectra are also shown in Fig. 6.15 (A). However, they are shown here again to compare the simulated spectra to the experiment. Right: Simulated Co spectra using the calculated optical response shown in Fig. 6.20 for opposite helicities. The qualitative change includes a significant reduction of the overall intensities at the energies of the absorption edge. The magnetic contrast is overestimated in the DFT calculations, especially at the  $L_2$  edge, where the dichroism is not reproduced well. This is also visible in the atomic form factors shown in Fig. 6.19.

The magnetic contrast is evaluated from the spectra in the same fashion as before. A comparison between the magnetic contrast change resulting from the new electron distribution is presented in Fig. 6.21 in the left panel. It should be stressed here that the simulation is not matched to the experiment in terms of the excitation profile in temporal width and fluence. Furthermore, only a small window, up to 180 fs delay time, is calculated. In addition to the evaluated contrast, the time evolution of the sum of the dichroic signal is presented in the right panel. A comparison to the experiment reveals that the reduction of the reflected intensity is overestimated in the simulation. However, in contrast to the simulations employing only heat-mediated mechanisms, the ultrafast drop in intensity is reproduced. A more refined match of the laser fluence and adjusting the temporal shape to the experimental profile might result in a better agreement between the simulation and the experiment.

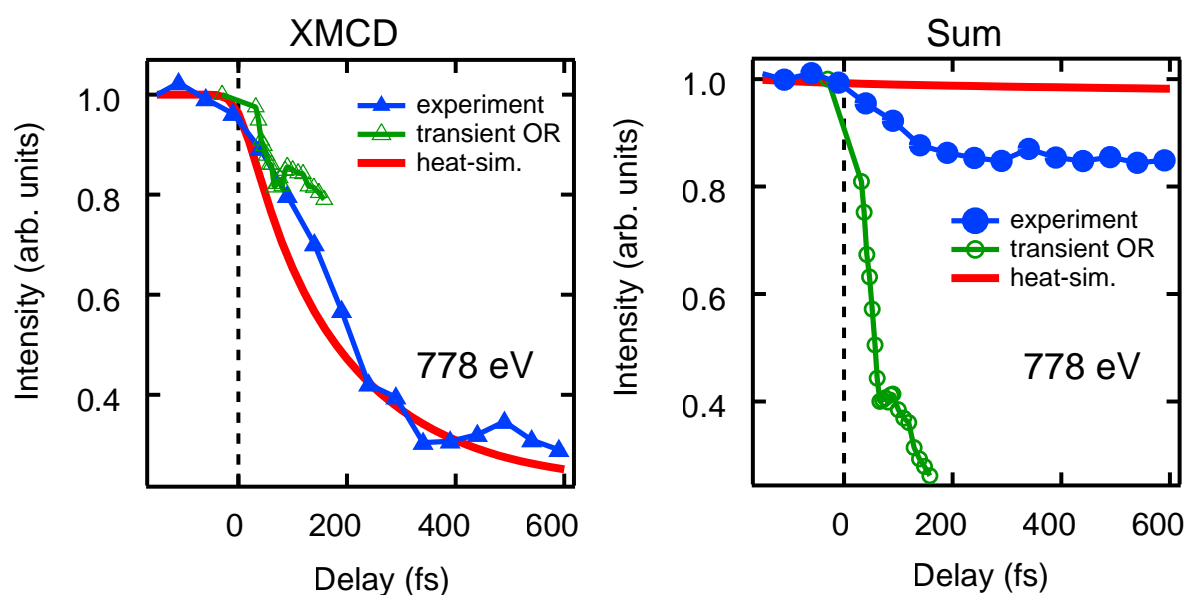


**Figure 6.21:** Left: Simulated and recorded normalized magnetic asymmetry as XMCD in Co at 778 eV. The recorded XMCD (filled triangles) compared to the simulated XMCD using the transient magneto-optical response (OR) function (open triangles) and the heat-induced changes (solid line). Right: Normalized sum of the dichroic signals in the experiment (filled circles) and the simulated time evolution using the transient optical response function (open circles) and the heat induced changes of the last section (solid line). The OR function is evaluated at several delay time steps which is why the value is indicated with markers.

In the simulations in this section, the magnetic contrast is quenched by spin-orbit mediated spin flips resulting in a smaller change than observed. However, the simulation does not consider the heat-induced change of the entire system, which, by transport and local spin flips, leads to a further reduction of the magnetic contrast at later delay times. The simulated change of the sum signal is higher than what is found in the experiment. Nevertheless, an important mechanism is now included, which explains the ultrafast reduction found in the sum signal. The signal in reflectivity is affected by the transient electron distribution in the same fashion as it would be in absorption, at least in the investigated system. The authors of [218] calculate a shift of the absorption edge in Ni, which is also reported in measurements of the transient absorption edges [219, 220]. This shift is found to be negligible in Co, based on the calculations presented here. Overall, the reflected X-ray intensity change is found to be a combination of the magnetic

contrast change and the electronic and structural change. The electronic and structural changes affect the recorded intensity in both helicities symmetrically, i.e., both reduce or increase. The magnetic contrast change leads to an asymmetric change of the helicity-dependent intensity, i.e., the intensity for one helicity increases and the other decreases. This finding is true for absorption, where the imaginary part of the (magneto-) optical response function uniformly decreases after excitation. Judging by the simulated spectra and the calculated optical response functions, the same is true in XRR on Co at the resonance.

So far, the simulated magnetic contrast change is always evaluated at the same energy as in the experiment. In the following part, the dependence of the observed contrast on the employed energy is investigated.

## 6.4 Photon energy dependence of the XRR

The magnetic contrast in reflectivity depends on the angle and energy used for the investigation. This is already observed in the spectra presented in Fig. 5.6, for example. We use the simulations established in the last sections to investigate the probing-energy dependence of the magnetic contrast.

We simulate the recorded dichroism by evaluating the energy- and helicity-dependent intensity at a fixed angle of  $8.75^\circ$  on the OISTR sample. The simulations are carried out separately, in one instance by evaluating the heat-induced changes of the magnetic contrast and afterward using the dynamic optical response function with a stationary temperature. The time evolution of the magnetic contrast in both cases is presented in Fig. 6.22.

First, we discuss the results obtained using the mechanisms of temperature and strain. The calculation reveals that there, the temporal evolution of the magnetic contrast after excitation is energy-dependent. This is most notable in the magnitude of the simulated contrast change. While the drop in intensity is virtually the same over the  $L_3$  resonance, the recovery is delayed at energies below the  $L_3$  peak compared to the ones above. At the  $L_2$  edge, the contrast is reversed, reduces less, and recovers quicker than at the  $L_3$  edge. Overall it is observed that the simulated reflected X-ray intensity remains comparable close to the peak energies of the resonance edges. Deviations in the magnitude and timescales are observed off-resonantly where the magnetic contribution recovers at a different timescale. It should be noted that the evaluation of the energy-dependent contrast considers an energy broadening of 3.2 eV as found in the slicing facility.

The simulation of the magnetic contrast evolution across the energies of the Co resonance using the transient optical response function reveals a similar dependence on the energy as described before. Here, the simulations do not advance far enough in time to account for remagnetization. However, a dependence of the signal reduction on the energy is observed at the early timescale when comparing energies close to the peak of the  $L_3$  edge and below.

The presented images highlight that the (time-dependent) magnetic resonant X-ray reflectivity is an energy-dependent observable. Although the underlying magnetic state is always the same, different dynamics are observed depending on the employed energy. In the investigated sample, the dependence of the magnetic-contrast evolution on the energy is small around the peak of the  $L_3$  resonance and resembles strongly the evolution of the magnetization in the top layers of the sample. It is, therefore, a good observable for the magnetic state.

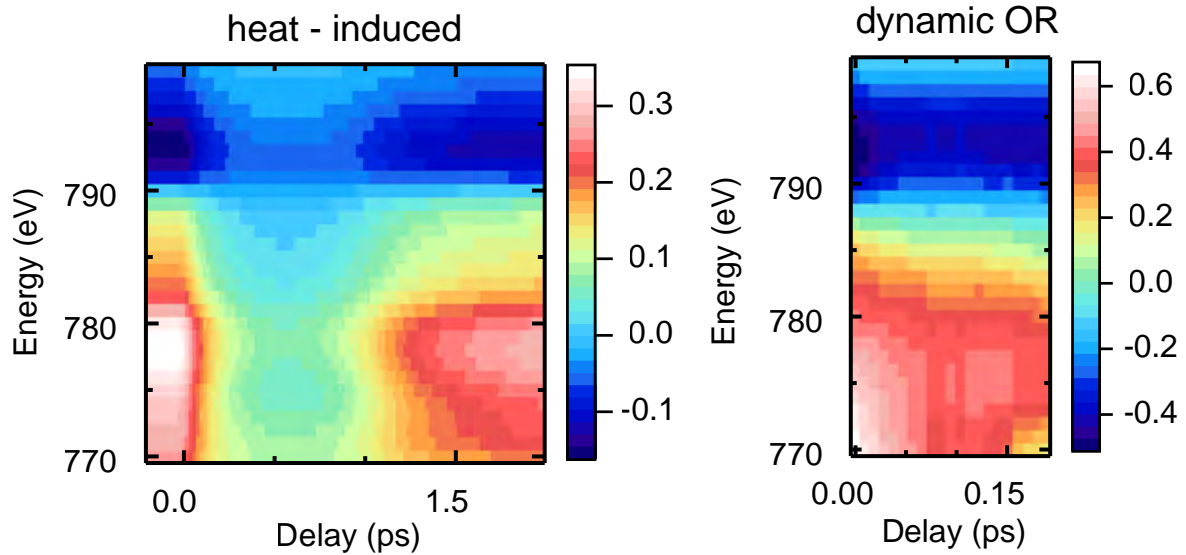


**Figure 6.22:** Magnetic contrast after laser excitation over the energies covering the Co  $L_{3,2}$  absorption edge simulated by the aforementioned means. Left: Magnetic contrast evolution in the simulations of the temperature-induced change. Right: Magnetic contrast evolution for different energies using the dynamic optical response function. All simulations are performed for an incident angle of  $8.75^\circ$ .

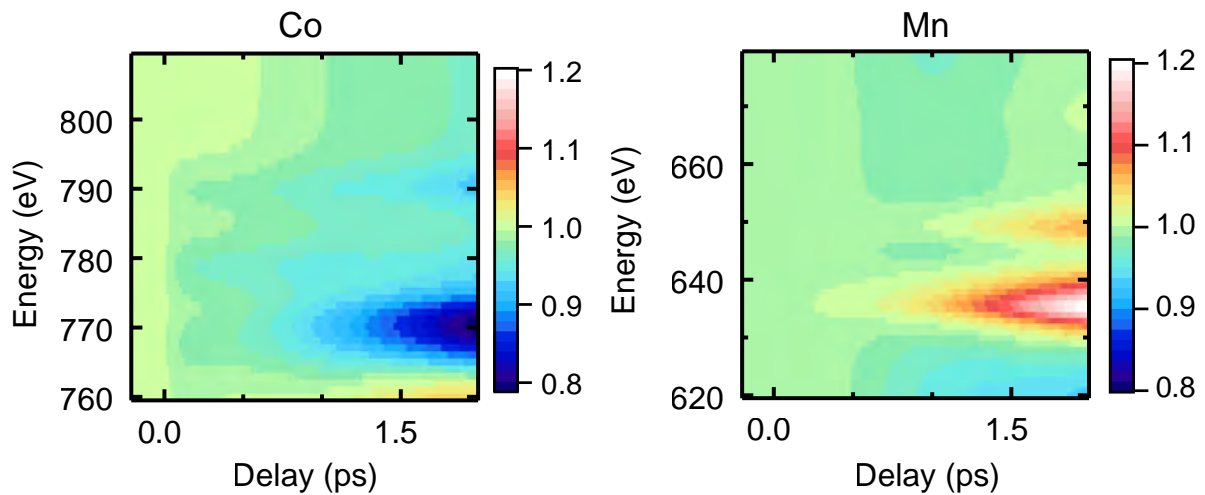


**Figure 6.23:** Sum of the dichroic signals in the simulation of the heat-induced XRR changes. Left: Co XRR sum signal evolution after laser excitation. The most significant change is not found at the peak energy of the absorption edge but at slightly lower energy. Right: Mn XRR sum signal after laser excitation. The time evolution of the XRR signals is evaluated in both cases using the OISTR sample at an incident angle of  $8.75^\circ$ .

Lastly, the sum signal evaluated from the simulations employing thermal mechanisms is presented in Fig. 6.23. The evolution of the sum signal at the Co and the Mn resonance simulated on the OISTR sample is presented up to 2 ps after excitation. The simulation predicts an increase in the XRR sum signal in Mn and a decrease in the XRR intensity at the Co resonance.

As already presented in Fig. 6.21, the sum signal at 778 eV reduces already at 200 fs. This is not predicted in the simulation presented in Fig. 6.23, and only after 1 ps the reduction of the signal becomes significant. This is especially true at 778 eV, where the change in intensity is simulated to be relatively small.

In Mn, an increase of the sum signal near the recorded energy is predicted. This is also observed in the experiment as already presented in Fig. 5.8. A direct comparison between the observed and the simulated sum signal in Mn is given in Fig. 6.24.

## 6.5 Summary and Conclusion

This chapter describes the features of time-dependent X-ray reflectivity on the Co/Mn multilayer sample. First, the magneto-optical constants relevant for the employed energies are evaluated from experimental data. Before simulating time-dependent dynamics, we use the optical constants to simulate the X-ray reflectivity in the static case for different energies and angles. Based on the sample structure and experimentally obtained optical constants, we investigate the mechanisms affecting the experimentally recorded intensities by simulations of the angle-, energy- and helicity-dependent reflectivity employing `udkm1Dsim` [188]. We use the OISTR sample, introduced in chapter 5, as an example to test the viability of the simulations and to connect the observable, i.e., the magnetic contrast in XRR, to the underlying physical property, that is the magnetization. We identify three mechanisms that contribute significantly to the time evolution of the XRR after excitation by light.

First, the photon-electron interaction drives transitions, leading to a new electron distribution that affects the elements' optical response function. This effect is short-lived and leads in the investigated sample to a drop of the reflectivity at the Co resonance within 200 fs. In Mn, the effect leads to a transient increase in the sum signal, see Fig. 6.24. Furthermore, in the investigated sample, the optically driven excitations lead to a contrast enhancement following the prediction of the OISTR mechanism [120]. The described effect is similarly present in absorption. However, a direct translation of the changes in the absorption due to a new electron distribution to reflectivity is not trivial. Therefore, we use the presented simulations in conjunction with the experimental data to verify that the observed effect can be expressed in the same fashion in the investigated case.

Secondly, the heat introduced by the light absorption strains the lattice, which consequently expands or compresses. A new lattice spacing or film thickness directly translates into different reflectivity properties, see Fig. 6.14. In the investigated case, this leads to a lattice expansion within 2 ps and an increase in the reflectivity at energies covering the Mn absorption edge. In Co, the lattice expansion reduces the X-ray reflectivity at the absorption edge energies. The timescale of the lattice expansion is comparable to phonon frequencies or sound velocities in the sample. For a sizable change of the XRR, an expansion in the order of nms is required. Using the sound velocities given in Table 6.1, a coherent phonon excitation can mediate the strain in about 0.5 ps to 1 ps depending on the film thickness, thereby setting the timescale of the lattice-induced effects.

Lastly, the magnetic contrast is reduced due to the quench of magnetization within the sample. Since we are primarily interested in the transient magnetic properties, the answer to the question to what extent the magnetic contrast recorded in XRR reveals the actual magnetic state of the system is of paramount importance. That the magnetization is quenched within several 100 fs is an established phenomenon. However, as presented, for example, in Fig. 6.13, magnetiza-

tion is a microscopic property that shows a clear vertical dependence in ultrafast light-induced magnetization experiments of samples thicker than the skin depth of the employed pump light. Furthermore, the magnetic contrast depends strongly on the probing angle and energy. We perform XRR simulations combined with magnetization evolution in the frame of the m3TM [54] to investigate the correlation between the simulated XRR, the simulated magnetization, and the experimentally recorded XRR. In the investigated sample, the simulations reveal that the change in XRR follows the magnetization change of the topmost layers. Most notably, the energy dependence of the magnetic contrast is not reflected strongly in the time evolution thereof, as presented in Fig. 6.22. Although slightly different timescales and quenches are recorded, the overall dynamics are comparable in a window of several eV around the absorption peaks. Not discussed here are macrospin precessions resulting from a transient rearrangement of the effective anisotropy field. The spin precession can be seen as oscillatory features in the delay trace of the recorded magnetic contrast [53]. In a similar fashion, magnetostriction effects are not included here. Effects of magnetostriction are a concomitant phenomenon following the lattice strain and can in principle be included using a spatial-dependent exchange coupling [223].

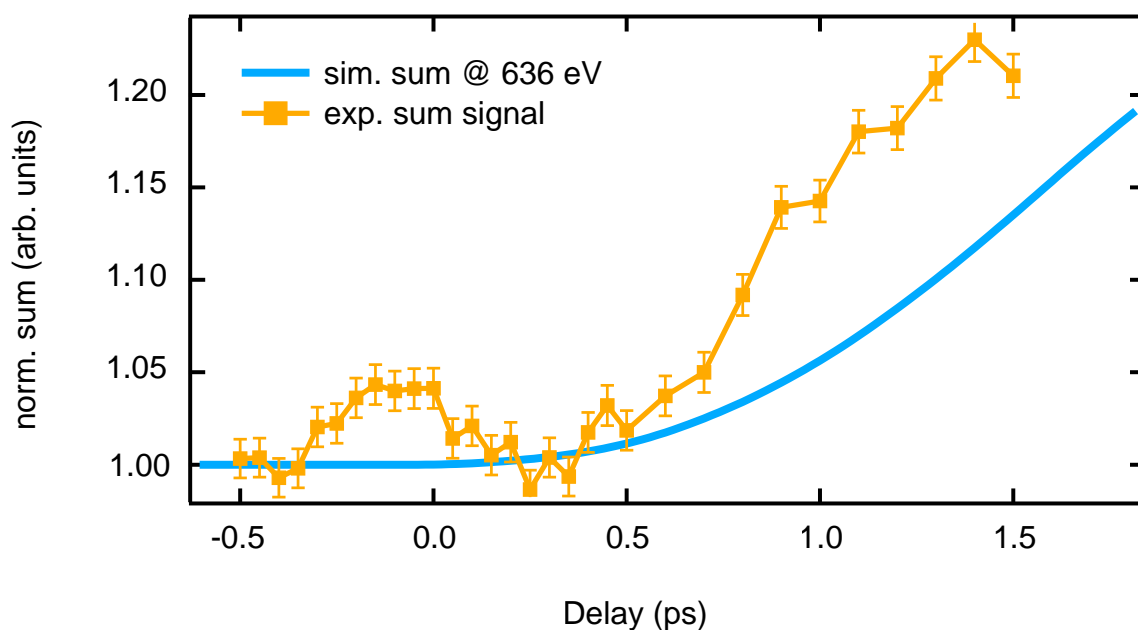


**Figure 6.24:** Simulated (solid line) and recorded (markers) sum of the dichroic signals at 636 eV on the OISTR sample under  $8.75^\circ$ . The simulated lattice expansion results in a similar increase of the reflected X-ray intensity as seen in the experiment. The initial rise of intensity around time zero is not seen in the simulation. The time zero feature is attributed to the coherent electron transitions driven by the laser excitation, see section 5, which is not included in the model employed here.

Ultimately, the findings in this section validate the conclusions drawn about the magnetic state of the system presented in the previous chapters. It showcases that a decomposition of the RMXR into a magnetic and an electronic component is possible, at least at the Co  $L_3$  resonance. We conclude that the interpretation of the dynamics observed in Co/NiMn and the Co/Mn multilayer sample presented in chapter 5 are correct, since the experimental signals are mostly reproduced. The initial timescale of excitation remains elusive to some extent as the

precise calculation of the non-equilibrium states is not in the scope of this thesis. Nevertheless, as presented in Fig. 6.24, we can reproduce the sum signal in Mn nicely, albeit with a slightly slower timescale than in the experiment. This difference could be remedied by fitting the linear thermal expansion coefficient or the sound velocities. However, since the presented simulations are mainly used to qualitatively describe the dynamics and highlight the applicability of the models, I refrain from fitting the parameters here. The initial rise around time zero, a feature of the light-driven dynamics, is not included in the simulation and requires more theoretical input.

## 6.6 Appendix

### 6.6.1 Examples

The concepts established in the chapter rely on already developed and mature tools used to simulate the helicity-dependent X-ray reflectivity [188]. The primary conclusion is the applicability of the understanding in absorption experiments to *most parts* of the reflectivity signals. In the main text, the simulations are presented to provide an indirect proof of our interpretation of the RMXR observable. In the following, two examples are presented to highlight the abovementioned concepts and their approximations.

#### Demagnetization in Co/NiMn

The first example is taken from the demagnetization traces recorded in the Co/NiMn/Cu(001) sample, analyzed and discussed in section 4. Here, we analyze the dynamics of the channels individually, applying the concepts of the described mechanisms of this section. We conclude that, when measured at the Co resonance, the absorption features are dominant and the XRR follows closely the underlying magnetic state of the system. Furthermore, a concomitant change of the electronic signal, on the one hand induced by electronic transitions and on the other hand mediated by strain, is present. The magnetic change is antisymmetric in both helicities, whereas the electronic change is symmetric. We apply this concept to fit an electronic and a magnetic dynamic to the experimental data. The decomposition into electronic and magnetic signal is presented in Fig. 6.25.

To fit the dynamics we use the same relative electronic and magnetic contrast change for both channels in each channel. The resulting fit is a superposition of both signals. Using this concept we can describe the dynamics in both XRR channels. The initial drop in the less intense channel and the following increase is modeled accurately. The XRR is understood as a combination of the electronic and magnetic signal, which leads to small but finite differences of the underlying magnetization dynamics and the observed RMXR intensities, also observed in Fig. 6.22. Furthermore, the magnetic signal and the electronic one change on slightly different timescales. The initial drop in intensity of the electronic signal is a direct result of the non-equilibrium population driven by the exciting laser pulse. The magnetic signal, which changes without delay, reacts slower, as the quench in magnetization is mediated by spin-flips in the process of the thermalization of the non-equilibrium electron distribution.

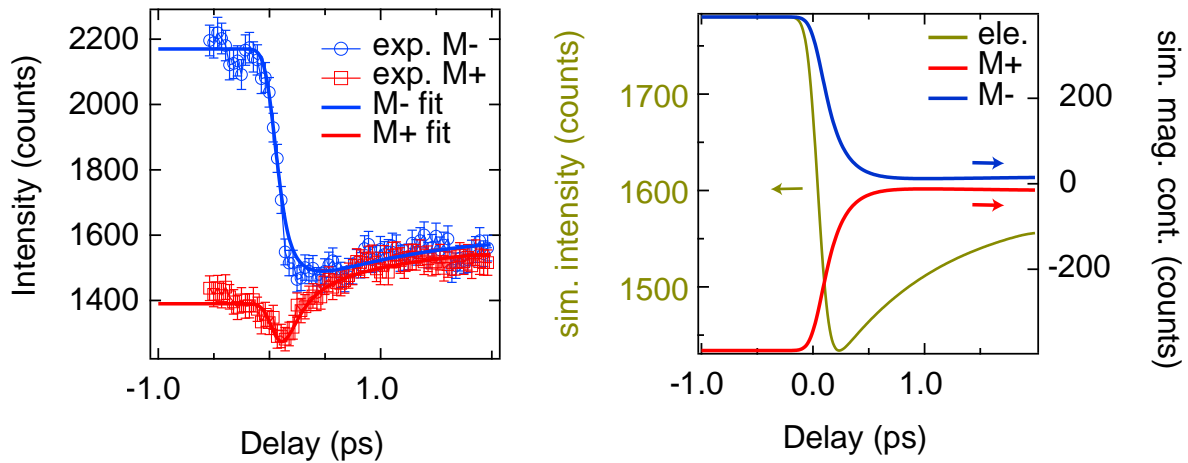


**Figure 6.25:** XRR intensity recorded after excitation by a 60 fs FWHM,  $40 \text{ mJ cm}^{-2}$  incident fluence laser pulse in the Co/NiMn/Cu(001) sample under  $7^\circ$  and at 778 eV probing energy. Left: The magnetization leads to a contrast in the recorded intensities (red and blue markers) at negative delay times which reduces after excitation. The fit resulting from the decomposition of the signal into an electronic and a magnetic component, shown in the right panel, is shown as the solid lines. Right: The intensity is split into an electronic (structural dynamics and electronic redistribution) and a magnetic component for each channel.

### Structural sample properties in XRR simulations

In the second example, we examine the time-dependent XRR recorded in a Co/Mn/Co/Cu(001) trilayer, and compare it to the XRR of a sputter-deposited Al/CoFe/MnIr/NiFe/SiO sample. We use the XRR delay traces to determine the layer thickness. Furthermore, the example showcases the applicability of the simulation and the boundaries of the approximations used here. The sum and the asymmetry, the latter labeled as magnetic contrast or  $x_{\text{mcd}}$ , of the RMXR signals is displayed in Fig. 6.26. The top panel shows the time evolution of the sum and the  $x_{\text{mcd}}$  signal recorded in the 15 ML Co/10 ML Mn/10 ML Co/Cu(001) sample. The traces are recorded at the slicing facility in BESSY II using 800 nm, 60 fs FWHM pulses of  $17 \text{ mJ cm}^{-2}$  incident fluence. Pump and probe pulses are aligned at an incident angle of  $5.66^\circ$  and the recording energy is 777 eV. The recorded traces are compared to the simulated dynamics employing the methodology described in this chapter.

The ultrafast quench of the magnetization is reproduced in the simulation, where we use an excitation of  $35 \text{ mJ cm}^{-2}$ . However, similar to the dynamics presented before, the recovery of magnetization in the frame of the m3TM is quicker in the simulation compared to the experiment. The sum signal in the simulation does reproduce the oscillations observed in the experiment at later delay times. At early times, the experimental signal oscillates oppositely compared to the simulation. The drastically different early dynamics most likely derive from anharmonic oscillations driven by the ultrafast excitation. In our model, only the linear thermal expansion is described. The recorded traces highlight the importance of non-linear effects in ultrafast dynamics. Nevertheless, the sample thickness can be estimated from the sound velocity in the system. The sample is characterized as a 2.7 nm Co/1.6 nm Mn/1.8 nm Co system on Cu(001). Using the sound velocities given in Table 6.1, an estimated travel time for the sound propagation of 1.36 ps is found. This is a very good match to the period of oscillation of  $(2.8 \pm 0.2)$  ps, that corresponds to twice the travel time.

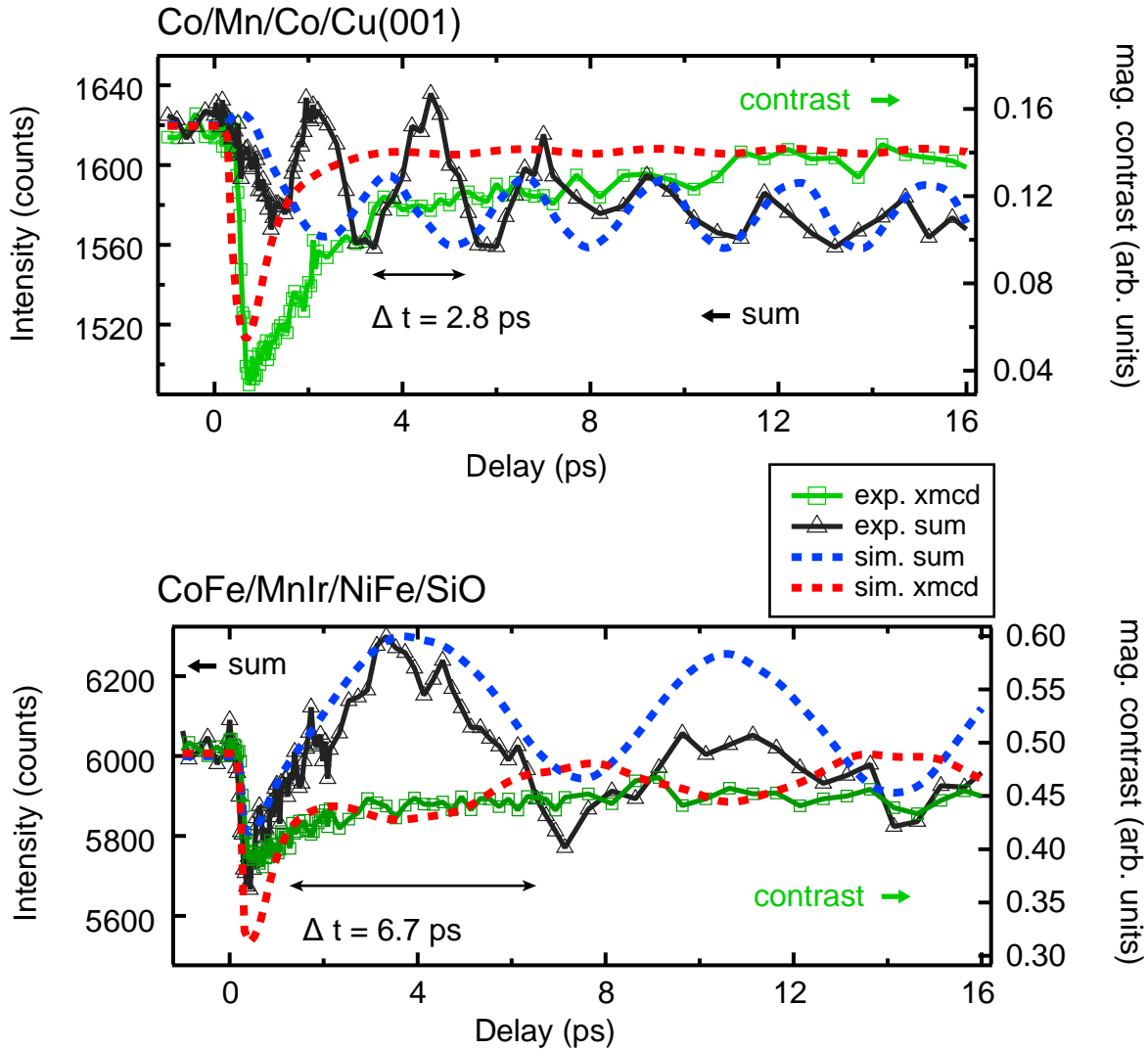


**Figure 6.26:** Recorded sum and asymmetry of the RMXR signal in a Co/Mn/Co/Cu(001) trilayer sample (top) and a sputter deposited Al/CoFe/MnIr/NiFe/SiO sample (bottom). The simulated traces are shown as the dashed lines. In the Co/Mn/Co trilayer, the sum signal is not simulated correctly at early times due to anharmonic oscillations driven by the ultrafast excitation. The sputter-deposited sample is only described well by approximating the sample as a 3 nm Al/10.8 nm Co film.

In the lower panel the sum and asymmetry signal recorded in the sputter-deposited 3 nm Al /3 nm Co<sub>80</sub>Fe<sub>20</sub>/2 nm Mn<sub>78</sub>Ir<sub>22</sub>/2 nm Ni<sub>80</sub>Fe<sub>20</sub>/SiO sample, employing the same excitation parameters as in the other sample, are presented. The simulations employing the actual sample geometry fail to reproduce the experiment satisfactorily. The sum signal in the multilayer sample is predicted to show beatings of many oscillations coming from the involved films. However, the experiment shows only one dominant oscillation period. The simulations presented along the experiment signal are calculated on a 3 nm Al /10.8 nm Co bilayer instead. The approximated bilayer and the original multilayer sample have a thickness of 13.8 nm and 10 nm, respectively. With the sound velocities of the majority elements in the alloys, where we use the

values of Table 6.1,  $v_{sound}^{Al} = 5.1 \text{ nm ps}^{-1}$ , and  $v_{sound}^{Ni} = 4.97 \text{ nm ps}^{-1}$ , a round-trip time of 4.1 ps for the original sample and 5.8 ps for the approximated one is found. Both numbers are well below the period observed in the sum signal. The sound velocities and linear thermal expansion parameters employed for the simulation are not adjusted for the alloys of the sample. Furthermore, the structure is amorphous since it is sputter-deposited. The sound velocity is estimated to be lower in the sputter-deposited samples giving rise to the difference in the experiment and the simulations.

To summarize, for accurate simulations, the rougher interfaces in sputtered samples, the material properties of the alloys, and the polycrystalline or amorphous nature of the films have to be taken into account. Furthermore, non-linear effects also play a role already in the early timescales after ultrafast excitation.



# Chapter 7

## Demagnetization in Co/Pt bilayers

The following chapter is concerned with observing ultrafast demagnetization in Co/Pt layered samples. The data collected on the samples demonstrate that the mechanism investigated in chapter 4 is found in other FM/AFM bilayers. Furthermore, the influence on ultrafast demagnetization of the spatial overlap between pump and probe pulse is investigated. The experiment demonstrates the working principle of the time-resolved MOKE setup assembled at the FU Berlin. Additional data is collected during a short research stay in the group of M. Münzenberg at a similar TR-MOKE setup. First, the investigation of Co/Pt bilayers and a comparison to Co/Pt/MnIr trilayers are shown. Secondly, the study of the dependence of the demagnetization dynamics on the spatial pump-probe overlap is presented.

### 7.1 Ultrafast magnetization dynamics in Co/Pt

As already mentioned initially, it is of great importance to improve our data storage and manipulation concepts to keep up with the demand of the exponentially growing digitalization in capacity, speed, and maybe most importantly, energy efficiency. Employing ultrafast laser pulses to manipulate the magnetic state could become a key player in tackling the challenges. Existing device designs can be altered to make use of the ultrafast processes and to employ the concept of ultrafast demagnetization in data storage or manipulation. Alternatively, devices that rely purely on light-induced processes like all-optical switching (AOS) are being discussed as a new approach. While ferromagnetic thin films have been the topic of many works [3, 4, 224–227], the attention shifts towards systems with an anti-ferromagnetic exchange coupling [228–232]. The AFM exchange interaction in an alloy with different magnitudes of magnetic moments leads to the formation of ferrimagnets where AOS is observed. The AOS process highlights the importance of the exchange interaction, especially in heterogeneous systems. This motivates us to conduct a study of FM Co/Pt multilayers with a high out-of-plane anisotropy coupled to an AFM. The Co/Pt system has a strong orbital anisotropy that pulls the magnetization out of the sample plane, a great application feature. Furthermore, the system has been studied extensively for its AOS properties since it can be switched by ultrashort laser pulses despite being ferromagnetic [233–240]. Here, we focus on the demagnetization properties recorded in TR-MOKE traces when combined in a multilayer with an adjacent AFM-ordered MnIr layer.

### 7.1.1 Comparison of Co/Pt and Co/Pt/MnPt

We study the demagnetization in a 1 nm Pt/0.5 nm Co/3 nm Pt/3 nm Ta/SiO<sub>2</sub> sample and compare it to a 2 nm Ta/3 nm MnPt/1 nm Pt/0.5 nm Co/3 nm Pt/3 nm Ta/SiO<sub>2</sub> sample. The samples are grown by M. Erkovan at the *Instituto de Engenharia de Sistemas e Computadores - Microsistemas e Nanotecnologias* (INESC-MN) by magnetron sputtering. The static magnetic properties are characterized by vibrating sample magnetometry and MOKE. In the following, we will refer to the samples as P1 and P1B (with the MnIr layer), respectively. Initially, we employ the samples to benchmark the TR-MOKE system assembled at our labs.

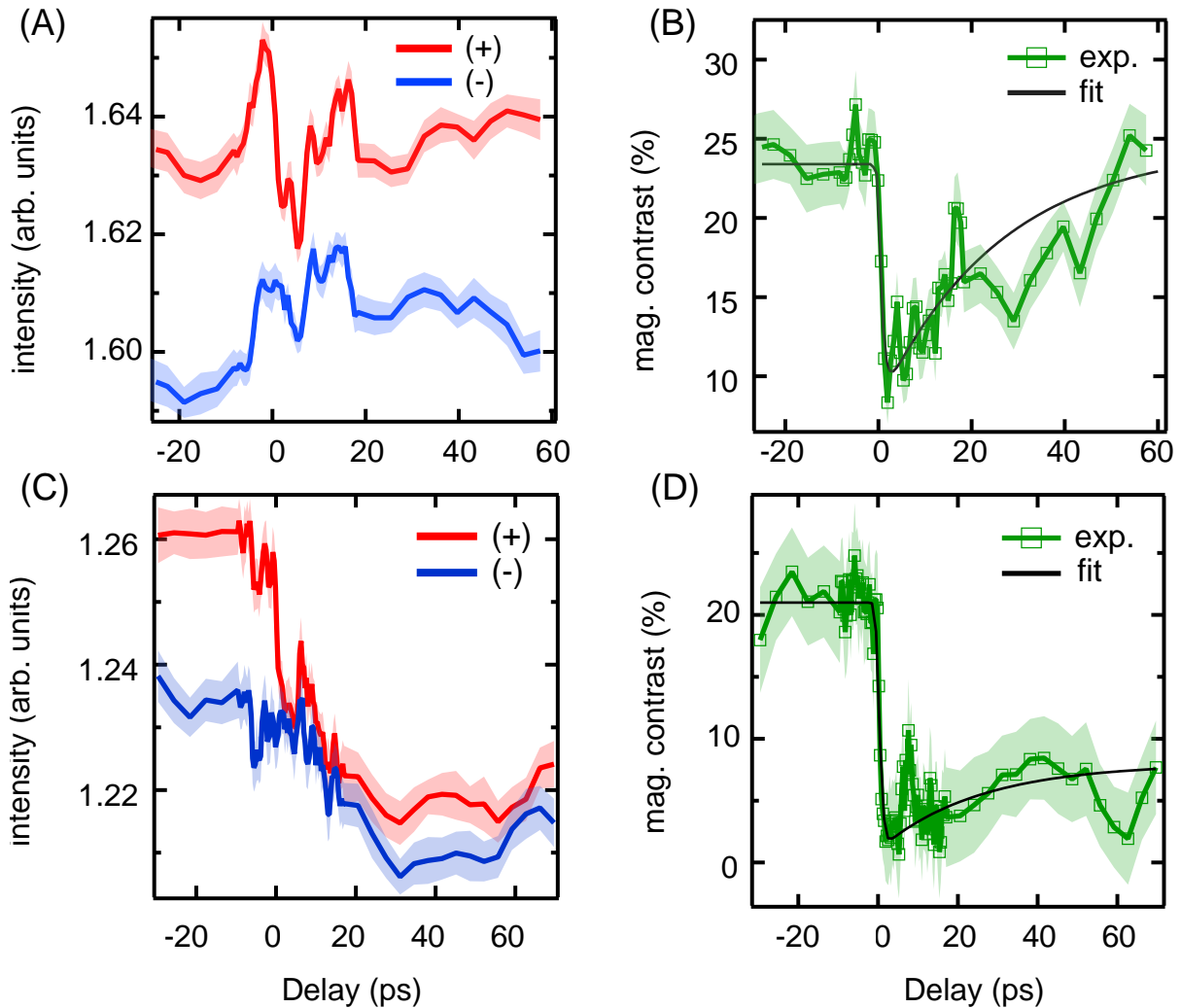


**Figure 7.1:** (A) and (C): MOKE signal as a function of delay time for two saturation magnetizations in P1B. In (A) an excitation fluence of  $(19.2 \pm 3.8) \text{ mJ cm}^{-2}$  is used. In (B) the sample is excited with  $(20.4 \pm 4.1) \text{ mJ cm}^{-2}$ . (B) and (D): Recorded and fitted change of the Kerr rotation upon optical excitation using the respective fluence of (A) and (C). The time for demagnetization is evaluated from the fits and found to be  $(680 \pm 60) \text{ fs}$  in (B), and  $(510 \pm 50) \text{ fs}$  in (D). The contrast is evaluated from the curves shown in (A) and (C). The error is shown as the shaded region and is estimated from the variance in the data.

In the second step, the demagnetization in the samples is compared at equal excitation fluence.

A difference in the demagnetization times and magnitude is found. We argue that the same mechanism as described in chapter 4 is responsible for an acceleration of the ultrafast magnetization dissipation in P1B.

Two traces demonstrating the ultrafast demagnetization in P1B are presented in Fig. 7.1. The data recording and its evaluation are described in section 2.1.3. We observe an ultrafast quench of magnetization, and similar to the dichroic XRR scans, the time evolution of the asymmetry is evaluated from a fit function. The data are fitted by the double-exponential model introduced in eq. (2.30) using a FWHM of 200 fs for the instrumental resolution. The demagnetization time is fitted with  $(680 \pm 60)$  fs at  $(19.2 \pm 3.8)$  mJ cm<sup>-2</sup> and  $(510 \pm 50)$  fs at  $(20.4 \pm 4.1)$  mJ cm<sup>-2</sup>. The incident fluence is estimated from the beam diameter and the average power recorded two mirrors in front of the sample.

The observed demagnetization time is higher than what is reported elsewhere, e.g., [54, 152] and in the previous chapters within this thesis. A likely reason for the overestimation is that the frequency-doubled probing pulse is larger in time than the underlying 800 nm pump pulse. We perform systematic studies of the fluence-dependent demagnetization to understand how the MnIr layer affects the Co dynamics. Furthermore, the data recorded in sample P1B needs to be compared to P1 to pinpoint possible effects on the MnIr layer. Issues with the laser source force us to switch to a different setup. The subsequent investigation is carried out at a comparable TR-MOKE system at the university in Greifswald in the labs of M. Münzenberg in cooperation with J. Walowski. The details of the setup are found in [241, 242]. A comparison of the demagnetization dynamics in P1 and P1B is presented in Fig. 7.2.

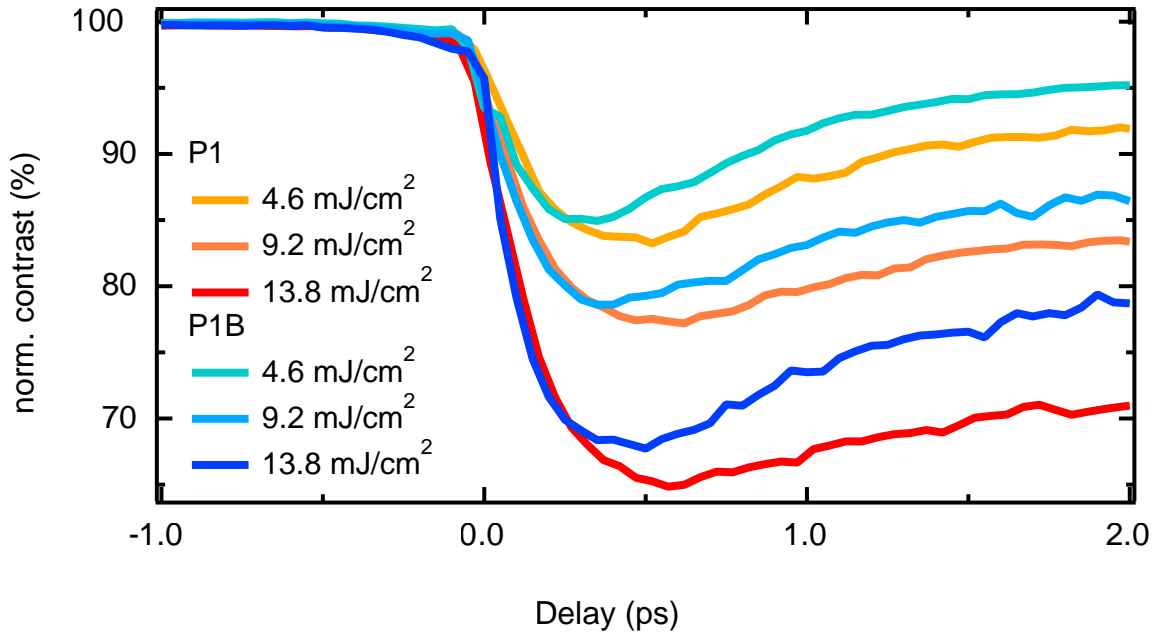


**Figure 7.2:** Time evolution of the magnetic contrast recorded in P1 and P1B. The samples are measured consecutively without changing other experimental parameters but the laser fluence in between scans. The minimum in magnetization is reached faster in P1B compared to P1 for all recorded fluences. However, using the same fluence, the magnetization in P1B is quenched less. Furthermore, a faster remagnetization in P1B is observed.

The data presented in Fig. 7.2 reveals demagnetization times for P1 and P1B that are compara-

ble to other measurements on Co, for example, in this thesis. More importantly, the recordings show a difference between P1 and P1B in the dynamics. In P1B, the change in the Kerr rotation, interpreted as the magnetic contrast, happens faster than in P1. The minimum of the magnetic contrast in P1B is reached at earlier times compared to P1 in all investigated fluences. However, the minimum of magnetic contrast remains higher in P1B than in P1. We interpret this as a sign of the mechanism described in chapter 4, where it is shown that an adjacent AFM layer, here the MnPt film, accelerates demagnetization.

The results suggest that the MnPt layer, although it is separated by 1 nm Pt from the Co layer, affects the demagnetization dynamics. That separated layers affected each other on the ultrafast timescale due to transport is extensively proven [127, 133, 198]. However, the effects between two *ferromagnetic* layers were investigated in detail in the previous investigations. Here, we show that an AFM layer, separated by a spacer layer, also affects the dynamics.

Since the only difference between P1 and P1B are the MnPt and the top Pt layer, the difference is either caused by them or by different experimental conditions. The latter is ruled out here since the measurements were taken consecutively using the same source and the same parameters, only changing the sample and varying the fluence by adjusting a half-wave plate in front of a polarizer. The probing position is, in both cases, slightly off-center with respect to the pumped region to ensure a fast recovery of the system. The reasons are elaborated on in the next section. However, no relative adjustment between pump and probe was done when changing the samples. Therefore, we conclude that the additional layers must be responsible for the difference in the dynamics.

First, we discuss possible oxidation effects of the Co/Pt bilayer, which caps the P1 sample but is lower-lying in P1B. The Pt layer, acting as the cap layer in both samples, terminates oxidation very efficiently. In X-ray-spectroscopy-assisted STM studies, a 98 % termination of oxygen is observed after 1 nm Pt, and no oxygen is measured below a Pt cap layer thickness of 1.3 nm [243]. It is, therefore, unlikely that the formation of PtO in the cap layer, or in Co for that matter, affects the Co magnetization in either sample.

Secondly, we want to discuss the excitation's thermal effect, which is felt different for the Co layer in the two samples. The findings presented in section 4 suggest that a higher rate of demagnetization is found in FM-AFM coupled systems. Here, the observed rate is almost the same in both samples since a higher quench is measured in P1. We argue that this is merely an effect of the higher energy absorbed in the Co film in the P1 sample. A calculation of the differential absorption, presented in Fig. 7.3, reveals that in P1B, only 0.76 % of the light is absorbed in the Co layer, whereas in P1 about 1.83 % are absorbed in Co, since the layer is closer to the surface. The actual difference might be smaller since we approximate the MnPt film by a pure Mn layer as we do not know the refractive index at 800 nm of MnPt. Nevertheless, the additional layers on top of Co reduce the absorbed fluence and, therefore, the final temperature in Co. The time delay is also not merely a concomitant effect of the higher energy deposited. This is evidenced by the observation that in P1B, the minimum is reached earlier regardless of the fluence compared. Following this argument, we reason that once the fluence is corrected for an equal quench of magnetization, a significant difference in the rates would be observed, with P1B showing a higher rate of demagnetization.

Ultimately, we tentatively reason that the mechanism for the acceleration in P1B is the same as described in chapter 4. The argument that the FM and AFM layer are separated by 1 nm Pt hindering the spin transport or reducing the effect is weakened by the fact that in Pt, a magnetization is induced by Co [244]. In the presented MOKE study, no element resolution is possible, and the magnetic contrast reflects the overall sample magnetization. Thereby, also the magnetic

contrast in the coupled Pt layer, which is adjacent to the MnPt film, is measured. However, the effect of Pt on the transport in the system is unclear and needs further research. Furthermore, due to its high spin-orbit coupling and efficient spin-to-charge conversion, additional effects might be present that accelerate the dynamics in the investigated system. Lastly, the high spin-orbit interaction in Pt could also influence the ultrafast unpolarized current generated in MnPt on the magnetization dynamics.

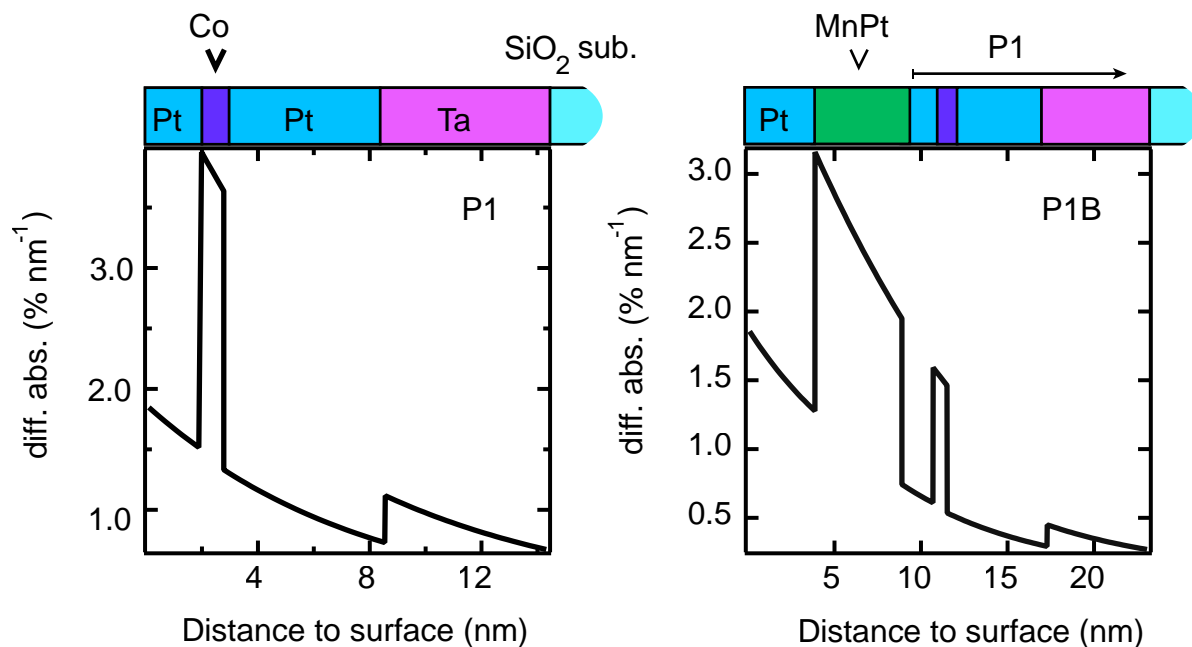


**Figure 7.3:** Differential absorption for 800 nm light evaluated on P1 and P1B. In total, only about 12 % of the incident light is absorbed in both samples. The left panel shows the absorption per nm in P1. The Co layer absorbs a relatively high amount of radiation, although it is only 0.5 nm thick. Integration over the Co thickness yields 1.83 % absorbed. The right panel shows the absorption per nm under the same conditions in P1B. The MnPt layer, approximated by a pure Mn film, absorbs a significant amount of the incident radiation. In total, only 0.76 % are absorbed in Co.

### 7.1.2 Slow and fast magnetic recovery in Co/Pt

In the studies presented so far, heat-diffusion is modeled as one-dimensional in the vertical direction. Generally, this is a reasonable assumption in pump-probe experiments since the probed region is carefully centered in the excited area. Therefore, no lateral thermal gradient is seen at the probe spot. Furthermore, additional channels of heat diffusion could likely also be modeled by a higher one-dimensional term, at least in terms of magnitude no further effect is expected, judging, for example, by the m3TM. In the following, a short study carried out on P1 is presented. We take a closer look at the spatial dependence of the time-resolved magnetization dynamics on the probe spot position relative to the center of the pump. The investigation differentiates between dynamics induced at varying sample base temperatures across the excitation profile and hints that a simple temperature dependence of the excitation is insufficient to explain the observed differences when moving the probe spot away from the center of excitation. We simulate the three-dimensional thermal transport in a finite-difference calculation

to include lateral transport in the m3TM. Ultimately, the observations combined with the simulations suggest that, in addition to thermal transport, ultrafast lateral spin transport may be necessary to describe the measurements accurately.

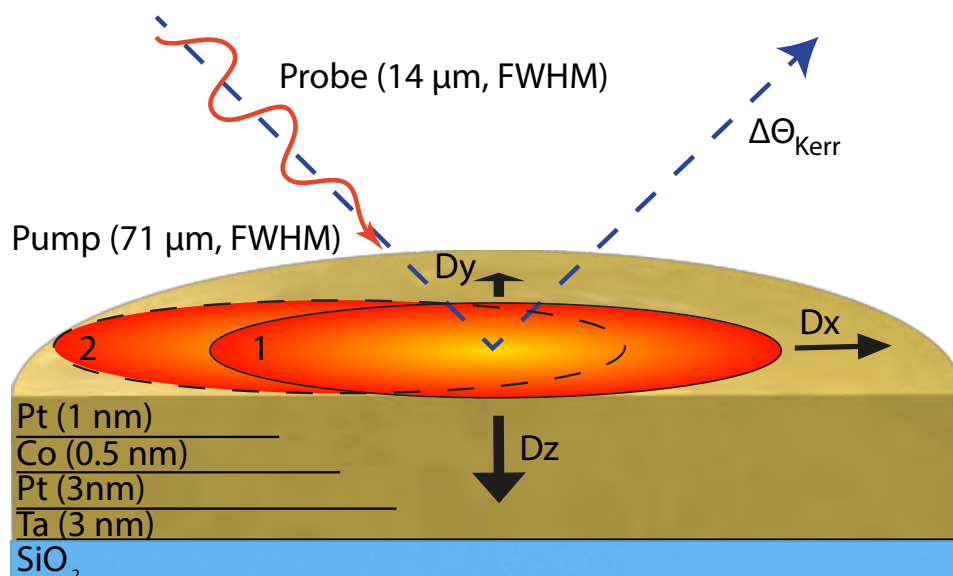


**Figure 7.4:** Cartoon of the experiment. The probe pulse remains at the same position on the sample while the pump spot is moved to a new position. The magnetization at the probe spot is derived from the change of the polarization angle, or Kerr angle  $\Delta\Theta_{\text{Kerr}}$ . Dynamics are recorded for three different pump-probe overlaps. In the Cartoon, only two positions labeled 1 and 2, are shown. Since the probed region is not uniformly heated once the pump is displaced, additional channels for heat transport are included. The heat dissipation is modeled using three independent diffusion coefficients,  $D_x$ ,  $D_y$ , and  $D_z$ .

The investigation is performed on the Co/Pt system without the MnPt layer on top, i.e., on the P1 sample. First, we record the magnetic contrast change when displacing the pump spot relative to the probed region. The experiment is illustrated in Fig. 7.4. In all recorded traces, the probe remained in the same position. Therefore, the detection is entirely unaffected. Experimentally, this is realized by turning the last mirror before the sample while observing the pump-induced change of the Kerr rotation. We choose three positions to investigate. The first position is where the contrast change is maximal, and 89.6 % of the magnetization is quenched. This is where the probe spot is centered in the pumped region. The second one captures 56.6 % of magnetization reduction. And the third one is where only about 28.5 % of the magnetization is quenched. The traces are shown in Fig. 7.5. The fluence is kept constant, and from measuring the pump- and probe-spot diameter together with the recorded demagnetization, we estimate the shift of the pump relative to the center position to be  $(31 \pm 1) \mu\text{m}$  and  $(49 \pm 1) \mu\text{m}$ , shown in the right panel of Fig. 7.7. The FWHM of the pump pulse is measured to be  $(71 \pm 1) \mu\text{m}$  and  $(14.1 \pm 0.1) \mu\text{m}$  for the probe pulse in normal incidence, see the left panel of Fig. 7.7. It should be noted that probing is carried out under an angle of  $45^\circ$  to the surface plane. Therefore, the Gaussian shape is stretched in the direction of the displacement. For all purposes, we assume a Gaussian of the width of  $\text{FWHM} = 14.1 / \cos(45^\circ) = 19.9 \mu\text{m}$  for the probe pulse. The pump

pulse arrives at the sample at near-normal incidence, and the increased lateral projection on the sample surface coming from tuning the angle is neglected. An angular change of about 17 mdeg/100  $\mu\text{m}$  is expected since the last mirror is at a distance of 30 cm from the sample. Lastly, since the probe pulse is passed through two beam splitters, reducing the ratio of the probe beam to the pump to 1:81, we rule out any influence of the probe light on the observed dynamics.

The delay traces follow the same trend expected when changing the fluence. At maximum fluence, or instead, in the center of the pump spot, the magnetization is reduced the most and recovers the slowest of all three cases. Furthermore, the early fast partial recovery seen at the other positions is absent. This is similar to what is described in [54, 154] for higher fluences, for example, or in [245] for high ambient temperatures.

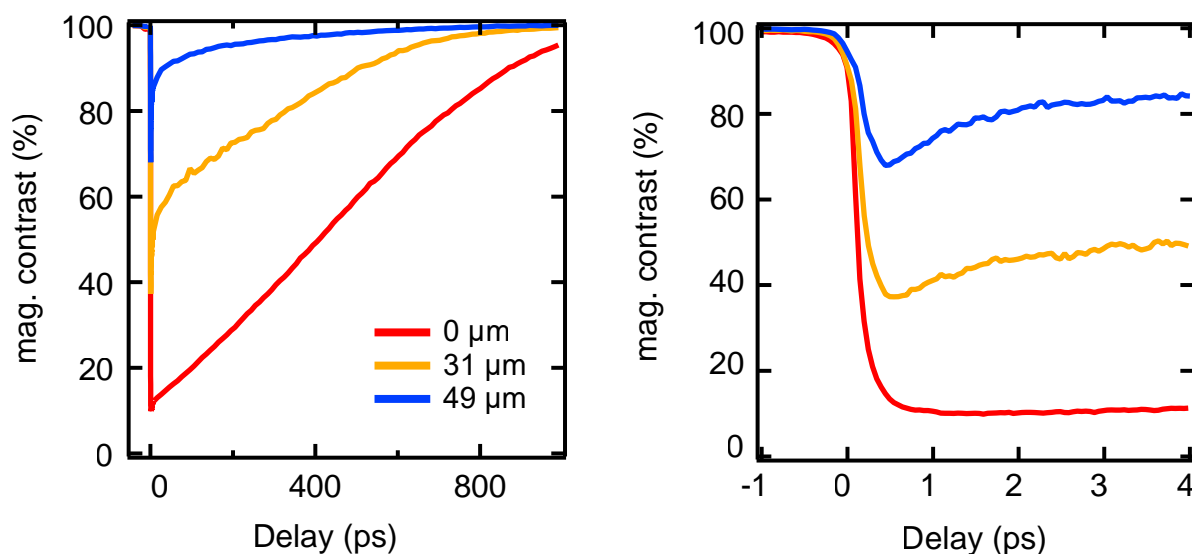


**Figure 7.5:** Left: Time evolution of the magnetic contrast measured in P1 after excitation with  $6.9 \text{ mJ cm}^{-2}$  recorded by TR-MOKE. Three positions corresponding to a shift of the pump pulse away from the central pump-probe overlap as indicated in the legend. The highest amount of magnetization is quenched in the center. Right: A zoom on the early timescales of the dynamics presented in the left panel. The overall shape follows the dynamics expected for an increased fluence from the edge to the center of the pump pulse.

Suppose the transient temperature reached, dictated by the fluence at the probing spot, were the only decisive factor for the de- and remagnetization. In that case, the same trend of the dynamics should be observed at each spot when changing the fluence accordingly. We vary the fluence at different pump-probe overlaps, aiming at a comparable quench of magnetization in each position to test this hypothesis. First we change the fluence while keeping the probe pulse in the center of the pump, and afterward, with the pump moved by 49  $\mu\text{m}$ . The recorded traces are shown in Fig. 7.6.

We observe that the dynamics at the edge, i.e., with the maximal displacement of the pump beam, are different compared to the ones in the center for all investigated fluences. Most notably, when the probe is not centered in the pumped region, a fast early recovery is measured even at the highest fluence. In the center, a slowdown of the recovery and the absence of the initial fast recovery is already found at a demagnetization of about 60%. Nevertheless, the

dynamics remain fast, both at the early times and later, with the displaced pump at a quench of about 80 %.

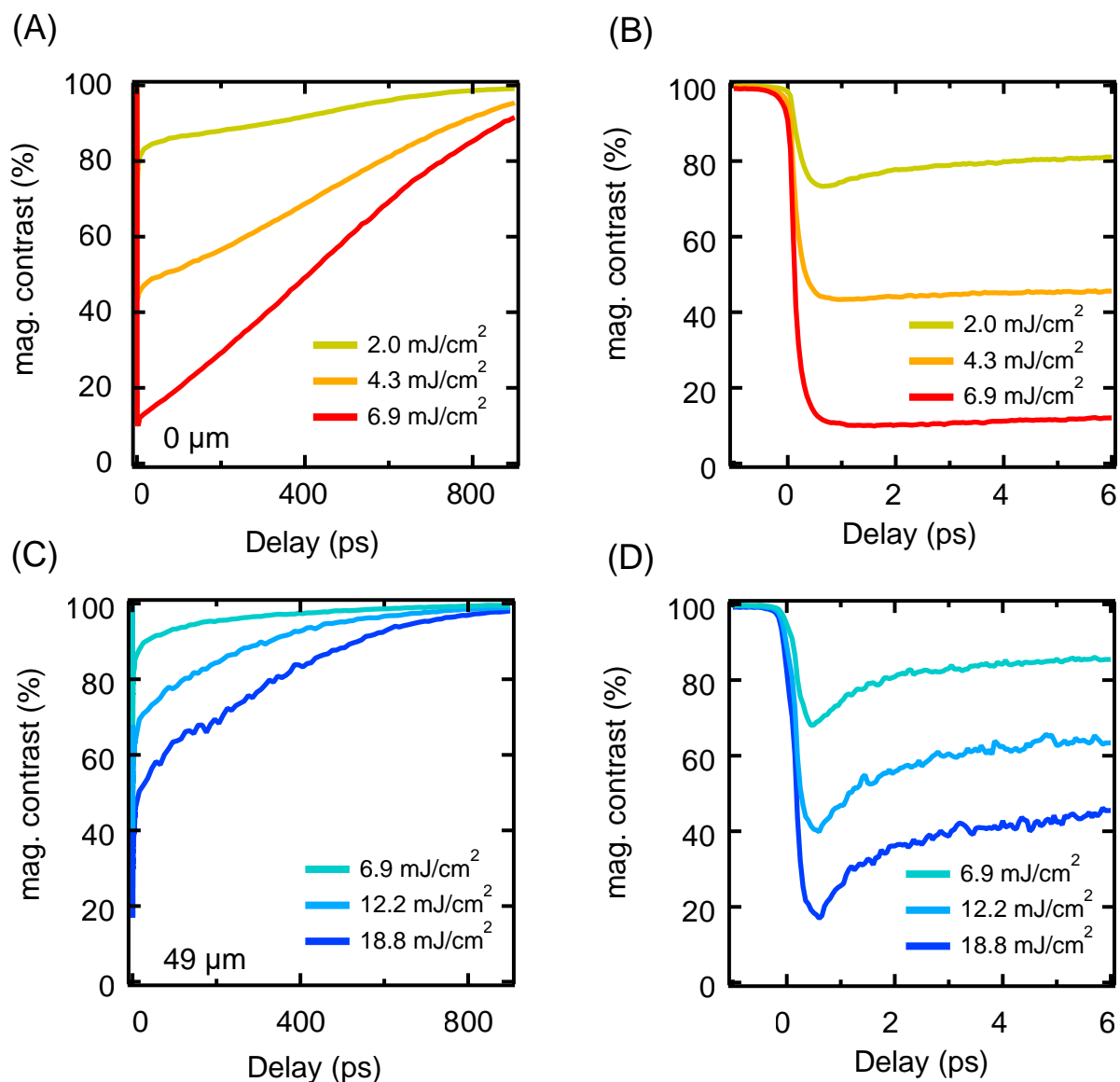


**Figure 7.6:** (A) Delay time trace of the magnetic contrast measured on P1 with the probe spot centered in the pumped region. (B) The same dynamics as shown in (A) around the early delay times. (C) Magnetic contrast after excitation with the pump displaced by 49 μm. The fluence is adjusted to achieve a reduction of the signal comparable to the traces measured with the probe centered. (D) Zoom of the dynamics shown in (C) around time zero.

The assumption that the contrast change is governed solely by the excitation power and, therefore, the temperature reached at a given position cannot explain this finding. Now, it is interesting to clarify if a lower sample base temperature off-center compared to the center explains the findings, or perhaps ultrafast thermal and even spin transport needs to be considered to explain the difference. A difference in the base temperature is caused by heat transport away from the region of interest. In the center, in contrast to the displaced scenario, no lateral thermal

gradient is present, and in-plane transport is negligible. However, the effect of lateral transport in the presence of a strong thermal gradient in ultrafast dynamics has not been investigated. We perform simulations of ultrafast heating in a 3D model system to describe the temperature evolution in the center and 49  $\mu\text{m}$  off-center transiently and in-between pulses.

First, we estimate the absolute displacement. As already mentioned, the displacement is calculated from the convolution of the probe with the pump beam, shown in Fig. 7.7. We use the FWHM for each pulse as measured and according to the angle of incidence, shown in the left panel of Fig. 7.7. The displacement is derived from the relative demagnetization amplitude measured for the three different positions. The highest amplitude is found in the center of the pump pulse, and the other two positions then correspond to the intensity of the convolution matching the relative demagnetization amplitude. In this estimation, we assume that the same fluence leads to the same quench of magnetization at each position. This is not contradicting the findings presented in Fig. 7.6 since mainly the recovery of magnetization is vastly different when displacing the pump.

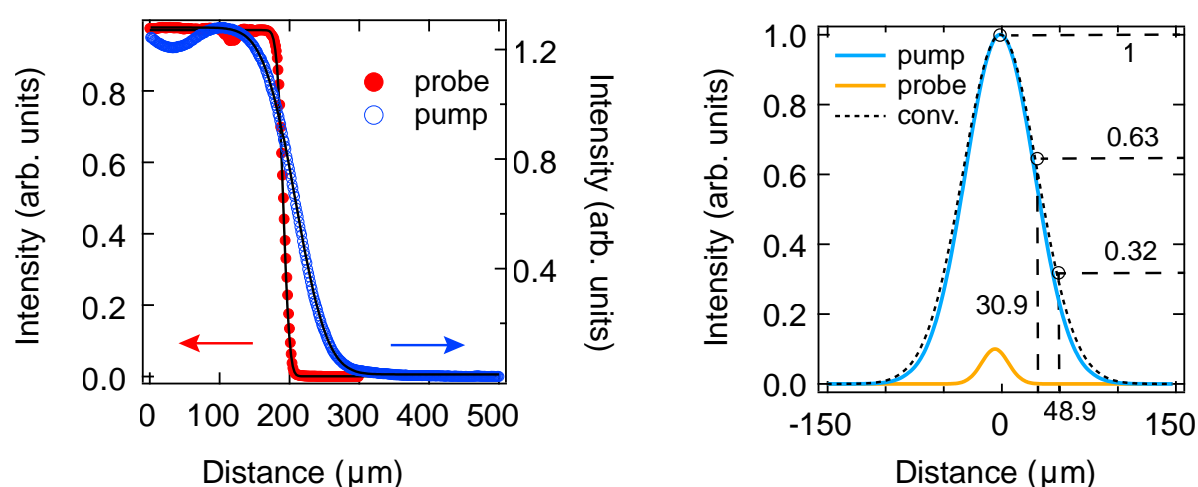


**Figure 7.7:** Left: Knife-edge measurement of the pump (open symbols) and probe (filled symbols) beams. The intensity is fitted by an error function (black, solid lines) to extract the FWHM of the beam. The probe diameter is found to be  $(14.1 \pm 0.1) \mu\text{m}$ , and  $(71 \pm 1) \mu\text{m}$  is found for the pump diameter. Right: Evaluation of the pump displacement. The absolute displacement is evaluated from the spot sizes of the pump and probe beam and the induced quench measured at the different positions. The displacement is found in the convolution of the two Gaussian pulses, where the intensity corresponds to the relative demagnetization amplitude. In other words, the maximum quench of 90 % at the center corresponds to 1, and a lower quench of, for example, 57 % corresponds to 0.63. The demagnetization amplitude is presented in Fig. 7.6. The open circles indicate the measured relative amplitude and the corresponding displacement.

Secondly, the sample base temperature is different at the probed position when changing the pump-probe overlap. The sample base temperature is estimated by hysteresis loops recorded in the center at negative delay times and different fluences. From the change of saturation magnetization, we derive the change of base temperature. The magnetization vs. temperature curve is obtained by fitting a critical exponent function of the form

$$M(T) = M_0(1 - (T/T_C)^{3/2})^{3/4} \quad (7.1)$$

to data published in [246] in Fig. 1 (b). The fit results in a  $T_C$  of  $(540 \pm 10)$  K. The error estimated here is larger than the one obtained from the variance since the data is manually digitalized from the plot. Furthermore, the sample in this study is slightly different. The data of [246] is recorded on 3 nm Pt/0.52 nm Co/2 nm Pt. The sample investigated here consists of 3 nm Pt/0.52 nm Co/1 nm Pt. It has been shown that the induced magnetization in the adjacent Pt layer stabilizes the magnetization and increases  $T_C$  [247]. However, the induced magnetization in the Pt layer saturates at about 1 nm [244]. In conclusion, the critical temperature in Co in our sample might be slightly lower than what is fitted from the data of [246]. Nevertheless, we expect the difference to be insignificant. The recorded hysteresis and the M vs. T curve are shown in Fig. 7.8 with the corresponding temperatures marked. Using a fluence of  $2.0 \text{ mJ cm}^{-2}$  did not result in a noticeable reduction of the magnetic contrast in saturation. Therefore, we assume a sample temperature of 300 K for this measurement. The temperatures corresponding to the other recorded fluences are derived from the relative change of magnetization. Indicated by the markers in the right panel of Fig. 7.8, we expect a sample base temperature in the center of the excited region of 300 K at  $2.0 \text{ mJ cm}^{-2}$ , 435 K at  $4.6 \text{ mJ cm}^{-2}$ , and 514 K at  $9.2 \text{ mJ cm}^{-2}$ .

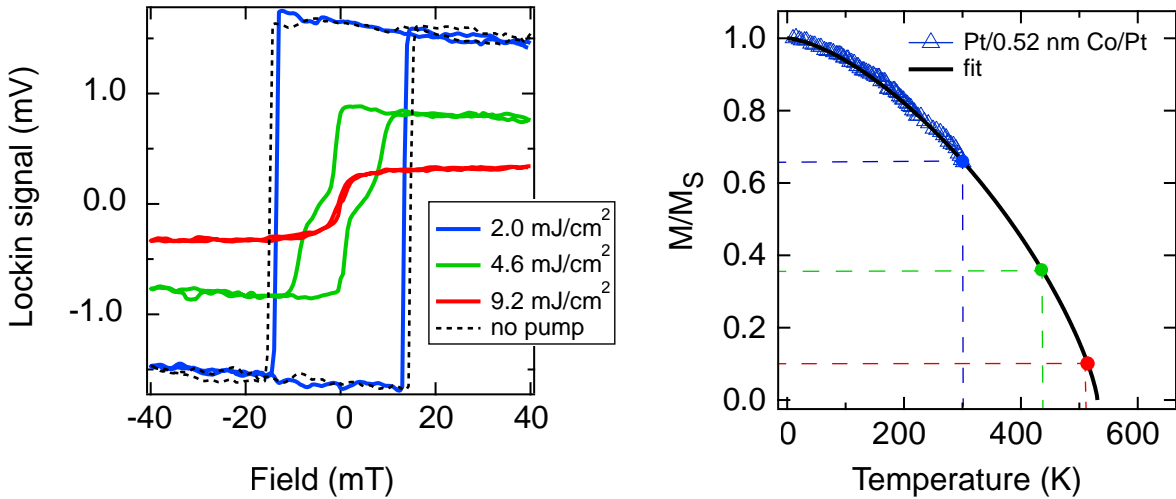


**Figure 7.8:** Left: Measured hysteresis loops on P1 at negative delay times. The sample base temperature rises upon increasing the laser fluence, resulting in a diminished saturation magnetization and coercive field. At  $2.0 \text{ mJ cm}^{-2}$ , the saturation magnetization is similar to the one measured without pumping, shown as the dashed line. Therefore, we approximate the sample base temperature to be 300 K at  $2.0 \text{ mJ cm}^{-2}$ . Right: Estimated magnetization vs. temperature curve in P1. The curve is modeled by a critical exponent function described in the text. The Curie temperature is fitted from data of a 2 nm Pt/0.52 nm Co/3 nm Pt/5 nm Ta/SiO sample published in [246], shown as the triangles. The sample investigated here is grown on a 3 nm Ta buffer layer and capped with only 1 nm Pt. However, we believe that neither of these properties significantly affects the Curie temperature. We estimate the sample base temperature for the employed fluence from the relative change in magnetization and the magnetization vs. temperature evolution.

Lastly, we model the magnetization dynamics by the m3TM, using the parameters for Co dis-

cussed in the previous section. On the one hand, to estimate the agreement between the experiment and the model. On the other hand, to estimate the fluence and the expected lattice temperature increase on the short timescale. We start by discussing the magnetization dynamics obtained with the m3TM presented in Fig. 7.9 in the right panel.

To model the magnetization in the m3TM, the parameters introduced in the last section and summarized in Table 6.1 are employed. A linear heat capacity and a reduced  $T_C$  of 540 K, according to Fig. 7.8 are employed. The fluence is matched to the experimental demagnetization resulting in  $3.5 \text{ mJ cm}^{-2}$  instead of the experimentally evaluated  $4.3 \text{ mJ cm}^{-2}$ . The fluence in the experiment is derived from the beam diameter, the repetition rate, and average power measured before each experiment. The sample base temperature at  $4.3 \text{ mJ cm}^{-2}$  is assumed to be 420 K, slightly below the estimated 435 K shown in Fig. 7.8 for  $4.6 \text{ mJ cm}^{-2}$ . The resulting magnetization dynamics describe the ultrafast magnetization change. However, the recovery, or rather the lack thereof, is not captured in the model. For comparison, the dynamics recorded at the displaced position using a different fluence are shown in the same graph. The magnetization dynamics at  $49 \mu\text{m}$  from the center are captured well by the model despite a slight mismatch of the overall demagnetization, which could, of course, be adjusted in the simulation.

The electron and lattice temperature increase resulting from laser heating is shown in the left panel. The model predicts an increase in the lattice temperature to about 479 K.

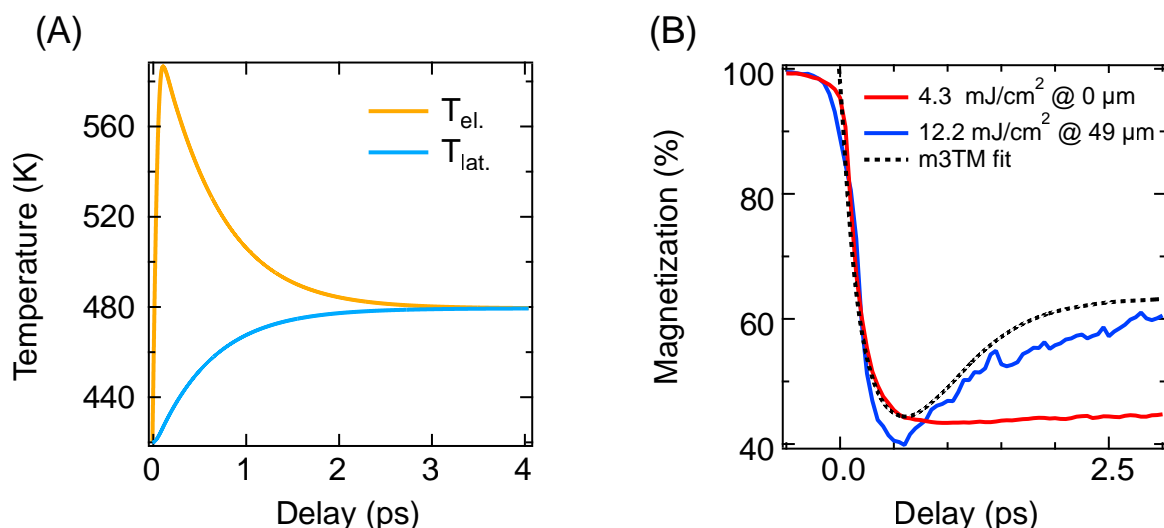


**Figure 7.9:** (A) Electron and lattice temperature evolution in Co evaluated by solving the m3TM equation using the constants described in Table 6.1. The fluence is fitted to match the experimental demagnetization shown in (B). In the simulation  $3.5 \text{ mJ cm}^{-2}$  is found to best describe the experiment. (B) Demagnetization determined from the magnetic contrast in the MOKE recording evaluated at the center of the pump (red) and at a higher fluence  $49 \mu\text{m}$  shifted. The fitted demagnetization is shown as the dashed black line.

The sample base temperature increase, judged by the diminished saturation magnetization shown in Fig. 7.8, and the transiently reached peak of the lattice temperature in Co is used in the following to model the sample in a 3D system after laser excitation. The simulations are employed to investigate the following hypothesis: The greatly reduced speed of magnetization recovery in the center compared to  $49 \mu\text{m}$  away is induced by a higher sample base temperature in the center. The higher base temperature leads to a lower saturation magnetization and,

therefore, a lesser driving force to align the magnetic moments. A similar effect is observed in the hysteresis loops when approaching remanence, see Fig. 7.8. Due to the absence of a recovery without the external field, the hysteresis loops show a step-like zero-crossing. In a similar fashion, the remagnetization is hindered even in the presence of the external field since the residual magnetization is significantly reduced.

We simulate the temperature evolution in a  $N_x \times N_y \times N_z$  point grid. In the lateral dimension, we use  $N_x = N_y = 250$  to capture the extent of the laser pulse and the heat diffusion in the sample plane. Since the sample depth is significantly smaller vertically, only  $N_z = 20$  points are used. The system corresponds to a  $250 \times 250 \times 1 \mu\text{m}^3$  slab. The vertical plane distance corresponds to 50 nm, and laterally the points are  $1 \mu\text{m}$  apart to keep the computation time reasonable. The system is illustrated in Fig. 7.10. An outer layer, kept at 300 K, is added to the system to model the heat dissipation away from the region of interest.

The model system is comprised of an air layer used to decouple the surface layer from a direct heat transfer into the boundary. The atomic layers of the sample are not modeled since the spacing is too small to be captured at the same time as the  $250 \mu\text{m}$  xy-dimension. Instead of the individual layers, a 50 nm thick "metal" layer is simulated, using the thermal properties of Co, Ta, and Pt according to their relative thickness. Below the metal layer, a 100 nm  $\text{SiO}_2$  layer is included. The remaining  $0.8 \mu\text{m}$  are modeled as pure Si. The constants employed in the simulation found to best describe the temperatures evaluated in Fig. 7.8 and Fig. 7.9 are presented in Table 7.1. Specific heat and thermal conductivity are approximated by a linear temperature dependence.

We model the thermal transport by a diffusion approach, given by

$$\rho(z)c_p(z,T)\frac{\partial T}{\partial t} = \kappa(z,T)\frac{\partial^2}{\partial^2 r}T(r,t) + S(t,r), \quad (7.2)$$

with the material density  $\rho$ , the specific heat  $c_p$ , the thermal conductivity  $\kappa$ , and a source term  $S$ . The source term is only acting on the metal layer. Judging by the evaluation of the optical absorption presented in Fig. 7.3 this is justified since hardly any light penetrates deeper and, furthermore, the dielectric  $\text{SiO}_2$  is mostly transparent at 800 nm. The heat capacity and thermal conductivity are both temperature- and depth-dependent since the thermal properties are different in each layer.

We solve the temperature evolution in  $0.1 \mu\text{s}$  steps using a finite difference approach, where the second derivative is solved as the central difference like

$$\frac{\partial^2 T}{\partial^2 r} = \sum_{ij} \frac{T(x_{i-1,j}) - 2T(x_{i,j}) + T(x_{i+1,j}))}{\Delta x_{i,j}^2}, \quad (7.3)$$

counting the dimensions by  $j$  and the points by  $i$ .

The result from heating the system by a single laser pulse and the heating from hitting the sample at a 250 kHz repetition rate, as used in the experiment, are shown in Fig. 7.10 (B). After about  $150 \mu\text{s}$ , the sample base temperature has stabilized at a new value. In the figure, the result of heating the sample with an incident fluence of  $4.3 \text{ mJ cm}^{-2}$  is shown. We use the  $4.3 \text{ mJ cm}^{-2}$  measurement to adjust the fluence in the simulation. All other fluences are consecutively scaled from this value and not fitted. Note that in the description, we always refer to the experimental value of the fluence. However, in the simulation, the fluence is scaled lower by a factor of 0.82, as explained in Fig. 7.9. Additionally, the spatial evolution of the temperature in the metal layer is presented in panels (C) and (D). Shown is the temperature profile at the elevated base

temperature,  $0.1 \mu\text{s}$  before the arrival of the consecutive pump pulse. A line profile along the  $y$ -dimension, shown as the dashed line in (C), is used to derive the sample base temperature at the center of the excitation and  $49 \mu\text{m}$  away, corresponding to the measurement with a displaced pump. The evaluated temperature profiles along the line for different excitation fluences are presented in Fig. 7.11.

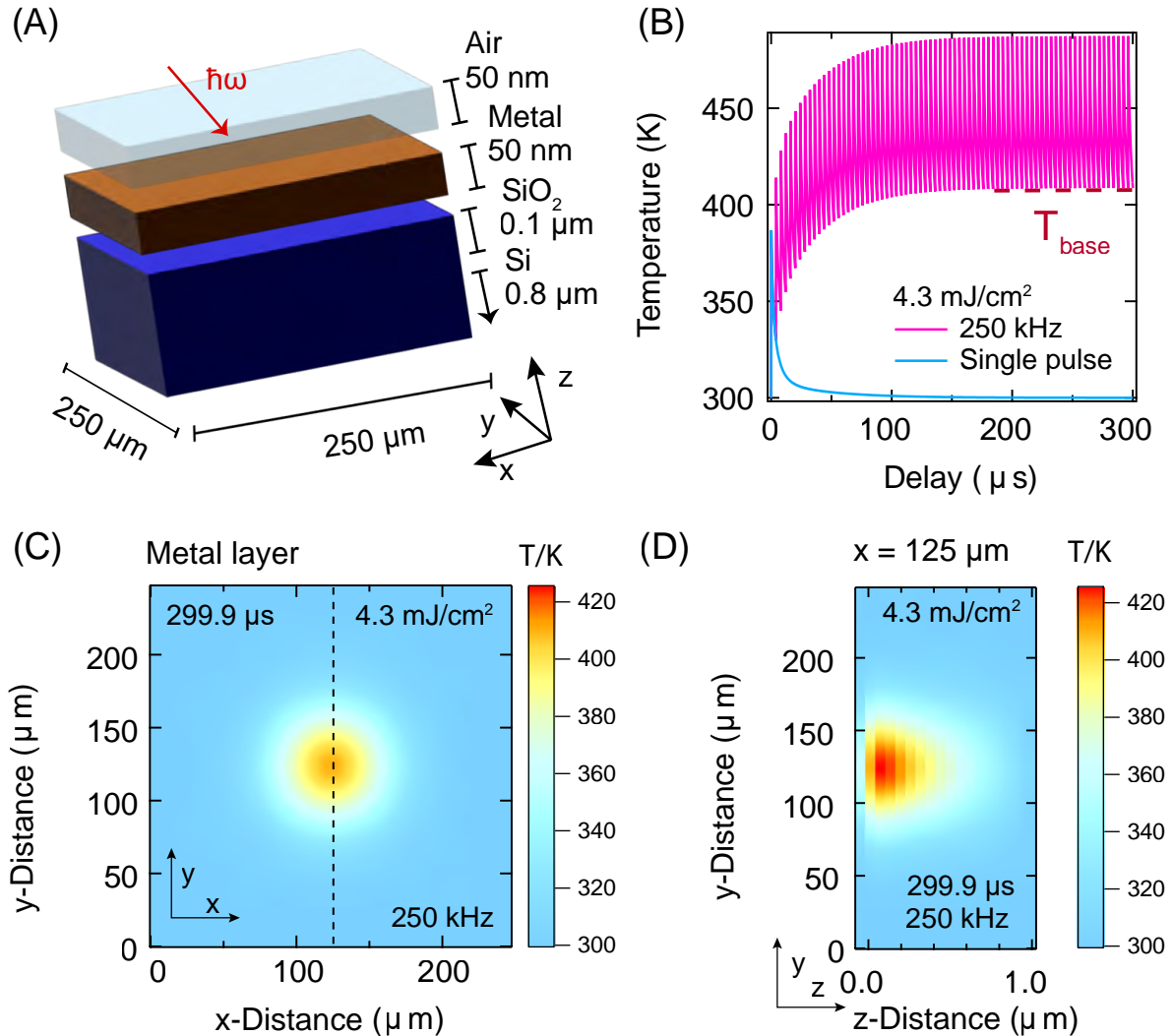


**Figure 7.10:** (A) Illustration of the geometry and dimensions used to simulate the thermal diffusion in a 3D system after laser excitation. The whole sample is approximated by a  $250 \times 250 \times 20$  point grid. The lateral spacing is  $1 \mu\text{m}$ , and the vertical spacing is  $0.05 \mu\text{m}$ . In the simulation, Dirichlet boundary conditions are implemented as a heat sink. In total  $N+2$  points are simulated in each dimension. (B) Simulated temperature evolution in the center of the heated region when applying a single pulse and with pulses every  $4 \mu\text{s}$  corresponding to a repetition rate of 250 kHz. After around  $150 \mu\text{s}$ , a new sample base temperature of 419 K is reached. (C) XY-slice of the metallic layer after  $299.9 \mu\text{s}$  heating with 250 kHz. The vertical dashed line indicates the position at which the temperatures are compared in Fig. 7.11. (D) YZ-slice at  $x = 125 \mu\text{m}$ .

Parameter	Air	Metal layer <sup>†</sup>	SiO <sub>2</sub>	Si
$\kappa$ (W/(m K))	$1.5 \times 10^{-3}$ <sup>A</sup>	$80 - 0.009T'$	$0.380 + 0.003T'$ <sup>B</sup>	$19.9 - 0.016T'$ <sup>C</sup>
$c_p$ (J/(kg K))	700 <sup>D</sup>	$169 + 0.06T'$	$670 + 0.65T'$ <sup>D</sup>	$710 + 0.2T'$ <sup>D</sup>
$\rho$ (kg/m <sup>3</sup> )	1.2923 <sup>D</sup>	18673	2650 <sup>E</sup>	2329 <sup>E</sup>

**Table 7.1:** Parameters used in eq. (7.2) to model the heat diffusion in the 3D system. The temperature  $T'$  is defined as  $T/K$ . <sup>†</sup> The thermal properties of the metal layer are mixed as 4 Pt:3 Ta:0.5 Co according to the thickness in nm of the actual sample. The properties of Pt, Co, and Ta are listed separately in Table 7.2. <sup>A</sup> ref. [248], <sup>B</sup> ref. [249], <sup>C</sup> ref. [250], <sup>D</sup> ref. [217], <sup>E</sup> ref. [214].

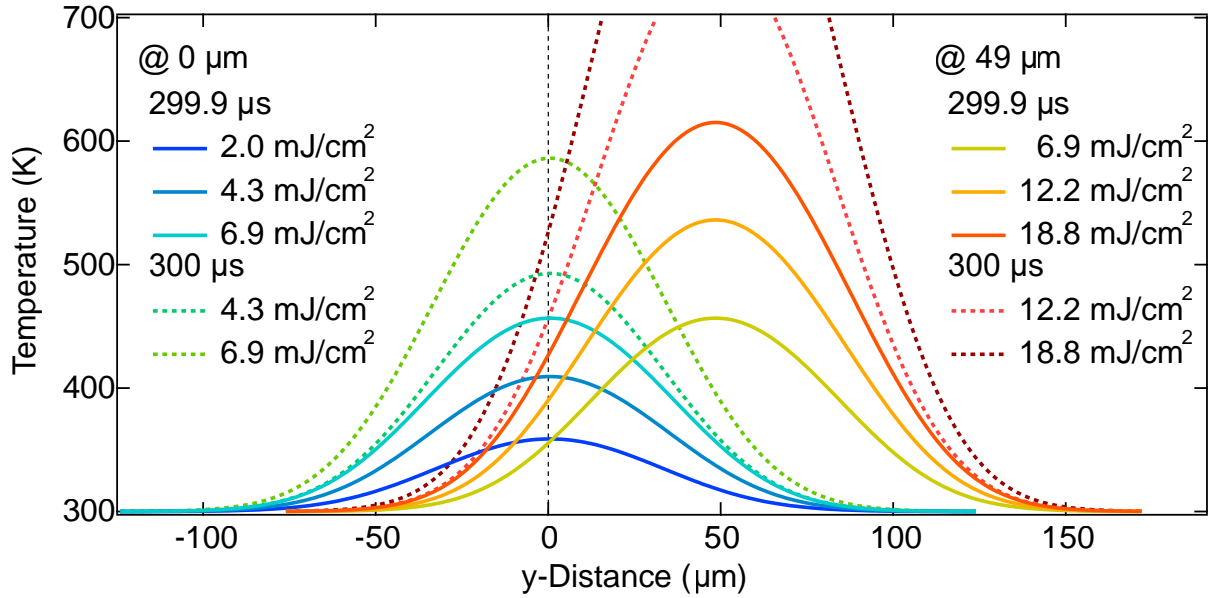


**Figure 7.11:** Temperature of the metal layer along the  $y$ -axis at the center of the  $x$ -axis as indicated in panel (C) of Fig. 7.10 with the center put to 0. The temperature profile is shown at 299.9  $\mu\text{s}$ , just before laser excitation (solid lines), and at 300  $\mu\text{s}$ , just after laser excitation (dashed lines). The temperature resulting from the fluences applied with the beam displaced along  $y$  are shifted by 49  $\mu\text{m}$  to allow a direct comparison at the probed position. Judging by the simulation, the sample base temperature as well as the transiently reached maximum are lower than the temperatures in the center at a comparable magnetic quench, compare Fig. 7.6.

From the simulated temperature profile, shown in Fig. 7.11, the sample base temperature upon repetitive pulsing and the maximum after pulse arrival is obtained. We can now compare the base temperature at the center and 49  $\mu\text{m}$  off-center using the same fluences as in the experiment. Comparing the 4.3  $\text{mJ cm}^{-2}$  and the 12.2  $\text{mJ cm}^{-2}$  curves, the temperature difference is about 18 K, with the one in the center being higher. The magnetic dynamics, however, are quite different and a difference of less than 20 K is most likely not sufficient to explain the different dynamics. Comparing 6.9  $\text{mJ cm}^{-2}$  and 18.8  $\text{mJ cm}^{-2}$  in the same fashion shows a difference of 28 K. After excitation, a transient temperature of 586 K (6.9  $\text{mJ cm}^{-2}$ , center) and 529 K (18.8  $\text{mJ cm}^{-2}$ , 49  $\mu\text{m}$ ) is reached. The difference in the transiently reached temperatures is more significant and might help explain the difference seen in the magnetization dynamics. It should be noted, though, that the sample base temperature at 18.8  $\text{mJ cm}^{-2}$  is already 19 K

Parameter	Co	Pt	Ta
$\kappa$ (W/(m K))	$3.6 + 0.012T'^A$	$106 - 0.02T'^B$	$58 + 0.0025T'^C$
$c_p$ (J/(kg K))	$693 + 0.6T'^D$	$128 + 0.025T'^E$	$137 + 0.018T'^F$
$\rho$ (kg/m <sup>3</sup> )	$8860^G$	$21450^H$	$16600^H$

**Table 7.2:** Relevant material properties for Co, Pt, and Ta. The linear temperature dependence of the specific heat and thermal conductivity is fitted in the region from 300 K to 1250 K. The temperature  $T'$  is defined as  $T/K$ . All values are taken from bulk measurements and finite size scaling might affect the properties. For example, the heat capacity in Co is likely underestimated here since a spin contribution around  $T_C$ , which is around 600 K in our sample, is neglected. <sup>A</sup> ref. [251], <sup>B</sup> ref. [252], <sup>C</sup> ref. [253], <sup>D</sup> ref. [209], <sup>E</sup> ref. [254], <sup>F</sup> ref. [255], <sup>G</sup> ref. [217], <sup>H</sup> ref. [214].

higher at 49  $\mu\text{m}$  from the center compared to the  $4.3 \text{ mJ cm}^{-2}$  measurement. The remagnetization dynamics of the latter are, however, not faster but significantly slower. Overall, although the temperature is lower off-center compared to the center, the difference is too small to explain the different remagnetization. Moreover, the base temperature reached off-center at a high fluence exceeds the base temperature in the center at lower fluences, yet a faster recovery is still measured.

The model employs several approximations and is only used to roughly estimate the temperature evolution after repetitive laser excitation. Nevertheless, the simulation is robust with respect to small changes in the material parameters, and a significant deviation from the temperature ratios described here is not found in a reasonable parameter space. It should be noted that the thermal diffusion model predicts that at the employed fluences, for example, comparing  $6.9 \text{ mJ cm}^{-2}$  in the center and  $18.8 \text{ mJ cm}^{-2}$  at 49  $\mu\text{m}$ , different sample base and maximal temperatures are reached. However, in the experiment, the fluences resulted in the same relative demagnetization. So far, we employed the assumption that the demagnetization amplitude is derived from the transiently reached temperature and vice-versa, for example, in Fig. 7.9. The dependence of the demagnetization on the sample temperature is not trivial, as has been discussed already in chapter 4 since most of the material parameters are also temperature-dependent, and their precise scaling is often unknown.

That different base temperatures across the excitation region are found, affects the estimation of the absolute displacement shown in Fig. 7.7. In case the demagnetization is not only affected by the local fluence but also by a temperature profile, different in shape compared to the exciting pulse, the estimated displacement is slightly off. Assuming a lateral profile as calculated in the diffusion model, we expect that the temperature off-center is lower compared to the center and, therefore, a higher relative fluence is needed compared to the case of an equal base temperature. Effectively this results in a smaller displacement than what is estimated in Fig. 7.7. Following this argumentation, we compare the temperatures in the center and, for example, at 45  $\mu\text{m}$  away in Fig. 7.11. Then, one finds virtually equal base and transiently reached temperatures in both positions.

Nevertheless, we employ the m3TM to calculate the expected demagnetization dynamics using the temperatures derived from the heat diffusion calculation. The spatial magnetization profile over delay time is calculated by solving the three coupled equations of the m3TM in the frame of the same system used for the "slow" heat diffusion. Instead of simulating the evolution over several  $\mu\text{s}$ , we now investigate the properties in 10 fs time steps up to several ps. The lattice heat capacity and thermal conductivity are split into a constant lattice and a temperature-

dependent electronic contribution. The laser acts only on the electron temperature, and the heat is consequently distributed to the lattice. The magnetization is calculated from the temperatures according to eq. (6.3) and the parameters used are listed in Table 6.1. The system is initialized with the temperature profile of the "slow" simulation at  $299.9\ \mu\text{s}$  to describe the experiment. The results of the simulation of the magnetization is presented in Fig. 7.12.

The demagnetization is captured quantitatively well. The simulated amplitudes at the lowest fluence are slightly lower than the experimentally observed quench. At the highest fluence in the simulated system, the magnetization is quenched entirely. In the experiment, the system remains at a finite magnetization. At a quench of about 60 %, the early remagnetization happens much faster in the simulation compared to the experiment. Most importantly, the simulation does not capture the complete absence of remagnetization in the center. Only in the case of the highest fluence, where the system completely demagnetizes because it is heated above  $T_C$ , the remagnetization is as slow as in the experiment. The early recovery of magnetization in the simulation is driven by the temperature equilibration between the heat reservoirs of the electrons and the lattice. However, if the system stays at a temperature above  $T_C$ , no magnetization is recovered, and the remagnetization happens on the timescale of lattice cooling.

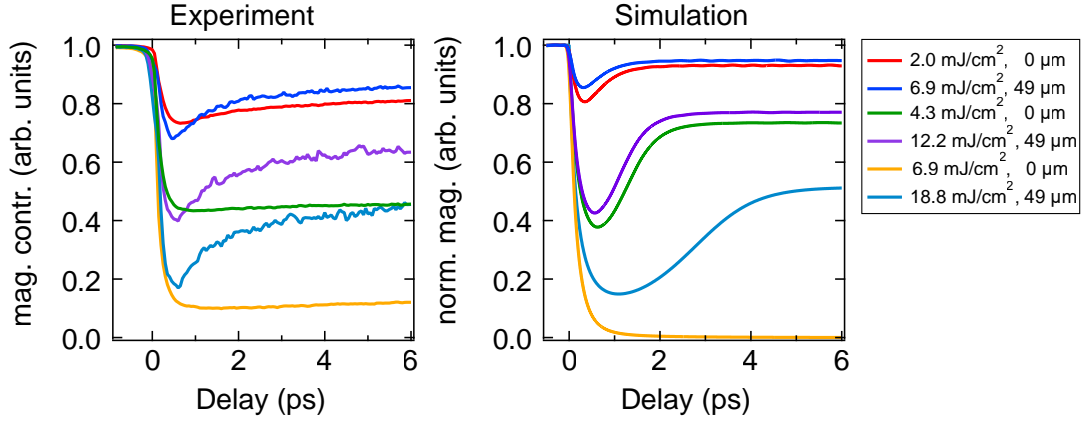


**Figure 7.12:** Experimental magnetic contrast (left panel) and simulated magnetic contrast (right panel) in the center of the pump and  $49\ \mu\text{m}$  off-center using the sample base temperature calculated by the heat diffusion model. Only the sample base temperature and the fluence are adjusted to the experiment. The  $T_C$  fitted in Fig. 7.8 is used. All other employed parameters are given in Table 6.1. The simulation does not predict a significant difference in the magnetization dynamics for the lower fluences. Only very close to  $T_C$  a noticeable difference similar to the experimental curve is predicted.

The different dynamics measured at the center of excitation and off-center are not explained by different sample base temperatures in the present model, judging by the comparison of the experiment and the simulation presented in Fig. 7.12. The simulation predicts a very slow remagnetization when the lattice system is heated above  $T_C$ . However, the slow dynamics are also observed at low and middle fluences in the experiment. Furthermore, the evaluation of the sample base temperature with a displaced pump shows that at the highest fluence, the base temperature is even higher than in the center with a lower fluence. Nevertheless, a fast recovery is measured with the displaced beam. The results shown here depend on the absolute displacement evaluated from the magnetic quench measured in the experiment. We consider

the estimation to be an upper bound since the effect of the local sample temperature is not considered. Considering a smaller absolute displacement, the difference is even less likely to be explained by a different sample base temperature since both are similar when comparing the different fluences.

The observations could be explained if the sample temperature at the center for all fluences is close to  $T_C$ , and the temperature with the displaced beam is always close to room temperature. This is not compatible with the predictions of the heat diffusion model presented here. At the time of writing, further avenues of explanations for the dynamics are explored. First, the model does not incorporate superdiffusive or ballistic transport. It is possible that, due to the dielectric substrate, superdiffusive currents driven by the excitation do not propagate vertically in the sample but only laterally. The redistribution of majority spins away from the center of excitation in the direction of the thermal gradient may exert a torque on the magnetization and drive a faster remagnetization compared to the one in the center. Secondly, the remagnetization in the center resembles the case of a complete demagnetization, see Fig. 7.12 or the remagnetization in the absence of an external field and a large demagnetized area. The latter results in a slow remagnetization since no magnetic dipole field recovers the magnetization, for example, in Co/Pt multilayers in [256]. Therefore, another hypothesis is that in the center, due to the high fluence and the high repetition rate, the system is driven into a multidomain state, seen in Co/Pt layers, for example, in [238, 239]. In the multidomain state, no preferential magnetization direction is recovered, and "slow" domain wall dynamics driven by the external field govern the recovery of magnetization. Adjustments to the model to incorporate local demagnetizing fields and ultrafast transport are currently being tested, and further spatially resolving experiments are planned to arrive at a conclusive answer.

## 7.2 Summary and conclusion

This chapter presents two experiments investigating the delay-time-dependent magnetization after optical excitation in Co/Pt with an out-of-plane easy axis. First, a comparison of a Co/Pt bilayer grown on Si with a native SiO<sub>2</sub> layer with a Co/Pt/MnPt/Pt system is shown. The data shows that the two samples are quenched differently when employing the same excitation. The bilayer sample is quenched more strongly, but the minimum of magnetization is reached later at all investigated fluences. We attribute the difference to exchange of spin currents between the antiferromagnetic MnPt and the Co/Pt layers.

In the second experiment, the dependence of the magnetization dynamics on the spatial overlap of the pump and probe beam is investigated. A significantly faster remagnetization is measured when the probed area is not centered in the pumped region. We study the temperature evolution after laser excitation in a 3D model system to estimate the effect of an increased sample base temperature. The base temperature is found to be up to 30 K higher in the center compared to the side at a fluence where the same relative magnetic quench is measured. The temperature difference is not enough to explain the observed difference in a simple m3TM calculation. Therefore, we conclude that a different base temperature induced by the repetitive pumping is not sufficient to explain the differences between the dynamics in the center and about 50  $\mu\text{m}$  away observed with the same local fluence. The mechanism responsible for the different dynamics is still unclear, and further avenues are investigated at the time of writing.



# Chapter 8

## Conclusion

This thesis presents four experimental reports focusing on different aspects of magnetization after ultrafast excitation. We investigate transition metal layers coupled to heavy metals and antiferromagnetically ordered films. The common denominator in all presented experiments is the ultrashort excitation by laser pulses and the concomitant reduction of magnetization in the ferromagnetic layer. Furthermore, evidence for a short-lived transient ferromagnetic state in an elemental antiferromagnet is presented. The investigations ultimately try to answer the questions posed initially.

We can conclude that the ultrafast demagnetization can not be treated exclusively as a local phenomenon within the ferromagnetic layer. Experimental evidence is presented that an antiferromagnetic layer adjacent to a FM layer influences the ultrafast dynamics. Furthermore, observations exploiting the magneto-optical Kerr effect suggest that even if a Pt spacer layer separates the FM and AFM layer, an influence on the demagnetization is measured. The findings highlight that spin transport and spin transport-related phenomena like scattering, reflection, and spin-transfer torque can affect ultrafast dynamics.

Coherent effects, suggested from the very beginning of ultrafast research, are investigated concerning the magnetic dynamics of Mn atoms, where an indication of a coherent realignment of spins is found in the presence of the light field. The findings support predictions by time-dependent density functional theory and highlight the importance of symmetry breaking at interfaces. Lastly, we can also add a small insight into remagnetization dynamics. Most importantly, in addition to what has been shown elsewhere, remagnetization, even with a static field applied, can be very different at the same relative quench of magnetization. The mechanism for the different remagnetization dynamics investigated in the last chapter remains elusive and different avenues for explanations are currently being explored.

Ultimately, we can summarize that the four presented studies illuminate the process of light-induced magnetization dynamics starting from the moment of excitation, where coherent dynamics are driven as shown in chapter 5, covering the thermalization of electrons and lattice within 1 ps to 2 ps, see chapter 4, and up to the equilibration of the sample temperature after several  $\mu\text{s}$ , see chapter 7. We support the experimental findings by simulations of the X-ray reflectivity, presented in chapter 6, the primary source of information in this thesis, which allows us to directly link the experimental observable to the underlying magnetization. Furthermore, the simulations allow us to follow the structural evolution of the lattice and describe the effect of the transient optical response function after excitation.

Put together, the observations presented in this thesis emphasize that the magnetic response at

the ultrafast timescale is directly linked to the nature of the exchange interaction in the investigated system. Although the antiferromagnetic system is not directly investigated, the influence thereof is observed indirectly in an adjacent layer. The findings are explained in the terminology of the current models and the measurements are for the most part reproduced by simulations. The interpretations of the experiments shown in chapter 4 and 7 emphasize the importance of ultrafast transport and its influence on the observed magnetic contrast after laser excitations. In the presence of the laser pulse, coherently driven electronic and thus also magnetic dynamics are investigated. That the observations are not only an artifact of the observable as discussed in many magneto-optical experiments is supported by DFT calculations and simulations of the samples' magnetic and structural evolution after excitation. Together, this highlights that there is still no unifying model which describes the ultrafast excitation from time zero to the recovery into a steady state. A conclusive theoretical description of the processes following laser excitation in magnetic metallic and dielectric systems is actively being researched and presents one of the challenges in ultrafast magnetism research. Refinements of the initial three-temperature model into the m3TM and more recently into the  $\mu$ 3TM need to be combined with transport models. The refined models further aim to include the descriptions of the non-thermal magneto-optical effects. And lastly, also the remagnetization influenced by local demagnetizing fields, the transient exchange interaction, and proximity effects needs to be included for a complete description.

Experimentally, the research of ultrafast magnetism has shifted its focus towards (synthetic) antiferromagnetic or ferrimagnetic structures implementing promising deterministic all-optical switching pathways [200] and combining these approaches with novel device designs [257]. Fundamental research aims to explore the details of energy flow between the involved reservoirs in antiferromagnetic materials [258–260]. Novel ultrafast research accompanies the advent of 2D (antiferro-) magnetic materials [261–263] that promise exciting possibilities for new physics and functional layers [264–266]. To summarize, the research of ultrafast light-induced spin dynamics is still far from reaching saturation and both fundamental research and transfer of lab observations into new devices remain interesting and challenging.

# List of Publications

## 2022

R. Hosseinifar, E. Goliias, I. Kumberg, Q. Guillet, K. Frischmuth, S. Thakur, M. Fix, M. Albrecht, F. Kronast, and W. Kuch: *Influence of magnetic domain walls on all-optical magnetic toggle switching in a ferrimagnetic GdFe film*. Beilstein J. Nanotechnol. **13**, 74.

## 2021

T. Shinwari, I. Gelen, Y. A. Shokr, I. Kumberg, Ikramullah, M. Sajjad, W. Kuch, and M. Y. Khan: *Bulk and interfacial effects in the Co/Ni<sub>x</sub>Mn<sub>100-x</sub> exchange-bias system due to creation of defects by Ar<sup>+</sup> sputtering*. Phys. Status Solidi RRL **15**, 2100195.

S. Thakur, E. Goliias, I. Kumberg, K. S. Kumar, R. Hosseinifar, J. Torres-Rodríguez, L. Kipgen, C. Lotze, L. M. Arruda, C. Luo, F. Radu, M. Ruben, and W. Kuch: *Thermal- and Light-Induced Spin-Crossover Characteristics of a Functional Iron(II) Complex at Submonolayer Coverage on HOPG*. J. Phys. Chem. C **125**, 13925.

E. Goliias, I. Kumberg, I. Gelen, S. Thakur, J. Gördes, R. Hosseinifar, Q. Guillet, J. K. Dewhurst, S. Sharma, C. Schüßler-Langeheine, N. Pontius and W. Kuch: *Ultrafast Optically Induced Ferromagnetic State in an Elemental Antiferromagnet*. Phys. Rev. Lett. **126**, 107202.

## 2020

I. Kumberg, E. Goliias, N. Pontius, R. Hosseinifar, K. Frischmuth, I. Gelen, T. Shinwari, S. Thakur, C. Schüßler-Langeheine, P. M. Oppeneer, and W. Kuch: *Accelerating the laser-induced demagnetization of a ferromagnetic film by antiferromagnetic order in an adjacent layer*. Phys. Rev. B **102**, 214418.

S. Ossinger, L. Kipgen, H. Naggert, M. Bernien, A. J. Britton, F. Nickel, L. M. Arruda, I. Kumberg, T. A. Engesser, E. Goliias, Ch. Näther, F. Tuczek, and W. Kuch: *Effect of ligand methylation on the spin-switching properties of surface-supported spin-crossover molecules*. J. Phys.: Condens. Matter **32**, 114003.



# List of Figures

1.1	Cartoon of the relevant ultrafast interactions in light-induced experiments. . . . .	2
2.1	Calculated Kerr rotation and ellipticity for an air-cobalt interface. . . . .	13
2.2	Simulated differential absorption and exponential decay in a multilayer sample. . . . .	14
2.3	Kerr rotation recorded in FeGd at different photon energies and applied fields. . . . .	15
2.4	Demonstration of the pulse retrieval by <i>pypret</i> using a recorded spectrogram. . . . .	17
2.5	Measured and retrieved temporal pulse shape and phase. . . . .	17
2.6	Schematics of the TR-MOKE setup established at the FU Berlin. . . . .	18
2.7	Photocurrent and applied magnetic field recorded in the TR-MOKE setup. . . . .	19
2.8	Magnetic contrast evolution after laser excitation recorded in Co/Pt. . . . .	20
2.9	Cartoon of the slicing principle employed at BESSY II. . . . .	24
2.10	Total electron yield recording of Co measured at the PM2 endstation in BESSY II. . . . .	27
2.11	Reflected resonant X-ray intensity recorded at the PM2 endstation in BESSY II. . . . .	30
2.12	Summary of the experimental techniques employed in the state-of-the-art ultrafast magnetization research. . . . .	32
3.1	Overview of exemplary publications in the early ultrafast magnetism research. . . . .	37
3.2	Reprinted depiction of the energy flow and the reservoirs in the microscopic three-temperature model. . . . .	38
3.3	Reprinted illustration of the superdiffusive transport and spin-dependent lifetimes. . . . .	40
3.4	Illustration of the OISTR process reprinted from the original literature. . . . .	42
4.1	Characterization of the deposition rate of Mn and Ni on Cu(001) by AES. . . . .	47
4.2	Calibration of the Co growth parameters by MEED intensity and AES. . . . .	48
4.3	Evaluation of the $\text{Ni}_x\text{Mn}_{1-x}$ alloy concentration using MEED intensity oscillations. . . . .	49
4.4	Overview of the growth characteristics for the Cu (20 ML)/Co (15 ML)/ $\text{Ni}_{31}\text{Mn}_{69}$ (20 ML)/Cu(001) sample. . . . .	50
4.5	MEED oscillations recorded during the growth of the Cu/Ni/NiMn/Cu(001) sample. . . . .	51
4.6	Example hysteresis loops detected by in-situ MOKE at different temperatures of the AFM/FM bilayer sample. . . . .	52
4.7	Coercive field ( $H_C$ ) and exchange bias field ( $H_{EB}$ ) for the samples S1 and S2. . . . .	53
4.8	Schematics of the measurement geometry at the PM3 scattering station and a corresponding example measurement of the resonant X-ray reflectivity. . . . .	54
4.9	Reflected X-ray intensity, magnetic contrast thereof, and evaluated measurement time for Co. . . . .	56

4.10	Reflected X-ray intensity, magnetic contrast thereof, and evaluated measurement time for Ni. . . . .	57
4.11	Reflected X-ray intensity vs delay time recorded at the Co L <sub>3</sub> absorption edge, with and without 800 nm pump, for magnetization along the beam direction and anti-parallel to the beam. . . . .	58
4.12	Evaluated XMCD signal from the data presented in Fig. 4.11. . . . .	58
4.13	Normalized time-resolved XMCD evaluated at the Co L <sub>3</sub> -edge recorded for different pump fluences at 390 K sample temperature. . . . .	59
4.14	Normalized time-resolved XMCD evaluated at the Co L <sub>3</sub> -edge recorded for different pump fluences at 80 K sample temperature. . . . .	60
4.15	Normalized time-resolved XMCD recorded at the Ni L <sub>3</sub> -edge for different pump fluences. . . . .	61
4.16	Simulation of the demagnetization in Co using the m3TM. . . . .	62
4.17	Magnetization v. temperature profile in Co and demagnetization in Ni/NiMn. . . . .	63
4.18	Delay-time traces recorded in Co at a sample base temperature of 80 K and 390 K. . . . .	64
4.19	Demagnetization times for the recorded fluences in Co. Change in XMCD or magnetic quench for the recorded fluences. . . . .	65
4.20	Demagnetization time plotted against relative magnetization change in Co and Ni. Demagnetization time plotted against absolute XMCD change. . . . .	66
4.21	Differential absorption simulated for the Co/NiMn sample for 800 nm p-polarized light. . . . .	68
4.22	Illustration of the transport processes responsible for the different demagnetization rates observed at the two investigated temperatures. . . . .	71
5.1	Predictions of the layerwise atomic moment evolution in Mn and Co during optical excitation by 800 nm reprinted from [120]. . . . .	74
5.2	MEED intensity recorded during growth of the Co/Mn multilayer samples. . . . .	75
5.3	Recorded X-ray reflectivity, magnetic contrast, and expected measurement time for Co in the OISTR sample. . . . .	76
5.4	Recorded X-ray reflectivity, magnetic contrast, and expected measurement time for Mn in the OISTR sample. . . . .	76
5.5	MEED intensity recorded during growth of the Co/Mn multilayer sample used for the slicing experiments. . . . .	77
5.6	Spectra recorded over the L <sub>3</sub> absorption edge of Mn (left) and Co (right) at the slicing facility in reflectivity under $\theta = 8.75^\circ$ . . . . .	78
5.7	Measured pumped and unpumped channels for two opposite directions of magnetization in slicing at Co energies on the OISTR sample. . . . .	79
5.8	Measured pumped and unpumped channels for two opposite directions of magnetization in slicing at Mn energies on the OISTR sample. . . . .	79
5.9	Comparison of the magnetic contrast in Co and Mn after excitation in the OISTR sample. . . . .	80
5.10	Schematics of the OISTR process in the 2 ML Mn system coupled to Co. Reprinted with permission from Ref. [201]. . . . .	82
6.1	X-ray absorption signal over photon energy, recorded in the Co/Mn multilayer sample. . . . .	84
6.2	Recorded absorption scaled to the tabulated attenuation of [205] and real part calculated by KKR. . . . .	85

6.3	Left: Evaluated $\delta$ and $\beta$ for the Co $L_{3,2}$ resonance. Right: Evaluated $\Delta\delta$ and $\Delta\beta$ for the Co $L_{3,2}$ resonance. . . . .	86
6.4	Left: Evaluated $\delta$ and $\beta$ for the Ni $L_{3,2}$ resonance. Right: Evaluated $\Delta\delta$ and $\Delta\beta$ for the Ni $L_{3,2}$ resonance. . . . .	86
6.5	Left: Evaluated $\delta$ and $\beta$ for the Mn $L_{3,2}$ resonance. Right: Evaluated $\Delta\delta$ and $\Delta\beta$ for the Mn $L_{3,2}$ resonance. . . . .	87
6.6	Real and imaginary part of the magneto-optical constants in Co, Mn, and Ni evaluated from experiments. . . . .	88
6.7	Recorded and simulated dichroic spectra measured at the Co and Mn $L_{2,3}$ resonance in the OISTR sample. . . . .	89
6.8	Simulated reflectivity spectra for Co for different angles of incidence with either the real part or the imaginary part set to zero. . . . .	90
6.9	Simulated reflectivity over angle at the Co resonance. . . . .	91
6.10	Simulated reflectivity maps at the Co resonance to illustrate the highlight the effect of real and imaginary part of the optical constants. . . . .	92
6.11	Schematic of the OISTR sample and calculated optical differential absorption. Reprinted with permission from Ref. [201]. . . . .	95
6.12	Electron and lattice temperature evolution after laser excitation simulated by udkm1Dsim. . . . .	96
6.13	Simulated magnetization in the Oistr sample after excitation and estimated X-ray reflectivity. . . . .	97
6.14	Strain map in the OISTR sample after laser excitation simulated by udkm1Dsim. . . . .	99
6.15	Comparison of measured spectra at the Co resonance and the ones simulated by udkm1Dsim. . . . .	100
6.16	Heat capacity scaling with temperature for Cu, Mn, and Co. . . . .	102
6.17	Experimental and simulated XMCD at 778 eV in Co on the multilayer OISTR sample. . . . .	103
6.18	Simulated change in the density of states of Co after excitation. . . . .	105
6.19	Simulated transient atomic form factors $f_1$ and $f_2$ in Co from 0 fs to 180 fs after excitation. . . . .	105
6.20	XRR spectra recorded under $8.75^\circ$ incident angle over the $L_{3,2}$ absorption edge energies compared to the simulated dynamics. . . . .	106
6.21	Simulated and recorded normalized magnetic asymmetry as XMCD and sum signal in Co at 778 eV. . . . .	107
6.22	Magnetic contrast vs. delay after laser excitation over the energies covering the Co $L_{3,2}$ absorption edge. . . . .	109
6.23	Sum of the dichroic signals vs. delay after laser excitation over the energies covering the Co $L_{3,2}$ absorption edge. . . . .	109
6.24	Simulated and recorded sum of the dichroic signals at 636 eV on the OISTR sample under $8.75^\circ$ . . . . .	111
6.25	XRR intensity recorded after excitation by a 60 fs FWHM, $40 \text{ mJ cm}^{-2}$ incident fluence laser pulse in the Co/NiMn/Cu(001) sample under $7^\circ$ and at 778 eV probing energy. . . . .	113
6.26	Recorded sum and asymmetry of the RMXR signal in a Co/Mn/Co/Cu(001) trilayer sample and a sputter-deposited Al/CoFe/MnIr/NiFe/SiO sample. . . . .	114

7.1	TR-MOKE curves recorded at the FUB. MOKE signal for two saturation magnetizations in P1B. . . . .	118
7.2	Time evolution of the magnetic contrast recorded in P1 and P1B. . . . .	119
7.3	Differential absorption for 800 nm light evaluated on P1 and P1B. . . . .	121
7.4	Cartoon of the experiment geometry used to investigate the pump-probe overlap influence on the dynamics.. . . .	122
7.5	Time evolution of the magnetic contrast measured in P1 recorded by TR-MOKE at three different overlaps. . . . .	123
7.6	Delay time trace of the magnetic contrast measured on P1 with the probe spot centered in the pumped region and displaced. . . . .	124
7.7	Measurement of the pump and probe beam diameter and estimation of the absolute displacement. . . . .	125
7.8	Hysteresis loops measured in P1 at negative delay times and estimated magnetization vs. temperature curve in P1. . . . .	126
7.9	Electron and lattice temperature, and magnetization evolution in Co evaluated by solving the m3TM equation. . . . .	127
7.10	Illustration of the geometry and dimensions used to simulate the thermal diffusion in a 3D system after laser excitation. Temperature maps for different slices through the sample. . . . .	129
7.11	Comparison of the simulated temperatures in the metal layer for different fluences and pump-probe overlaps. . . . .	130
7.12	Calculation of the magnetic contrast in the center of the pump and 49 $\mu\text{m}$ off-center using the sample base temperature calculated by the heat diffusion model. . . . .	132

# List of Tables

4.1	Material parameters for AES determined for Co, Ni, and Mn. . . . .	48
4.2	Time constants evaluated from fitting the demagnetization traces of the Co/NiMn sample. . . . .	60
4.3	Time constants evaluated from fitting the demagnetization traces of the Ni/NiMn sample. . . . .	61
6.1	Parameters employed for the simulation of the light-induced heating and the coupled magnetization dynamics using udkm1Dsim. . . . .	102
7.1	Parameters used to model the heat diffusion in the 3D system. . . . .	130
7.2	Material properties for Co, Pt, and Ta used in the 3D heat diffusion simulation.	131



# Bibliography

- [1] A. Kirilyuk, A. V. Kimel, and T. Rasing: *Ultrafast optical manipulation of magnetic order*. Reviews of Modern Physics **82**, 2731–2784 (2010).
- [2] I. Tudosa, C. Stamm, A. B. Kashuba, F. King, H. C. Siegmann, J. Stöhr, G. Ju, B. Lu, and D. Weller: *The ultimate speed of magnetic switching in granular recording media*. Nature **428**, 831–833 (2004).
- [3] R. J. Hicken: *Ultrafast nanomagnets: seeing data storage in a new light*. Philosophical Transactions of the Royal Society of London. Series A: Mathematical, Physical and Engineering Sciences **361**, 2827–2841 (2003).
- [4] J. Walowski and M. Münzenberg: *Perspective: Ultrafast magnetism and THz spintronics*. Journal of Applied Physics **120**, 140901 (2016).
- [5] M. B. Gaarde, J. L. Tate, and K. J. Schafer: *Macroscopic aspects of attosecond pulse generation*. Journal of Physics B: Atomic, Molecular and Optical Physics **41**, 132001 (2008).
- [6] P. F. Moulton: *Spectroscopic and laser characteristics of Ti:Al<sub>2</sub>O<sub>3</sub>*. J. Opt. Soc. Am. **3**, 125-133 (1968).
- [7] C. Rulliere: *Femtosecond laser pulses*. Springer, 108 (2005).
- [8] M. G. Holland: *Thermal Conductivity of Several Optical Maser Materials*. J. Appl. Phys. **33**, 2910 (1962).
- [9] J. Carvill: *Thermodynamics and heat transfer*. Mechanical Engineer's Data Handbook, 102-145 (1993).
- [10] L. E. Hargrove, R. L. Fork, and M. A. Pollack: *Locking of He-Ne Laser Modes Induced By Synchronous Intracavity Modulation*. Appl. Phys. Lett. **5**, 4 (1964).
- [11] U. Keller, W. H. Knox, and H. Roskos: *Coupled-cavity resonant passive mode-locked Ti:sapphire laser*. Optics Lett. **15**, 1377-1379 (1990).
- [12] D. E. Spence, P. N. Kean, and W. Sibbett: *60-fsec pulse generation from a self-mode-locked Ti:sapphire laser*. Optics Lett. **16**, 42-44 (1991).
- [13] C. Chudoba, J. G. Fujimoto, E. P. Ippen, H. A. Haus, U. Morgner, F. X. Kärtner, V. Scheuer, G. Angelow, and T. Tschudi: *All-solid-state Cr:forsterite laser generating 14-fs pulses at 1.3 μm*. Optics Lett. **26**, 292-294 (2001).
- [14] C. Hönninger, R. Paschotta, M. Graf, F. Morier-Genoud, G. Zhang, S. B. M. Moser, J. Nees, A. Braun, G. Mourou, I. Johannsen, A. Giesen, W. Seeber, and U. Keller: *Ultrafast ytterbium-doped bulk lasers and laser amplifiers*. Appl. Physics B **69**, 3-17 (1999).

- [15] M. Fermann, A. Galvanauskas, and M. Hofer: *Ultrafast pulse sources based on multi-mode optical fibers*. Appl. Physics B **70**, 13-23 (2000).
- [16] P. E. Ciddor: *Refractive index of air: new equations for the visible and near infrared*. Appl. Optics **35**, 1566-1573 (1996).
- [17] P. B. Johnson and R. W. Christy: *Optical constants of transition metals: Ti, V, Cr, Mn, Fe, Co, Ni, and Pd*. Physical Review B **9**, 5056–5070 (1974).
- [18] W. H. Lowdermilk and J. E. Murray: *The multipass amplifier: Theory and numerical analysis*. J. of Appl. Physics **51**, 2436 (1980).
- [19] P. Georges, F. Estable, F. Salin, J. P. Poizat, P. Grangier, , and A. Brun: *High-efficiency multipass Ti:sapphire amplifiers for a continuous-wave single-mode laser*. Optics Lett. **16**, 144-146 (1991).
- [20] D. Strickland and G. Mourou: *Compression of amplified chirped optical pulses*. Optics Comm. **55**, 447-449 (1985).
- [21] P. Maine, D. Strickland, P. Bado, M. Pessot, and G. Mourou: *Generation of ultrahigh peak power pulses by chirped pulse amplification*. IEEE J. of Quantum Electronics **24**, 2 (1988).
- [22] E. Hecht: *Optik*. De Gruyter and Pearson Education, Inc., USA **7**, (2018).
- [23] Z. Q. Qiu and S. D. Bader: *Surface magneto-optic Kerr effect*. Review of Scientific Instruments **71**, 1243 (2000).
- [24] J. Zak, E. R. Moog, and C. L. et al.: *Fundamental magneto-optics*. Journal of Applied Physics **68**, 4203 (1990).
- [25] C.-Y. You and S.-C. Shin: *Generalized analytic formulae for magneto-optical Kerr effects*. Journal of Applied Physics **84**, 541 (1998).
- [26] P. S. Pershan: *Magneto-Optical Effects*. Journal of Applied Physics **38**, 1482 (1967).
- [27] K. H. J. Buschow and P. M. Oppeneer: *Handbook of Magnetic Materials*. Elsevier, Amsterdam 2001 **23**, 229-422 (2015).
- [28] P. B. Johnson and R. W. Christy: *Optical Constants of the Noble Metals*. Physical Review B **6**, 4370–4379 (1972).
- [29] L. Chen, N. Dai, X. Jiang, K. Jin, H. Liu, and H. Zhao: *Advances in Condensed Matter Optics*. Shanghai Jiao Tong University Press and Walter de Gruyter GmbH, Berlin/Munich/Boston **7**, 107-137 (2015).
- [30] O. V. Miloslavskaya, Y. N. Kharchenko, N. F. Kharchenko, and et al.: *Photoinduced magnetic linear dichroism in a YIG:Co film*. Low Temperature Physics **28**, 267 (2002).
- [31] C. Scarlat, K. M. Mok, S. Zhou, M. Vinnichenko, M. Lorenz, M. Grundmann, M. Helm, M. Schubert, and H. Schmidt: *Voigt effect measurement on PLD grown NiO thin films*. Phys. Status Solidi C **7**, 334-337 (2009).
- [32] K. Ohta and H. Ishida: *Matrix formalism for calculation of electric field intensity of light in stratified multilayered films*. Appl. Opt. **29**, 1952–1959 (1990).
- [33] J. Zak, E. R. Moog, C. Liu, and S. D. Bader: *Magneto-optics of multilayers with arbitrary magnetization directions*. Physical Review B **43**, 6423–6429 (1991).
- [34] S. A. Stepanov and S. K. Sinha: *X-ray resonant reflection from magnetic multilayers: Recursion matrix algorithm*. Physical Review B **61**, 15302–15311 (2000).

- [35] D. Schick, A. Bojahr, M. Herzog, R. Shayduk, C. von Korff Schmising, and M. Bargheer: *udkmIDsim - A Simulation Toolkit for 1D Ultrafast Dynamics in Condensed Matter*. Comput. Phys. Commun. **185**, 651 (20014).
- [36] D. Schick: *udkmIDsim - A Python toolbox for simulating 1D ultrafast dynamics in condensed matter*. Comput. Phys. Commun. **266**, 108031 (2021).
- [37] F. Dörr: *private communication*. PhD student, Freie Universität Berlin, (2020).
- [38] M. Polyanskiy: <https://refractiveindex.info>. , (2021).
- [39] J. Hohlfeld, S.-S. Wellershoff, J. Güdde, U. Conrad, V. Jähnke, and E. Matthias: *Electron and lattice dynamics following optical excitation of metals*. Chemical Physics **251**, 237-258 (2000).
- [40] K. W. DeLong, R. Trebino, J. Hunter, and W. E. White: *Frequency-resolved optical gating with the use of second-harmonic generation*. Journal of the Optical Society of America B **11**, 2206-2215 (1994).
- [41] N. C. Geib, M. Zilk, T. Pertsch, and F. Eilenberger: *Common pulse retrieval algorithm: a fast and universal method to retrieve ultrashort pulses*. Optica **6**, 495-505 (2019).
- [42] A. Joshua and V. Venkataraman: *Enhanced sensitivity in detection of Kerr rotation by double modulation and time averaging based on Allan variance*. Review of Scientific Instruments **80**, 023908 (2009).
- [43] E. Beaurepaire, J.-C. Merle, A. Daunois, and J.-Y. Bigot: *Ultrafast spin dynamics in ferromagnetic nickel*. Physical Review Letters **76**, 4250–4253 (1996).
- [44] G. Ju, A. V. Nurmikko, R. F. C. Farrow, R. F. Marks, M. J. Carey, and B. A. Gurney: *Ultrafast Time Resolved Photoinduced Magnetization Rotation in a Ferromagnetic/Antiferromagnetic Exchange Coupled System*. Physical Review Letters **82**, 3705–3708 (1999).
- [45] B. Koopmans, M. van Kampen, J. T. Kohlhepp, and W. J. M. de Jonge: *Ultrafast Magneto-Optics in Nickel: Magnetism or Optics?*. Physical Review Letters **85**, 844–847 (2000).
- [46] A. Scholl, L. Baumgarten, R. Jacquemin, and W. Eberhardt: *Ultrafast Spin Dynamics of Ferromagnetic Thin Films Observed by fs Spin-Resolved Two-Photon Photoemission*. Physical Review Letters **79**, 5146–5149 (1997).
- [47] J. Güdde, U. Conrad, V. Jähnke, J. Hohlfeld, and E. Matthias: *Magnetization dynamics of Ni and Co films on Cu(001) and of bulk nickel surfaces*. Physical Review B **59**, R6608–R6611 (1999).
- [48] T. Ogasawara, K. Ohgushi, Y. Tomioka, K. S. Takahashi, H. Okamoto, M. Kawasaki, and Y. Tokura: *General Features of Photoinduced Spin Dynamics in Ferromagnetic and Ferrimagnetic Compounds*. Physical Review Letters **94**, 087202 (2005).
- [49] H. Regensburger, R. Vollmer, and J. Kirschner: *Time-resolved magnetization-induced second-harmonic generation from the Ni(110) surface*. Physical Review B **61**, 14716–14722 (2000).
- [50] P. M. Oppeneer and A. Liebsch: *Ultrafast demagnetization in Ni: theory of magneto-optics for non-equilibrium electron distributions*. Journal of Physics: Condensed Matter **16**, 5519–5530 (2004).
- [51] G. P. Zhang, W. Hübner, G. Lefkidis, Y. Bai, and T. F. George: *Paradigm of the time-resolved magneto-optical Kerr effect for femtosecond magnetism*. Nature Physics **5**, 499–502 (2009).
- [52] J.-Y. Bigot, L. Guidoni, E. Beaurepaire, and P. N. Saeta: *Femtosecond Spectrotemporal Magneto-optics*. Physical Review Letters **93**, 077401 (2004).

- [53] B. Koopmans, J. J. M. Ruigrok, F. D. Longa, and W. J. M. de Jonge: *Unifying Ultrafast Magnetization Dynamics*. Physical Review Letters **95**, 267207 (2005).
- [54] B. Koopmans, G. Malinowski, F. Dalla Longa, D. Steiauf, M. Fähnle, T. Roth, M. Cinchetti, and M. Aeschlimann: *Explaining the paradoxical diversity of ultrafast laser-induced demagnetization*. Nat. Mater. **9**, 259–265 (2010).
- [55] A. Kirilyuk and T. Rasing: *Magnetization-induced-second-harmonic generation from surfaces and interfaces*. Journal of the Optical Society of America B **22**, 148 (2005).
- [56] J. Hohlfeld, E. Matthias, R. Knorren, and K. H. Bennemann: *Nonequilibrium Magnetization Dynamics of Nickel*. Physical Review Letters **78**, 4861–4864 (1997).
- [57] U. Conrad, J. Güdde, V. Jähnke, and E. Matthias: *Ultrafast electron and magnetization dynamics of thin Ni and Co films on Cu(001) observed by time-resolved SHG*. Applied Physics B: Lasers and Optics **68**, 511–517 (1999).
- [58] M. Lisowski, P. A. Loukakos, A. Melnikov, I. Radu, L. Ungureanu, M. Wolf, and U. Bovensiepen: *Femtosecond Electron and Spin Dynamics in Gd(0001) Studied by Time-Resolved Photoemission and Magneto-optics*. Physical Review Letters **95**, 137402 (2005).
- [59] R. Gort, K. Bühlmann, S. Däster, G. Salvatella, N. Hartmann, Y. Zemp, S. Hohenstein, C. Stieger, A. Fognini, T. U. Michlmayr, T. Bähler, A. Vaterlaus, and Y. Acremann: *Early Stages of Ultrafast Spin Dynamics in a 3 d Ferromagnet*. Physical Review Letters **121**, 087206 (2018).
- [60] M. Aeschlimann, M. Bauer, S. Pawlik, W. Weber, R. Burgermeister, D. Oberli, and H. C. Siegmann: *Ultrafast Spin-Dependent Electron Dynamics in fcc Co*. Physical Review Letters **79**, 5158–5161 (1997).
- [61] M. Keunecke, C. Möller, D. Schmitt, H. Nolte, G. S. M. Jansen, M. Reutzel, M. Gutberlet, G. Halasi, D. Steil, S. Steil, and S. Mathias: *Time-resolved momentum microscopy with a 1 MHz high-harmonic extreme ultraviolet beamline*. Review of Scientific Instruments **91**, 063905 (2020).
- [62] K. Yao, F. Willems, C. von Korff Schmising, C. Strüber, P. Hessing, B. Pfau, D. Schick, D. Engel, K. Gerlinger, M. Schneider, and S. Eisebitt: *A tabletop setup for ultrafast helicity-dependent and element-specific absorption spectroscopy and scattering in the extreme ultraviolet spectral range*. Review of Scientific Instruments **91**, 093001 (2020).
- [63] F. Willems, C. T. L. Smeenk, N. Zhavoronkov, O. Kornilov, I. Radu, M. Schmidbauer, M. Hanke, C. von Korff Schmising, M. J. J. Vrakking, and S. Eisebitt: *Probing ultrafast spin dynamics with high-harmonic magnetic circular dichroism spectroscopy*. Physical Review B **92**, 220405 (2015).
- [64] C. La-O-Vorakiat, M. Siemens, M. M. Murnane, H. C. Kapteyn, S. Mathias, M. Aeschlimann, P. Grychtol, R. Adam, C. M. Schneider, J. M. Shaw, H. Nembach, and T. J. Silva: *Ultrafast Demagnetization Dynamics at the M Edges of Magnetic Elements Observed Using a Tabletop High-Harmonic Soft X-Ray Source*. Physical Review Letters **103**, 257402 (2009).
- [65] S. Jana, J. A. Terschlüsen, R. Stefanuik, S. Plogmaker, S. Troisi, R. S. Malik, M. Svanqvist, R. Knut, J. Söderström, and O. Karis: *A setup for element specific magnetization dynamics using the transverse magneto-optic Kerr effect in the energy range of 30-72 eV*. Review of Scientific Instruments **88**, 033113 (2017).
- [66] K. Yao, F. Willems, C. von Korff Schmising, I. Radu, C. Strüber, D. Schick, D. Engel, A. Tsukamoto, J. K. Dewhurst, S. Sharma, and S. Eisebitt: *Distinct spectral response in M -edge magnetic circular dichroism*. Physical Review B **102**, 100405 (2020).

- [67] C. von Korff Schmising, F. Willems, S. Sharma, K. Yao, M. Borchert, M. Hennecke, D. Schick, I. Radu, C. Strüber, D. W. Engel, V. Shokeen, J. Buck, K. Bagschik, J. Viefhaus, G. Hartmann, B. Manschwetus, S. Grunewald, S. Düsterer, E. Jal, B. Vodungbo, J. Lüning, and S. Eisebitt: *Element-Specific Magnetization Dynamics of Complex Magnetic Systems Probed by Ultrafast Magneto-Optical Spectroscopy*. Applied Sciences **10**, 7580 (2020).
- [68] F. Willems, S. Sharma, C. v. Korff Schmising, J. Dewhurst, L. Salemi, D. Schick, P. Hessian, C. Strüber, W. Engel, and S. Eisebitt: *Magneto-Optical Functions at the 3p Resonances of Fe, Co, and Ni: Ab initio Description and Experiment*. Physical Review Letters **122**, 217202 (2019).
- [69] C. La-O-Vorakiat, E. Turgut, C. A. Teale, H. C. Kapteyn, M. M. Murnane, S. Mathias, M. Aeschlimann, C. M. Schneider, J. M. Shaw, H. T. Nembach, and T. J. Silva: *Ultrafast Demagnetization Measurements Using Extreme Ultraviolet Light: Comparison of Electronic and Magnetic Contributions*. Physical Review X **2**, 011005 (2012).
- [70] M. Hofherr, S. Häuser, J. K. Dewhurst, P. Tengdin, S. Sakshath, H. T. Nembach, S. T. Weber, J. M. Shaw, T. J. Silva, H. C. Kapteyn, M. Cinchetti, B. Rethfeld, M. M. Murnane, D. Steil, B. Stadtmüller, S. Sharma, M. Aeschlimann, and S. Mathias: *Ultrafast optically induced spin transfer in ferromagnetic alloys*. Science Advances **6**, eaay8717 (2020).
- [71] T. Popmintchev, M.-C. Chen, D. Popmintchev, P. Arpin, S. Brown, S. Alisauskas, G. Andriukaitis, T. Balciunas, O. D. Mücke, A. Pugzlys, A. Baltuska, B. Shim, S. E. Schrauth, A. Gaeta, C. Hernandez-Garcia, L. Plaja, A. Becker, A. Jaron-Becker, M. M. Murnane, and H. C. Kapteyn: *Bright Coherent Ultrahigh Harmonics in the keV X-ray Regime from Mid-Infrared Femtosecond Lasers*. Science **336**, 1287–1291 (2012).
- [72] I. Mantouvalou, K. Witte, D. Grötzsch, M. Neitzel, S. Günther, J. Baumann, R. Jung, H. Stiel, B. Kanngießer, and W. Sandner: *High average power, highly brilliant laser-produced plasma source for soft X-ray spectroscopy*. Review of Scientific Instruments **86**, 035116 (2015).
- [73] D. Schick, M. Borchert, J. Braenzel, H. Stiel, J. Tümmeler, D. E. Bürgler, A. Firsov, C. von Korff Schmising, B. Pfau, and S. Eisebitt: *Laser-driven resonant magnetic soft-x-ray scattering for probing ultrafast antiferromagnetic and structural dynamics*. Optica **8**, 1237 (2021).
- [74] P. Willmot: *An Introduction to Synchrotron Radiation: Techniques and Applications*. John Wiley and Sons Ltd **2**, (2019).
- [75] D. Attwood: *Soft X-rays and extreme ultraviolet radiation: principles and applications*. Cambridge University Press, (2000).
- [76] H. Wiedemann: *Synchrotron Radiation*. Springer Berlin / Heidelberg, (2007).
- [77] P. Duke: *Synchrotron radiation - production and properties*. Oxford Science Publications, (2009).
- [78] E. M. McMillan: *The Synchrotron - A Proposed High Energy Particle Accelerator*. Physical Review **68**, 143–144 (1945).
- [79] A. Jankowiak and G. Wüstefeld: *Low- $\alpha$  Operation of BESSY II and Future Plans for an Alternating Bunch Length Scheme BESSY<sup>VSR</sup>*. Synchrotron Radiation News **26**, 22–24 (2013).
- [80] K. Holldack, J. Bahrtdt, A. Balzer, U. Bovensiepen, M. Brzhezinskaya, A. Erko, A. Eschenlohr, R. Follath, A. Firsov, W. Frentrop, L. Le Guyader, T. Kachel, P. Kuske, R. Mitzner, R. Müller, N. Pontius, T. Quast, I. Radu, J.-S. Schmidt, C. Schübler-Langeheine, M. Sperling, C. Stamm, C. Trabant, and A. Föhlisch: *FemtoSpeX: a versatile optical pump-soft X-ray probe facility with 100 fs X-ray pulses of variable polarization*. Journal of Synchrotron Radiation **21**, 1090–1104 (2014).

- [81] N. Pontius, K. Holldack, C. Schüßler-Langeheine, T. Kachel, and R. Mitzner: *The FemtoSpeX facility at BESSY II*. Journal of large-scale research facilities JLSRF **2**, A46 (2016).
- [82] R. W. Schoenlein, S. Chattopadhyay, H. H. W. Chong, T. E. Glover, P. A. Heimann, C. V. Shank, A. A. Zholents, and M. S. Zolotarev: *Generation of Femtosecond Pulses of Synchrotron Radiation*. Science **287**, 2237–2240 (2000).
- [83] R. Schoenlein, S. Chattopadhyay, H. Chong, T. Glover, P. Heimann, W. Leemans, C. Shank, A. Zholents, and M. Zolotarev: *Generation of femtosecond X-ray pulses via laser-electron beam interaction*. Applied Physics B **71**, 1–10 (2000).
- [84] G. Ingold, A. Streun, B. Singh, R. Abela, P. Beaud, G. Knopp, L. Rivkin, V. Schlott, T. Schmidt, H. Sigg, J. van der Veen, A. Wrulich, and S. Khan: *Sub-picosecond optical pulses at the SLS storage ring*. in: PACS2001. Proceedings of the 2001 Particle Accelerator Conference (Cat. No.01CH37268), p. 2656–2658 (2001).
- [85] P. Beaud, S. L. Johnson, A. Streun, R. Abela, D. Abramsohn, D. Grolimund, F. Krasniqi, T. Schmidt, V. Schlott, and G. Ingold: *Spatiotemporal Stability of a Femtosecond Hard-X-Ray Undulator Source Studied by Control of Coherent Optical Phonons*. Physical Review Letters **99**, 174801 (2007).
- [86] A. A. Zholents and M. S. Zolotarev: *Femtosecond X-Ray Pulses of Synchrotron Radiation*. Physical Review Letters **76**, 912–915 (1996).
- [87] C. Bostedt, S. Boutet, D. M. Fritz, Z. Huang, H. J. Lee, H. T. Lemke, A. Robert, W. F. Schlotter, J. J. Turner, and G. J. Williams: *Linac Coherent Light Source: The first five years*. Reviews of Modern Physics **88**, 015007 (2016).
- [88] R. Schoenlein, T. Elsaesser, K. Holldack, Z. Huang, H. Kapteyn, M. Murnane, and M. Woerner: *Recent advances in ultrafast X-ray sources*. Philosophical Transactions of the Royal Society A: Mathematical, Physical and Engineering Sciences **377**, 20180384 (2019).
- [89] E. Beaurepaire, H. Bulou, F. Scheurer, and J. Kappler: *Magnetism and Synchrotron Radiation*. Springer Proceedings in Physics **133**, 86–102 (2010).
- [90] Y. Joly, S. D. Matteo, and O. Bunau: *Resonant X-ray diffraction: Basic theoretical principles*. The European Physical Journal Special Topics **208**, 21–38 (2012).
- [91] J. Stöhr and H. Siegmann: *Magnetism - From Fundamentals to Nanoscale Dynamics*. Springer-Verlag Berlin Heidelberg, 370–386 (2006).
- [92] F. de Groot and A. Kotani: *Core Level Spectroscopy of Solids*. Taylor and Francis Group, 287–334 (2008).
- [93] J. Stöhr and H. König: *Determination of Spin- and Orbital-Moment Anisotropies in Transition Metals by Angle-Dependent X-Ray Magnetic Circular Dichroism*. Physical Review Letters **75**, 3748–3751 (1995).
- [94] P. Carra, B. T. Thole, M. Altarelli, and X. Wang: *X-ray circular dichroism and local magnetic fields*. Physical Review Letters **70**, 694–697 (1993).
- [95] B. T. Thole, P. Carra, F. Sette, and G. van der Laan: *X-ray circular dichroism as a probe of orbital magnetization*. Physical Review Letters **68**, 1943–1946 (1992).
- [96] B. Henke, E. Gullikson, and J. Davis: *X-ray interactions: photoabsorption, scattering, transmission, and reflection at  $E=50\text{-}30000$  eV,  $Z=1\text{-}92$* . Atomic Data and Nuclear Data Tables **54**, (1993).

- [97] M. Elzo, E. Jal, O. Bunau, S. Grenier, Y. Joly, A. Y. Ramos, H. C. N. Tolentino, J. M. Tonnerre, and N. Jaouen: *X-ray resonant magnetic reflectivity of stratified magnetic structures: Eigenwave formalism and application to a W/Fe/W trilayer*. *Journal of Magnetism and Magnetic Materials* **324**, 105–112 (2012).
- [98] S. Macke and E. Goering: *Magnetic reflectometry of heterostructures*. *Journal of Physics: Condensed Matter* **26**, 363201 (2014).
- [99] S. Macke, A. Radi, J. E. Hamann-Borrero, A. Verna, M. Bluschke, S. Brück, E. Goering, R. Sartato, F. He, G. Cristiani, M. Wu, E. Benckiser, H.-U. Habermeier, G. Logvenov, N. Gauquelin, G. A. Botton, A. P. Kajdos, S. Stemmer, G. A. Sawatzky, M. W. Haverkort, B. Keimer, and V. Hinkov: *Element Specific Monolayer Depth Profiling*. *Advanced Materials*, n/a–n/a (2014).
- [100] J. Pudell, A. von Reppert, D. Schick, F. Zamponi, M. Rössle, M. Herzog, H. Zabel, and M. Bargheer: *Ultrafast negative thermal expansion driven by spin disorder*. *Physical Review B* **99**, 094304 (2019).
- [101] J.-E. Pudell, M. Mattern, M. Hehn, G. Malinowski, M. Herzog, and M. Bargheer: *Heat Transport without Heating?—An Ultrafast X-Ray Perspective into a Metal Heterostructure*. *Advanced Functional Materials* **30**, 2004555 (2020).
- [102] F. Zamponi, Z. Ansari, C. Korff Schmising, P. Rothhardt, N. Zhavoronkov, M. Woerner, T. Elsaesser, M. Bargheer, T. Trobitzsch-Ryll, and M. Haschke: *Femtosecond hard X-ray plasma sources with a kilohertz repetition rate*. *Applied Physics A* **96**, 51–58 (2009).
- [103] T. Ishikawa, H. Aoyagi, T. Asaka, Y. Asano, N. Azumi, T. Bizen, H. Ego, K. Fukami, T. Fukui, Y. Furukawa, S. Goto, H. Hanaki, T. Hara, T. Hasegawa, T. Hatsui, A. Higashiya, T. Hirono, N. Hosoda, M. Ishii, T. Inagaki, Y. Inubushi, T. Itoga, Y. Joti, M. Kago, T. Kameshima, H. Kimura, Y. Kirihara, A. Kiyomichi, T. Kobayashi, C. Kondo, T. Kudo, H. Maesaka, X. M. Maréchal, T. Masuda, S. Matsubara, T. Matsumoto, T. Matsushita, S. Matsui, M. Nagasono, N. Nariyama, H. Ohashi, T. Ohata, T. Ohshima, S. Ono, Y. Otake, C. Saji, T. Sakurai, T. Sato, K. Sawada, T. Seike, K. Shirasawa, T. Sugimoto, S. Suzuki, S. Takahashi, H. Takebe, K. Takeshita, K. Tamasaku, H. Tanaka, R. Tanaka, T. Tanaka, T. Togashi, K. Togawa, A. Tokuhisa, H. Tomizawa, K. Tono, S. Wu, M. Yabashi, M. Yamaga, A. Yamashita, K. Yanagida, C. Zhang, T. Shintake, H. Kitamura, and N. Kumagai: *A compact X-ray free-electron laser emitting in the sub-ångström region*. *Nature Photonics* **6**, 540–544 (2012).
- [104] K. Yamamoto, Y. Kubota, M. Suzuki, Y. Hirata, K. Carva, M. Berritta, K. Takubo, Y. Uemura, R. Fukaya, K. Tanaka, W. Nishimura, T. Ohkochi, T. Katayama, T. Togashi, K. Tamasaku, M. Yabashi, Y. Tanaka, T. Seki, K. Takanashi, P. M. Oppeneer, and H. Wadati: *Ultrafast demagnetization of Pt magnetic moment in  $L1_0$ -FePt probed by magnetic circular dichroism at a hard x-ray free electron laser*. *New Journal of Physics* **21**, 123010 (2019).
- [105] Y. Cao, D. G. Mazzone, D. Meyers, J. P. Hill, X. Liu, S. Wall, and M. P. M. Dean: *Ultrafast dynamics of spin and orbital correlations in quantum materials: an energy- and momentum-resolved perspective*. *Philosophical Transactions of the Royal Society A: Mathematical, Physical and Engineering Sciences* **377**, 20170480 (2019).
- [106] S. Bonetti, M. Hoffmann, M.-J. Sher, Z. Chen, S.-H. Yang, M. Samant, S. Parkin, and H. Dürr: *THz-Driven Ultrafast Spin-Lattice Scattering in Amorphous Metallic Ferromagnets*. *Physical Review Letters* **117**, 087205 (2016).
- [107] T. Kampfrath, A. Sell, G. Klatt, A. Pashkin, S. Mährlein, T. Dekorsy, M. Wolf, M. Fiebig, A. Leitenstorfer, and R. Huber: *Coherent terahertz control of antiferromagnetic spin waves*. *Nature Photonics* **5**, 31–34 (2011).

- [108] E. Beaurepaire, G. M. Turner, S. M. Harrel, M. C. Beard, J.-Y. Bigot, and C. A. Schmuttenmaer: *Coherent terahertz emission from ferromagnetic films excited by femtosecond laser pulses*. Applied Physics Letters **84**, 3465–3467 (2004).
- [109] T. Kampftrath, M. Battiato, P. Maldonado, G. Eilers, J. Nötzold, S. Mährlein, V. Zbarsky, F. Freimuth, Y. Mokrousov, S. Blügel, M. Wolf, I. Radu, P. M. Oppeneer, and M. Münzenberg: *Terahertz spin current pulses controlled by magnetic heterostructures*. Nature Nanotechnology **8**, 256–260 (2013).
- [110] W. Zhang, P. Maldonado, Z. Jin, T. S. Seifert, J. Arabski, G. Schmerber, E. Beaurepaire, M. Bonn, T. Kampftrath, P. M. Oppeneer, and D. Turchinovich: *Ultrafast terahertz magnetometry*. Nature Communications **11**, 4247 (2020).
- [111] D. Zahn, F. Jakobs, Y. W. Windsor, H. Seiler, T. Vasileiadis, T. A. Butcher, Y. Qi, D. Engel, U. Atxitia, J. Vorberger, and R. Ernstorfer: *Lattice dynamics and ultrafast energy flow between electrons, spins, and phonons in a 3d ferromagnet*. Physical Review Research **3**, 023032 (2021).
- [112] F. Steinbach, D. Schick, C. von Korff Schmising, K. Yao, M. Borchert, W. D. Engel, and S. Eisebitt: *Wide-field magneto-optical microscope to access quantitative magnetization dynamics with femtosecond temporal and sub-micrometer spatial resolution*. Journal of Applied Physics **130**, 083905 (2021).
- [113] M. Garcia-Lechuga, J. Siegel, J. Hernandez-Rueda, and J. Solis: *Imaging the ultrafast Kerr effect, free carrier generation, relaxation and ablation dynamics of Lithium Niobate irradiated with femtosecond laser pulses*. Journal of Applied Physics **116**, 113502 (2014).
- [114] G. Schönhense and H. J. Elmers: *PEEM with high time resolution-imaging of transient processes and novel concepts of chromatic and spherical aberration correction*. Surface and Interface Analysis **38**, 1578–1587 (2006).
- [115] T. L. Cocker, V. Jelic, M. Gupta, S. J. Molesky, J. A. J. Burgess, G. D. L. Reyes, L. V. Titova, Y. Y. Tsui, M. R. Freeman, and F. A. Hegmann: *An ultrafast terahertz scanning tunnelling microscope*. Nature Photonics **7**, 620–625 (2013).
- [116] T. Ostler, J. Barker, R. Evans, R. Chantrell, U. Atxitia, O. Chubykalo-Fesenko, S. El Moussaoui, L. Le Guyader, E. Mengotti, L. Heyderman, F. Nolting, A. Tsukamoto, A. Itoh, D. Afanasiev, B. Ivanov, A. Kalashnikova, K. Vahaplar, J. Mentink, A. Kirilyuk, T. Rasing, and A. Kimel: *Ultrafast heating as a sufficient stimulus for magnetization reversal in a ferrimagnet*. Nature Communications **3**, 666 (2012).
- [117] L. Le Guyader, M. Savoini, S. El Moussaoui, M. Buzzi, A. Tsukamoto, A. Itoh, A. Kirilyuk, T. Rasing, A. V. Kimel, and F. Nolting: *Nanoscale sub-100 picosecond all-optical magnetization switching in GdFeCo microstructures*. Nature Communications **6**, 5839 (2015).
- [118] A. Kirilyuk, A. V. Kimel, and T. Rasing: *Ultrafast optical manipulation of magnetic order*. Rev. Mod. Phys. **82**, 2731–2784 (2010).
- [119] M. Battiato, K. Carva, and P. M. Oppeneer: *Superdiffusive spin transport as a mechanism of ultrafast demagnetization*. Physical Review Letters **105**, 027203 (2010).
- [120] J. K. Dewhurst, P. Elliott, S. Shallcross, E. K. U. Gross, and S. Sharma: *Laser-Induced Intersite Spin Transfer*. Nano Letters **18**, 1842–1848 (2018).
- [121] M. Aeschlimann, A. Vaterlaus, M. Lutz, M. Stampanoni, and F. Meier: *Ultrafast thermomagnetic writing processes in rare-earth transition-metal thin films*. Journal of Applied Physics **67**, 4438–4440 (1990).

- [122] A. Vaterlaus, D. Guarisco, M. Lutz, M. Aeschlimann, M. Stampanoni, and F. Meier: *Different spin and lattice temperatures observed by spin-polarized photoemission with picosecond laser pulses*. Journal of Applied Physics **67**, 5661–5663 (1990).
- [123] M. Agranat, S. Ashitkov, A. Granovskii, and G. Rukman: *Interaction of picosecond laser pulses with the electron, spin, and phonon subsystems of nickel*. Sov. Phys. JETP **86**, 804–806 (1984).
- [124] S. D. Brorson, A. Kazeroonian, J. S. Moodera, D. W. Face, T. K. Cheng, E. P. Ippen, M. S. Dresselhaus, and G. Dresselhaus: *Femtosecond room-temperature measurement of the electron-phonon coupling constant  $\gamma$  in metallic superconductors*. Physical Review Letters **64**, 2172–2175 (1990).
- [125] Q. Zhang, A. V. Nurmikko, G. X. Miao, G. Xiao, and A. Gupta: *Ultrafast spin-dynamics in half-metallic CrO<sub>2</sub> thin films*. Physical Review B **74**, 064414 (2006).
- [126] G. M. Müller, J. Walowski, M. Djordjevic, G.-X. Miao, A. Gupta, A. V. Ramos, K. Gehrke, V. Moshnyaga, K. Samwer, J. Schmalhorst, A. Thomas, A. Hütten, G. Reiss, J. S. Moodera, and M. Münzenberg: *Spin polarization in half-metals probed by femtosecond spin excitation*. Nature Materials **8**, 56–61 (2009).
- [127] G. Malinowski, F. Dalla Longa, J. H. H. Rietjens, P. V. Paluskar, R. Huijink, H. J. M. Swagten, and B. Koopmans: *Control of speed and efficiency of ultrafast demagnetization by direct transfer of spin angular momentum*. Nature Physics **4**, 855–858 (2008).
- [128] M. Battiato, K. Carva, and P. M. Oppeneer: *Superdiffusive Spin Transport as a Mechanism of Ultrafast Demagnetization*. Physical Review Letters **105**, 027203 (2010).
- [129] M. Battiato, K. Carva, and P. M. Oppeneer: *Theory of laser-induced ultrafast superdiffusive spin transport in layered heterostructures*. Physical Review B **86**, 024404 (2012).
- [130] J. Hohlfeld, S.-S. Wellershoff, J. Güdde, U. Conrad, V. Jähnke, and E. Matthias: *Electron and lattice dynamics following optical excitation of metals*. Chemical Physics **251**, 237–258 (2000).
- [131] M. Battiato, K. Carva, and P. M. Oppeneer: *Theory of laser-induced ultrafast superdiffusive spin transport in layered heterostructures*. Physical Review B **86**, 024404 (2012).
- [132] K. Bühlmann, G. Saerens, A. Vaterlaus, and Y. Acremann: *Detection of femtosecond spin injection into a thin gold layer by time and spin resolved photoemission*. Scientific Reports **10**, 12632 (2020).
- [133] D. Rudolf, C. La-O-Vorakiat, M. Battiato, R. Adam, J. M. Shaw, E. Turgut, P. Maldonado, S. Mathias, P. Grychtol, H. T. Nembach, T. J. Silva, M. Aeschlimann, H. C. Kapteyn, M. M. Murnane, C. M. Schneider, and P. M. Oppeneer: *Ultrafast magnetization enhancement in metallic multilayers driven by superdiffusive spin current*. Nature Communications **3**, 1037 (2012).
- [134] A. Eschenlohr, M. Battiato, P. Maldonado, N. Pontius, T. Kachel, K. Holldack, R. Mitzner, A. Föhlisch, P. M. Oppeneer, and C. Stamm: *Ultrafast spin transport as key to femtosecond demagnetization*. Nature Materials **12**, 332–336 (2013).
- [135] K. Carva, M. Battiato, and P. M. Oppeneer: *Ab Initio Investigation of the Elliott-Yafet Electron-Phonon Mechanism in Laser-Induced Ultrafast Demagnetization*. Physical Review Letters **107**, 207201 (2011).
- [136] K. Carva, M. Battiato, D. Legut, and P. M. Oppeneer: *Ab initio theory of electron-phonon mediated ultrafast spin relaxation of laser-excited hot electrons in transition-metal ferromagnets*. Physical Review B **87**, 184425 (2013).

- [137] A. J. Schellekens, W. Verhoeven, T. N. Vader, and B. Koopmans: *Investigating the contribution of superdiffusive transport to ultrafast demagnetization of ferromagnetic thin films*. Applied Physics Letters **102**, 252408 (2013).
- [138] J. Wieczorek, A. Eschenlohr, B. Weidtmann, M. Rösner, N. Bergeard, A. Tarasevitch, T. O. Wehling, and U. Bovensiepen: *Separation of ultrafast spin currents and spin-flip scattering in Co/Cu(001) driven by femtosecond laser excitation employing the complex magneto-optical Kerr effect*. Physical Review B **92**, 174410 (2015).
- [139] W. Hübner and G. P. Zhang: *Ultrafast spin dynamics in nickel*. Physical Review B **58**, R5920–R5923 (1998).
- [140] J.-Y. Bigot, M. Vomir, and E. Beaurepaire: *Coherent ultrafast magnetism induced by femtosecond laser pulses*. Nature Physics **5**, 515–520 (2009).
- [141] S. R. Woodford: *Conservation of angular momentum and the inverse Faraday effect*. Physical Review B **79**, 212412 (2009).
- [142] F. Hansteen, A. Kimel, A. Kirilyuk, and T. Rasing: *Femtosecond Photomagnetic Switching of Spins in Ferrimagnetic Garnet Films*. Physical Review Letters **95**, 047402 (2005).
- [143] F. Hansteen, A. Kimel, A. Kirilyuk, and T. Rasing: *Nonthermal ultrafast optical control of the magnetization in garnet films*. Physical Review B **73**, 014421 (2006).
- [144] M. O. A. Ellis, E. E. Fullerton, and R. W. Chantrell: *All-optical switching in granular ferromagnets caused by magnetic circular dichroism*. Scientific Reports **6**, 30522 (2016).
- [145] J. Hohlfeld, C. D. Stanciu, and A. Rebei: *Athermal all-optical femtosecond magnetization reversal in GdFeCo*. Applied Physics Letters **94**, 152504 (2009).
- [146] R. John, M. Berritta, D. Hinzke, C. Müller, T. Santos, H. Ulrichs, P. Nieves, J. Walowski, R. Mondal, O. Chubykalo-Fesenko, J. McCord, P. M. Oppeneer, U. Nowak, and M. Münzenberg: *Magnetisation switching of FePt nanoparticle recording medium by femtosecond laser pulses*. Scientific Reports **7**, 4114 (2017).
- [147] J. Gorchon, Y. Yang, and J. Bokor: *Model for multishot all-thermal all-optical switching in ferromagnets*. Physical Review B **94**, 020409 (2016).
- [148] Y. Quessab, M. Deb, J. Gorchon, M. Hehn, G. Malinowski, and S. Mangin: *Resolving the role of magnetic circular dichroism in multishot helicity-dependent all-optical switching*. Physical Review B **100**, 024425 (2019).
- [149] F. Siegrist, J. A. Gessner, M. Ossiander, C. Denker, Y.-P. Chang, M. C. Schröder, A. Guggenmos, Y. Cui, J. Walowski, U. Martens, J. K. Dewhurst, U. Kleineberg, M. Münzenberg, S. Sharma, and M. Schultze: *Light-wave dynamic control of magnetism*. Nature **571**, 240–244 (2019).
- [150] F. Willems, C. von Korff Schmising, C. Strüber, D. Schick, D. W. Engel, J. K. Dewhurst, P. Elliott, S. Sharma, and S. Eisebitt: *Optical inter-site spin transfer probed by energy and spin-resolved transient absorption spectroscopy*. Nature Communications **11**, 871 (2020).
- [151] D. Steil, J. Walowski, F. Gerhard, T. Kiessling, D. Ebke, A. Thomas, T. Kubota, M. Oogane, Y. Ando, J. Otto, A. Mann, M. Hofherr, P. Elliott, J. K. Dewhurst, G. Reiss, L. Molenkamp, M. Aeschlimann, M. Cinchetti, M. Münzenberg, S. Sharma, and S. Mathias: *Efficiency of ultrafast optically induced spin transfer in Heusler compounds*. Physical Review Research **2**, 023199 (2020).

- [152] J. Chen, U. Bovensiepen, A. Eschenlohr, T. Müller, P. Elliott, E. Gross, J. Dewhurst, and S. Sharma: *Competing Spin Transfer and Dissipation at Co / Cu ( 001 ) Interfaces on Femtosecond Timescales*. Physical Review Letters **122**, 067202 (2019).
- [153] B. Y. Mueller, T. Roth, M. Cinchetti, M. Aeschlimann, and B. Rethfeld: *Driving force of ultrafast magnetization dynamics*. New Journal of Physics **13**, 123010 (2011).
- [154] B. Y. Mueller, A. Baral, S. Vollmar, M. Cinchetti, M. Aeschlimann, H. C. Schneider, and B. Rethfeld: *Feedback Effect during Ultrafast Demagnetization Dynamics in Ferromagnets*. Physical Review Letters **111**, 167204 (2013).
- [155] B. Y. Mueller and B. Rethfeld: *Thermodynamic  $\hat{I}^{1/4}$  T model of ultrafast magnetization dynamics*. Physical Review B **90**, 144420 (2014).
- [156] A. W. Fognini: *Ultrafast demagnetization: An electronic point of view*. Ph. D. thesis, ETH Zurich, (2014).
- [157] M. O. A. Ellis, R. F. L. Evans, T. A. Ostler, J. Barker, U. Atxitia, O. Chubykalo-Fesenko, and R. W. Chantrell: *The Landau-Lifshitz equation in atomistic models*. Low Temperature Physics **41**, 705–712 (2015).
- [158] R. F. L. Evans, T. A. Ostler, R. W. Chantrell, I. Radu, and T. Rasing: *Ultrafast thermally induced magnetic switching in synthetic ferrimagnets*. Applied Physics Letters **104**, 082410 (2014).
- [159] U. Atxitia, T. Ostler, J. Barker, R. F. L. Evans, R. W. Chantrell, and O. Chubykalo-Fesenko: *Ultrafast dynamical path for the switching of a ferrimagnet after femtosecond heating*. Physical Review B **87**, 224417 (2013).
- [160] I. Radu, K. Vahaplar, C. Stamm, T. Kachel, N. Pontius, H. A. Dürr, T. A. Ostler, J. Barker, R. F. L. Evans, R. W. Chantrell, A. Tsukamoto, A. Itoh, A. Kirilyuk, T. Rasing, and A. V. Kimel: *Transient ferromagnetic-like state mediating ultrafast reversal of antiferromagnetically coupled spins*. Nature **472**, 205–208 (2011).
- [161] I. Radu, C. Stamm, A. Eschenlohr, F. Radu, R. Abrudan, K. Vahaplar, T. Kachel, N. Pontius, R. Mitzner, K. Holldack, A. Föhlisch, T. A. Ostler, J. H. Mentink, R. F. L. Evans, R. W. Chantrell, A. Tsukamoto, A. Itoh, A. Kirilyuk, A. V. Kimel, and T. Rasing: *Ultrafast and Distinct Spin Dynamics in Magnetic Alloys*. SPIN **05**, 1550004 (2015).
- [162] I. Kumberg, E. Golias, N. Pontius, R. Hosseinifar, K. Frischmuth, I. Gelen, T. Shinwari, S. Thakur, C. Schübler-Langeheine, P. M. Oppeneer, and W. Kuch: *Accelerating the laser-induced demagnetization of a ferromagnetic film by antiferromagnetic order in an adjacent layer*. Physical Review B **102**, 214418 (2020).
- [163] C. Tieg, W. Kuch, S. G. Wang, and J. Kirschner: *Growth, structure, and magnetism of single-crystalline Ni<sub>x</sub>Mn<sub>100-x</sub> films and NiMn/Co bilayers on Cu(001)*. Physical Review B **74**, (2006).
- [164] M. Yaqoob Khan, C.-B. Wu, S. K. Kreft, and W. Kuch: *Concentration- and thickness-dependent magnetic properties of Ni<sub>x</sub>Mn<sub>100-x</sub> in epitaxially grown Ni<sub>x</sub>Mn<sub>100-x</sub>/Ni(Co)/Cu<sub>3</sub>Au(001)*. Journal of Physics: Condensed Matter **25**, 386005 (2013).
- [165] M. Yaqoob Khan, M. Erkovan, and W. Kuch: *Probing antiferromagnetism in NiMn/Ni(Co)/Cu<sub>3</sub>Au(001) single-crystalline epitaxial thin films*. Journal of Applied Physics **113**, 023913 (2013).
- [166] M. Reinhardt, J. Seifert, M. Busch, and H. Winter: *Magnetic interface coupling between ultrathin Co and Ni<sub>x</sub>Mn<sub>100-x</sub> films on Cu(001)*. Physical Review B **81**, (2010).

- [167] J. R. Cerda, P. L. d. Andres, A. Cebollada, R. Miranda, E. Navas, P. Schuster, C. M. Schneider, and J. Kirschner: *Epitaxial growth of cobalt films on Cu(100): a crystallographic LEED determination*. Journal of Physics: Condensed Matter **5**, 2055–2062 (1993).
- [168] C. M. Schneider, P. Bressler, P. Schuster, J. Kirschner, J. J. de Miguel, and R. Miranda: *Curie temperature of ultrathin films of fcc-cobalt epitaxially grown on atomically flat Cu(100) surfaces*. Physical Review Letters **64**, 1059–1062 (1990).
- [169] P. Krams, F. Lauks, R. L. Stamps, B. Hillebrands, and G. Güntherodt: *Magnetic anisotropies of ultrathin Co(001) films on Cu(001)*. Physical Review Letters **69**, 3674–3677 (1992).
- [170] W. Weber, A. Bischof, R. Allenspach, C. H. Back, J. Fassbender, U. May, B. Schirmer, R. M. Jungblut, G. Güntherodt, and B. Hillebrands: *Structural relaxation and magnetic anisotropy in Co/Cu(001) films*. Physical Review B **54**, 4075–4079 (1996).
- [171] A. Schmid and J. Kirschner: *In situ observation of epitaxial growth of Co thin films on Cu(100)*. Ultramicroscopy **42-44**, 483–489 (1992).
- [172] F. Nouvertné, U. May, M. Bammig, A. Rampe, U. Korte, G. Güntherodt, R. Pentcheva, and M. Scheffler: *Atomic exchange processes and bimodal initial growth of Co/Cu(001)*. Physical Review B **60**, 14382–14386 (1999).
- [173] B. Schulz and K. Baberschke: *Crossover from in-plane to perpendicular magnetization in ultrathin Ni/Cu(001) films*. Physical Review B **50**, 13467–13471 (1994).
- [174] K. Baberschke: *The magnetism of nickel monolayers*. Applied Physics A Materials Science and Processing **62**, 417–427 (1996).
- [175] M. Farle, W. Platow, A. N. Anisimov, P. Pouloupoulos, and K. Baberschke: *Anomalous reorientation phase transition of the magnetization in fct Ni/Cu(001)*. Physical Review B **56**, 5100–5103 (1997).
- [176] M. Farle, B. Mirwald-Schulz, A. N. Anisimov, W. Platow, and K. Baberschke: *Higher-order magnetic anisotropies and the nature of the spin-reorientation transition in face-centered-tetragonal Ni(001)/Cu(001)*. Physical Review B **55**, 3708–3715 (1997).
- [177] W. L. O'Brien and B. P. Tonner: *Anomalous perpendicular magnetism in Ni/Cu(001) films and the effects of capping layers*. Journal of Applied Physics **79**, 5623 (1996).
- [178] Focus GmbH 2022: <https://www.focus-gmbh.com/efm-evaporators/deposition-parameters/>. , (accessed 15.02.2022).
- [179] G. Koster: *1 - Reflection high-energy electron diffraction (RHEED) for in situ characterization of thin film growth*. in: In Situ Characterization of Thin Film Growth, edited by Gertjan Koster and Guus Rijnders, Woodhead Publishing (2011).
- [180] J. H. Neave, B. A. Joyce, P. J. Dobson, and N. Norton: *Dynamics of film growth of GaAs by MBE from Rheed observations*. Applied Physics A Solids and Surfaces **31**, 1–8 (1983).
- [181] S. Hofmann: *Atomic mixing, surface roughness and information depth in high-resolution AES depth profiling of a GaAs/AlAs superlattice structure*. Surface and Interface Analysis **21**, 673–678 (1994).
- [182] A. Jablonski and C. J. Powell: *Formalism and parameters for quantitative surface analysis by Auger electron spectroscopy and x-ray photoelectron spectroscopy*. Surface and Interface Analysis **20**, 771–786 (1993).

- [183] Y. Shokr: *Interaction Mechanisms and Magnetization Dynamics in Ultrathin Antiferromagnetic Films and their Correlation with Structure and Morphology*. Ph. D. thesis, (2016).
- [184] R. Morales, A. C. Basaran, J. Villegas, D. Navas, N. Soriano, B. Mora, C. Redondo, X. Batlle, and I. K. Schuller: *Exchange-Bias Phenomenon: The Role of the Ferromagnetic Spin Structure*. *Physical Review Letters* **114**, 097202 (2015).
- [185] J. Nogués and I. K. Schuller: *Exchange bias*. *Journal of Magnetism and Magnetic Materials* **192**, 203–232 (1999).
- [186] P. Miltényi, M. Gierlings, M. Bammig, U. May, G. Güntherodt, J. Nogués, M. Gruyters, C. Leighton, and I. K. Schuller: *Tuning exchange bias*. *Applied Physics Letters* **75**, 2304–2306 (1999).
- [187] T. Shinwari, I. Gelen, Y. A. Shokr, I. Kumberg, Ikramullah, M. Sajjad, W. Kuch, and M. Y. Khan: *Bulk and Interfacial Effects in the Co/NixMn100-x Exchange-Bias System due to Creation of Defects by Ar+ Sputtering*. *physica status solidi (RRL) - Rapid Research Letters* **15**, 2100195 (2021).
- [188] D. Schick, A. Bojahr, M. Herzog, R. Shayduk, C. von Korff Schmising, and M. Bargheer: *udkm1Dsim-A simulation toolkit for 1D ultrafast dynamics in condensed matter*. *Computer Physics Communications* **185**, 651–660 (2014).
- [189] N. Pontius: *Estimating data acquisition times at FemtoSpeX*. <https://www.helmholtz-berlin.de/pubbin/>, (accessed 25.02.2022).
- [190] T. Roth, A. J. Schellekens, S. Alebrand, O. Schmitt, D. Steil, B. Koopmans, M. Cinchetti, and M. Aeschlimann: *Temperature Dependence of Laser-Induced Demagnetization in Ni: A Key for Identifying the Underlying Mechanism*. *Physical Review X* **2**, 021006 (2012).
- [191] L. Waldecker, R. Bertoni, R. Ernstorfer, and J. Vorberger: *Electron-Phonon Coupling and Energy Flow in a Simple Metal beyond the Two-Temperature Approximation*. *Phys. Rev. X* **6**, 021003 (2016).
- [192] Z. Lin, L. V. Zhigilei, and V. Celli: *Electron-phonon coupling and electron heat capacity of metals under conditions of strong electron-phonon nonequilibrium*. *Physical Review B* **77**, 075133 (2008).
- [193] N. Medvedev and I. Milov: *Electron-phonon coupling in metals at high electronic temperatures*. *Physical Review B* **102**, 064302 (2020).
- [194] Z. Tong, S. Li, X. Ruan, and H. Bao: *Comprehensive first-principles analysis of phonon thermal conductivity and electron-phonon coupling in different metals*. *Physical Review B* **100**, 144306 (2019).
- [195] K. Ohta and H. Ishida: *Matrix formalism for calculation of electric field intensity of light in stratified multilayered films*. *Appl. Opt.* **29**, 1952–1959 (1990).
- [196] S. Eich, M. Plötzing, M. Rollinger, S. Emmerich, R. Adam, C. Chen, H. C. Kapteyn, M. M. Murnane, L. Plucinski, D. Steil, B. Stadtmüller, M. Cinchetti, M. Aeschlimann, C. M. Schneider, and S. Mathias: *Band structure evolution during the ultrafast ferromagnetic-paramagnetic phase transition in cobalt*. *Science Advances* **3**, e1602094 (2017).
- [197] E. Turgut, D. Zusin, D. Legut, K. Carva, R. Knut, J. M. Shaw, C. Chen, Z. Tao, H. T. Nembach, T. J. Silva, S. Mathias, M. Aeschlimann, P. M. Oppeneer, H. C. Kapteyn, M. M. Murnane, and P. Grychtol: *Stoner versus Heisenberg: Ultrafast exchange reduction and magnon generation during laser-induced demagnetization*. *Physical Review B* **94**, 220408 (2016).

- [198] A. Alekhin, I. Razdolski, N. Ilin, J. P. Meyburg, D. Diesing, V. Roddatis, I. Rungger, M. Stamenova, S. Sanvito, U. Bovensiepen, and A. Melnikov: *Femtosecond Spin Current Pulses Generated by the Nonthermal Spin-Dependent Seebeck Effect and Interacting with Ferromagnets in Spin Valves*. Physical Review Letters **119**, 017202 (2017).
- [199] A. Ghosh, S. Auffret, U. Ebels, and W. E. Bailey: *Penetration Depth of Transverse Spin Current in Ultrathin Ferromagnets*. Physical Review Letters **109**, 127202 (2012).
- [200] Y. L. W. van Hees, P. van de Meughevel, B. Koopmans, and R. Lavrijsen: *Deterministic all-optical magnetization writing facilitated by non-local transfer of spin angular momentum*. Nature Communications **11**, 3835 (2020).
- [201] E. Golias, I. Kumberg, I. Gelen, S. Thakur, J. Gördes, R. Hosseinifar, Q. Guillet, J. Dewhurst, S. Sharma, C. Schüßler-Langeheine, N. Pontius, and W. Kuch: *Ultrafast Optically Induced Ferromagnetic State in an Elemental Antiferromagnet*. Physical Review Letters **126**, 107202 (2021).
- [202] R. Gómez-Abal, O. Ney, K. Satitkovitchai, and W. Hübner: *All-Optical Subpicosecond Magnetic Switching in NiO(001)*. Physical Review Letters **92**, 227402 (2004).
- [203] E. Jal, V. López-Flores, N. Pontius, T. Ferté, N. Bergéard, C. Boeglin, B. Vodungbo, J. Lüning, and N. Jaouen: *Structural dynamics during laser-induced ultrafast demagnetization*. Physical Review B **95**, 184422 (2017).
- [204] V. Chardonnet, M. Hennes, R. Jarrier, R. Delaunay, N. Jaouen, M. Kuhlmann, N. Ekanayake, C. Léveillé, C. von Korff Schmising, D. Schick, K. Yao, X. Liu, G. S. Chiuzbăian, J. Lüning, B. Vodungbo, and E. Jal: *Toward ultrafast magnetic depth profiling using time-resolved x-ray resonant magnetic reflectivity*. Structural Dynamics **8**, 034305 (2021).
- [205] C. Chantler, K. Olsen, R. Dragoset, J. Chang, A. Kishore, S. Kotochigova, and D. Zucker: *Detailed Tabulation of Atomic Form Factors, Photoelectric Absorption and Scattering Cross Section, and Mass Attenuation Coefficients for Z = 1-92 from E = 1-10 eV to E = 0.4-1.0 MeV*. T, Physical Measurement Laboratory, (1995).
- [206] S. Seltzer: *X-ray Form Factor, Attenuation and Scattering Tables*. NIST Standard Reference Database, (1995).
- [207] B. Henke, E. Gullikson, and J. Davis: *X-Ray Interactions: Photoabsorption, Scattering, Transmission, and Reflection at E = 50-30,000 eV, Z = 1-92*. Atomic Data and Nuclear Data Tables **54**, 181–342 (1993).
- [208] E. Gullikson: *X-Ray Database: [https://henke.lbl.gov/optical\\_constants](https://henke.lbl.gov/optical_constants)*. The Center for X-Ray Optics, Lawrence Berkeley National Laboratory's Materials Sciences Division, (1995).
- [209] M. W. Chase, C. A. Davies, J. R. Downey, D. J. Frurip, R. A. McDonald, and A. N. Syverud: *JANAF Thermochemical Tables (Third Edition)*. J. Phys. Chem. Ref. Data **Suppl. 1**, (1985).
- [210] T. Flores, M. Hansen, and M. Wuttig: *Structure and growth of Mn on Cu(100)*. Surface Science **279**, 251–264 (1992).
- [211] B.-Y. Wang, P.-H. Lin, M.-S. Tsai, C.-W. Shih, M.-J. Lee, C.-W. Huang, N.-Y. Jih, P.-Y. Cheng, and D.-H. Wei: *Crucial role of interlayer distance for antiferromagnet-induced perpendicular magnetic anisotropy*. Physical Review B **92**, 214435 (2015).
- [212] M. Wuttig, Y. Gauthier, and S. Blügel: *Magnetically driven buckling and stability of ordered surface alloys: Cu(100) c(2x2)Mn*. Physical Review Letters **70**, 3619–3622 (1993).

- [213] G. V. Samsonov: *Handbook of the Physicochemical Properties of the Elements*. Springer US (1968).
- [214] W. M. Haynes, R. L. David, and J. B. Thomas: *CRC Handbook of Chemistry and Physics, 95th edition*. CRC Press, Taylor & Francis Group, 6000 Broken Sound Parkway NW, Suite 300, (2014).
- [215] K. Thurnay: *Thermal Properties of Transition Metals*. Karlsruhe, Germany: Karlsruhe FZKA, (1998).
- [216] B. D. Dunn: *Materials and Processes*. Springer International Publishing (2016).
- [217] U. S. of Commerce: *NIST Chemistry WebBook: <https://webbook.nist.gov>*. National Institute of Standards and Technology, U.S. Department of Commerce, (accessed 2022).
- [218] K. Carva, D. Legut, and P. M. Oppeneer: *Influence of laser-excited electron distributions on the X-ray magnetic circular dichroism spectra: Implications for femtosecond demagnetization in Ni*. EPL (Europhys. Lett.) **86**, 57002 (2009).
- [219] C. Stamm, T. Kachel, N. Pontius, R. Mitzner, T. Quast, K. Holldack, S. Khan, C. Lupulescu, E. F. Aziz, M. Wietstruk, H. A. Dürr, and W. Eberhardt: *Femtosecond modification of electron localization and transfer of angular momentum in nickel*. Nat. Mater. **6**, 740–743 (2007).
- [220] T. Kachel, N. Pontius, C. Stamm, M. Wietstruk, E. F. Aziz, H. A. Dürr, W. Eberhardt, and F. M. F. de Groot: *Transient electronic and magnetic structures of nickel heated by ultrafast laser pulses*. Physical Review B **80**, 092404 (2009).
- [221] J. Dewhurst, K. Krieger, S. Sharma, and E. Gross: *An efficient algorithm for time propagation as applied to linearized augmented plane wave method*. Computer Physics Communications **209**, 92–95 (2016).
- [222] <http://elk.sourceforge.net>, .
- [223] C. v. Korff Schmising, A. Harpoeth, N. Zhavoronkov, Z. Ansari, C. Aku-Leh, M. Woerner, T. Elsaesser, M. Bargheer, M. Schmidbauer, I. Vrejoiu, D. Hesse, and M. Alexe: *Ultrafast magnetostriction and phonon-mediated stress in a photoexcited ferromagnet*. Physical Review B **78**, 060404 (2008).
- [224] G. Malinowski, N. Bergeard, M. Hehn, and S. Mangin: *Hot-electron transport and ultrafast magnetization dynamics in magnetic multilayers and nanostructures following femtosecond laser pulse excitation*. Eur. Phys. J. B **91**, 98 (2018).
- [225] D. Rudolf, C. La-o Vorakiat, M. Battiato, R. Adam, J. M. Shaw, E. Turgut, P. Maldonado, S. Mathias, P. Grychtol, H. T. Nembach, T. J. Silva, M. Aeschlimann, H. C. Kapteyn, M. M. Murnane, C. M. Schneider, and P. M. Oppeneer: *Ultrafast magnetization enhancement in metallic multilayers driven by superdiffusive spin current*. Nat. Commun. **3**, 1037 (2012).
- [226] M. Djordjevic, M. Lüttich, P. Moschkau, P. Guderian, T. Kampfrath, R. G. Ulbrich, M. Münzenberg, W. Felsch, and J. S. Moodera: *Comprehensive view on ultrafast dynamics of ferromagnetic films*. physica status solidi (c) **3**, 1347–1358 (2006).
- [227] G. Woltersdorf: *Lost magnetism pinned on atomic rotations*. Nature **602**, 36–38 (2022).
- [228] M. Fiebig, N. P. Duong, T. Satoh, B. B. Van Aken, K. Miyano, Y. Tomioka, and Y. Tokura: *Ultrafast magnetization dynamics of antiferromagnetic compounds*. Journal of Physics D: Applied Physics **41**, 164005 (2008).

- [229] N. Berggaard, V. López-Flores, V. Halté, M. Hehn, C. Stamm, N. Pontius, E. Beaurepaire, and C. Boeglin: *Ultrafast angular momentum transfer in multisublattice ferrimagnets*. Nature Communications **5**, 3466 (2014).
- [230] G. Batignani, D. Bossini, N. Di Palo, C. Ferrante, E. Pontecorvo, G. Cerullo, A. Kimel, and T. Scopigno: *Probing ultrafast photo-induced dynamics of the exchange energy in a Heisenberg antiferromagnet*. Nature Photonics **9**, 506–510 (2015).
- [231] G. Bonfiglio, K. Rode, G. Y. P. Atcheson, P. Stamenov, J. M. D. Coey, A. V. Kimel, T. Rasing, and A. Kirilyuk: *Sub-picosecond exchange-relaxation in the compensated ferrimagnet  $Mn_2Ru_xGa$* . Journal of Physics: Condensed Matter **33**, 135804 (2021).
- [232] K. Mishra, A. Ciuciulkaite, M. Zapata-Herrera, P. Vavassori, V. Kapaklis, T. Rasing, A. Dmitriev, A. Kimel, and A. Kirilyuk: *Ultrafast demagnetization in a ferrimagnet under electromagnetic field funneling*. Nanoscale **13**, 19367–19375 (2021).
- [233] C.-H. Lambert, S. Mangin, B. S. D. C. S. Varaprasad, Y. K. Takahashi, M. Hehn, M. Cinchetti, G. Malinowski, K. Hono, Y. Fainman, M. Aeschlimann, and E. E. Fullerton: *All-optical control of ferromagnetic thin films and nanostructures*. Science **345**, 1337–1340 (2014).
- [234] M. S. El Hadri, P. Pirro, C.-H. Lambert, S. Petit-Watelot, Y. Quessab, M. Hehn, F. Montaigne, G. Malinowski, and S. Mangin: *Two types of all-optical magnetization switching mechanisms using femtosecond laser pulses*. Physical Review B **94**, 064412 (2016).
- [235] M. S. El Hadri, M. Hehn, P. Pirro, C.-H. Lambert, G. Malinowski, E. E. Fullerton, and S. Mangin: *Domain size criterion for the observation of all-optical helicity-dependent switching in magnetic thin films*. Physical Review B **94**, 064419 (2016).
- [236] R. Medapalli, D. Afanasiev, D. K. Kim, Y. Quessab, S. Manna, S. A. Montoya, A. Kirilyuk, T. Rasing, A. V. Kimel, and E. E. Fullerton: *Multiscale dynamics of helicity-dependent all-optical magnetization reversal in ferromagnetic Co/Pt multilayers*. Physical Review B **96**, 224421 (2017).
- [237] Y. Quessab, R. Medapalli, M. S. El Hadri, M. Hehn, G. Malinowski, E. E. Fullerton, and S. Mangin: *Helicity-dependent all-optical domain wall motion in ferromagnetic thin films*. Physical Review B **97**, 054419 (2018).
- [238] U. Parlak, R. Adam, D. E. Bürgler, S. Gang, and C. M. Schneider: *Optically induced magnetization reversal in [Co/Pt] $_N$  multilayers: Role of domain wall dynamics*. Physical Review B **98**, 214443 (2018).
- [239] G. Kichin, M. Hehn, J. Gorchon, G. Malinowski, J. Hohlfeld, and S. Mangin: *From Multiple- to Single-Pulse All-Optical Helicity-Dependent Switching in Ferromagnetic Co/Pt Multilayers*. Physical Review Applied **12**, 024019 (2019).
- [240] F. Cheng, Z. Du, X. Wang, Z. Cai, L. Li, C. Wang, A. Benabbas, P. Champion, N. Sun, L. Pan, and Y. Liu: *All-Optical Helicity-Dependent Switching in Hybrid Metal-Ferromagnet Thin Films*. Advanced Optical Materials **8**, 2000379 (2020).
- [241] M. Djordjević Kaufmann: *Magnetization dynamics in all-optical pump-probe experiments: spin-wave modes and spin-current damping*. Ph. D. thesis, Georg-August-University Göttingen, (2007).
- [242] J. Walowski: *Physics of laser heated ferromagnets: Ultrafast demagnetization and magneto-Seebeck effect*. Ph. D. thesis, Georg-August-University Göttingen, (2012).
- [243] S. Kuhrau, F. Klodt-Twesten, C. Heyn, H. P. Oepen, and R. Frömter: *Cap-layer-dependent oxidation of ultrathin cobalt films and its effect on the magnetic contrast in scanning electron microscopy with polarization analysis*. Applied Physics Letters **113**, 172403 (2018).

- [244] M. Suzuki, H. Muraoka, Y. Inaba, H. Miyagawa, N. Kawamura, T. Shimatsu, H. Maruyama, N. Ishimatsu, Y. Isohama, and Y. Sonobe: *Depth profile of spin and orbital magnetic moments in a subnanometer Pt film on Co*. *Physical Review B* **72**, 054430 (2005).
- [245] T. Roth, A. J. Schellekens, S. Alebrand, O. Schmitt, D. Steil, B. Koopmans, M. Cinchetti, and M. Aeschlimann: *Temperature Dependence of Laser-Induced Demagnetization in Ni: A Key for Identifying the Underlying Mechanism*. *Phys. Rev. X* **2**, 021006 (2012).
- [246] V. M. Parakkat, K. R. Ganesh, and P. S. Anil Kumar: *Tailoring Curie temperature and magnetic anisotropy in ultrathin Pt/Co/Pt films*. *AIP Advances* **6**, 056118 (2016).
- [247] T. Koyama, A. Obinata, Y. Hibino, A. Hirohata, B. Kuerbanjiang, V. K. Lazarov, and D. Chiba: *Dependence of Curie temperature on Pt layer thickness in Co/Pt system*. *Applied Physics Letters* **106**, 132409 (2015).
- [248] E. of Engineering Toolbox: *Air Thermal Conductivity vs. Temperature and Pressure*. [online] Available at: [https://www.engineeringtoolbox.com/air-properties-viscosity-conductivity-heat-capacity-d\\_1509.html](https://www.engineeringtoolbox.com/air-properties-viscosity-conductivity-heat-capacity-d_1509.html), (Accessed 02.05.2022).
- [249] I. Abdulgatov, S. Emirov, T. Tsomaeva, K. Gairbekov, S. Askerov, and N. Magomedova: *Thermal conductivity of fused quartz and quartz ceramic at high temperatures and high pressures*. *Journal of Physics and Chemistry of Solids* **61**, 779–787 (2000).
- [250] H. R. Shanks, P. D. Maycock, P. H. Sidles, and G. C. Danielson: *Thermal Conductivity of Silicon from 300 to 1400 K*. *Physical Review* **130**, 1743–1748 (1963).
- [251] Y. Terada, K. Ohkubo, T. Mohri, and T. Suzuki: *Thermal conductivity of cobalt-base alloys*. *Metallurgical and Materials Transactions A* **34**, 2026–2028 (2003).
- [252] G. A. Slack: *Platinum as a Thermal Conductivity Standard*. *Journal of Applied Physics* **35**, 339–344 (1964).
- [253] I. V. Savchenko and S. V. Stankus: *Thermal conductivity and thermal diffusivity of tantalum in the temperature range from 293 to 1800 K*. *Thermophysics and Aeromechanics* **15**, 679–682 (2008).
- [254] A. H. Seville: *The heat capacity of platinum at high temperatures*. *The Journal of Chemical Thermodynamics* **7**, 383–387 (1975).
- [255] N. D. Milošević, G. S. Vuković, D. Z. Pavičić, and K. D. Maglić: *Thermal properties of tantalum between 300 and 2300 K*. *International Journal of Thermophysics* **20**, 1129–1136 (1999).
- [256] F. Wang, D. E. Bürgler, R. Adam, U. Parlak, D. Cao, C. Greb, S. Heidtfeld, and C. M. Schneider: *Magnetization relaxation dynamics in [Co/Pt]3 multilayers on pico- and nanosecond timescales*. *Physical Review Research* **3**, 033061 (2021).
- [257] P. Li, T. J. Kools, R. Lavrijsen, and B. Koopmans: *Ultrafast racetrack based on compensated Co/Gd-based synthetic ferrimagnet with all-optical switching*. arXiv:2204.11595 [cond-mat], (2022).
- [258] I. A. Dolgikh, T. G. H. Blank, G. Li, K. H. Prabhakara, S. K. K. Patel, A. G. Buzdakov, R. Medapalli, E. E. Fullerton, O. V. Koplak, J. H. Mentink, K. A. Zvezdin, A. K. Zvezdin, P. C. M. Christianen, and A. V. Kimel: *Ultrafast Emergence of Ferromagnetism in Antiferromagnetic FeRh in High Magnetic Fields*. , (2022).
- [259] Y. W. Windsor, S.-E. Lee, D. Zahn, V. Borisov, D. Thonig, K. Kliemt, A. Ernst, C. Schüßler-Langeheine, N. Pontius, U. Staub, C. Krellner, D. V. Vyalikh, O. Eriksson, and L. Rettig: *Exchange*

*scaling of ultrafast angular momentum transfer in 4f antiferromagnets*. Nature Materials **21**, 514–517 (2022).

- [260] X. Wang, R. Y. Engel, I. Vaskivskyi, D. Turenne, V. Shokeen, A. Yaroslavtsev, O. Grånäs, R. Knut, J. O. Schunck, S. Dziarzhytski, G. Brenner, R.-P. Wang, M. Kuhlmann, F. Kuschewski, W. Bronsch, C. Schüßler-Langeheine, A. Styervoyedov, S. S. P. Parkin, F. Parmigiani, O. Eriksson, M. Beye, and H. A. Dürr: *Ultrafast manipulation of the NiO antiferromagnetic order via sub-gap optical excitation*. , (2022).
- [261] H. Li, S. Ruan, and Y. Zeng: *Intrinsic Van Der Waals Magnetic Materials from Bulk to the 2D Limit: New Frontiers of Spintronics*. Advanced Materials **31**, 1900065 (2019).
- [262] K. F. Mak, J. Shan, and D. C. Ralph: *Probing and controlling magnetic states in 2D layered magnetic materials*. Nature Reviews Physics **1**, 646–661 (2019).
- [263] M. Gibertini, M. Koperski, A. F. Morpurgo, and K. S. Novoselov: *Magnetic 2D materials and heterostructures*. Nature Nanotechnology **14**, 408–419 (2019).
- [264] M. P. M. Dean, Y. Cao, X. Liu, S. Wall, D. Zhu, R. Mankowsky, V. Thampy, X. M. Chen, J. G. Vale, D. Casa, J. Kim, A. H. Said, P. Juhas, R. Alonso-Mori, J. M. Glowonia, A. Robert, J. Robinson, M. Sikorski, S. Song, M. Kozina, H. Lemke, L. Patthey, S. Owada, T. Katayama, M. Yabashi, Y. Tanaka, T. Togashi, J. Liu, C. Rayan Serrao, B. J. Kim, L. Huber, C.-L. Chang, D. F. McMorrow, M. Först, and J. P. Hill: *Ultrafast energy- and momentum-resolved dynamics of magnetic correlations in the photo-doped Mott insulator Sr2IrO4*. Nature Materials **15**, 601–605 (2016).
- [265] J. M. Losada, A. Brataas, and A. Qaiumzadeh: *Ultrafast control of spin interactions in honeycomb antiferromagnetic insulators*. Physical Review B **100**, 060410 (2019).
- [266] J. He and T. Frauenheim: *Optically Driven Ultrafast Magnetic Order Transitions in Two-Dimensional Ferrimagnetic MXenes*. The Journal of Physical Chemistry Letters **11**, 6219–6226 (2020).

# Acknowledgments

First, I want to express my gratitude to Prof. Wolfgang Kuch. For the opportunity to work on this project and, more importantly, the trust, appreciation, enthusiasm, and ongoing dedication you expressed towards me and this work. This thesis would not have been possible without your continuing support, whether in the lab, at the synchrotron, or when evaluating data.

I also want to thank Prof. Dr. Alexei Erko for supervising this thesis and showing interest in my work. Equally important to this work is the team that helped perform all the necessary tasks required to carry out measurements, grow samples, analyze data, present data, and survive the everyday chaos. Therefore, I want to thank all the members of the AG that I had the pleasure of working with. In the following, I want to express my individual thanks in no particular order.

- Tauqir Shinwari for all the discussions and work we shared, which have helped me grow more than you might think.
- Fabian Nickel helped me get started and gave me essential pointers on developing my work.
- Lucas Arruda always found time to help me and share his experience. I truly miss our bouldering sessions.
- Ismet Gelen for the invaluable experiences and, more importantly, for always offering a helping hand whenever I needed anything.
- Lalmin Kipgen for the tips on UHV chambers and the shared beamtimes.
- Evangelos Golias for sharing invaluable insights into physics, lab work, teaching, love, anger, and simply life.
- Marion Badow for the assistance in all paperwork-related tasks. I can not stress the importance of your work enough.
- Jendrik Gördes for the lively discussions and teamwork during beamtimes.
- Sebastien Hadjadj, you inspired me with your dedication to our work and the fruitful collaborations you launched.
- Rahil Hosseinifar for the amazing teamwork and powerful synergy during beamtimes and all the TRR-related work.
- Sangeeta Thakur, you always helped me with every issue I encountered, and I hope that we can publish more work together in the future.
- Uwe Lipowski for the ongoing technical support. It did not matter if it was a pneumatic table or a UHV chamber. You always find a solution.

- Jorge Torres for the successful beamtimes and the good discussions.
- Marcel Walter for supporting me with your amazing programming skills and motivating me to go running together.
- Christiane Cech for taking care of everything when Marion left.
- Chowdhury Shadman Awsaf, not limited to, but most importantly for helping me set up the TR-MOKE and realizing the first successful measurements.
- Karl Frischmuth helped with the initial set-up of the MOKE-1 chamber and did all the hard calibration work.

I also want to thank all the other students I had the opportunity to work with. Your help in realizing projects and ideas was vital for the successful measurements. Also I want to thank Yasser Shokr who introduced me to many of the instruments in the lab. Similarly, I want to thank the electronic and mechanic workshop of the physics department that provided assistance and repairs for virtually everything that broke during my time. Many thanks also go to Julia Walter, Christian Frischkorn, and Britta Anstötz for the organizing work in the frame of the TRR227. I am incredibly grateful for the fantastic opportunities you created to network and meet the students of the associated groups. The exchange of knowledge and experience helped me throughout the Ph.D time. Equally important for me were the possibilities offered by the TRR to go to conferences and present my research. I also want to express my thanks to Sangeeta Sharma, who helped me understand the concepts of DFT and optical response functions, and to Peter M. Oppeneer for the successful collaboration.